ST. LOUIS PUBLIC LIBRARY AUG 3 1957

# JOURNAL OF THE AERONAUTICAL SCIENCES

VOLUME 24 AUGUST, 1957 NUMBER 8

## CONTENTS

Effects of Compressibility at Low Reynolds Number ..... SIR GEOFFREY TAYLOR AND P. G. SAFFMAN 553

Flutter of Rectangular Simply Supported Panels at High Supersonic Speeds ..... JOHN M. HEDGEPETH 563

The Aerodynamic Action of Triangular Horn-Balanced Control Surfaces on the Supersonic Delta Wing ..... DEREK NAYLOR 574

Fixing Boundary-Layer Transition on Supersonic Wind-Tunnel Models ..... MARVIN LUTHER 579

The Stability of Thin-Walled Unstiffened Circular Cylinders Under Axial Compression Including the Effects of Internal Pressure ..... LEONARD A. HARRIS, HERBERT S. SUER, WILLIAM T. SKENE, AND ROLAND J. BENJAMIN 587

Effects of Leading-Edge Separation on Thin Wings in Two-Dimensional Incompressible Flow ..... L. F. CRABTREE 597

Bending Strength of Tubing in the Plastic Range ..... CLIFFORD S. ADES 605

A Simple Model Study of Transient Temperature and Thermal Stress Distribution Due to Aerodynamic Heating ..... GABRIEL ISAKSON 611

The Effect of Amplitude on the Torsional Vibrations of Solid Wings Subjected to Aerodynamic Heating ..... JOSEF SINGER 620

Readers' Forum ..... 623

*Published by*
INSTITUTE OF THE AERONAUTICAL SCIENCES, INC.

# JOURNAL OF THE AERONAUTICAL SCIENCES

*Editor:* W. R. SEARS
*Director, Graduate School of Aeronautical Engineering, Cornell University*

*Associate Editor:* ROBERT R. DEXTER *Managing Editor:* RITA J. TURINO
*Editorial Assistant:* CAROLINE TAYLOR

## Editorial Committee

**Aerodynamics and Fluid Mechanics**
Holt Ashley
H. Julian Allen
Dean R. Chapman
Francis H. Clauser
Hugh L. Dryden
John C. Evvard
Antonio Ferri
Alexander Flax
Wallace D. Hayes
R. T. Jones
Carl Kaplan
H. W. Liepmann
C. C. Lin
H. F. Ludloff
Harold Luskin
Clark B. Millikan
H. J. E. Reid
George S. Schairer
G. B. Schubauer
John Stack
Theodore Theodorsen
Arthur N. Tifford
Th. von Kármán

**Flight Testing**
R. R. Gilruth
Melvin N. Gough
W. L. Howland
W. F. Milliken, Jr.

**Rotating Wing Aircraft**
F. B. Gustafson
K. H. Hohenemser
Bartram Kelley
R. B. Maloy
Ralph McClarren
R. H. Miller
R. H. Prewitt
Igor I. Sikorsky

**Structures**
John E. Duberg
R. R. Heldenfels
N. J. Hoff
Samuel Levy
J. F. McBrearty
W. Ramberg
E. E. Sechler
F. R. Shanley
C. R. Strang
S. Timoshenko

**Meteorology**
C. F. Brooks
D. M. Little
F. W. Reichelderfer
K. C. Spengler

**Vibration and Flutter**
Lee Arnold
M. A. Biot
R. L. Bisplinghoff
Harold A. Cheilek
I. E. Garrick
Martin Goland

**Aircraft Design**
W. E. Beall
E. H. Heinemann
Hall L. Hibbard
Richard Hutton
C. L. Johnson
A. A. Kartveli
F. K. Teichmann

**Electronics**
K. C. Black
M. V. Kiebert, Jr.
David S. Little
Paul Rosenberg
Giles J. Strickroth

**Physiologic Problems**
H. G. Armstrong
Louis H. Bauer
Robert J. Benford
W. Randolph Lovelace, II
Ross A. MacFarland

**Flight Propulsion**
William Bollay
George W. Brady
R. P. Kroon
Frank E. Marble
Abe Silverstein
E. S. Taylor

**Instruments**
Alan G. Binnie
Charles H. Colvin
Frank R. Cook
C. S. Draper
S. G. Eskin
C. F. Savage
R. C. Sylvander

## SUBSCRIPTION RATES

JOURNAL OF THE AERONAUTICAL SCIENCES, Published Monthly. United States and Possessions: 1 Year, $15.00; Single Copies, $1.50. Foreign Countries Including Canada (American Currency Rates): 1 Year, $16.00; Single Copies, $1.50.

AERONAUTICAL ENGINEERING REVIEW, Published Monthly. United States and Possessions: 1 Year, $3.00; Single Copies, $0.50. Foreign Countries Including Canada (American Currency Rates): 1 Year, $3.50; Single Copies, $0.50.

Notices of change of address should be sent to the Institute at least 30 days prior to actual change of address.

Manuscripts for publication, proofs, and all correspondence should be addressed to the Editorial Office of the JOURNAL.

Publication Office, 20th and Northampton Sts., Easton, Pa. Correspondence regarding subscriptions may be addressed to the Editorial Office of the JOURNAL OF THE AERONAUTICAL SCIENCES, 2 East 64th Street, New York 21, N.Y.

© *Copyright, 1957, by the Institute of the Aeronautical Sciences, Inc.*

Entered as Second-Class Matter at the Post Office, Easton, Pa., May 1, 1937. Acceptance for mailing at a special rate of Postage provided for in the Act of August 24, 1912. Authorized April 29, 1937.

JOURNAL OF THE AERONAUTICAL SCIENCES

VOLUME 24 AUGUST, 1957 NUMBER 8

# Effects of Compressibility at Low Reynolds Number

SIR GEOFFREY TAYLOR AND P. G. SAFFMAN

*Cavendish Laboratory, University of Cambridge*

SUMMARY

Reiner[1] has observed a high pressure amounting to half an atmosphere at the center of the airspace between two parallel plates when they are very close together and one of them rotates. These observations were interpreted by him as being due to assumed non-Newtonian properties in air. Since aerodynamic theory is founded on the Navier-Stokes equations which do not allow for non-Newtonian effects, it seemed desirable to explore possible conditions in which these equations might predict a high pressure between the plates. The effect of geometrical and dynamical imperfections in the experimental apparatus is calculated, two particular cases being considered in detail: (A) a small error in the perpendicularity of either of the plates to the axis of rotation and (B) a small vibration of the rotor parallel to its axis. When the fluid is assumed incompressible, the mean value of the excess pressure is found to be zero. The compressibility of the air changes this result, and mean pressures of the same order of magnitude as those observed experimentally are then predicted.

The effect is compared with that of compressibility in air-lubricated bearings. A corollary of the analysis leads to the conclusion that, when two wavy or rough surfaces slide over one another, the effect of compressibility is to make the air layer between them exert a pressure tending to keep them apart.

## INTRODUCTION

POPPER AND REINER[2] describe a most interesting experiment which was demonstrated by Professor Reiner at the 9th International Congress of Applied Mechanics at Brussels, 1956. A flat rotor disc 6.7 cm. in diameter was spun at about 7,000 r.p.m. about its axis of symmetry opposite a fixed stator disc which was also perpendicular to this axis. The stator was then moved slowly toward the rotor by means of a fine micrometer screw. A hole about 4 mm. in diameter in the center of the stator was connected to one side of a manometer, the other side of which was open to the atmosphere. When the gap between the plates was 0.5 mm. apart, the manometer recorded a suction of about 1 cm. of water. This is close to what would be expected, for Stewartson[3] has calculated that the suction at the center should be $(3/20)\rho\omega^2a^2$, provided that the Reynolds Number $\rho\omega h^2/\mu$ is not too large compared with 1, where $a$ is the radius of the discs, $h$ the gap between them, $\omega$ the angular velocity, and $\rho$ and $\mu$ the density and viscosity of air. This is 1.1 cm. of water under the conditions of the above experiment.

This gap was then carefully closed, and the suction grew less till at 0.02 mm.—i.e., 20 microns—it disappeared. As the gap closed still further, the suction turned into a positive excess pressure. Excess pressures of up to half an atmosphere were reported before contact of the two plates occurred.

Reiner[1] interprets this experimental result as being due to a non-Newtonian or viscoelastic property of air analogous to that exhibited by certain fluids like rubber solution. These fluids have an elastic resistance to shear as well as viscosity and therefore possess a time of relaxation which manifests itself as a decreasing stress when the moving fluid is brought to rest or by the presence of "cross stresses"—i.e., normal stresses in the direction of the velocity and velocity gradient—when the fluid is sheared. Weissenberg[4] has demonstrated the existence of such non-Newtonian properties with apparatus very similar to that described above. When the space between rotor and stator was filled with certain fluids possessing long molecular chains, the pressure at the center was found to be higher than at the circumference.

Reiner puts forward his experiment as a demonstration that air possesses elasticity for shear stress. However, the kinetic theory of gases predicts a time of relaxation, $\mu/p_0$, for air equal to $1.9 \times 10^{-10}$ sec., where $p_0$ is atmospheric pressure; this time is, in fact, equal to the mean time between molecular collisions. Reiner cites Jeffreys as pointing out that it seems unlikely that any experiment could be devised which would involve times short enough or, as is equivalent, sufficiently large rates of shear to detect such effects. Under the con-

Presented at the Aerodynamics—I Session, Twenty-Fifth Annual Meeting, IAS, New York, January 28–31, 1957. Revised and received April 14, 1957.

ditions of Reiner's experiment, the separation of the discs would have to be about $4 \times 10^{-7}$ cm., which is about 1/25th of the mean free path, for the rate of shear to be comparable with the reciprocal of the relaxation time.

The non-Newtonian properties can be calculated, according to the kinetic theory of gases (see, for example, Chapman and Cowling,[5] page 265), as an effect which is described by the second approximation to the relationship between the stress and rate of strain tensors. On substituting into the expression for the non-Newtonian properties the velocity field given by the low Reynolds Number solution of the Navier-Stokes equations (i.e., Stewartson's solution) and neglecting the thermal stresses (which can be shown to be small), it is found that the non-Newtonian properties of the air are equivalent to a body force

$$(\mu^2\omega^2/2p_0h_0^2)\ [(\bar{\omega}_6 - \bar{\omega}_2)r,\ 0,\ \bar{\omega}_2(3r + 2z)]$$

per unit volume, where cylindrical polar coordinates $(r, \theta, z)$ are used, and $\bar{\omega}_2$, $\bar{\omega}_6$ are numbers related to the molecular structure of air. According to Chapman and Cowling, it is not unreasonable to take $\bar{\omega}_2 = 2$, $\bar{\omega}_6 = 8$. It can then be shown that this body force gives rise to a suction at the center of amount $3\mu^2\omega^2a^2 \div 2p_0h_0^2$, which is about 0.02 cm. of water when the gap is as small as 1 micron. Nevertheless, Reiner states that he disagrees with Jeffreys and that he believes that the very large effects he observes are due to the existence of non-Newtonian properties in air.

It is important to realize that, if Reiner's interpretation of his experiment is correct, the Navier-Stokes equations do not describe the mechanics of airflow. These equations are founded on the assumption that there is a linear (Newtonian) relationship between the stress and rate of strain tensors. The non-Newtonian effects postulated by Reiner to explain his experimental results would, if they exist, be important in other aerodynamical phenomena such as boundary layers or turbulence where similar rates of shear occur. On the other hand, the Navier-Stokes equations have been used to make predictions about these phenomena which have been verified in numerous experiments; in fact, all existing theories of aerodynamics which take account of viscosity are based on them. For this reason it seemed to us important to find out whether Reiner's experimental results can be interpreted in the light of the Navier-Stokes equations without assuming that air has the non-Newtonian properties which he postulates.

This was the primary object of the work described in the present paper, but the flow situation in Reiner's experiment is similar to that investigated in the theory of hydrodynamic lubrication, and our results seem to have some application in that field.

When two parallel discs, rotor and stator, are brought sufficiently close together, the Reynolds Number based on their mutual velocity and their distance apart is small and Stewartson's result, according to which the suction is independent of Reynolds Number, should apply. This result was given for incompressible fluids, but it seems that a similar result can be given if the fluid is compressible. The suction at the center has a different value but is constant if $h$ varies while $\omega$ and $a$ remain constant. There is therefore no possibility of explaining Reiner's experimental result using the Navier-Stokes equations if his apparatus is really functioning in the ideal manner which mathematicians postulate for engineering constructions—that is, as a perfect plane exactly parallel to another plane and rotating at uniform speed about a point in the plane.

The questions to be considered now are what sort of deviations from the ideal may be expected in apparatus constructed by competent engineers and what effect would these have on the distribution of pressure between the discs. Perhaps the most obvious deviations from the mathematical ideal is the rise in temperature arising from the large amount of work done on the film of air. This can be shown, however, to be far too small to produce any measurable effect on the central pressure. Further deviations are the inevitable lack of geometrical and dynamical perfection in the apparatus. These give rise to effects which, in turn, can be idealized and discussed in the light of the Navier-Stokes equations. We shall now discuss two of these in some detail:

The first (A) is the effect of a slight error in the perpendicularity of the plane of either the stator or rotor to the axis of rotation. The second (B) is the effect of vibration of the rotor in the direction of its axis. We have, in fact, analyzed more and shall give the relevant results later.

## Effect of Small Error in Perpendicularity and Effect of Vibration

It has been seen that the effect observed by Reiner was very much larger than, and of opposite sign to, that which would arise from inertia. In the first instance, therefore, inertia will be neglected, and the equations of hydrodynamic lubrication which involve only the effect of Newtonian viscosity will be used (see, for example, Lamb,[6] section 330a). The thickness $h$ of the thin layer between rotor and stator is taken as a function of polar coordinates $r$, $\theta$ and of the time $t$. When the rotor is rotating with angular velocity $\omega$, the relevant equations for the pressure $p$ are

$$(h^3/12\mu)\ (\partial p/\partial r) + \bar{u}h = 0 \qquad (1)$$

$$(h^3/12\mu)\ (\partial p/r\partial\theta) + \bar{v}h - (1/2)h\omega r = 0 \qquad (2)$$

Here $\mu$ is the viscosity, $u$ and $v$ are the radial and tangential components of the velocity, and the bars indicate that the mean value through the thickness of the layer has been taken. These equations are a good approximation provided that $\|\text{grad } h\|$, which is of order $h/a$ where $a$ is the radius of the discs, is small compared with 1 and the pressure gradient due to inertia, which is of order $(3/10)\rho\omega^2 r$, is small compared with that due to the viscous stress which is of order

$6\mu\omega r/h^2$—i.e., provided that $\rho\omega h^2/20\mu$ is small compared with 1.

The equation of continuity is

$$(\partial/\partial r)\,(rh\bar{u}\rho) + (\partial/\partial\theta)\,(h\bar{v}\rho) + r(\partial/\partial t)\,(\rho h) = 0 \quad (3)$$

and the density $\rho$ will be taken either as constant if the fluid is incompressible or as proportional to the pressure if it is compressible so that $\rho/\rho_0 = p/p_0$. The justification for this assumption is that the layer is so thin that conductivity prevents any appreciable variation in temperature due to adiabatic compression from occurring. Eliminating $\bar{u}$ and $\bar{v}$ between Eqs. (1), (2), and (3), the equation for $p$ is

$$(\partial/\partial r)\,[(\rho rh^3/\mu)\,(\partial p/\partial r)] + (\partial/\partial\theta)\,[(\rho h^3/\mu r)\,(\partial p/\partial\theta)] = 6\omega(\partial/\partial\theta)\,(\rho rh) + 12(\partial/\partial t)\,(\rho rh) \quad (4)$$

This may be expressed nondimensionally by writing

$$\left.\begin{aligned} r' &= r/a, \quad t' = t\omega, \quad p' = (p - p_0)/p_0 \\ h' &= h/h_0, \quad \rho = \rho_0(1 + p') \end{aligned}\right\} \quad (5)$$

Eq. (4) then becomes, taking the viscosity as independent of the density,

$$(\partial/\partial r')\,[r'h'^3(1 + p')\,(\partial p'/\partial r')] + (\partial/\partial\theta)\,[(h'^3/r) \times (1 + p')\,(\partial p'/\partial\theta)] = \lambda r'(\partial/\partial\theta)\,[h'(1 + p')] + 2\lambda r'(\partial/\partial r')\,[h'(1 + p')] \quad (6)$$

where $\lambda = 6\omega\mu a^2/p_0h_0^2$, and the condition to be satisfied at the edge $r' = 1$ is $p' = 0$. Eq. (6) can be used to represent either of the two deviations from the mathematical ideal.

For case (A), the error in perpendicularity, we take

$$h' = 1 + er' \cos\theta \quad (7)$$

where $eh_0/a$ is the angle between the plates. For case (B), vibration parallel to the axis, we take

$$h' = 1 + b \cos t'' \quad (8)$$

where $bh_0$ is the amplitude of the vibration, $t'' = nt = nt'/\omega$, and $n/2\pi$ is the frequency of the oscillation. Both $e$ and $b$ are numbers which range from 0 when the plates are parallel and free from vibration to 1 when they touch.

For case (A), Eq. (6) becomes

$$(\partial/\partial r')\left\{r'(1 + er'\cos\theta)^3\,(1 + p')\,(\partial p'/\partial r')\right\} + (\partial/\partial\theta)\left\{[(1 + er'\cos\theta)^3/r']\,(1 + p')\,(\partial p'/\partial\theta)\right\} = \lambda r'(\partial/\partial\theta)\left\{(1 + p')\,(1 + er'\cos\theta)\right\} \quad (9)$$

and, for case (B),

$$(1/r')\,(\partial/\partial r')\left\{r'(1 + p')\,(\partial p'/\partial r')\right\} = [N/(1 + b\cos t'')^3]\,(\partial/\partial t'')\left\{(1 + p')\,(1 + b\cos t'')\right\} \quad (10)$$

where $N = 12n\mu a^2/p_0h_0^2$.

## Incompressible Fluid

If the fluid is incompressible, $\rho$ disappears from Eq. (4), and Eqs. (9) and (10) are changed only by the omission of the factors $(1 + p')$. In case (A) it will be noticed that, since the boundary condition is $p' = 0$ at $r' = 1$, $p'$ must be antisymmetrical about the line $\theta = 0$. Thus the value of $p'$ at the point $(r', \theta)$ becomes $-p'$ at $(r', -\theta)$. The mean value of $p'$ over a circle at any given radius is therefore zero.

Similar considerations apply to case (B), for, taking the mean value of $p'$ at a fixed point, the right-hand side of Eq. (10) can be integrated when the factor $(1 + p')$ is omitted, and its mean value over a period is therefore zero.

Thus, it will be seen that, if the fluid between the plates is incompressible, neither of the deviations (A) or (B) from the mathematical ideal could account for the rise in pressure at the center which Reiner observed. Nonzero pressures at the center will arise only if the lack of geometrical perfection is asymmetrical about every diameter—for example, if there is a spiral marking or elevation on one of the plates. But an examination of the equation for an incompressible fluid shows that the excess pressure then depends on the direction of rotation, and a pressure rise is altered to a pressure drop of equal magnitude when the direction of rotation of the motor is reversed. It follows that a mean pressure rise independent of the direction of rotation and different from zero cannot occur if the fluid is incompressible.

## Compressible Fluid

It is commonly thought that the effects of compressibility are important only when Mach Numbers are high. In Reiner's experiment where the speed of rotation of the rotor was, say, 9,000 r.p.m. and the diameter of the discs 6.7 cm., the Mach Number of the fluid was less than 0.05. At first sight, therefore, one might not expect compressibility to alter the conclusion just reached for incompressible fluids that the small errors of construction just considered cannot give rise to the central pressure observed by Reiner. On the other hand, it has been found in the study of the mechanics of air-lubricated bearings that compressibility may have importance in cases where fluid is dragged into a narrow space and that the flow of a compressible fluid may be very different from that of an incompressible one.[7]

Unfortunately, Eqs. (9) and (10) are nonlinear and their complete solution would be difficult, but, if $e$ is assumed small in Eq. (9) or $b$ in Eq. (10), analytical solutions of the linearized equation can be obtained. It is also possible to linearize these equations in another way. If we had considered a compressible gas for which $\mu/\rho$ was independent of density instead of $\mu$, the factor $(1 + p')$ would have disappeared from the left-hand side of Eq. (9), and the resulting linear equation could be solved numerically using the relaxation technique even if $e$ were not small. Since the greatest effect of compressibility seems to arise from the factor $(1 + p')$ on the right-hand side of Eq. (9) (this is indicated by the analytical solution obtained below for small $e$), it is useful to have such a solution, and Miss G. Vaisey has given the one represented in Fig. 1(b) for the case when the error in perpendicularity

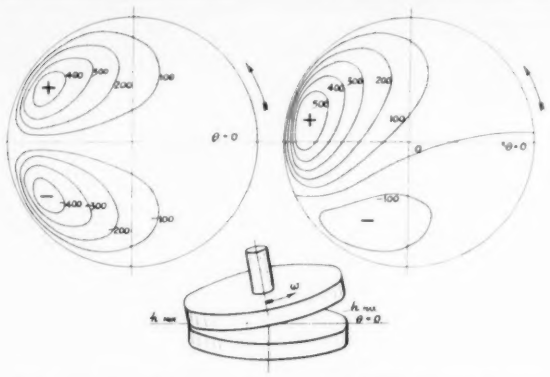

FIG. 1. Pressure between disc rotating about its axis of symmetry and a fixed disc set at a small angle to it. *Left:* (a) Contours for incompressible fluid with $\lambda = 4$, $e = 0.8$, atmosphere = 1,000. *Right:* (b) Contours for compressible fluid under the same conditions. (Relaxation solutions by G. Vaisey.)

of the stator is $e = 0.8$, $\lambda = 4$. In Fig. 1 the contours represent values of 1,000 $p'$.

For comparison, the contours of $p'$ are also shown in Fig. 1(a) for the case when the fluid is incompressible (this Figure is also due to Miss Vaisey), but otherwise the conditions are the same as for the compressible case. It will be seen that the effect of compressibility is very large. The part of the field where there is suction which covered half the field in the incompressible case has contracted, and the maximum suction is now only about one fifth of the maximum excess pressure. The maximum pressure is in fact 1.6 atmospheres while the minimum is 0.9 atmospheres. It will be noticed that the effect of compressibility is to raise the average pressure at all radii including that at the center. The value $\lambda = 4$ was chosen for numerical computation because it corresponds with that of Reiner's rotor rotating at 9,000 r.p.m. when $h_0 = 16.7$ microns—i.e., near the distance at which Reiner's effect appeared.

## Analytical Solutions

When $e$ or $b$ are small, analytical solutions of Eqs. (9) and (10) can be found. Eq. (10) for case (B) will be considered first since the analysis is simpler.

*Case (B):* We expand the dimensionless pressure $p'$ as a power series in $b$

$$p' = p_1 b + p_2 b^2 + p_3 b^3 + \ldots \tag{11}$$

substitute into Eq. (10), and equate the coefficients of $b$ and $b^2$, obtaining

$$(1/r')\,(\partial/\partial r')\,[r'(\partial p_1/\partial r')] - N(\partial p_1/\partial t'') = -Nb\sin t'' \tag{12}$$

$$(1/r')\,(\partial/\partial r')\,[r'(\partial p_2/\partial r')] - N(\partial p_2/\partial t'') = N(\partial/\partial t'')\,(p_1\cos t'') - (1/r')\,(\partial/\partial r')r' \times [p_1(\partial p_1/\partial r') + 3(\partial p_1/\partial r')\cos t''] \tag{13}$$

The boundary conditions on $p_1$ and $p_2$ are that they should be zero at the edge of the discs where $r' = 1$ and finite at the center where $r' = 0$. To solve Eq. (12), put

$$p_1 = f(r')\cos t'' + g(r')\sin t''$$

and equate coefficients of $\cos t''$ and $\sin t''$, obtaining

$$(1/r')\,(d/dr')\,[r'(df/dr')] - Ng = 0$$
$$(1/r')\,(d/dr')\,[r'(dg/dr')] + Nf = -N$$

We subtract $i$ times the second equation from the first and write

$$\chi = f(r') - ig(r')$$

giving

$$(1/r')\,(d/dr')\,[r'(d\chi/dr')] - Ni\chi = Ni \tag{14}$$

The solution of Eq. (14) which satisfies $\chi(1) = 0$, $\chi(0)$ finite is (see McLachlan[8])

$$\chi(r') = [J_0(r'\sqrt{-iN})/J_0(\sqrt{-iN})] - 1$$

Writing

$$J_0(x\sqrt{-i}) = ber\,x + i\,bei\,x$$

and

$$|J_0(x\sqrt{-i})| = M(x)$$

the solution of Eq. (14) is

$$\left.\begin{aligned} f(r') &= [M(\sqrt{N})]^{-2}\,(ber\sqrt{N}\,ber\,r'\sqrt{N} + bei\sqrt{N}\,bei\,r'\sqrt{N}) - 1 \\ g(r') &= [M(\sqrt{N})]^{-2}\,(ber\sqrt{N}\,bei\,r'\sqrt{N} - bei\sqrt{N}\,ber\,r'\sqrt{N}) \end{aligned}\right\} \tag{15}$$

We note that $\bar{p}_1 = 0$, where the bar denotes a mean at a given point with respect to time. This is to be expected since the value of $p_1$ is clearly unaltered if the fluid is taken as incompressible and also because the mean pressure must be independent of the sign of $b$ since a change of sign of $b$ corresponds to the addition of $\pi$ to $t''$. We are, of course, interested primarily in the mean pressure since this is what is observed experimentally; so, taking the mean of Eq. (13), we have

$$(1/r')\,(d/dr')\,[r'(d\bar{p}_2/dr')] = -(1/r')\,(d/dr')r'(d/dr')\,[(1/2)\bar{p}_1^2 + \overline{3p_1\cos t''}]$$

This equation can be integrated immediately to give

$$\bar{p}_2 = -(3/2)f(r') - (1/4)\,[f^2(r') + g^2(r')] \tag{16}$$

where $f(r')$ and $g(r')$ are given by Eq. (15).

Eq. (16) gives the distribution of mean pressure across the discs due to vibration. For values of $N$ small compared with 3, it is found that a first approximation to Eq. (16) is

$$\bar{p}_2 = (N^2/2^7)\,(7 - 8r'^2 + r'^4) \tag{17}$$

For $N$ large, $\bar{p}_2 \sim 5/4$ provided that $(1 - r')N^{1/2} \gg 1$—that is, the pressure between the discs is constant and independent of the frequency except in the neighborhood of the edges of the discs where a rapid transition to atmospheric pressure takes place.

Inspection of the equation for $p_3$ shows that $\bar{p}_3 = 0$ so that the error is using Eq. (16) is of order $b^4$. In particular, the mean pressure $\bar{p}'$ at the center is

$$\bar{p}' = b^2\{(5/4) - [ber\sqrt{N}/M^2(\sqrt{N})] - [1/4M^2(\sqrt{N})]\} + O(b^4) \quad (18)$$

This expression is always positive so that this effect of vibration is to raise the pressure at the center.

*Case (A):* Here the plates are inclined at a small angle, and Eq. (9) applies. We expand the dimensionless pressure as a power series in $e$, substitute into Eq. (9), and equate the coefficients of $e$ and $e^2$, obtaining

$$(1/r')(\partial/\partial r')[r'(\partial p_1/\partial r')] + (1/r'^2)(\partial^2 p_1/\partial\theta^2) - \lambda(\partial p_1/\partial\theta) = -\lambda r \sin\theta \quad (19)$$

$$(1/r')(\partial/\partial r')[r'(\partial p_2/\partial r')] + (1/r'^2)(\partial^2 p_2/\partial\theta^2) - \lambda(\partial p_2/\partial\theta) = \lambda(\partial/\partial\theta)(r' p_1\cos\theta) - (1/r'^2)\times(\partial/\partial\theta)[p_1(\partial p_1/\partial\theta) + 3r'\cos\theta(\partial p_1/\partial\theta)] - (1/r')\times(\partial/\partial r')[r' p_1(\partial p_1/\partial r') + 3r'^2\cos\theta(\partial p_1/\partial r')] \quad (20)$$

The boundary conditions on $p_1$ and $p_2$ are identical with those for case (B).

By a method very similar to that employed above, we find that

$$p_1 = A(r')\cos\theta + B(r')\sin\theta$$

where $C(r') = A - iB$ satisfies the equation

$$(1/r')(d/dr')[r'(dC/dr')] - (C/r'^2) - i\lambda C = \lambda i r' \quad (21)$$

The solution of Eq. (21) which fits the boundary conditions is

$$C(r') = [J_1(r'\sqrt{-i\lambda})/J_1(\sqrt{-i\lambda})] - r'$$

Hence,

$$\left.\begin{aligned} A(r') &= [M_1(\sqrt{\lambda})]^{-2}(ber_1\sqrt{\lambda}\, ber_1 r'\sqrt{\lambda} + bei_1\sqrt{\lambda}\, bei_1 r'\sqrt{\lambda}) - r' \\ B(r') &= [M_1(\sqrt{\lambda})]^{-2}(ber_1\sqrt{\lambda}\, bei_1 r'\sqrt{\lambda} - bei_1\sqrt{\lambda}\, ber_1 r'\sqrt{\lambda}) \end{aligned}\right\} \quad (22)$$

where $J_1(x\sqrt{-i}) = ber_1 x + ibei_1 x$ and $M_1(x) = |J_1(x\sqrt{-i})|$.

We again note that $\bar{p}_1 = 0$, where the bar denotes the mean value of the pressure around a circle of given radius—i.e.,

$$\bar{p}_1 = (1/2\pi)\int_0^{2\pi} p_1\, d\theta$$

To calculate $\bar{p}_2$, we take the mean of Eq. (20) and integrate to give

$$\bar{p}_2 = -3\int_{r'}^{1}\overline{r'\cos\theta(\partial p_1/\partial r')}dr' - (1/2)\bar{p}_1^2$$

Substituting for $p_1$, we then obtain

$$\bar{p}' = (3e^2/2)\int_{r'}^{1} r'(dA/dr')dr' - (e^2/4)(A^2 + B^2) + O(e^4) \quad (23)$$

$\bar{p}_3 = 0$ since the mean pressure over a circle of fixed radius must be independent of the sign of $e$.

The radial distribution of the mean pressure as given by expression (23) is shown in Fig. 2. Curve (1) represents the values of $2^8\bar{p}'/e^2\lambda^2$ which is applicable when $\lambda$ is small compared with 16 and is derived from the first term in a series expansion in powers of $\lambda^2$—namely,

$$\bar{p}' = (e^2\lambda^2/2^8)[(2/3)r'^6 - (5/2)r'^4 + r'^2 + (5/6)] \quad (24)$$

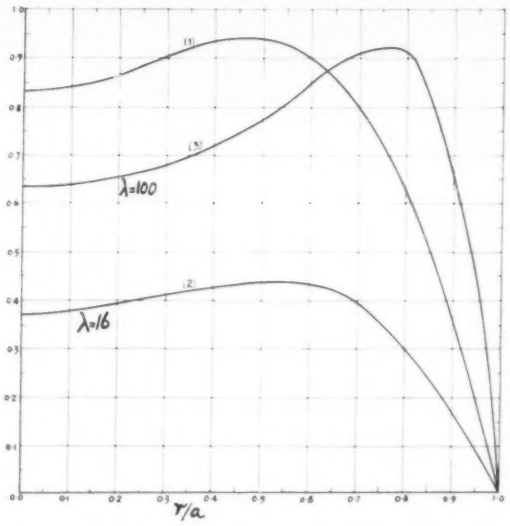


FIG. 2. Radial distribution of mean pressure between rotating and fixed inclined discs. Curve (1) gives the values of $256\bar{p}'/\rho_0 e^2\lambda^2$ valid for $\lambda$ small compared with 16. Curves (2) and (3) give $\bar{p}'/\rho_0 e^2$ for $\lambda = 16$ and $\lambda = 100$, respectively.

Curves (2) and (3) were calculated using the tabulated values of the Bessel functions of complex argument,[9] and they represent the values of $\bar{p}'/e^2$ for $\lambda = 16$ and $\lambda = 100$, respectively. Curve (1) gives, in fact, the value of $\bar{p}'/e^2$ for $\lambda = 16$ as calculated from the approximate expression (24). Since the actual values for $\lambda = 16$ are about one half of these, it follows that the mean pressure does not increase as rapidly as the square of the angular velocity of the rotor, the difference becoming noticeable as $\lambda$ approaches 16.

The second term on the right-hand side of Eq. (23) turns out to be small compared with the first, and, since it can be seen that the second term arises from the factor $(1 + p')$ on the left-hand side of Eq. (9), this provides some justification for the method of linearization adopted for the solution obtained using the relaxation technique. In fact, the values of the mean pressure calculated from Miss Vaisey's numerical solution of Eq. (9) with $e = 0.8$ and $\lambda = 4$ are in reasonable agreement with those predicted by the expression (23) with the same values for $e$ and $\lambda$, the latter being about 15 to 25 per cent lower. For instance, the value of 1,000 $\bar{p}'$ at the center is calculated from Eq. (24) to be 33, while from the numerical solution it is 38. However, the numerical solution has a large peak near $r' = 1$, and the agreement there with the analytical solution is not good. The reasons for this peak will be discussed in the next section.

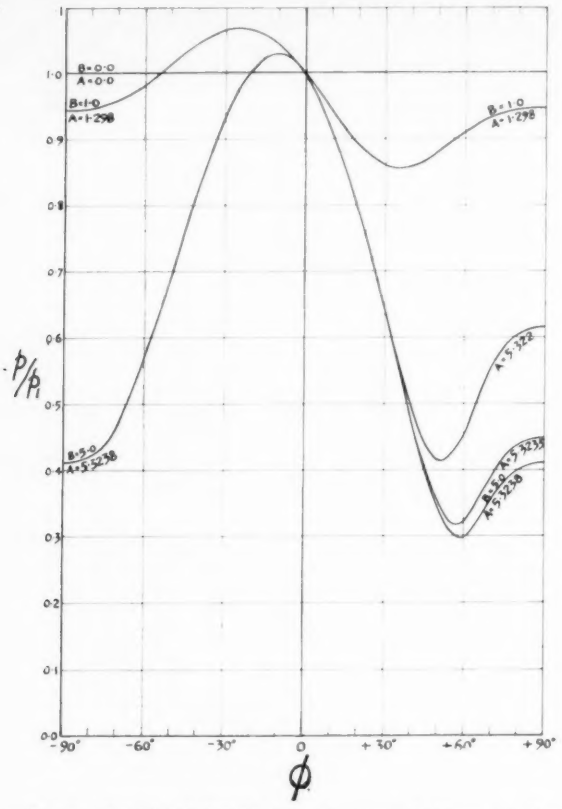


FIG. 3. Calculated distributions of pressure between rotating cylinder and plane when separated by a small gap. Solutions of $(d/d\phi)\,(p/p_1) = B\cos^2\phi - A(p_1/p)\cos^4\phi$.

To conclude this section, we remark that the solutions obtained above of Eqs. (9) and (10) are linearly superposable—that is, the effect of the deviations from the mathematical ideal represented by cases (A) and (B) may be calculated separately and added to give the mean pressure with error of order $e^2b^2$ when there are both vibration and an error in perpendicularity.

## Comparison With the Effect of Compressibility in Air-Lubricated Bearings

It will be noticed in Fig. 1 that there is a high concentration of pressure near the point $r' = 1$, $\theta = \pi$ where the plates are closest together. In this region the air is dragged by the rotor along a circular path into a passage which first narrows and then expands. When the plates nearly touch—i.e., when $1 - e$ is small—the flow in the region of near contact is like that in the space between a cylinder of radius $R = a^2/h_0$ and a fixed plane when the cylinder rotates with surface velocity $a\omega$ and the minimum gap is $h_1 = h_0(1 - e)$. If $x$ is the distance from the point where the gap is a minimum and $h_1$ is small compared with $R$,

$$h = h_1 + (1/2)\,(x^2/R) \tag{25}$$

Using Sommerfeld's variable $\phi$, $x = \sqrt{2Rh_1}\tan\phi$, $h = h_1\sec^2\phi$, and the range $-\infty < x < +\infty$ is covered by $-(1/2)\pi < \phi < (1/2)\pi$. Assuming that the temperature of the film of air is constant and equal to that of the plane and cylinder, the equation for the distribution of pressure can be reduced to

$$(d/d\phi)\,(p/p_1) = B\cos^2\phi - A(p_1/p)\cos^4\phi \tag{26}$$

where $B = 6\mu a\omega\sqrt{2Rh_1}/h_1^2p_1$

and $p_1$ is the pressure at $\phi = 0$. The required solution of Eq. (26) is one for which the pressure is equal to $p_0$ at $\phi = \pm(\pi/2)$. This condition, in fact, determines the value of $A$ which, in nondimensional form, represents the rate at which air passes through the gap.

When $B$ is very small, $p/p_1$ is nearly 1 and it may be taken as 1 in the last term of Eq. (26). It is then found that $A = 4B/3$ and that the solution of Eq. (26) is

$$(p - p_1)/p_1 = -(1/24)\,(2\sin 2\phi + \sin 4\phi) \tag{27}$$

and $p_1 = p_0$ since $\sin 2\phi$ and $\sin 4\phi$ both vanish at $\phi = \pm(\pi/2)$. This solution is well known in the theory of hydrodynamic lubrication when the lubricant is assumed to be incompressible, and in that case it is not limited to small values of $B$. The excess pressure $p - p_0$ is antisymmetrical, being positive when $\phi$, and therefore $x$, is negative and negative when $x$ is positive. Evidently the lubricant produces no resultant pressure perpendicular to the plane.

Eq. (27) may be solved numerically for any given value of $B$. Two examples, $B = 1$ and $B = 5$, have been solved by Dr. J. C. Miller. These are shown in Fig. 3, and in the case of $B = 5$ the method of solution is displayed. The calculated distributions of pressure for $A = 5.3220$ and $A = 5.3235$ were followed through, and it was found by extrapolation that the value of $A = 5.3238$ gives $p_0 = 0.412$ at $\phi = +(\pi/2)$ as well as at $\phi = -(\pi/2)$. The pressure at the center is therefore $p_1 = p_0/0.412 = 2.44$ atmospheres.

In Fig. 4 the distribution of pressure with $x$ for $B = 5$ is shown, and for comparison the distribution of pressure on an incompressible fluid of the same viscosity and under the same conditions is shown. It will be seen that the effect of compressibility is to increase the area where there is a positive excess pressure at the expense of the area where it is negative. Thus Miss Vaisey's calculation exhibited in Fig. 1(b) can be interpreted as physically analogous to the hydrodynamic regime in an air-lubricated bearing.

The distribution of pressure for $B = 1$ (see Fig. 3) is much nearer to the antisymmetrical distribution obtained with incompressible fluids, so that it is qualitatively true that the main change due to compressibility occurs as $B$ increases from 1 to 5. Ultimately, for large values of $B$ the pressure distribution becomes symmetrical. The broken curve in Fig. 4 shows the limiting form as $B$ tends to infinity.*

* An analytical solution of Eq. (26) valid for large values of $B$ has been obtained and will form the subject of a separate note. It is found that $p_0/p_1 \sim 10.5/B^2$ as $B \to \infty$. This is in good agreement with the value of $p_0/p_1$ obtained by Miller with $B = 5$

### Effect of Roughness When Two Surfaces Slide Past One Another

It will be noticed that the situation where the cylinder and plane are close together is the same as that between two wavy or rough surfaces when they move past one another tangentially. Thus, when two such surfaces move past one another so that they are nearly in contact at the high spots, the effect of compressibility is to make the air layer between them exert a pressure tending to hold them apart.

### Numerical Comparison With Reiner's Experiment

Popper and Reiner[2] report that at 7,000 r.p.m. the manometer connected to the hole in the center of the stator registered a suction, but, when the gap was closed to 0.02 mm.—i.e., 20 microns—the suction disappeared and excess pressure began. If $a = 3.35$ cm., this corresponds to $\lambda = 2.2$, so that this is just the point at which the effects of compressibility might be expected to begin to show themselves if there is any error of manufacture of the type considered under case (A).

In this connection it is worth noticing that, if it were argued that Reiner's apparatus is so exceedingly well made that it is unlikely that any large effect could be produced by a manufacturing error of the kind contemplated here, one should consider how the experiment was carried out. The stator was moved up towards the rotor, the pressure increasing as the gap closed. If there was literally no manufacturing error, the gap would close until $h_0 = 0$. This is evidently not a realistic approach. There must be some angular error in the placing of the stator. Suppose it is $\alpha$. The gap can then be closed until, when $h_0 = a\alpha$, there will be contact on the edge and $e = 1$. The value of $\lambda$ will then be $6\mu\omega/p_0\alpha^2$. Thus, the better the apparatus is constructed and the smaller therefore is $\alpha$, the bigger will be the value of $\lambda$ attained before actual contact of the discs. For this reason and because the mean pressure is an increasing function of $\lambda$, we come to the curious conclusion that, if the pressure observed by Reiner is due to this particular error of manufacture, the smaller this error is, the bigger is the pressure which can be produced by narrowing the gap between the

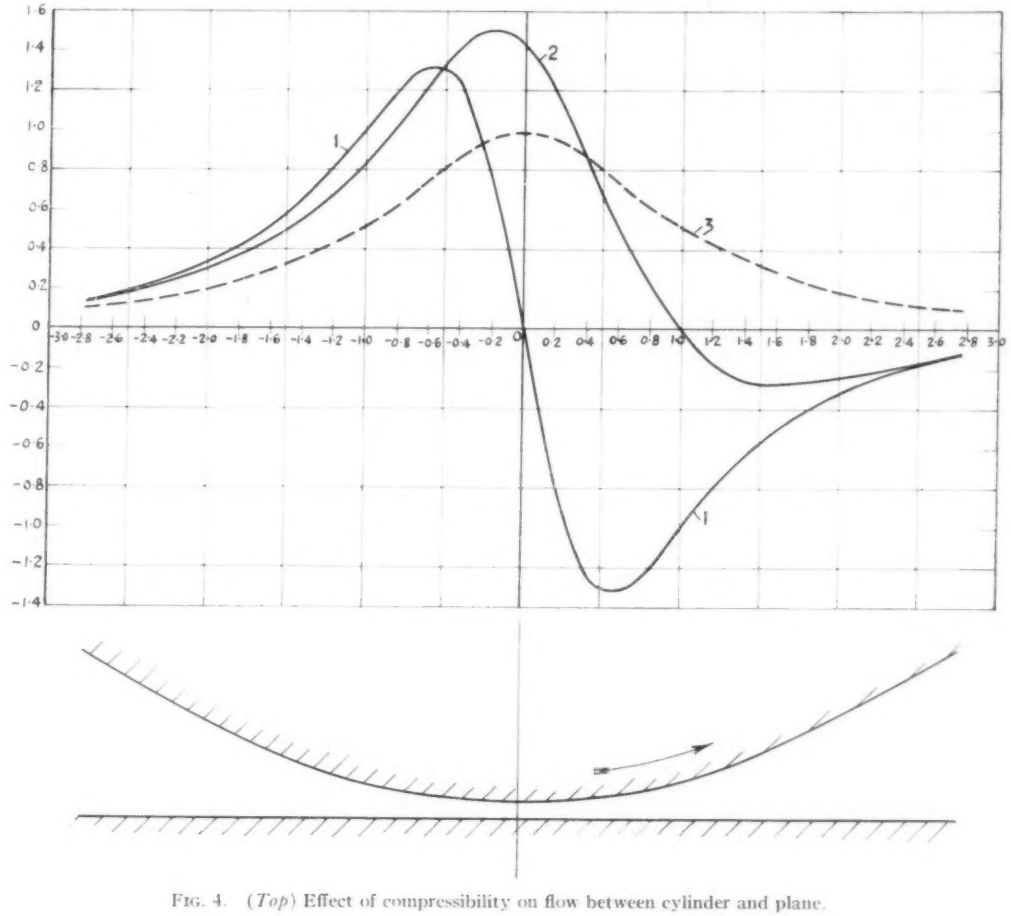


Fig. 4. (*Top*) Effect of compressibility on flow between cylinder and plane.

1 Fluid incompressible
2 Fluid compressible } $B = \dfrac{6\mu a\omega\sqrt{2Rh_1}}{p_1h_1^2} = 5$
3 Limiting form as $B \to \infty$ (not to scale)

(*Bottom*) Sketch of cylinder and plane. Vertical scale arbitrary, horizontal scale $x/\sqrt{2h_1R}$.

TABLE 1
Pressure at Center of Stator When Rotor Vibrates in Direction of the Axis of Rotation

| | | | |
|---|---|---|---|
| (1) $h_0$ (microns) | 20 | 10 | 5 |
| (2) $\sqrt{N}$ | 2.32 | 4.65 | 9.3 |
| (3) $\bar{p}'/b^2$ | 0.82 | 1.04 | 1.24 |
| (4) $b$ (with $\delta = 2.5$ microns) | 0.125 | 0.25 | 0.5 |
| (5) $\bar{p} - p_0$ (atmospheres) | 0.0128 | 0.065 | 0.31 |
| (6) $\bar{p} - p_0$ (cm. of water) | 13 | 66 | 320 |

TABLE 2
Pressure at Center of Stator When Inclined at Small Angle to Rotor

| | | | |
|---|---|---|---|
| (1) $h_0$ (microns) | 20 | 10 | 5 |
| (2) $\sqrt{\lambda}$ | 2 | 4 | 8 |
| (3) $\bar{p}'/e^2$ for $\gamma' = 0$ | 0.21 | 0.37 | 0.6(approx.) |
| (4) $e$ (with $\alpha = 4 \times 10^{-3}$ deg.) | 0.125 | 0.25 | 0.5 |
| (5) $\bar{p} - p_0$ (cm. of water) | 3 | 23 | 150 |

plates. This remark must, of course, be qualified by the condition that the gap should be large compared with the mean free path. This, however, is about 0.1 micron at atmospheric pressure, so that the fluid may be treated as a continuum in the range of Reiner's experiment.

Similar remarks can be made about the effect of vibrations which also produce a positive pressure at the center of the discs. Reiner appreciated the necessity for reducing this error and stated that the frequency of the natural vibrations of his apparatus was well above that of the rotation of his disc so that resonance would not be expected. On the other hand, shafts running in ball bearings are always liable to suffer a certain amount of longitudinal vibration, and, until that has been measured, it is not possible to say which of the two inevitable deviations (A) or (B) from the ideal produces the larger effect at the centers of the discs. In practice, dust of dimensions of 1 or 2 microns, or even more, may be expected in the unfiltered air in which Reiner's apparatus has been operated. Nevertheless, it is worth while to put some figures into our formulas to find out whether the observed pressure is within the range predicted by the Navier-Stokes equations for a well-made apparatus operated by carefully making the plates approach without touching.

For a numerical example for case (B), we may imagine a disc 7.3 cm. in diameter (approximately of the size used in Reiner's apparatus) running at 7,000 r.p.m., and suppose that it executes forced oscillations of small amplitude $\delta$ in the direction of the axis of rotation at frequency 7,000 cps. In Table 1 the corresponding values of $\sqrt{N}$ (see Eq. 10) are given in line 2 for various gaps $h_0$. In line 3 are given the values of $\bar{p}'/p_0b^2$ calculated from Eq. (18) using tables of Bessel functions. To obtain values for the mean excess pressure $\bar{p}' \ p_0$ at the center, it is necessary to assume a value for $\delta$. A disc running at 7,000 r.p.m. mounted on a well-constructed ball-bearing shaft might be expected to have longitudinal oscillation of amplitude at least 0.0001 in.—i.e., 2.5 microns. Assuming $\delta = 2.5$ microns, the values of $b = \delta/h_0$ are given in line 4, and the values of the excess pressure $\bar{p} - p_0$ in atmospheres are given in line 5. The corresponding pressures in centimeters of water are given in line 6.

It appears from Table 1 that at 7,000 cps a vibration of amplitude of only 0.0001 in. would give rise to a pressure of 7 cm. of water when the gap was closed to 0.02 mm. = 20 microns. When the gap is closed to 5 microns, the mean pressure produced would be 0.31 atmospheres, and still higher pressures would be produced as the gap closes still further and $b$ approaches the value 1 which it would have when $h_0 = 2.5$ microns and the plates touch.

For case (A) a similar table may be constructed. We imagine a disc 9 cm. in diameter rotating at an angular velocity of 7,000 r.p.m., and suppose that the stator is inclined at a small angle $\alpha$. In Table 2 the corresponding values of $\sqrt{\lambda}$ are given in line 2 for the various gaps. In line 3 are given the corresponding values of $\bar{p}'/p_0e^2$ at the center calculated from Eq. (23). We assume, for the sake of example, that $\alpha = 0.004°$. The values of $e = \alpha a/h_0$ are given in line 4 and the values of the excess pressure $\bar{p} - p_0$ in centimeters of water in line 5.

It appears from Table 2 that, at an angular velocity of 7,000 r.p.m. and an angle between the plates of 0.004°, a pressure rise of 3 cm. of water occurs when the separation of the centers is 20 microns and rises to 150 cm. of water when the gap closes to 5 microns. Still higher pressures will be produced as the gap closes further.

It is of interest to notice that the approximate formulas (18) and (23) lead to finite limiting values of the central pressure. Thus, in case (A) when $e = 1$ and $\lambda \sim$ infinity, $(p - p_0)/p_0 \sim 0.75$; and, in case (B) as $b = 1$ and $N \sim$ infinity, $(p - p_0)/p_0 \sim 1.25$. It must be remembered, however, that these formulas have only been proved for small values of $e$ and $b$.

## EXPERIMENTAL RESULTS

We have seen that the Navier-Stokes equations will predict pressures of the order of magnitude observed by Reiner if account is taken of the variable thickness of the gap between the plates. However, it is not possible to determine whether the above theory is essentially correct and is the explanation of the phenomena observed by Reiner until the experiment is repeated under conditions for which the gap between the plates may be accurately measured.

To test our conclusions about the effect of angular error, we enlisted the help of Professor Hawthorne and Mr. Barker of the Engineering Laboratory, Cambridge. We first mounted two ground and lapped steel plates of 4-in. diameter on a high-class boring machine capable of running up to 2,500 r.p.m. The lower plate was insulated so that if contact occurred we would know it and so that we could measure the gap using the plates as a condenser. The stator had five 1/2-mm. holes drilled along one radius so that we could

measure the radial distribution of mean pressure. In order that the pressure we measured would be the mean overall points on a circle, we set the stator as perfectly as we could, the irreducible error being about 2 microns. When the machine was set in motion and taking very great precautions to ensure the best possible degree of parallelism, we observed pressures up to 9 cm. of water when the machine was rotating at 2,000 r.p.m., but the excess pressure was greatest at about half radius and nearly zero, both at the center and at the outermost hole. We then found that one of the plates was very slightly conical; we lapped it again, repeated the experiment, and obtained only 1.0 cm. pressure. We then set the rotor at a small angle to the stator so that its edge moved up and down relative to the stator through a distance of $2d = 0.25 \times 0.001$ in.—i.e., $d = 0.00012$ in. $= 3.2 \times 10^{-4}$ cm. The pressure distributions obtained with this setting at 2,000 r.p.m. are shown in Fig. 5.

When running the machine the gap gradually closed down, owing no doubt to the slight heating of the rotating shaft, and the curves show successive distributions at intervals of roughly 2 min. The initial value of $h_0$ was 15 microns. This corresponds with $e = 3.2/15 = 0.21$. No doubt the value of $e$ rose, but unfortunately we were unable to measure $h_0$ while the machine was running because our electrical arrangements were upset by an axial vibration which undoubtedly existed. We do not therefore know what value of $e$ corresponded with any except the lowest of the four curves in Fig. 5. After obtaining the fourth distribution, the central pressure rapidly rose, and before we could make another set of measurements the discs touched at the edge, the spindle bent, and the plates were destroyed.

The value of $\lambda$ corresponding to $h_0 = 15$ microns, $\omega = 2{,}000$ r.p.m., and a diameter of 4 in. is 2.7. The pressure at the center predicted by Eq. (23) with $e = 0.21$ is then about 1 cm. of water. This is considerably less than the observed pressure of 12 cm. of water. However, if $d$ remains constant while $h_0$ varies, so that $e = d/h_0$ is inversely proportional to $h_0$ and if $\lambda$ is small compared with 16—as is the case here—then, according to Eq. (24), the pressure at the center is inversely proportional to the sixth power of $h_0$. The discrepancy could therefore be accounted for if there were an error of 5 microns in the measurement of $h_0$ and the actual gap were 10 microns instead of the measured 15. We do not wish to suggest that this is the sole explanation of the discrepancy—for instance, it will not explain the shape of the curves of the radial distribution of mean pressure which are somewhat different from those shown in Fig. 2 especially in the later stages of the experiment—but it serves to illustrate the need for really accurate measurements of the gap between the discs.

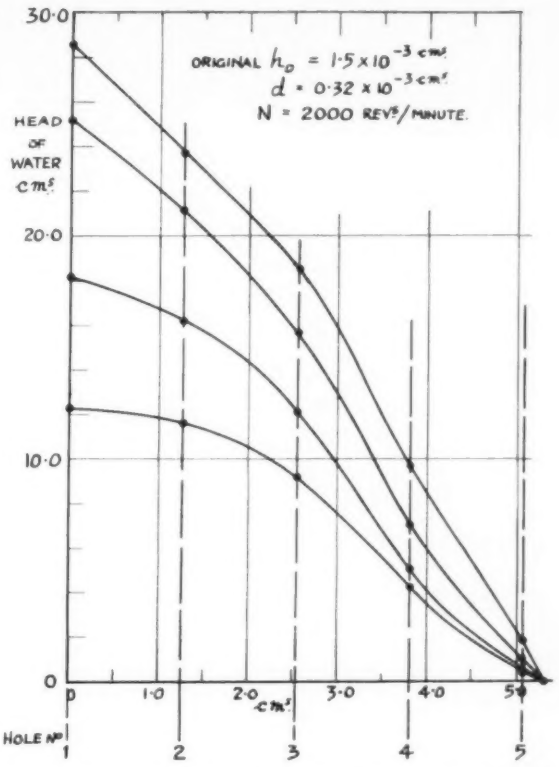


FIG. 5. Observed distribution of pressure when angle between discs was 0.0033°.

## APPENDIX—FURTHER ANALYTICAL SOLUTIONS

In an attempt to explain certain features of the experimental observations—in particular the large maximum which occurred at the center when the experiment with inclined plates was performed—the analytical solution was obtained for several other deviations from the mathematical ideal. The problem consists of solving Eq. (6) with a given choice of the function $h'(r', \theta, t')$. As in cases (A) and (B), it is assumed that $h' = 1 + \epsilon f(r', \theta, t')$ where $\epsilon$ is small compared with 1, and the mean pressure correct to order $\epsilon^2$ (or higher orders if necessary) is calculated. The analysis is essentially similar to that employed before when $f$ is resolved into its Fourier components with respect to $\theta$ and $t'$, and an analytical expression can be obtained for $p'$ in terms of these components. In general, these expressions are complicated and not suited for numerical evaluation without prohibitive labor, and the general character of the solutions is therefore best seen by obtaining the asymptotic expansion valid for large values of $\lambda$ and the power series expansion in $\lambda^2$ valid for small $\lambda$.

We first considered the case of flat discs inclined at a variable angle—i.e., $h' = 1 + e(t')r' \cos \theta$. This is a generalization of case (A) and occurs when the axis of rotation is not perpendicular to either the rotor or the stator. It was found that the solution was essentially the same as case (A) with $e$ replaced by a suitable mean value of $e(t')$.

We next considered the case of conical plates inclined at a constant angle—i.e., $h' = 1 + er' \cos \theta + cr'$. In this case, the effect of the conicality is to superpose on the pressure distribution for inclined

flat plates an extra pressure, which is of amount $-4{,}371\ e^2c\lambda^2p_0/2^8\cdot 1{,}225$ at the center when $\lambda$ is small. If the rotor is convex this is a suction.

The effect of a large central hole of radius $aR$ in the stator was also worked out for cases (A) and (B). The presence of the hole changes the boundary conditions on $p'$; the condition $p'$ finite when $r' = 0$ has to be replaced by $p' =$ constant when $r' = R$. It was found that the effect of the hole was to reduce the central value of the mean pressure.

Finally, the oscillations of a flexible plate executing forced vibrations were considered. Three special cases were dealt with: (1) $h' = 1 + b(1 - r')\cos t''$; here the rim of the rotor does not move, but the center vibrates with dimensionless amplitude $b$. (2) $h' = 1 + b(1 - 2r')\cos t''$; here the nodal line consists of the points $r' = 1/2$, and the center and rim of the rotor vibrate with amplitude $b$ but are $\pi$ out of phase. (3) $h' = 1 + br'\cos t''$; here the center of the rotor does not move, and the rim vibrates with amplitude $b$.

For $N$ small, the values of the mean pressure at the center for the three cases are (1) $\approx 5.2 \times 10^{-2}b^2N^2p_0$, (2) $\approx -2 \times 10^{-4}b^2N^2p_0$, and (3) $\approx 2 \times 10^{-2}b^2N^2p_0$. The radial distribution of mean pressure is in all cases comparatively flat. These figures should be compared with case (B), in particular Eq. (17), according to which the mean pressure at the center for case (B), which is the oscillation of a rigid plate, is $\approx 5.5 \times 10^{-2}b^2N^2p_0$.

For $N$ large, the asymptotic radial distributions of mean pressure are (1) $\bar{p}'/p_0 = (1/2)b^2(1 - r')^2$, (2) $\bar{p}'/p_0 = b^2[(5/4) - 2r' + 2r'^2]$, and (3) $\bar{p}'/p_0 = b^2[(3/4) + (r'^2/2)]$, provided that $r'$ lies in the range $N^{-1/2} \ll r' \ll 1 - N^{-1/2}$. Case (1) has a large central peak and decreases to zero rapidly as $r' \to 1$ and, in this respect, is similar to the later experimental curves shown in Fig. 5. Case (2) has a maximum at $r' = 0$ and $r' = 1$, with a minimum in the middle at $r' = 1/2$. Case (3) has a minimum at the center and rises to a maximum near $r' = 1$.

It is not impossible for the experimental observations shown in Fig. 5 to be explained by the existence of a vibration of type (1), but if so this would be a most curious phenomenon because there seems to be no obvious way in which such a vibration could be set up.

## References


[1] Reiner, M., *Researches on the Physics of Air Viscosity*, Technical Report, Technion Research and Development Foundation, Haifa, Israel, 1956.

[2] Popper, B., and Reiner, M., *The Application of the Centripetal Effect in Air to the Design of a Pump*, Brit. J. Appl. Physics Vol. 7, p. 452, 1956.

[3] Stewartson, K., *On the Flow between Two Rotating Discs*, Proc. Cambridge Philos. Society, Vol. 49, p. 333, 1953.

[4] Weissenberg, K., *A Continuum Theory of Rheological Phenomena*, Nature, Vol. 159, p. 310, 1947.

[5] Chapman, S., and Cowling, T. G., *The Mathematical Theory of Non-Uniform Gases*, 2nd Ed.; Oxford University Press, 1952.

[6] Lamb, H., *Hydrodynamics*, 6th Ed.; Cambridge University Press, 1932.

[7] Harrison, W. J., *The Hydrodynamical Theory of Lubrication with Special Reference to Air as a Lubricant*, Trans. Cambridge Philos. Society, Vol. 22, p. 39, 1913.

[8] McLachlan, N. W., *Bessel Functions for Engineers;* Oxford University Press, 1934.

[9] *Tables of Bessel Functions $J_0(z)$, $J_1(z)$ for Complex Arguments;* Columbia University Press, New York, 1943.



## THIRD U.S. NATIONAL CONGRESS OF APPLIED MECHANICS

*Brown University, Providence, R.I., June 11–14, 1958*

All research workers in the field are cordially invited to submit papers constituting original experimental or theoretical contributions to Applied Mechanics, including mechanics of rigid bodies and deformable solids, mechanics of fluids and gases, thermodynamics and heat transfer. Instructions to authors of papers may be obtained from the Organizing Committee. It is expected that papers accepted by the Editorial Committee, with the advice of recognized authorities, and presented at the Congress will be published in full in the Proceedings of the Congress.

To be considered for presentation at the Congress, complete papers and manuscripts must be submitted to the Chairman of the Editorial Committee before January 1, 1958; to be scheduled for presentation the final manuscript of a paper must have been accepted before May 1, 1958. To avoid delays caused by overburdening reviewers and editorial staff, authors are urged to submit manuscripts well ahead of the deadline of January 1, 1958.

The papers will be grouped by subject, and 30 minutes will be allotted for presentation and discussion of each paper. Arrangements will also be made for general lectures by outstanding authorities on subjects of general interest to members of the Congress. Facilities will be provided for informal discussions and social contact.

The Organizing Committee: Chairman, W. Prager; Secretary, Daniel C. Drucker; Treasurer, E. H. Lee; Chairman, Editorial Committee, R. M. Haythornthwaite; and Committee on Arrangements, E. T. Onat and R. T. Shield.

*Inquiries regarding the Congress should be addressed to the Secretary of the Congress, Brown University, Box D, Providence 12, R.I.*

# Flutter of Rectangular Simply Supported Panels at High Supersonic Speeds

JOHN M. HEDGEPETH*

*Langley Aeronautical Laboratory, NACA*

SUMMARY

The problem of panel flutter of rectangular simply supported plates subjected to supersonic flow over one surface is treated theoretically. The assumption is made, and subsequently verified, that the "static" approximation to the aerodynamic flutter forces yields flutter boundaries with satisfactory accuracy for Mach Numbers greater than about 2. Two panel flutter analyses are performed using this static approximation in conjunction with thin-plate theory—one employs aerodynamic strip theory, the other aerodynamic surface theory. The influence of Mach Number, dynamic pressure, panel aspect ratio, and midplane stress on the panel thickness required to prevent flutter is determined for extensive ranges of these parameters.

SYMBOLS

| | |
|---|---|
| $A$ | $= R_x - 2n^2\pi^2(a/b)^2$ |
| $\bar{A}$ | $= \bar{R}_x - 2n^2(a/b)^2$ (note that flutter is usually most critical for $n = 1$) |
| $B$ | $= k^2 + n^2\pi^2(a/b)^2R_y - n^4\pi^4(a/b)^4$ |
| $\bar{B}$ | $= k^2 + n^2(a/b)^2R_y - n^4(a/b)^4$ |
| $\bar{B}_0$ | $= (a/b)^2R_y - (a/b)^4$ |
| $C(m, \sigma)$ | = integral defined by Eq. (A-14) |
| $D$ | = plate stiffness, $Eh^3/12(1 - \mu^2)$ |
| $E$ | = Young's modulus of elasticity |
| $I_{mn}, J_{mn}, K_{mn}, L_{mn}$ | = functions used in evaluation of generalized force (see Appendix A) |
| $\bar{L}_{mn,\,rs}$ | = generalized force of $(rs)$ mode on $(mn)$ mode |
| $M$ | = Mach Number |
| $N_x, N_y$ | = midplane stresses (positive in compression) |
| $R_x$ | $= N_xa^2/D$ |
| $R_y$ | $= N_ya^2/D$ |
| $\bar{R}_x$ | $= R_x/\pi^2$ |
| $\bar{R}_y$ | $= R_y/\pi^2$ |
| $S(m, \sigma)$ | = integral defined by Eq. (A-10) |
| $U$ | = velocity of air flow |
| $W_n$ | = complex amplitude of panel vibration [see Eq. (4)] |
| $a, b$ | = dimensions of panel (see Fig. 1) |
| $c_{mn}$ | = amplitude of $(mn)$ mode [see Eq. (19)] |
| $h$ | = panel thickness |
| $k$ | = frequency parameter, $\omega a^2\sqrt{\gamma h/D}$ |
| $\bar{k}$ | $= k/\pi^2$ |
| $l$ | = lateral aerodynamic loading |
| $l_{mn}$ | = lateral aerodynamic loading due to $(mn)$ mode |
| $j, m, n, r, s$ | = integers |
| $q$ | = dynamic pressure, $\rho U^2/2$ |
| $t$ | = time |
| $w$ | = lateral deflection of panel |
| $x, y, z$ | = Cartesian coordinates (see Fig. 1) |
| $x_1$ | $= x/a$ |
| $\beta$ | $= \sqrt{M^2 - 1}$ |
| $\gamma$ | = mass density of plate |
| $\epsilon$ | = mass ratio, $\rho a/\gamma h$ |
| $\varphi$ | = perturbation velocity potential |
| $\lambda$ | = dynamic pressure parameter, $2qa^3/\beta D$ |
| $\lambda_{cr}$ | = critical value of $\lambda$ |
| $\lambda_T$ | = transtability value of $\lambda$ |
| $\mu$ | = Poisson's ratio |
| $\rho$ | = mass density of air |
| $\sigma$ | $= (m/n)\,(\beta b/a)$ |
| $\omega$ | = circular frequency |
| $1(y)$ | = step function, equal to zero for $y < 0$ and equal to unity for $y > 0$ |

Presented at the Aeroelasticity—I Session, Twenty-Fifth Annual Meeting, IAS, New York, January 28–31, 1957.

* Head, Structural Mechanics Branch.

## INTRODUCTION

THE AEROELASTIC INSTABILITY of aircraft skin panels has been the subject of a number of theoretical investigations.[1–21] Most of these papers[1–16] have dealt in some detail with the problem of a one-dimensional panel in a two-dimensional flow and have been attempts either to establish approximate stability boundaries for use in the design of flat or slightly curved panels or to investigate some of the apparent peculiarities of the panel-flutter phenomenon. The aeroelastic behavior of thin cylinders has also been considered,[17, 18] although in a somewhat preliminary fashion. In addition, the flutter of two-dimensional flat panels in a three-dimensional flow has been treated by Eisley[19] and Luke, St. John, and Gross.[20, 21] It is to the latter subject that the present paper is directed.

The work both of Eisley and of Luke, St. John, and Gross concerns the flutter of rectangular simply supported plates subjected to supersonic flow over one side; both analyses employ modal solutions and present numerical results for a variety of panel aspect ratios for a limited range of supersonic Mach Numbers. No attention is paid, however, either to the higher Mach Numbers (greater than 2) or to the effects of midplane tension and compression stresses on flutter. In addition, neither analysis is completely satisfactory for an isolated panel; Eisley used linearized two-dimensional unsteady flow theory and Luke, *et al.*, while employing three-dimensional theory, actually solved the problem of an infinite-span panel separated into rectangular bays by equally spaced rigid streamwise stiffeners.

In the present paper we consider again the flat rectangular simply supported plate. The important departure from the previous analyses is in the use of so-called "static" air forces,[2] for solving the flutter problem. Experience has shown that this static approximation yields flutter boundaries that exhibit excellent agreement with those yielded by more refined (with

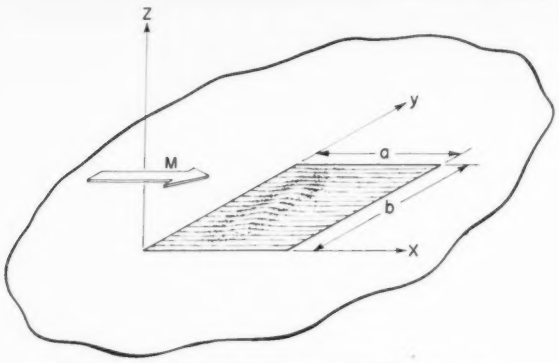


FIG. 1. Rectangular panel and coordinate system.

regard to unsteady effects) aerodynamic theories, provided that the Mach Number is sufficiently high.* The use of the static air forces has the obvious virtue of simplicity and allows the inclusion of three-dimensional aerodynamic forces in a relatively simple manner. In addition, large ranges of the pertinent parameters of the problem can be readily investigated. Also, studies of the effects on the flutter boundaries of the midplane stresses that might arise as a result of loading and aerodynamic heating are feasible.

## STATEMENT OF PROBLEM

The configuration to be analyzed herein is shown in Fig. 1. It consists of a simply supported flat plate of uniform thickness $h$ mounted in a rigid wall with air flowing over the top at a Mach Number $M$. The plate has a length $a$ and a width $b$ and is subjected to constant midplane force intensities $N_x$ and $N_y$ (positive in compression).

In the following analysis, small-deflection thin-plate theory is assumed to apply. The appropriate equilibrium equation and boundary conditions are

$$\left.\begin{aligned} &D\nabla^4 w + N_x w_{xx} + N_y w_{yy} + \gamma h w_{tt} = l(x, y, t) \\ &w(x, 0, t) = w(x, b, t) = w(0, y, t) = \\ &\qquad w(a, y, t) = 0 \\ &w_{yy}(x, 0, t) = w_{yy}(x, b, t) = w_{xx}(0, y, t) = \\ &\qquad w_{xx}(a, y, t) = 0 \end{aligned}\right\}, \quad (1)$$

where $w(x, y, t)$ is the lateral deflection of the plate and $l(x, y, t)$ is the lateral load per unit area due to aerodynamic pressures; $D$ is the plate stiffness $Eh^3/12(1 - \mu^2)$ and $\gamma$ is the density of the plate material.

As was mentioned in the Introduction, we will assume that the air forces yielded by linearized static aerodynamic theory give an adequate approximation for this problem. In this theory, the loading at each instant is taken to be the loading which would result from flow over a stationary surface with a shape the same as the shape of the deflected plate at that instant. Thus, no time-dependent effects are considered in either the potential equation, the boundary conditions, or the pressure-potential relations. Note that this differs (on the side of simplicity) from the so-called "quasi-steady" theory, in which time derivatives are included in the boundary conditions and pressure-potential relations, and from the first-order theory,[22] in which time-dependent effects are included approximately in all three governing relations.

In the following sections a closed-form solution of Eq. (1) is first carried out for two-dimensional aerodynamic theory (strip theory). The same problem is then solved by the Galerkin procedure in order to investigate the convergence of this modal approach. Finally, a modal solution of Eq. (1) for three-dimensional theory (surface theory) is presented.

## ANALYSIS

### *Aerodynamic Strip Theory*

For strip theory, the lateral loading is given by the simple Ackeret value

$$l(x, y, t) = -(2q/\beta)w_x(x, y, t) \quad (2)$$

where $q$ is the dynamic pressure $\rho U^2/2$, and $\beta = \sqrt{M^2 - 1}$. Eq. (1) then becomes

$$D\nabla^4 w + N_x w_{xx} + N_y w_{yy} + (2q/\beta)w_x + \gamma h w_{tt} = 0 \quad (3)$$

For the simply supported plate the solution of Eq. (2) can be written in the form

$$w = Re[W_n(x) \sin (n\pi y/b)e^{i\omega t}] \quad (4)$$

The frequency $\omega$ is, in general, complex; however, we direct our attention primarily to real values of $\omega$ for which the motion is harmonic.

Substituting Eq. (4) into Eq. (3) and the associated boundary conditions and nondimensionalizing yields

$$W_n^{IV} - 2n^2\pi^2(a/b)^2 W_n'' + n^4\pi^4(a/b)^4 W_n + R_x W_n'' - R_y n^2\pi^2(a/b)^2 W_n + \lambda W_n' - k^2 W_n = 0 \quad (5)$$

$$W_n(0) = W_n''(0) = W_n(1) = W_n''(1) = 0$$

where the primes denote differentiation with respect to $x_1 = x/a$, and

$$\left.\begin{aligned} R_x &= N_x a^2/D, \quad R_y = N_y a^2/D, \\ \lambda &= 2qa^3/\beta D, \quad k^2 = (\gamma h a^4/D)\,\omega^2 \end{aligned}\right\} \quad (6)$$

Eq. (5) and the boundary conditions constitute an eigenvalue problem where $k^2$ can be considered to be the eigenvalue. We seek, in fact, the values of $\lambda$, $R_x$ and $R_y$ for which one of the eigenvalues $k^2$ becomes complex and, hence, the panel becomes unstable [see Eq. (4)].

Eq. (5) can be rewritten

$$W_n^{IV} + AW_n'' + \lambda W_n' - BW_n = 0 \quad (7)$$

where

$$\left.\begin{aligned} A &= R_x - 2n^2\pi^2(a/b)^2 \\ B &= k^2 + n^2\pi^2(a/b)^2 R_y - n^4\pi^4(a/b)^4 \end{aligned}\right\} \quad (8)$$

Note that $B$ now takes on the role of the eigenvalue.

* Comparisons presented in a subsequent section show that the lower limit on Mach Number is somewhere between $\sqrt{2}$ and 2.

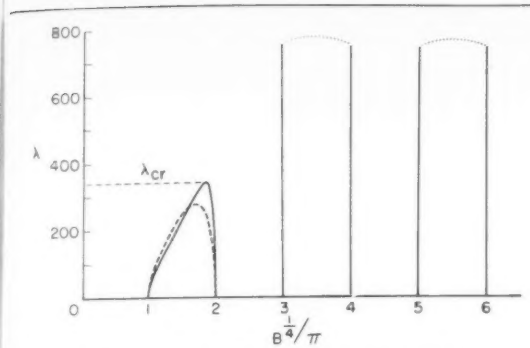


FIG. 2. Influence of airflow on panel frequencies.

*Exact Solution*—The solution of Eq. (7) can be obtained directly from the analysis[13] of the limiting case of the infinite aspect ratio simply supported plate. In the present notation, the condition for a nontrivial solution of Eq. (7) becomes

$$[(\epsilon^2 + \delta^2)^2 + 4\alpha^2(\delta^2 - \epsilon^2)] \sin \delta \sinh \epsilon = 8\alpha^2\epsilon\delta(\cosh \epsilon \cos \delta - \cosh 2\alpha) \quad (9)$$

where

$$\left.\begin{aligned} \delta &= \sqrt{(\lambda/4\alpha) + \alpha^2 + (A/2)} \\ \epsilon &= \sqrt{(\lambda/4\alpha) - \alpha^2 - (A/2)} \\ B &= (\lambda^2/16\alpha^2) - 4[\alpha^2 + (A/4)]^2 \end{aligned}\right\} \quad (10)$$

The eigenvalue $B$ can be computed for fixed values of $\lambda$ and $A$ by varying $\alpha$ until Eq. (9) is satisfied and then using the last of Eqs. (10) to determine $B$. The resulting solutions can be shown in the form of plots of $\lambda$ versus $B$ for various values of $A$. An example plot for $A = 0$ is indicated by the solid line in Fig. 2. (The abscissa is $\sqrt[4]{B}/\pi$ instead of $B$ in order to allow the inclusion of large ranges of $B$ conveniently.)

It can be seen that for a fixed value of $\lambda$ there exists an infinite discrete set of values of $B$. For $\lambda = 0$, the values of $B$ can be shown to correspond to the natural frequencies of the plate in a vacuum. Increasing the dynamic-pressure parameter $\lambda$ merely changes the values of $B$ (and, hence, the natural frequencies) smoothly until a critical value (denoted $\lambda_{cr}$ in Fig. 2) is reached. At this value, two of the roots for $B$ become equal. For $\lambda < \lambda_{cr}$, the values of the frequencies remain real (provided the panel is unbuckled for $\lambda = 0$) and, thus, the panel is stable. For $\lambda > \lambda_{cr}$, two of the values of $B$ become complex; hence, in view of Eqs. (4), (6), and (8), the panel has at least one unstable mode of oscillation. Therefore, the value $\lambda_{cr}$ defines the flutter boundary. It should be noted that this value is characterized by the relation

$$\partial\lambda/\partial B = \partial\lambda/\partial k^2 = 0 \quad (11)$$

where the partial derivatives are performed while keeping $A$ constant.

The variation of $\lambda_{cr}$ with $A$ has been calculated and is shown by the solid line in Fig. 3. The abscissa here is

$$\bar{A} = A/\pi^2 = \bar{R}_x - 2n^2(a/b)^2 \quad (12)$$

where $\bar{R}_x = R_x/\pi^2$

Note that, for $\bar{A} < 5$, $\lambda_{cr}$ decreases monotonically with $\bar{A}$; thus, for fixed values of $\bar{R}_x$ and $a/b$, the lowest value of $\lambda_{cr}$ would be achieved for $n = 1$. The resulting shape of the flutter mode in the $y$-direction would be a half sine wave.

Although a full discussion of the flutter boundary in Fig. 3 is included in a later section of the paper, a mention of several salient points is warranted here. First, the flutter speed is independent of $R_y$. This result, which comes about from the lack of coupling between the various modes in the $y$-direction, is of interest in connection with wing panels for which the greatest stress is usually in the spanwise ($y$) direction. Second, the range of validity of the results in Fig. 3 is limited by the buckling characteristics of the plate. For instance, a square plate with no stress in the $y$-direction ($R_y = 0$) would buckle (for $\lambda = 0$) if $\bar{R}_x \geq 4$; for this reason, the curve in Fig. 3 would be valid only for $\bar{A} < 2$.* Other values of $a/b$ and $R_y$ would yield other ranges of validity. Third, the critical dynamic-pressure parameter is finite when the panel is on the verge of buckling, even though the "effective stiffness" of the panel (as measured by the lowest in-vacuo natural frequency) approaches zero. Finally, the critical dynamic-pressure parameter goes to zero at $\bar{A}$ equal to 5. The need of large panel thicknesses if $\bar{A} \sim 5$ is obvious.

*Galerkin Solution*—In order to investigate the convergence of the modal procedure, a Galerkin solution of Eq. (7) will be performed.

Let

$$W_n = \sum_{m=1}^{j} c_{mn} \sin m\pi x_1$$

Substituting into Eq. (7), multiplying by $\sin r\pi x_1$, and integrating yields the following set of equations for the coefficients $c_{mn}$:

$$(m^4 - m^2\bar{A} - \bar{B})c_{mn} - (\lambda/\pi^3) \sum_{r=1}^{j} \bar{L}_{mn,\,rn}\, c_{rn} = 0 \quad (m = 1, 2, \ldots, j) \quad (13)$$

* Since the buckling load is affected by the air forces, this inequality is not strictly correct. This phenomenon is discussed in Appendix B.

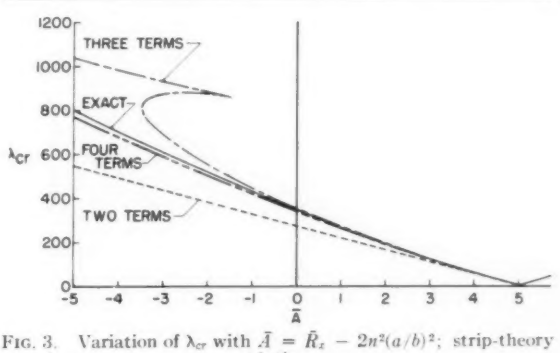


FIG. 3. Variation of $\lambda_{cr}$ with $\bar{A} = \bar{R}_x - 2n^2(a/b)^2$; strip-theory solution.

where

$$\left.\begin{aligned} &\bar{B} = B/\pi^4 = (k^2/\pi^4) + n^2(a/b)^2\bar{R}_y - n^4(a/b)^4 \\ &\bar{L}_{mn,\,rs} = (4/\pi)\,[rm/(r^2 - m^2)]; \\ &\qquad\qquad n = s, \quad m + r \text{ odd} \\ &\bar{L}_{mn,\,rs} = 0; \quad n = s, \quad m + r \text{ even} \\ &\bar{L}_{mn,\,rs} = 0; \quad n \neq s \end{aligned}\right\} \tag{14}$$

In the first of the latter expressions, $\bar{R}_y = R_y/\pi^2$. The seemingly overcomplicated form for the generalized aerodynamic-force coefficient $\bar{L}_{mn,\,rs}$ is introduced at this point to agree with the notation in the next section.

For a nontrivial solution, the determinant of the coefficients of $c_{mn}$ must equal zero. If $j = 2$, for instance,

$$\begin{vmatrix} 1 - \bar{A} - \bar{B} & -(8/3\pi^4)\lambda \\ (8/3\pi^4)\lambda & 16 - 4\bar{A} - \bar{B} \end{vmatrix} = 0$$

Upon expanding and solving for $\lambda$ we get

$$\lambda = (3\pi^4/8)\sqrt{(\bar{A} + \bar{B} - 1)\,(16 - 4\bar{A} - \bar{B})} \tag{15}$$

This relation is illustrated by the dashed line in Fig. 2 for $\bar{A} = 0$. The two-term approximation to the critical value of $\lambda$ can be obtained by finding the maximum; the result is

$$\lambda_{cr} = (9\pi^4/16)|5 - \bar{A}| \tag{16}$$

This approximation and the three-term and four-term approximations ($j = 3$ and 4) are compared in Fig. 3 with the exact result. It can be seen that the two-term approximation consistently underestimates $\lambda_{cr}$, the error increasing as $\bar{A}$ becomes large negatively. The three-term approximation is satisfactory for small values of $\bar{A}$ but is again unsatisfactory for the larger negative values of $\bar{A}$. On the other hand, the four-term solution yields good results over the entire range of $\bar{A}$ considered.*

### *Aerodynamic Surface Theory*

The results in the preceding section were obtained on the basis of aerodynamic strip theory. The influence of three-dimensional aerodynamic effects on the flutter boundary is of interest. In this section, the flutter of the rectangular panel in a three-dimensional flow is analyzed by means of the Galerkin solution.

*Air Forces*—The lateral loading due to the supersonic flow above the panel can be found in a straightforward manner by means of source-superposition techniques. Thus, if the deflection of the panel is $w(x, y, t)$, the lateral load $l(x, y, t)$ is[24]

$$l(x, y, t) = \rho U(\partial\varphi/\partial x)\;(x, y, t) \tag{17}$$

where

$$\varphi(x, y, t) = -\frac{U}{\pi}\iint \frac{(\partial w/\partial\xi)\;(\xi, \eta, t)\;d\xi\,d\eta}{\sqrt{(x - \xi)^2 - \beta^2(y - \eta)^2}} \tag{18}$$

The integration is carried out over the forward Mach cone from the point $(x, y)$.

In the modal solution the deflection is expressed as the series

$$w = R_e\left[\sum_r\sum_s c_{rs}\sin(r\pi x/a)\sin(s\pi y/b)e^{i\omega t}\right] \tag{19}$$

in the region $0 \leq x \leq a$, $0 \leq y \leq b$. The corresponding loading is

$$l(x, y, t) = R_e\left[\sum_r\sum_s c_{rs}l_{rs}(x, y)e^{i\omega t}\right] \tag{20}$$

where

$$l_{rs}(x, y) = -2q\,\frac{r}{a}\,\frac{\partial}{\partial x}\int_0^x\int_{y-(1/\beta)\,(x-\xi)}^{y+(1/\beta)\,(x-\xi)} \frac{\cos(r\pi\xi/a)\sin(\xi\pi\eta/b)}{\sqrt{(x - \xi)^2 - \beta^2(y - \eta)^2}}\,[1(\eta) - 1(\eta - b)]\,d\eta\,d\xi \tag{21}$$

Note that the step-function expression

$$\begin{aligned} 1(\eta) - 1(\eta - b) &= 0; \quad \eta < 0 \\ &= 1; \quad 0 < \eta < b \\ &= 0; \quad \eta > b \end{aligned}$$

excludes the regions outside of the plate from the integration.

*Modal Solution*—Substituting Eqs. (19) and (20) into the equilibrium equation, Eq. (1), gives

$$\sum_r\sum_s\left\{\left[D\left(\frac{r^2\pi^2}{a^2} + \frac{s^2\pi^2}{b^2}\right)^2 - N_x\frac{r^2\pi^2}{a^2} - N_y\frac{s^2\pi^2}{b^2} - \gamma h\omega^2\right]c_{rs}\sin\frac{r\pi x}{a}\sin\frac{s\pi y}{b} - c_{rs}l_{rs}(x, y)\right\} = 0$$

If this equation is multiplied by $\sin(m\pi x/a)\sin(n\pi y/b)$ and integrated, the result is

$$\left\{[m^2 + n^2(a/b)^2]^2 - m^2\bar{R}_x - n^2(a/b)^2\bar{R}_y - \bar{k}^2\right\}c_{mn} = (\lambda/\pi^3)\sum_r\sum_s \bar{L}_{mn,\,rs}c_{rs} \tag{22}$$

where $\bar{k} = k/\pi^2$ and

$$\bar{L}_{mn,\,rs} = \frac{4\beta r}{\pi ab}\int_0^b\int_0^a \sin\frac{m\pi x}{a}\sin\frac{n\pi y}{b}\left\{\frac{\partial}{\partial x}\int_0^x\int_{y-(1/\beta)\,(x-\xi)}^{y+(1/\beta)\,(x-\xi)} \frac{\cos(r\pi\xi/a)\sin(s\pi\eta/b)}{\sqrt{(x - \xi)^2 - \beta^2(y - \eta)^2}}\,[1(\eta) - 1(\eta - b)]\,d\eta\,d\xi\right\}dx\,dy$$

is the generalized force of the $(rs)$ mode on the $(mn)$ mode. Integration by parts yields

* It should be mentioned that the four-term solution would also be inaccurate for very large negative values of $A$. In this case, the behavior of the plate approaches that of a membrane for which the Galerkin solution is known to be inapplicable.[23]

$$\bar{L}_{mn,\,rs} = \frac{4\beta mr}{a^2 b} \int_0^b \int_0^a \int_0^x \int_{y-(1/\beta)(x-\xi)}^{y+(1/\beta)(x-\xi)} \frac{\cos(m\pi x/a)\sin(n\pi y/b)\cos(r\pi\xi/a)\sin(s\pi\eta/b)}{\sqrt{(x-\xi^2)-\beta^2(y-\eta)^2}} \times [1(\eta) - 1(\eta - b)]\, d\eta\, d\xi\, dx\, dy \quad (23)$$

Before continuing, it is necessary to determine these generalized forces. As is usual for supersonic aerodynamic problems, the generalized forces can be shown to be functions of the modified aspect ratio parameter $\beta b/a$. For $\beta b/a \geq 1$, the reduction of the expression for $\bar{L}_{mn,\,rs}$ in terms of Bessel and Struve functions and two readily evaluated single numerical integrations is possible; this reduction is carried out in Appendix A. Values of $\bar{L}_{mn,\,rs}$ for $\beta b/a = 1, 2, 4$ and $m, n, r, s = 1, 2, 3, 4$ are given in Table 1. Also given are the values for the two-dimensional case ($\beta b/a = \infty$) obtained from Eq. (15).

It should be noted that $\bar{L}_{mn,\,rs} = 0$ when $n + s$ is odd. Thus, flutter modes are either symmetric ($n = 1, 3, \ldots$) or antisymmetric ($n = 2, 4, \ldots$) about the midspan. Also, the generalized force possesses the following symmetry properties:

$$\bar{L}_{mn,\,rs} = \bar{L}_{ms,\,rn}$$

$$\bar{L}_{mn,\,rs} = \bar{L}_{rn,\,ms}; \quad m + r \text{ even}$$

$$\bar{L}_{mn,\,rs} = -\bar{L}_{rn,\,ms}; \quad m + r \text{ odd}$$

For $\beta b/a < 1$, a similar, but more complicated, reduction can be made. No results have been obtained for this case, however, primarily because they would be useful only for very low aspect ratio panels. For example, values of $\beta b/a < 1$ would correspond to Mach Numbers less than $\sqrt{2}$ for a panel of unit aspect ratio. But, as will be demonstrated, the static aerodynamic theory cannot be expected to yield good results for this region.

*Calculations for an Example Panel*—In view of the results obtained for the modal solution for strip theory, it is evident that the use of four modes in the $x$-direction should give satisfactory accuracy. In the $y$-direction, it is convenient to include two modes—$n = 1$, since this constituted the most critical value for the strip-theory solution; and $n = 3$, in order to include effects of spanwise coupling.

Eq. (22) then becomes

$$\{[m^2 + n^2(a/b)^2]^2 - m^2\bar{R}_x - n^2(a/b)^2\bar{R}_y - \bar{k}^2\}\, c_{mn} = (\lambda/\pi^3) \sum_{r=1,2,3,4} \sum_{s=1,3} \bar{L}_{mn,\,rs}\, c_{rs} = 0 \qquad \begin{pmatrix} m = 1, 2, 3, 4 \\ n = 1, 3 \end{pmatrix}$$

For a nontrivial solution, the determinant of the coefficients of $c_{mn}$ must be zero. When expanded, this determinant yields an eighth-order equation in $\bar{k}^2$ in which the coefficients are dependent on $\lambda$, $\bar{R}_x$, $\bar{R}_y$, and $a/b$. As before, we seek the lowest value of $\lambda$ for fixed $\bar{R}_x$, $\bar{R}_y$ and $a/b$ for which two of the eight roots for $\bar{k}^2$ become complex. (For $\lambda = 0$, all roots are obviously real.) The calculations have been carried out for $a/b = 1$ and for a number of values of $\bar{R}_x$ and $\bar{R}_y$. Values for $\lambda_{cr}$ were obtained as shown in Table 2.

In the calculations for $\beta b/a = 1$, 2, and 4, an automatic high-speed digital computer was used. For each set of values for $\bar{R}_x$ and $\bar{R}_y$ the determinant was expanded for various selected values of $\lambda$. The resulting eighth-order equation in $\bar{k}^2$ was then solved. The critical value of $\lambda$ was found by an interpolation procedure.

A significant outcome of these calculations is the virtual independence of $\lambda_{cr}$ on the value of $\bar{R}_y$. Evidently the coupling between the various modes in the $y$-direction is slight, even for $\beta b/a = 1$. Since the coupling is so slight, it is improbable that the addition of more modes in the $y$-direction would change the results appreciably. Thus, the tabulated values can be considered to be essentially correct.

The lack of dependence on $\bar{R}_y$ also suggests the possibility that the value of $\lambda_{cr}$ is dependent only on the parameter

$$\bar{A} = \bar{R}_x - 2(a/b)^2$$

as it was for the strip-theory solution. If this were the case, the results for $a/b = 1$ could be extended to apply to other aspect ratios through the use of this parameter. As a check, the values of $\lambda_{cr}$ were calculated for $a/b = 2$, $\bar{R}_x = 4$, $\bar{R}_y = 0$ and $a/b = 1/2$, $\bar{R}_x = -3.5$, $\bar{R}_y = 0$. For $\beta b/a = 1$, the resulting values of $\lambda_{cr}$ are 647.7 and 626.6, respectively, in reasonable agreement with the tabulated value for $a/b = 1$, $\bar{R}_x = -2$, $\bar{R}_y = 0$. Thus, the extension can apparently be made. The variation of $\lambda_{cr}$ with $\bar{A}$ is shown in Fig. 4 for $\beta b/a = 1$, 2, 4, and $\infty$ (strip theory); the values are also given in Table 3. Note that for $\bar{A} = 5$, the critical dynamic-pressure parameter is zero for all values of $\beta b/a$.

The significant results of this paper are embodied in Table 3. From this Table, the critical values of $\lambda$ for isolated rectangular simply supported panels can be found in terms of $\bar{A}$ for a large range of panel aspect

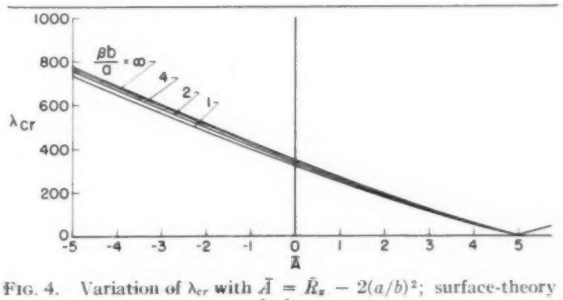


FIG. 4. Variation of $\lambda_{cr}$ with $\bar{A} = \bar{R}_x - 2(a/b)^2$; surface-theory solution.

ratio, midplane stress, and Mach Number. The necessary panel thickness to prevent panel flutter can then be calculated from the value of $\lambda_{cr}$. In this regard, it is interesting to note that the aerodynamic effect of finite aspect ratio on the panel thickness is very small. For the range considered the variation of $\lambda_{cr}$ between $\beta b/a = \infty$ and $\beta b/a = 1$ is approximately 6 per cent; the corresponding variation of thickness would be less than 2 per cent.

## Discussion

### *Accuracy of Static Aerodynamic Approximation*

The results obtained by Eisley[19] by using linearized two-dimensional unsteady flow theory provide an excellent basis for evaluating the accuracy of the static aerodynamic approximation employed in this paper. The results calculated by a two-mode Galerkin solution for unstressed plates of aspect ratio 4, 2, 1, and 1/2 subjected to $M = 2$ flow are shown in Fig. 5. The abscissa in this Figure is the well-known mass ratio

$$\epsilon = \rho a / \gamma h$$

which does not appear in the present analysis because of the simplicity of the aerodynamic theory. Indeed, the values of $\lambda_{cr}$ obtained from the static approximation are the same as those in Fig. 5 for $\epsilon = 0$. It is therefore apparent that the static approximation is adequate if $\epsilon$ is small enough.

In order to define the practical range of $\epsilon$, it is convenient to make use of the following combined parameter:

Table 1
Values of Generalized Force ($\bar{L}_{mn,rs}$)

(a) $\beta b/a = 1$

| rs / mn | 11 | 21 | 31 | 41 | 13 | 23 | 33 | 43 |
|---|---|---|---|---|---|---|---|---|
| 11 | 0.280779 | 0.418688 | -0.016774 | 0.342554 | -0.040424 | 0.027096 | 0.071548 | 0.051672 |
| 21 | -.418688 | [illegible] | 1.707419 | .060365 | -.027096 | -.225040 | -.171612 | -.052125 |
| 31 | -.016774 | -1.707419 | .070016 | 2.278778 | .071548 | .171612 | -.005225 | -.122598 |
| 41 | -.342554 | .060365 | -2.278778 | .044784 | -.051672 | -.052125 | .122598 | .115964 |
| 13 | -.040424 | .027096 | .071548 | .051672 | .594560 | .171035 | -.517892 | .271504 |
| 23 | -.027096 | -.225040 | -.171612 | -.052125 | -.171035 | 1.583401 | 1.330117 | -.442857 |
| 33 | .071548 | .171612 | -.005225 | -.122598 | -.517892 | -1.330117 | 2.566015 | 5.147549 |
| 43 | -.051672 | -.052125 | .122598 | .115964 | -.271504 | -.442857 | -5.147549 | 1.281462 |

| rs / mn | 12 | 22 | 32 | 42 | 14 | 24 | 34 | 44 |
|---|---|---|---|---|---|---|---|---|
| 12 | 0.517757 | 0.645152 | -0.028472 | 0.240044 | 0.000651 | 0.158693 | 0.078655 | -0.008104 |
| 22 | -.645152 | 1.117025 | 1.409184 | .035543 | -.158693 | -.286560 | .033655 | .178954 |
| 32 | -.028472 | -1.409184 | .704846 | 2.752580 | .078655 | .033655 | -.482867 | -.411662 |
| 42 | -.240044 | .035543 | -2.752580 | .216047 | .008104 | .178954 | .411662 | .050538 |
| 14 | .000651 | .158693 | .078655 | -.008104 | .382584 | .056001 | -.089248 | .206460 |
| 24 | -.158693 | -.286560 | .033655 | .178954 | -.056001 | 1.227699 | .576750 | -.617150 |
| 34 | .078655 | -.033655 | -.482867 | -.411662 | -.089248 | -.576750 | 2.884906 | 3.125151 |
| 44 | .008104 | .178954 | .411662 | .050538 | -.206460 | -.617150 | -3.125151 | 5.655424 |

(b) $\beta b/a = 2$

| rs / mn | 11 | 21 | 31 | 41 | 13 | 23 | 33 | 43 |
|---|---|---|---|---|---|---|---|---|
| 11 | 0.115757 | 0.410129 | 0.022577 | 0.259008 | -0.056992 | -0.045405 | -0.018266 | -0.012048 |
| 21 | -.410129 | .056086 | 1.566619 | .012605 | .045405 | .005858 | -.019678 | -.013284 |
| 31 | .022577 | -1.566619 | .011487 | 2.205615 | .018266 | .019678 | .025548 | .006047 |
| 41 | -.259008 | .012605 | -2.205615 | .008108 | .012048 | .015284 | -.006047 | .005112 |
| 13 | -.056992 | -.045405 | -.018266 | -.012048 | .550582 | .889221 | -.127650 | .287169 |
| 23 | .045405 | .005858 | -.019678 | -.015284 | -.889221 | .726612 | 2.009015 | .171298 |
| 33 | -.018266 | -.019678 | .025548 | .006047 | -.127650 | -2.009015 | .168158 | 2.429559 |
| 43 | -.012048 | -.013284 | -.006047 | .005112 | -.287169 | .171298 | -2.429559 | .087475 |

| rs / mn | 12 | 22 | 32 | 42 | 14 | 24 | 34 | 44 |
|---|---|---|---|---|---|---|---|---|
| 12 | 0.364129 | 0.389523 | 0.013851 | 0.362869 | -0.080855 | -0.051587 | 0.012926 | 0.010780 |
| 22 | -.389523 | .241100 | 1.729682 | .078351 | .051587 | -.069568 | -.098219 | -.058536 |
| 32 | .013851 | -1.729682 | .039044 | 2.269501 | .012926 | .098219 | .068260 | .010209 |
| 42 | -.362869 | .078351 | -2.269501 | .042120 | -.010780 | -.058536 | -.010209 | .015761 |
| 14 | -.080855 | -.051587 | .012926 | .010780 | .569556 | .595959 | -.343632 | .191677 |
| 24 | .051587 | -.069568 | -.098219 | -.058536 | -.595959 | 1.339618 | 2.168749 | .114766 |
| 34 | .012926 | .098219 | .068260 | .010209 | -.343632 | -2.168749 | .657950 | 2.805101 |
| 44 | -.010780 | -.058536 | -.010209 | .015761 | -.191677 | .114766 | -2.805101 | 1.532676 |

(c) $\beta b/a = 4$

| rs / mn | 11 | 21 | 31 | 41 | 13 | 23 | 33 | 43 |
|---|---|---|---|---|---|---|---|---|
| 11 | 0.034825 | 0.870251 | 0.004706 | 0.547509 | -0.010958 | -0.010364 | -0.000599 | -0.004678 |
| 21 | -.870251 | .004086 | 1.553149 | .001479 | .010364 | .006573 | .001822 | .001331 |
| 31 | .004706 | -1.553149 | .000634 | 2.189541 | -.000599 | -.001822 | .000568 | -.000820 |
| 41 | -.547509 | .001478 | -2.189541 | .000993 | .004678 | .001331 | .000820 | .001416 |
| 13 | -.010958 | -.010364 | -.000599 | -.004678 | .284711 | .985087 | .045501 | .579860 |
| 23 | .010364 | .006573 | .001822 | .001331 | -.985087 | .033516 | 1.628195 | .056687 |
| 33 | -.000599 | -.001822 | .000568 | -.000820 | .045501 | -1.628195 | .017556 | -2.231651 |
| 43 | .004678 | .001331 | .000820 | .001416 | -.579860 | .056687 | -2.231651 | .022051 |

| rs / mn | 12 | 22 | 32 | 42 | 14 | 24 | 34 | 44 |
|---|---|---|---|---|---|---|---|---|
| 12 | 0.150759 | 0.924487 | 0.051381 | 0.365621 | -0.025207 | -0.022527 | -0.012470 | -0.008852 |
| 22 | -.924487 | .026649 | 1.565657 | .010455 | .022527 | .010974 | -.000289 | -.000247 |
| 32 | .051381 | -1.565657 | .011565 | 2.206362 | -.012470 | .000289 | .004495 | .000228 |
| 42 | -.365621 | .010455 | -2.206362 | .006054 | .008852 | -.000247 | -.000228 | .002661 |
| 14 | -.025207 | -.022527 | -.012470 | -.008852 | .405734 | 1.018790 | .029144 | .573036 |
| 24 | .022527 | .010974 | -.000289 | -.000247 | -1.018790 | .252958 | 1.740565 | .086199 |
| 34 | -.012470 | .000289 | .004495 | .000228 | .029144 | -1.740565 | .280215 | 2.264861 |
| 44 | .008852 | -.000247 | -.000228 | .002661 | -.573036 | .086199 | -2.264861 | .290[illegible] |

(d) $\beta b/a = \infty$

| rs / mn | 11 | 21 | 31 | 41 | 13 | 23 | 33 | 43 |
|---|---|---|---|---|---|---|---|---|
| 11 | 0 | 0.848826 | 0 | 0.339531 | 0 | 0 | 0 | 0 |
| 21 | -.848826 | 0 | 1.527887 | 0 | 0 | 0 | 0 | 0 |
| 31 | 0 | -1.527887 | 0 | 2.182698 | 0 | 0 | 0 | 0 |
| 41 | -.339531 | 0 | -2.182698 | 0 | 0 | 0 | 0 | 0 |
| 13 | 0 | 0 | 0 | 0 | 0 | .848826 | 0 | .339531 |
| 23 | 0 | 0 | 0 | 0 | -.848826 | 0 | 1.527887 | 0 |
| 33 | 0 | 0 | 0 | 0 | 0 | -1.527887 | 0 | 2.182698 |
| 43 | 0 | 0 | 0 | 0 | -.339531 | 0 | -2.182698 | 0 |

| rs / mn | 12 | 22 | 32 | 42 | 14 | 24 | 34 | 44 |
|---|---|---|---|---|---|---|---|---|
| 12 | 0 | 0.848826 | 0 | 0.339531 | 0 | 0 | 0 | 0 |
| 22 | -.848826 | 0 | 1.527887 | 0 | 0 | 0 | 0 | 0 |
| 32 | 0 | -1.527887 | 0 | 2.182698 | 0 | 0 | 0 | 0 |
| 42 | -.339531 | 0 | -2.182698 | 0 | 0 | 0 | 0 | 0 |
| 14 | 0 | 0 | 0 | 0 | 0 | .848826 | 0 | .339531 |
| 24 | 0 | 0 | 0 | 0 | -.848826 | 0 | 1.527887 | 0 |
| 34 | 0 | 0 | 0 | 0 | 0 | -1.527887 | 0 | 2.182698 |
| 44 | 0 | 0 | 0 | 0 | -.339531 | 0 | -2.182698 | 0 |

TABLE 2
Values of $\lambda_{cr}$ for Square Panel

For $\beta b/a = 1$

| $\bar{R}_y$ \ $\bar{R}_x$ | -4 | -2 | 0 | 2 | 4 | 6 | 8 |
|---|---|---|---|---|---|---|---|
| -4 | 822.0 | 647.7 | 480.0 | 322.8 | 179.6 | 54.38 | 46.63 |
| -2 | | 647.7 | 480.0 | 322.8 | 179.6 | 54.38 | |
| 0 | | 647.7 | 480.0 | 322.8 | 179.6 | | |
| 2 | | 647.8 | 480.1 | 322.9 | | | |
| 4 | | 648.0 | 480.3 | | | | |

For $\beta b/a = 2$

| $\bar{R}_y$ \ $\bar{R}_x$ | -4 | -2 | 0 | 2 | 4 | 6 | 8 |
|---|---|---|---|---|---|---|---|
| -4 | 847.7 | 668.2 | 495.8 | 333.9 | 186.3 | 56.56 | 46.35 |
| -2 | | 668.2 | 495.8 | 333.9 | 186.3 | 56.56 | |
| 0 | | 668.2 | 495.8 | 333.9 | 186.3 | | |
| 2 | | 668.2 | 495.8 | 333.9 | | | |
| 4 | | 668.2 | 495.8 | | | | |

For $\beta b/a = 4$

| $\bar{R}_y$ \ $\bar{R}_x$ | -4 | -2 | 0 | 2 | 4 | 6 | 8 |
|---|---|---|---|---|---|---|---|
| -4 | 859.8 | 676.9 | 502.5 | 338.6 | 189.1 | 57.55 | 49.39 |
| -2 | | 676.9 | 502.5 | 338.6 | 189.1 | 57.55 | |
| 0 | | 676.9 | 502.5 | 338.6 | 189.1 | | |
| 2 | | 676.9 | 502.5 | 338.6 | | | |
| 4 | | 676.9 | 502.5 | | | | |

TABLE 3
Critical Values of Dynamic Pressure Parameter $\lambda$

| $\bar{A}$ \ $\frac{\beta b}{a}$ | 1 | 2 | 4 | $\infty$ |
|---|---|---|---|---|
| -6 | 822 | 848 | 860 | 863 |
| -4 | 648 | 668 | 677 | 680 |
| -2 | 480 | 496 | 502 | 505 |
| 0 | 323 | 334 | 339 | 341 |
| 2 | 179.6 | 186.3 | 189.1 | 190.3 |
| 4 | 54.4 | 56.6 | 57.6 | 58.0 |

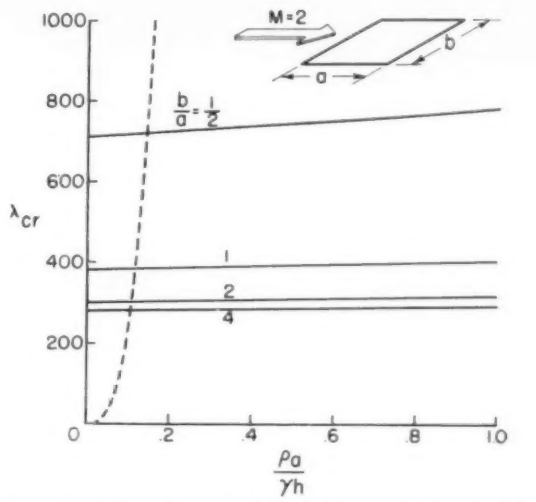


FIG. 5. Results for $M = 2$ obtained from a two-mode strip-theory solution using unsteady air forces.

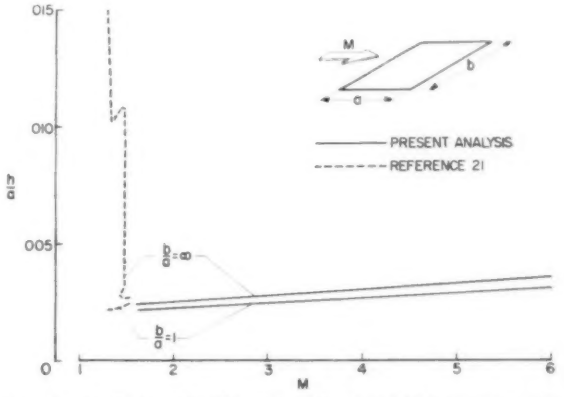


FIG. 6. Variation of thickness ratio with Mach Number for unstressed aluminum panels at 50,000 ft.

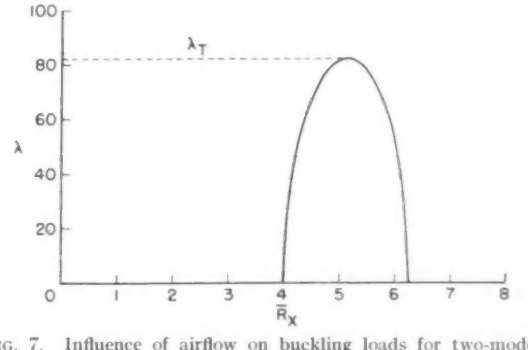


FIG. 7. Influence of airflow on buckling loads for two-mode solution; $\bar{R}_y = 0$, $a/b = 1$.

$$\lambda/\epsilon^3 = 12(1 - \mu^2)(\rho c^2/E)(\gamma/\rho)^3(M^2/\beta)$$

where $c$ is the speed of sound in the air. Note that, for fixed Mach Number, this parameter is dependent only on the properties of the air and the plate material. For a particular altitude-material combination, therefore, $\lambda$ would vary as $\epsilon^3$. The variation for magnesium at sea level is indicated by the dashed line in Fig. 5. For this altitude-material combination the error of the static approximation can be seen to be negligible. For higher altitudes or denser materials the corresponding cubic line would lie above the one shown and the error would be less. It is reasonable to conclude, therefore, that the static approximation yields satisfactory accuracy for $M = 2$.

Investigations of the frequency expansions of the flutter forces (see reference 6, for example) show that the accuracy of the static approximation would be even better for Mach Numbers greater than 2 For $M < 2$, however, the accuracy decreases. At $M = \sqrt{2}$, for instance, the unsteady flow theory yields two flutter boundaries,[6, 19] whereas the static theory predicts only one. It is probable, therefore, that a lower limit, somewhere between $\sqrt{2}$ and 2, exists on the Mach Number range for which the results obtained in this paper are applicable.

### *Panel Thickness*

Two examples of the variation of the critical thickness ratio with Mach number as obtained by the present theory are indicated by the solid lines in Fig. 6. The results apply to unstressed aluminum panels at an altitude of 50,000 ft. with aspect ratios of one and infinity. As could be expected, the effect of reducing the aspect ratio is to reduce the required $h/a$.

Also shown in Fig. 6 are the results calculated from unsteady flow theory for the lower supersonic Mach Numbers by Luke and St. John.[21] These results, which are indicated by the dashed lines, merge well with the predictions of the present analysis. The meeting is nearly exact for the aspect ratio of infinity if account is taken of the fact that the dashed lines were obtained from a two-mode solution,[21] whereas the solid lines were obtained from a four-mode solution; the effect of going from four to two modes is to increase the thickness by 7.5 per cent. For the case of unit aspect ratio, the results are again not directly comparable; in addition to being based on fewer modes, the dashed line applies to a spanwise array of panels rather than to an isolated panel. The effect of this latter disparity is probably small for $M \sim 1.5$, however, since strip theory yields the same results for both configurations and the aerodynamic influence of finite aspect ratio is rather unimportant. The correction for number of modes mentioned above would again produce excellent agreement.

Past analyses of two-dimensional panel flutter have indicated that the most critical condition for design occurs at a value of Mach Number of about 1.3. This is illustrated strikingly by the infinite aspect ratio curves in Fig. 6. The required thickness decreases rapidly between $M = 1.3$ and 1.5 and then increases very slowly. Even at $M = 6$, the thickness ratio is only about one-fourth of that at $M = 1.3$. However, the situation is apparently different for finite aspect ratios a virtually monotonic increase of required thickness with Mach Number is experienced for an aspect ratio of one. Thus, the high Mach Number theory of this paper should provide useful design information for panels of moderately low aspect ratio.

The numerical values of the critical thickness ratios in Fig. 6 are fairly small and would be of consequence only for lightly loaded portions of the structure, such as fairings and control surfaces. It should be emphasized, however, that large thickness ratios would be required if the parameter $\bar{A}$ were close to 5. This situation would not be difficult to attain. For instance, if a panel of aspect ratio equal to 1/2 were subjected to a compressive midplane stress in the chordwise direction only, $\bar{A} = 5$ could be achieved without buckling. Even for a panel of unit aspect ratio, $\bar{A} = 5$ could be obtained without buckling by compressing in the $x$-direction and pulling in the $y$-direction. It is obvious that such configurations should be assiduously avoided in design.

## Concluding Remarks

The panel flutter analysis presented herein has been restricted to the problem of an isolated simply supported plate of uniform thickness. The same type of analysis can be applied, however, to other panel configurations. Clamped panels, integrally stiffened panels, arrays of panels, and others can be treated by the modal approach based on the static aerodynamic approximation; the results should be accurate for the higher Mach Numbers.

The emphasis in this paper has been on the flutter of flat unbuckled panels. There is a considerable amount of interest in the flutter of panels buckled by loading or heating. For this reason, the results of a preliminary investigation of the flutter behavior of buckled simply supported panels are included in Appendix B.

It is generally agreed that flutter analyses should be supported by experiment. In this regard, the small amount of data[16, 25] which is available indicates that theoretical panel-flutter calculations are somewhat conservative. Most of these data, however, relate either to buckled panels or to the lower supersonic Mach Numbers. More experimental data, especially on unbuckled panels, are needed in order to assess the validity of panel-flutter analyses.

## Appendix A—Evaluation of $\bar{L}_{mn,\,rs}$

The generalized force $\bar{L}_{mn,\,rs}$ is given by Eq. (23)

$$\bar{L}_{mn,\,rs} = \frac{4\beta mr}{a^2 b} \int_0^b \int_0^b \int_0^a \int_0^x \int_{y-(1/\beta)\,(x-\xi)}^{y+(1/\beta)\,(x-\xi)} \frac{\cos\,(m\pi x/a)\,\sin\,(n\pi y/b)\,\cos\,(r\pi\xi/a)\,\sin\,(s\pi\eta/b)}{\sqrt{(x-\xi)^2 - \beta^2(y-\eta)^2}} \times$$
$$[1(\eta) - 1(\eta - b)]\, d\eta\, d\xi\, dx\, dy \quad \text{(A-1)}$$

If $\xi$ and $\eta$ are replaced by

$$u = (x - \xi) - \beta(y - \eta)$$
$$v = (x - \xi) + \beta(y - \eta)$$

the result is

$$\bar{L}_{mn,\,rs} = \frac{2mr}{a^2 b} \int_0^{2a} \int_0^{2a-U} \frac{du\, dv}{\sqrt{uv}} \int_0^b \sin \frac{n\pi y}{b} \sin \frac{s\pi}{b}\left(y - \frac{v-u}{2\beta}\right) \times$$
$$\left[1\left(y - \frac{v-u}{2\beta}\right) - 1\left(y - b - \frac{v-u}{2\beta}\right)\right] dy \int_{(u+v)/2}^a \cos \frac{m\pi x}{a} \cos \frac{r\pi}{a}\left(x - \frac{u+v}{2}\right) dx \quad \text{(A-2)}$$

where the order of integration has been changed. Carrying out the $x$- and $y$-integrations yields the following result after some manipulation:

When $n + s$ is odd,

$$\bar{L}_{mn,\,rs} = 0 \quad \text{(A-3)}$$

When $n + s$ is even,

$$\left.\begin{aligned}
\bar{L}_{mn,\,rs} &= \frac{4}{\pi^2} \frac{mnrs}{(r^2 - m^2)\,(s^2 - n^2)} (-1)^m (I_{rs} - I_{rn} - I_{ms} + I_{mn}) \quad \begin{pmatrix} m \neq r \\ n \neq s \end{pmatrix} \\
&= \frac{2}{\pi^2} \frac{ns}{s^2 - n^2} (-1)^m (I_{ms} - I_{mn} - K_{ms} + K_{mn}) \quad \begin{pmatrix} m = r \\ n \neq s \end{pmatrix} \\
&= \frac{2}{\pi^2} \frac{mr}{r^2 - m^2} (-1)^m (I_{mn} - I_{rn} - J_{rn} + J_{mn}) \quad \begin{pmatrix} m \neq r \\ n = s \end{pmatrix} \\
&= \frac{1}{\pi^2} (-1)^m (-I_{mn} - J_{mn} + K_{mn} + L_{mn}) \quad \begin{pmatrix} m = r \\ n = s \end{pmatrix}
\end{aligned}\right\} \quad \text{(A-4)}$$

In these expressions,

$$\left.\begin{aligned}
I_{mn} &= \frac{(-1)^m}{a} \frac{m}{n} \iint_R \frac{\sin m\pi[(u+v)/2a] \sin n\pi[(v-u)/2\beta b]}{\sqrt{uv}}\, du\, dv \\
J_{mn} &= \frac{(-1)^m}{a} m\pi \iint_R \frac{\{1 - [(v-u)/2\beta b]\} \sin m\pi[(u+v)/2a] \cos n\pi[(v-u)/2\beta b]}{\sqrt{uv}}\, du\, dv \\
K_{mn} &= \frac{(-1)^m}{a} \frac{m^2\pi}{n} \iint_R \frac{\{1 - [(u+v)/2a]\} \cos m\pi[(u+v)/2a] \sin n\pi[(v-u)/2\beta b]}{\sqrt{uv}}\, du\, dv \\
L_{mn} &= \frac{(-1)^m}{a} (m\pi)^2 \iint_R \\
&\qquad \frac{\{1 - [(u+v)/2a]\}\{1 - [(v-u)/2\beta b]\} \cos m\pi[(u+v)/2a] \cos n\pi[(v-u)/2\beta b]}{\sqrt{uv}}\, du\, dv
\end{aligned}\right\} \quad \text{(A-5)}$$

The region of integration $R$ is bounded by the lines $u = 0$, $u = v$, and $u + v = 2a$ for $\beta b/a \geq 1$ and by the additional line $v - u = 2\beta b$ for $\beta b/a < 1$.

Hereinafter we confine our attention to values of $\beta b/a$ greater than or equal to one. For this range the expressions for $I_{mn}$, $J_{mn}$, $K_{mn}$, and $L_{mn}$ can be reduced to simpler forms, as follows:

Let

$$\left.\begin{aligned} u &= a\zeta(1 - \sin\theta) \\ u &= a\zeta(1 + \sin\theta) \end{aligned}\right\} \quad \text{(A-6)}$$

Then $I_{mn}$, for example, becomes

$$I_{mn} = (2m/n)\,(-1)^m \int_0^{\pi/2} \int_0^1 \sin m\pi\zeta \times$$
$$\sin\,[(m\pi/\sigma)\zeta \sin\theta]\, d\theta\, d\zeta \quad \text{(A-7)}$$

where
$$\sigma = (m/n)\,(\beta b/a) \quad \text{(A-8)}$$

Carrying out the $\zeta$-integration yields

$$I_{mn} = -\frac{\sigma}{n\pi}\left\{\int_0^{\pi/2}\frac{\sin\left[(m\pi/\sigma)\sin\theta\right]d\theta}{\sigma+\sin\theta} + \int_0^{\pi/2}\frac{\sin\left[(m\pi/\sigma)\sin\theta\right]d\theta}{\sigma-\sin\theta}\right\}$$

or

$$I_{mn} = -(\sigma/n\pi)\left[S(m,\sigma) - S(m,-\sigma)\right] \tag{A-9}$$

where

$$S(m,\sigma) = \int_0^{\pi/2}\frac{\sin\left[(m\pi/|\sigma|)\sin\theta\right]d\theta}{\sin\theta+\sigma} \tag{A-10}$$

By a similar procedure we find

$$J_{mn} = [\sigma/(\sigma^2-1)](1/n\pi)\left[S(m,\sigma) - S(m,-\sigma)\right] - \sigma[C(m,\sigma) - C(m,-\sigma)] + [\sigma/(\sigma^2-1)](m/n)\left[2 - \pi H_1(m\pi/\sigma)\right] \tag{A-11}$$

$$K_{mn} = -[\sigma^3/(\sigma^2-1)](1/n\pi)\left[S(m,\sigma) - S(m,-\sigma)\right] - \sigma(m/n)\left[C(m,\sigma) + C(m,-\sigma)\right] - [\sigma/(\sigma^2-1)](m/n)\left[2 - \pi H_1(m\pi/\sigma)\right] \tag{A-12}$$

$$L_{mn} = [3\sigma^3/(\sigma^2-1)^2](1/n\pi)\left[S(m,\sigma) - S(m,-\sigma)\right] + \sigma m\pi[S(m,\sigma) + S(m,-\sigma)] - [\sigma^3/(\sigma^2-1)]\left[C(m,\sigma) - C(m,-\sigma)\right] + [\sigma/(\sigma^2-1)](m/n)\left[C(m,\sigma) + C(m,-\sigma)\right] + [\sigma/(\sigma^2-1)]m\pi^2 J_1(m\pi/\sigma) + [\sigma(2+\sigma^2)/(\sigma^2-1)^2](m/n)\left[2 - \pi H_1(m\pi/\sigma)\right] + [2\sigma/(\sigma^2-1)](m/n)(-1)^m \tag{A-13}$$

where

$$C(m,\sigma) = \int_0^{\pi/2}\frac{\cos\left[(m\pi/|\sigma|)\sin\theta\right] - \cos m\pi}{\sin\theta+\sigma}\,d\theta \tag{A-14}$$

and $J_1$ and $H_1$ are Bessel and Struve functions.

The functions $S(m, \sigma)$ and $C(m, \sigma)$ can be evaluated accurately by means of numerical integration; the presence of the term cos $m\pi$ in Eq. (A-14) ensures well-behaved integrands. For the calculations of the values of $\bar{L}_{mn,\,rs}$ in Table 1, Gaussian integration with ten points on the interval (0, $\pi/2$) was used; this procedure yields values of the integrals accurate to at least five significant figures.

Except in the special case $\sigma = 1$ the values of $\bar{L}_{mn,\,rs}$ can be calculated from Eqs. (A-3), (A-4), and (A-9) through (A-14). For $\sigma = 1$, it is convenient to go back to Eq. (A-5) and obtain expressions for $I_{mn}$, $J_{mn}$, $K_{mn}$, and $L_{mn}$ directly. Thus, since $m\pi/a = n\pi/\beta b$ for this case, we can write, for example,

$$\sin m\pi[(u+v)/2a]\sin n\pi\left[(v-u)/2\beta b\right] = (1/2)\left[\cos(m\pi u/a) - \cos(m\pi v/a)\right]$$

and the necessary integrations can be performed without changing variables. The results for $\sigma = 1$ are

$$\left.\begin{aligned} I_{mn} &= (m/n)\left[2 - \pi H_1(m\pi)\right] \\ J_{mn} &= (2/3)(m/n) + (1/3)\left[(m\pi)^2/n\right]H_0(m\pi) - m\pi^2 J_1(m\pi) - (2/3)(m\pi/n)H_1(m\pi) \\ K_{mn} &= 2(m/n)(-1)^m - (2/3)(m/n) + (2/3)\left[(m\pi)^2/n\right]H_0(m\pi) - (1/3)(m\pi/n)H_1(m\pi) \\ L_{mn} &= (2/3)(m/n)(-1)^m + (2/15)(m/n) + (2/3)m^2\pi^3 J_0(m\pi) - (1/3)m\pi^2 J_1(m\pi) - \\ &\quad (4/15)(m^3\pi^2/n) + (1/5)\left[(m\pi)/n\right]^2 H_0(m\pi) + (m\pi/n)\left[(2/15)m^2\pi^2 - (2/5)\right]H_1(m\pi) \end{aligned}\right\} \tag{A-15}$$

## Appendix B—Flutter of Buckled Simply Supported Panels

It is generally agreed that buckling has an adverse effect on the flutter speed of panels. Past theoretical work on this subject, however, has dealt with only the two-dimensional panel-flutter problem. This work was pioneered by Isaacs,[1] who introduced the concept of the "transtability" speed, a speed calculated from purely *static* considerations that constitutes an upper limit on the *flutter* speed of the buckled panel. Hayes[2] and Miles[3] then demonstrated that the transtability speed is indeed equal to the flutter speed for small perturbations about the static equilibrium position.

The similarity between the governing equations of two- and three-dimensional panel flutter for strip theory with static air forces [see Eq. (7) and reference 12] indicates that the flutter speed of a buckled finite aspect ratio panel might also be obtained through a transtability type of approach. A preliminary investigation, limited by the use of small-deflection plate theory to small buckle depths, of the static buckling behavior of panels is outlined here. Since some of the results obtained are of uncertain validity, being unsupported by a dynamic analysis, the investigation is limited to a two-mode solution for simplicity.

The effect of the air forces on the buckling load can be determined by setting $\bar{k}$ equal to zero in Eq. (15). Slightly rewritten, the equation becomes

$$(8\lambda/3\pi^4)^2 = (\bar{A} + \bar{B}_0 - 1)(16 - 4\bar{A} - \bar{B}_0) \tag{B-1}$$

where, for $n = 1$,

$$\bar{B}_0 = \bar{R}_x(a/b)^2 - (a/b)^4$$

The buckling loads can be calculated from this equation. An example plot of the variation of $\bar{R}_x$ with $\lambda$ for $a/b = 1$, $\bar{R}_y = 0$ is shown in Fig. 7. Similar plots would result for other values of $a/b$ and $\bar{R}_y$.

The transtability analysis for the two-dimensional problem is based on a plot like that in Fig. 7. It is argued that a buckled panel subjected to air flow would exhibit the midplane load given by the left-hand branch of the curve. If $\lambda$ is increased, the load would increase

until the maximum of the curve is reached. Further increase of $\lambda$ would necessarily produce motion of the panel since there would be no stable static equilibrium position of the buckled panel. (Presumably, the panel would be unstable at the higher buckling loads not considered in the two-mode solution.) The maximum value of $\lambda$ given by the curve is the transtability value.

The same line of reasoning can be used for the three-dimensional problem, provided that the buckle depth is kept small. For this case, the results are dependent on the boundary conditions on in-plane deflections and stresses at the edges. Consider, for instance, a buckled panel with streamwise edges having a prescribed stress and spanwise edges having a prescribed displacement. For such boundary conditions the value of $\bar{B}_0$ would be fixed and the value of $\bar{A}$ would be that given by Eq. (B-1). The resulting transtability value of $\lambda$ would be found from the condition

$$\partial\lambda/\partial\bar{A} = 0$$

which gives

$$\lambda_T = (9\pi^4/32)\ |4 + \bar{B}_0| \qquad \text{(B-2)}$$

On the other hand, a panel with the edge boundary conditions reversed would have a fixed value of $\bar{A}$ and the appropriate transtability condition would be

$$\partial\lambda/\partial\bar{B}_0 = 0$$

The resulting value of $\lambda_T$ is

$$\lambda_T = (9\pi^4/16)\ |5 - \bar{A}| \qquad \text{(B-3)}$$

which is the same as that obtained for the unbuckled panel [see Eq. (16)]; this result can, of course, be quite different from that given by Eq. (B-2).

In a practical situation, the edge boundary conditions would probably be different from either of the foregoing cases, and different values of $\lambda_T$ would result; each situation requires separate treatment.

A question might arise as to the usefulness of the small-deflection theory in obtaining results pertaining to finite aspect ratio buckled panels. It is felt, however, that such results represent correctly the limiting case of vanishingly small buckle depths and, furthermore, that this limiting case establishes a lower bound on the critical value of $\lambda$ for buckled panels. The latter conjecture is based on the demonstrated independence of $\lambda_{cr}$ on buckle depth for the two-dimensional problem[12, 16] and the more rapid increase of stiffness with buckle depth for a finite aspect ratio plate than for an infinite aspect ratio plate (beam).[26] A test of the validity of the conjecture, and others implied in this Appendix, must await a full-fledged dynamic analysis of the aeroelastic behavior of three-dimensional buckled panels including large-deflection structural effects.

## References


[1] Isaacs, R. P., *Transtability Flutter of Supersonic Aircraft Panels*, U. S. Air Force Project RAND P-101, The RAND Corp., July 1, 1949.

[2] Hayes, W., *A Buckled Plate in a Supersonic Stream*, North American Aviation Report AL-1029, May 10, 1950.

[3] Miles, J. W., *Dynamic Chordwise Stability at Supersonic Speeds*, North American Aviation Report AL-1140, October 18, 1950.

[4] Miles, J. W., *On the Aerodynamic Instability of Thin Panels*, Journal of The Aeronautical Sciences, Vol. 23, No. 8, pp. 771–780, August, 1956.

[5] Shen, S. F., *Non-stationary Aerodynamics of a Two-Dimensional Bump in a Uniform Stream and Its Effect on the Vibration Characteristics of an Elastic Panel*, Massachusetts Institute of Technology, Contract No. N5ori-07833, Office Naval Res. (Project NR-064-259), May, 1952.

[6] Shen, S. F., *Flutter of a Two-Dimensional Simply Supported Uniform Panel in a Supersonic Stream*, Massachusetts Institute of Technology, Contract No. N5ori-07833, Office Naval Res. (Project NR-064-259), August 6, 1952.

[7] Goland, M., and Luke, Y. L., *An Exact Solution for Two-Dimensional Linear Panel Flutter at Supersonic Speeds*, Readers' Forum, Journal of the Aeronautical Sciences, Vol. 21, No. 4, pp. 275, 276, April, 1954.

[8] Shen, S. F., *Remarks on "An Exact Solution for Two-Dimensional Linear Panel Flutter at Supersonic Speeds,"* Readers' Forum, Journal of The Aeronautical Sciences, Vol. 22, No. 9, pp. 656, 657, September, 1955.

[9] Hedgepeth, J. M., Budiansky, B., and Leonard, R. W., *Analysis of Flutter in Compressible Flow of a Panel on Many Supports*, Journal of The Aeronautical Sciences, Vol. 21, No. 7, pp. 475–486, July, 1954.

[10] Nelson, H. C., and Cunningham, H. J., *Theoretical Investigation of Flutter of Two-Dimensional Flat Panels with One Surface Exposed to Supersonic Potential Flow*, NACA TN 3465, July, 1955.

[11] Fung, Y. C., *The Static Stability of a Two-Dimensional Curved Panel in a Supersonic Flow, with An Application to Panel Flutter*, Journal of The Aeronautical Sciences, Vol. 21, No. 8, pp. 556–565, August, 1954.

[12] Fung, Y. C., *The Flutter of a Buckled Plate in Supersonic Flow*, GALCIT Report No. OSR-TN-55-237, July, 1955.

[13] Hedgepeth, J. M., *On the Flutter of Panels at High Mach Numbers*, Readers' Forum, Journal of the Aeronautical Sciences, Vol. 23, No. 6, pp. 609, 610, June, 1956.

[14] Leonard, R. W., and Hedgepeth, J. M., *On the Flutter of Infinitely Long Panels on Many Supports*, Readers' Forum, Journal of the Aeronautical Sciences, Vol. 24, No. 4, pp. 381–383, May, 1957.

[15] Luke, Y. L., St. John, A. D., and Goland, M., *An Exact Solution for Two-Dimensional Linear Panel Flutter at Supersonic Speeds*, Midwest Research Institute, WADC TN 56-460, Contract No. AF 33(616)-2897, March 15, 1956.

[16] Eisley, J. G., *The Flutter of a Two-Dimensional Buckled Plate with Clamped Edges in a Supersonic Flow*, GALCIT Report No. OSR-TN-56-296, July, 1956.

[17] Miles, J. W., *Supersonic Flutter of a Cylindrical Shell*, The Ramo-Wooldridge Corporation, *Part I: General Theory*, Report No. AM5-2, August 19, 1955; *Part II: Pressurization and Internal Fluid Effects*, Report No. AM5-11, November 14, 1955; *Part III: Aeolotropic Shell*, Report No. AM5-12, December 2, 1955; *Part IV: Effects of Non-Uniform Steady Flow*, Report No. AM5-16, December 7, 1955.

[18] Leonard, R. W., and Hedgepeth, J. M., *On Panel Flutter and Divergence of Infinitely Long Unstiffened and Ring-Stiffened Thin-Walled Circular Cylinders*, NACA TN 3638, April, 1956.

[19] Eisley, J. G., *The Flutter of Simply Supported Rectangular Plates in a Supersonic Flow*, GALCIT Report No. OSR-TN-55-236, July, 1955.

[20] Luke, Y. L., St. John, A. D., and Gross, B., *Panel Flutter at Supersonic Speeds*, Midwest Research Institute reports to WADC, Contract No. AF 33(616)-2897, Third Quarterly Progress Report, March 29, 1956, Fourth Quarterly Progress Report, May 29, 1956.


(*Continued on page 586*)

# The Aerodynamic Action of Triangular Horn-Balanced Control Surfaces on the Supersonic Delta Wing

DEREK NAYLOR*

*A. V. Roe & Co., Limited*

SUMMARY

The pressure distribution of a supersonic delta wing in the region of influence of a deflected flap type of control with a triangular horn balance is determined on the basis of linearized theory. Both subsonic and supersonic leading edges are considered. General formulas for the control hinge moment increments $\Delta H_\alpha$, $\Delta H_\eta$ are calculated to estimate the effectiveness of an aerodynamic balance of the type considered, and corresponding formulas for the increment in the lift $\Delta L_\eta$ are also developed.

The final expressions for the increments are expressed as functions of the delta wing parameter $n = \tan \Gamma \tan \mu$ ($\Gamma$ being the leading-edge sweepback and $\mu$ the free-stream Mach angle) and a geometrical parameter determined by the control surface configuration. These functions are represented graphically. The results are applicable to full span flaps, provided the Mach waves from the apex of each balance do not intersect the balance area or the leading edge of the opposite wing, and to partial span flaps if the inboard edge does not lie within the Mach cone from the apex of the balance. Formulas for the total hinge moments are given in the case of full span flaps.

SYMBOLS

| | |
|---|---|
| $\alpha$ | = wing incidence |
| $\eta$ | = control deflection |
| $\Gamma$ | = leading-edge sweepback |
| $\mu$ | = free-stream Mach angle |
| $M$ | = free-stream Mach Number |
| $B$ | = cot $\mu$ |
| $K$ | = tan $\Gamma$ |
| $n$ | = $K/B$ |
| $c$ | = delta wing chord (Fig. 1) |
| $S$ | = flap area behind the hinge line |
| $b$ | = flap total span (Fig. 1) |
| $\bar{c}$ | = mean flap chord ($S = b\bar{c}$) |
| $x_0$ | = the maximum forward extension of the balance (the length RT in Fig. 1) |
| $m$ | = $x_0/c$ |
| $x_1$ | = basic flap chord (Fig. 1) |
| $t$ | = $x_1/c$ |
| $\sigma$ | = $m/t$ |
| $\lambda$ | = $(1 - t - m)/(1 - t)$ |
| $\beta$ | = $(1 + n)/(1 - n)$ |
| $\phi$ | = perturbation potential |
| $\psi$ | = pressure function (Eq. 3) |
| $(x, y)$ | = rectangular coordinates in the wing plane, with $x$-axis streamwise |
| $\theta$ | = $Ky/x$ |
| $U$ | = free-stream velocity |
| $E$ | = complete elliptic integral of second kind with modulus $n^{-1}(n^2 - 1)^{1/2}$ |
| $H_\alpha$ | = control hinge moment due to wing incidence |
| $H_\eta$ | = control hinge moment due to control deflection |
| $\Delta H_\alpha$, $\Delta H_\eta$ | = control hinge moment increments, defined by Eqs. (6) and (17) |
| $g(\sigma, n)$ | = hinge moment increment function defined by Eq. (9) |
| $h(\lambda, n)$ | = hinge moment increment function defined by Eq. (20) |
| $L_\eta$ | = control lift due to control deflection |
| $f(\sigma, n)$ | = control lift increment function defined by Eq. (29) |

Received July 10, 1956.

* Formerly, Aerodynamicist. Now, with the Department of Applied Mathematics, University of Toronto.

## PRESSURE DISTRIBUTION DUE TO CONTROL DEFLECTION

THE TYPE of horn balance considered occupies the region RVT of Fig. 1, and it is assumed that the hinge line coincides with the flap boundary TT′. To find the pressure distribution due to control deflection it is sufficient to consider a uniform incidence $\eta$ over the control only and zero incidence over the remainder of the wing.

### *Supersonic Leading Edge*

When the leading edge is supersonic (see Fig. 2) a systematic application of the integral formula,[1] Eq. (1), is necessary:

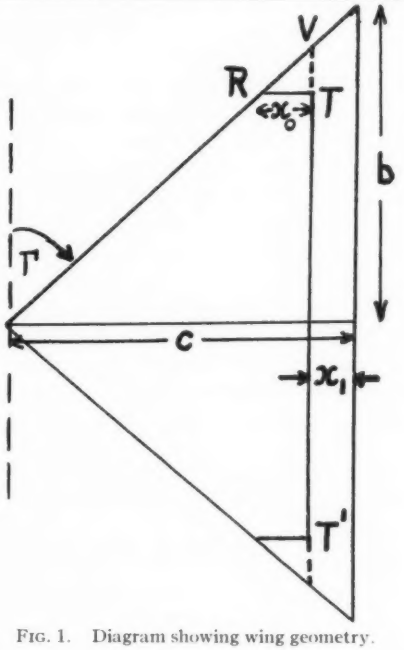


FIG. 1. Diagram showing wing geometry.

$$\phi(x, y) = \frac{1}{\pi} \iint_{D(x,y)} \frac{w(\xi, \eta) d\xi d\eta}{[(x - \xi)^2 - B^2(y - \eta)^2]^{1/2}} \quad (1)$$

where $w$ denotes the downwash in the wing plane and $D(x, y)$ the interior domain contained between the Mach lines $x - \xi = \pm B(y - \eta)$ drawn forward from the field point $(x, y)$. It is possible to apply Eq. (1) directly when the leading edge is supersonic since the downwash is known over the entire domain of integration. On the control, $w = \eta$, while on the wing, $w = 0$; therefore, $D(x, y)$ reduces to the interior of the Figure PQRS in which the wing region RSS′T may be omitted. The configuration of Mach lines shown in Fig. 2 divides the tip region into zones where the potential takes different analytic forms. When axes through the tip R of the balance are selected, the results for the pressure distribution in the regions 1, 2, 3, 4, and 5 influenced by the balance are given by

$$\left.\begin{aligned}
\psi_1 &= (\pi/2)(1 - n^2)^{-(1/2)} \\
\psi_2 = \psi_5 &= (1 - n^2)^{-(1/2)} \cot^{-1} [\beta(x - By)/(x + By)]^{1/2} \\
\psi_3 &= (1 - n^2)^{-(1/2)} \cot^{-1} [\beta(x - By)/(x + By)]^{1/2} + (1/2) \cos^{-1} [By/(x - x_0)] \\
\psi_4 &= (\pi/2) + (1 - n^2)^{-(1/2)} \cot^{-1} [\beta(x - By)/(x + By)]^{1/2}
\end{aligned}\right\} \quad (2)$$

where $$\psi(x, y) = \pi B \phi_x / 2U\eta \quad (3)$$

$\beta = (1 + n)/(1 - n)$, and $x_0$ denotes the maximum forward extension of the balance (the dimension RT of Fig. 1). The overall pressure distribution according to Eqs. (2) is finite and continuous everywhere except across the hinge line, where a discontinuity $\rho U^2 \eta / B$ in the pressure persists.

### *Subsonic Leading Edge*

When the leading edge is subsonic (see Fig. 3), Eq. (1) cannot be applied directly since the downwash is not known in the region between the leading edge and the Mach wave from the apex R. The influence at P of the region RSS′ must then be determined by subsonic leading-edge wing tip theory.[2,3] In the case of a wing of zero thickness the correction simplifies. Here the method developed by Evvard[3] is that adopted. Evvard's result states that the contributions of the zones RSS′ and RR′S′ to the velocity at P are equal and opposite so that the integral (1) may be evaluated over the region PQR′S′ only. When expressed in terms of the pressure function $\psi(x, y)$, the results of the integration in the different regions are

$$\left.\begin{aligned}
\psi_1 &= [1/(n + 1)] [(x + By)/(x - Ky)]^{1/2} + (1/2) \cos^{-1} [By/(x - x_0)] \\
\psi_2 &= [1/(n + 1)] \{[n(x + By) - (n + 1)x_0]/(x - Ky)\}^{1/2} + \tan^{-1} \{(x - Ky)/[n(x + By) - (n + 1)x_0]\}^{1/2} \\
\psi_3 &= [1/(n + 1)] [(x + By)/(x - Ky)]^{1/2} \\
\psi_4 &= (\pi/2) + [1/(n + 1)] [(x + By)/(x - Ky)]^{1/2}
\end{aligned}\right\} \quad (4)$$

It is noted that TA, one of the Mach lines from the hinge axis extremity T (Fig. 3), may meet the subsonic leading edge and be reflected back across the control to determine the zone 2. The condition for this is

$$n \geqslant 1 + \sigma \geqslant 1$$

If, however,

$$1 + \sigma \geqslant n \geqslant 1$$

then the Mach lines from the intersection T intersect the supersonic trailing edge and the reflected waves are of no consequence.

### Calculation of $\Delta H\eta$

The hinge moment will be given by

$$\eta H_\eta = -2\rho U \iint (x - x_0) \phi_x(x, y)\, dxdy$$

that is, in terms of the function $\psi(x, y)$,

$$\pi B H_\eta = -4\rho U^2 \iint (x - x_0) \psi(x, y)\, dxdy \quad (5)$$

evaluated over the control only.

The hinge moment increment $\Delta H_\eta$ is defined by

$$\Delta H_\eta = H_\eta - \bar{H}_\eta \quad (6)$$

where $\bar{H}_\eta$ denotes the hinge moment exerted on the control when no horn is present. The hinge moment $H_\eta$ and the hinge moment increment $\Delta H_\eta$ are most conveniently expressed in terms of the functions $g_0$, $g(\sigma, n)$ by writing

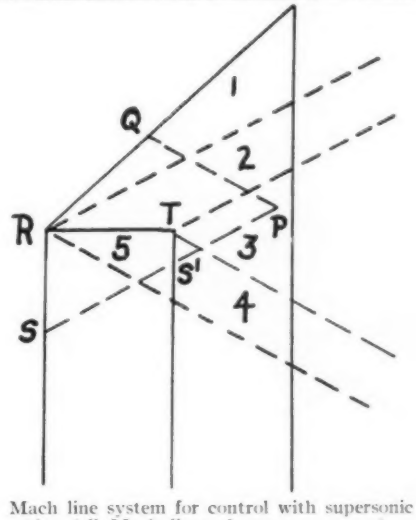


Fig. 2. Mach line system for control with supersonic leading edge (all Mach lines shown — — — —).

$$3\pi K^2 \bar{H}_\eta = 2\rho U^2 c^3 t^3 \, g_0 \tag{7}$$

$$3\pi K^2 \, H_\eta = 2\rho U^2 c^3 t^3 \, [g_0 + g(\sigma, n)] \tag{8}$$

so that, from Eq. (6),

$$3\pi K^2 \Delta H_\eta = 2\rho U^2 c^3 t^3 \, g(\sigma, n) \tag{9}$$

To illustrate the derivation of the expressions for $g_0$, $g(\sigma, n)$ it will be sufficient to set out the steps in the case when the leading edge is supersonic. The results will simply be stated when the leading edge is subsonic.

***Supersonic Leading Edge***

When the functions $\psi$ given by Eq. (2) are inserted in Eq. (5) and the integral evaluated over one control, the result is

$$B^2 H_\eta / 2\rho U^2 c^3 = (m^3/12n) \times \left\{1 + [2 \, (\cos^{-1} n)/\pi(1 - n^2)^{1/2}]\right\} - [(3 - t)t^2/6n] \tag{10}$$

When no horn balance occurs, $m = 0$, so that

$$B^2 \bar{H}_\eta / 2\rho U^2 c^3 = -[(3 - t)t^2/6n] \tag{11}$$

Therefore, from Eqs. (7) and (11),

$$g_0 = -[n\pi(3 - t)/2t] \tag{12}$$

Similarly, from Eqs. (6), (10), and (11),

$$B^2 \Delta H_\eta / 2\rho U^2 c^3 = (m^3/12n) \times \left\{1 + [2 \, (\cos^{-1} n)/\pi(1 - n^2)^{1/2}]\right\}$$

so that $g(\sigma, n)$, as defined by Eq. (9), is given in this case by

$$g(\sigma, n) = (n\sigma^3/2) \times \left\{(\pi/2) + [(\cos^{-1} n)/(1 - n^2)^{1/2}]\right\} \tag{13}$$

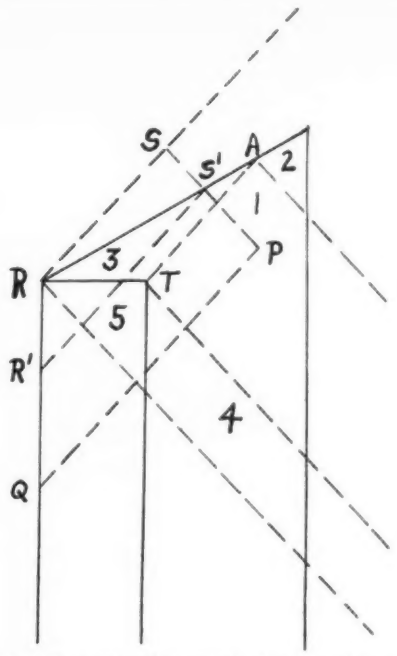


FIG. 3. Mach line system for control with subsonic leading edge.

Eqs. (12) and (13) apply only when the leading edge is supersonic, so that $0 \leqslant n \leqslant 1$.

***Subsonic Leading Edge***

In this case, the pressure distribution is given by the Eqs. (4), and the results of the integrations may be expressed in the form

$$g_0 = [-n\pi(3 - nt)]/2t \qquad \text{for} \quad 1 \leqslant n \tag{14}$$

$$g(\sigma, n) = [n\sigma^3/(n + 1)] \left\{1 - [(n + 1)/n^{1/2}] \tan^{-1} n^{1/2}\right\} - (n\pi/2) \, [n - 3 - 3\sigma + (2 + 3\sigma - \sigma^3) n^{-(1/2)}] \qquad \text{for} \quad 1 \leqslant n \leqslant 1 + \sigma \tag{15}$$

$$g(\sigma, n) = [n\sigma^3/(n + 1)] \left\{1 - [(n + 1)/n^{1/2}] \tan^{-1} n^{1/2}\right\} + [n(n - 1 + \sigma^2)/(n - 1)] \times [\sigma(n - 1 - \sigma)]^{1/2} - n^{1/2}(2 + 3\sigma - \sigma^3) \tan^{-1}[n\sigma/(n - 1 - \sigma)]^{1/2} - n(n - 3 - 3\sigma) \tan^{-1} [\sigma/(n - 1 - \sigma)]^{1/2} \qquad \text{for} \quad 1 \leqslant 1 + \sigma \leqslant n \tag{16}$$

CALCULATION OF $\Delta H_\alpha$

The hinge moment increment $\Delta H_\alpha$ is defined by

$$\Delta H_\alpha = H_\alpha - \bar{H}_\alpha \tag{17}$$

$\bar{H}_\alpha$ denoting the hinge moment when no horn occurs. Analogously to Eqs. (7) and (8), it is found convenient to write the moments in terms of functions $h_0$, $h(\lambda, n)$, as follows:

$$3K^2 \bar{H}_\alpha = \rho U^2 c^3 (1 - t)^3 \, h_0 \tag{18}$$

$$3K^2 \, H_\alpha = \rho U^2 c^3 (1 - t)^3 \, [h_0 + h(\lambda, n)] \tag{19}$$

$$3K^2 \, \Delta H_\alpha = \rho U^2 c^3 (1 - t)^3 \, h(\lambda, n) \tag{20}$$

The formulas for $\bar{H}_\alpha$ are to be found in references 5 and 6 and, when expressed in the above notation, are equivalent to

$$h_0 = -nt^2(3 - t) \, (1 - t)^{-3} \quad (0 \leqslant n \leqslant 1) \tag{21}$$

$$h_0 = -(\pi t^2/2E) \, (3 - t) \, (1 - t)^{-3} \quad (1 \leqslant n) \tag{22}$$

To evaluate control hinge moments with respect to incidence it is sufficient to consider the pressure distribution due to uniform incidence $\alpha$ over the entire wing and integrate the hinge moment of the pressure over the relevant control area. To obtain the increment $\Delta H_\alpha$, it is only necessary to integrate over the horn itself. Therefore,

$$\alpha \Delta H_\alpha = -2\rho U \iint (x - x_0) \, \phi_x(x, y) \, dxdy \tag{23}$$

integrated over the horn only.

***Supersonic Leading Edge***

The Mach wave from the delta apex (see Fig. 4) divides the wing into zones 1 and 2. In zone 1, between the leading edge and the Mach wave,

$$B\phi_x = U\alpha(1 - n^2)^{-(1/2)}$$

In zone 2, behind the Mach wave,

$$B\phi_x = U\alpha(1 - n^2)^{-(1/2)}(2/\pi) \times \cos^{-1}[(n^2 - \theta^2)/(1 - \theta^2)]^{1/2}$$

when axes through the delta apex are now used and $\theta = Ky/x$.

When the integral of Eq. (23) is evaluated, there are two cases to distinguish, depending on whether the balance is intersected by the Mach wave from the delta apex.

If $0 \leqslant n \leqslant \lambda \leqslant 1$, the Mach wave does not meet the balance and the function $h(\lambda, n)$ defined by Eq. (20) takes the form

$$h(\lambda, n) = n(1 - \lambda)^3(1 - n^2)^{-(1/2)} \qquad (24)$$

If $0 \leq \lambda \leq n \leq 1$, the wave intersects the balance and

$$h(\lambda, n) = [2n/\pi(1 - n^2)^{1/2}]\{(1 - n^2)^{1/2}[\cos^{-1}(\lambda/n) + (\lambda^3/n)\cosh^{-1}(n/\lambda)] - \lambda(3 + \lambda^2)\tan^{-1}[(1 - n^2)/(n^2 - \lambda^2)]^{1/2} + (1 + 3\lambda^2)\tan^{-1}[(1 - n^2)\lambda^2/(n^2 - \lambda^2)]^{1/2}\} \qquad (25)$$

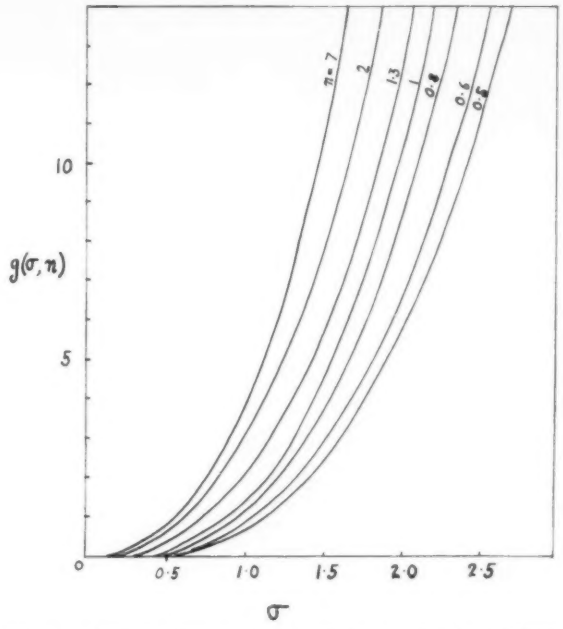


FIG. 5. Control hinge moment function $g(\sigma, n)$ for different values of $n$.

***Subsonic Leading Edge***

In this case,[4]

$$\phi_x = (U\alpha/KE)(1 - \theta^2)^{-(1/2)}$$

and one obtains

$$h(\lambda, n) = (1/E)[\cos^{-1}\lambda + \lambda^3\cosh^{-1}(1/\lambda) - 2\lambda(1 - \lambda^2)^{1/2}] \qquad (26)$$

for $0 \leqslant \lambda \leqslant 1 \leqslant n$.

## EXPRESSIONS FOR $\Delta C_{H_\alpha}$, $\Delta C_{H_\eta}$

Defining the hinge moment coefficients in terms of the control area $S$ behind the hinge line and a mean chord $\bar{c}$ such that $S = b\bar{c}$ where $b$ denotes half the total wing span, then, in the present notation,

$$S = tc^2(2 - t)/(2K) \qquad (27)$$

$$b = c/K, \quad \bar{c} = tc(2 - t)/2$$

$$\Delta H_\alpha = (1/2)\rho U^2 Sc\Delta C_{H_\alpha}$$

$$\Delta H_\eta = (1/2)\rho U^2 Sc\Delta C_{H_\eta}$$

therefore, from Eqs. (20) and (9),

$$\left.\begin{aligned}\Delta C_{H_\alpha} &= [8(1 - t)^3/3Kt^2(2 - t)^2]\,h(\lambda, n)\\ \Delta C_{H_\eta} &= [16t/3\pi K(2 - t)^2]\,g(\sigma, n)\end{aligned}\right\} \qquad (28)$$

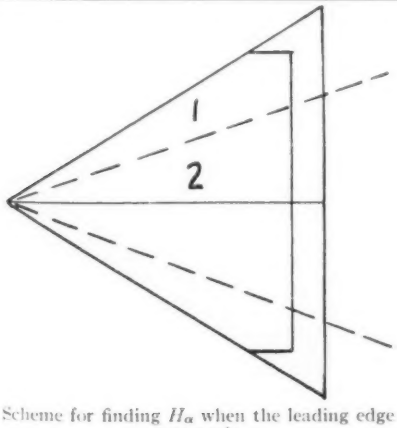


FIG. 4. Scheme for finding $H_\alpha$ when the leading edge is supersupersonic.

## LIFT DUE TO CONTROL DEFLECTION

In this case, it is necessary to evaluate the simpler integral

$$\eta L_\eta = 2\rho U \iint \phi_x(x, y)dxdy$$

over the area of the control and wing contained in the Mach wave from the apex of the horn balance. Therefore, in addition to the pressure distribution on the control, which is given by Eqs. (2) when the leading edge is supersonic and by Eqs. (4) when subsonic, it is necessary to calculate the pressure distribution over the region of the wing influenced by the balance. This region is zone 5 of Figs. 2 and 3.

The results for the pressure distribution in zone 5 when the leading edge is supersonic may be expressed

$$\psi_5 = (1 - n^2)^{-(1/2)}\cot^{-1}\{\beta[(x - By)/(x + By)]\}^{1/2}$$

for $0 < n < 1$

when axes through the apex of the balance are used. If the leading edge is subsonic, then

$$\psi_b = [1/(\eta + 1)]\,[(x + By)/(x - Ky)]^{1/2} \quad \text{for} \quad 1 \leqslant n$$

Defining the increment for lift in the usual manner,

$$\Delta L_\eta = L_\eta - \bar{L}_\eta$$

where $\bar{L}_\eta$ denotes the lift exerted due to control deflection on the control when the balance is absent, and $L_\eta$ denotes the lift exerted on the control and the wing regions influenced by the balance, and introducing a function $f(\sigma, n)$ by means of

$$\pi K^2 \Delta L_\eta = 2\rho U^2 c^2 t^2 f(\sigma, n) \tag{29}$$

one finds

$$\left.\begin{aligned} f(\sigma, n) &= n\pi\sigma^2/2 \qquad \text{for} \quad 0 \leqslant n \leqslant 1 \\ f(\sigma, n) &= (n\pi/4)\,[n - 3 - 4\sigma + 2(1 + \sigma)^2 n^{-(1,2)}] \qquad \text{for} \quad 1 \leqslant n \leqslant 1 + \sigma \\ f(\sigma, n) &= n^{1/2}(1 + \sigma)^2 \tan^{-1}[n\sigma/(n - 1 - \sigma)]^{1/2} + (n/2)\,(n - 3 - 4\sigma)\tan^{-1}[\sigma/(n - 1 - \sigma)]^{1/2} - \\ &\qquad (n/2)\,[\sigma(n - 1 - \sigma)]^{1/2} \qquad \text{for} \quad 1 \leqslant 1 + \sigma \leqslant n \end{aligned}\right\} \tag{30}$$

### Use of the Charts for $g(\sigma, n)$, $h(\lambda, n)$, $f(\sigma, n)$

Eqs. (13), (15), and (16) for $g(\sigma, n)$ and Eqs. (24), (25), and (26) for $h(\lambda, n)$ enable these functions to be calculated, and the results for selected values of $n$ are represented graphically in Figs. 5 and 6. To obtain the hinge moment increments $\Delta H_\eta$, $\Delta H_\alpha$ for a given control and horn balance it is only necessary to compute the parameters

$$\sigma = m/t, \quad \lambda = (1 - t - m)/(1 - t), \quad n = K/B$$

read off the values of the functions $g(\sigma, n)$, $h(\lambda, n)$ from the charts and substitute in Eqs. (9) and (20). The quantities $\Delta H_\eta$, $\Delta H_\alpha$ so obtained then give the increments in the hinge moments exerted on a control due to an added horn balance of the type considered. If the total hinge moments are required, then the functions $g_0$, $h_0$ may be calculated from Eqs. (12), (14), (21), or (22) and Eqs. (8) and (19) may be used, provided full span flaps are being considered. In the case of partial span flaps, the results are still applicable as here derived provided the inboard edge does not lie within the Mach cone from the apex of the near balance, and, in this case, the quantities $\Delta H_\eta$, $\Delta H_\alpha$ may be added onto data for such flaps without the horn balances.

Similarly, Fig. 7 gives the values of the function $f(\sigma, n)$ computed from Eqs. (30). $\Delta L_\eta$ may then be obtained from Eq. (29). Reference should be made to the work of Coale,[7] who considers a rectangular horn balance mounted on a rectangular flap. Comparison of the results is difficult, as both the type of balance and the basic flap differ from those considered in the present work. The geometrical configuration

(Continued on page 610)

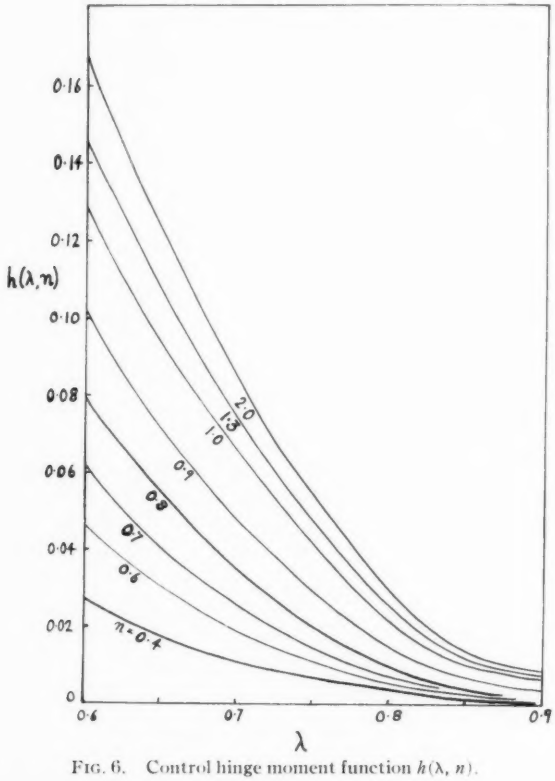


FIG. 6. Control hinge moment function $h(\lambda, n)$.

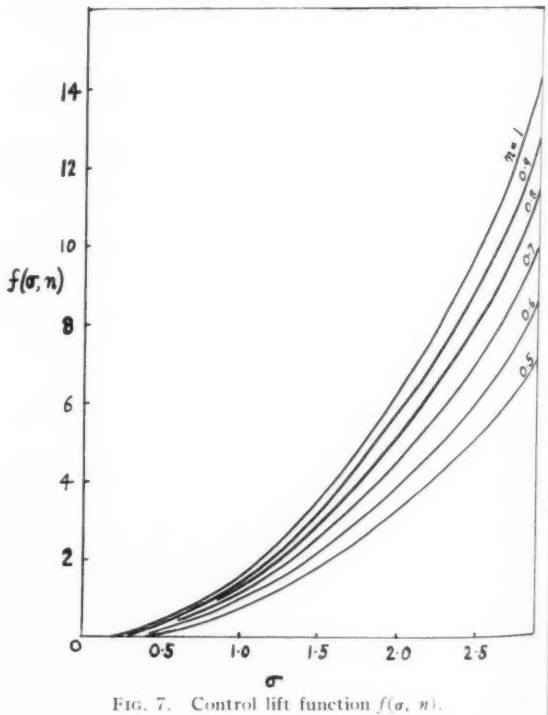


FIG. 7. Control lift function $f(\sigma, n)$.

# Fixing Boundary-Layer Transition on Supersonic Wind-Tunnel Models

MARVIN LUTHER*

*California Institute of Technology*

SUMMARY

In order to reduce or eliminate scale effects of supersonic wind-tunnel models, it often is important to fix transition to turbulent flow, in the boundary layer of the model, by some artificial method. A systematic series of wind-tunnel tests was conducted to study the use of single-element and distributed roughness for this purpose, and to determine the character of roughnesses which would promote transition with minimum collateral effect on the flow. Curves are presented showing critical roughness height as a function of Mach and Reynolds Numbers; also presented are schlieren photographs showing the effect of Reynolds Number, roughness height, and angle of attack on the transition point. The models used for the study are a family of cone-ogive-cylinders with a fineness ratio of 10.6.

SYMBOLS

$A$ = cylinder cross-sectional area = base area = 2.011 sq.in.
$A_l$ = model lateral surface area
$A_t$ = model lateral surface area forward from station $t$
$c$ = constant defined by Eq. (6)
$C_D$ = drag coefficient
$C_{DL}$ = drag coefficient for model with laminar boundary layer
$C_{DT}$ = drag coefficient for model with turbulent boundary layer
$D$ = drag force measured by balance
$k$ = height of roughness element
$M$ = Mach Number
$p$ = static pressure
$q$ = dynamic pressure = $\rho u^2/2$
$R_x$ = Reynolds Number
$S$ = Sutherland's constant = 216°R.
$t$ = static temperature
$u$ = velocity
$x$ = coordinate along model surface, positive aft, with origin at tip of model
$y$ = coordinate normal to model surface with origin at model surface
$\alpha$ = indicated angle of attack
$\gamma$ = ratio of specific heats
$\delta^*$ = boundary-layer displacement thickness
$\mu$ = viscosity
$\nu$ = kinematic viscosity
$\rho$ = mass density

*Subscripts*

$aw$ = adiabatic surface condition
$b$ = model base
$c$ = critical
$k$ = station at which the roughness element is located
$t$ = transition point
$w$ = model surface
$0$ = free-stream conditions

Received December 26, 1956.

* Formerly, Research Engineer, Jet Propulsion Laboratory. Now, Research Engineer, Military Operations Research Division, Lockheed Aircraft Corporation, Burbank

## (1) INTRODUCTION

SINCE supersonic wind tunnels are limited in size and stagnation pressure by power requirements and other considerations, many model tests are made at Reynolds Numbers much lower than those of the full-scale aircraft or missile. As a result, the boundary layer may be laminar over a large part or all of the model surface instead of turbulent as it frequently is at the higher Reynolds Numbers of flight. This difference affects the skin-friction drag, the rate of growth of the boundary layer (and therefore the pressure distribution), the conditions under which the boundary layer separates, its behavior after separation, and the effectiveness of control surfaces that are partially immersed in the boundary layer. As the flight speed increases, these effects become more important because of the fact that, in general, the boundary-layer thickness increases with Mach Number (at constant Reynolds Number).

In order to reduce or eliminate these scale effects it is often necessary to fix transition to turbulent flow, in the boundary layer on the model, by some artificial method. This requirement presents the problem of choosing a mechanism which will promote transition with minimum collateral effect on the flow.

Although a fair amount of data on this subject has been published,[1–4] (cf. also, bibliography of reference 1), most of the material concerns two-dimensional models and/or low-speed flow. A series of five tests were performed[1] at the Jet Propulsion Laboratory during the period from December, 1954 to November, 1955, to study the production of transition on three-dimensional models at supersonic speeds; the tests were conducted in the 20-in. wind tunnel on cone-ogive-cylinder models at Mach Numbers 1.63, 3.07, 4.09, and 5.04. The method used to produce transition was the addition of roughness to the tip of the cones, two types of roughness being used—single-element (wire) and distributed (carborundum grit).

## (2) METHODS OF FIXING TRANSITION

The methods which have been used for fixing transition† include (1) attaching carborundum grit, single or multiple wires, or ridges to the model surface; (2) cutting multiple grooves into the surface; and (3) injecting air into the boundary layer. The attachment of grit or

† The term "fixing transition" is used to indicate the artificial establishment of the boundary-layer transition point at or near the device used for that purpose.

FIG. 1. Basic model configurations with windshield.

wires to the model surface appears to be the most practical technique for use in supersonic wind tunnels, and the present investigation was limited to the use of grit and single wires. Multiple wires may prove more satisfactory in some situations since their size can be smaller than that of the single wire, and consequently the disturbances produced in the free stream might be expected to be less severe. Inasmuch as grooves have been found less satisfactory than ridges,[3,4] they were not considered in this study. Air injection is probably the most elegant way of producing transition, and the size of the disturbance can be varied by controlling the air flow. Its application to general models is limited, however, because of the increased complexity of the models.

Carborundum grit has the disadvantage that it tends to be eroded away in time. If grit is used in a lengthy test, the forward tip of the model must be readily detachable in order to permit reapplication of the grit at the end of the day. A possible advantage of the grit is that, in low-speed tests, it has been shown to provide less distortion of the turbulent boundary-layer velocity profile.[3,4] The average size of grit used during the tests are listed in Table 1. The sizes were supplied by the manufacturer and correlate well with measurements made with an optical microscope. The sizes of wire used as single element roughnesses are also given in Table 1.

TABLE 1
Roughness Elements

| Grit No. | Mean Grit Height (in.) | American Wire Gage No. | Wire Diameter (in.) |
|---|---|---|---|
| 320 | 0.0014 | 38 | 0.0040 |
| 220 | 0.0027 | 33 | 0.0071 |
| 150 | 0.0039 | 32 | 0.0080 |
| 120 | 0.0052 | 29 | 0.0113 |
| 100 | 0.0066 | 27 | 0.0142 |
| 80 | 0.0094 | 24 | 0.0201 |
| 60 | 0.0131 | 19 | 0.0359 |

### (3) Description of Models

The models were bodies of revolution composed of conical noses and cylindrical afterbodies joined by tangent circular ogives. The three basic models had small-radius, tangent, circular ogives and cones of 12, 20, and 30 degrees included angle; they are designated models $N_{12}B_1$, $N_{20}B_1$, and $N_{30}B_1$, respectively. A fourth model uses the same conical tip as $N_{20}B_1$ and the same afterbody, but has a large-radius ogive. This model was designed for the purpose of observing the effect of pressure gradient and is designated $N_{20A}B_1$. The four models are shown with basic dimensions in Fig. 1. Model profile coordinates are given in Table 2.

Several tips were made for each cone in order to facilitate the exchange of roughness elements. Nose tips for the 20° cone, with typical roughness elements applied.

TABLE 2
Model Profile Coordinates

| $N_{12}$ | | $N_{20}$ | | $N_{20A}$ | | $N_{30}$ | |
|---|---|---|---|---|---|---|---|
| Station† (in.) | Diameter (in.) | Station (in.) | Diameter (in.) | Station (in.) | Diameter (in.) | Station (in.) | Diameter (in.) |
| 0.000 | 0.0000 | 0.000 | 0.0000 | 0.000 | 0.0000 | 0.000 | 0.0000 |
| 7.309 | 1.5351 | 4.160 | 1.4693 | 2.000 | 0.7021 | 2.712 | 1.4468 |
| 7.359 | 1.5450 | 4.210 | 1.4861 | 2.250 | 0.7827 | 2.762 | 1.4677 |
| 7.409 | 1.5531 | 4.260 | 1.5020 | 2.500 | 0.8590 | 2.812 | 1.4868 |
| 7.459 | 1.5611 | 4.310 | 1.5170 | 2.750 | 0.9323 | 2.862 | 1.5040 |
| 7.509 | 1.5677 | 4.360 | 1.5307 | 3.000 | 1.0029 | 2.912 | 1.5195 |
| 7.559 | 1.5734 | 4.410 | 1.5430 | 3.250 | 1.0695 | 2.962 | 1.5341 |
| 7.609 | 1.5787 | 4.460 | 1.5542 | 3.500 | 1.1333 | 3.012 | 1.5468 |
| 7.659 | 1.5835 | 4.510 | 1.5641 | 3.750 | 1.1942 | 3.062 | 1.5582 |
| 7.709 | 1.5876 | 4.560 | 1.5728 | 4.000 | 1.2491 | 3.112 | 1.5676 |
| 7.759 | 1.5917 | 4.610 | 1.5800 | 4.250 | 1.2978 | 3.162 | 1.5756 |
| 7.809 | 1.5948 | 4.660 | 1.5860 | 4.500 | 1.3423 | 3.212 | 1.5822 |
| 7.859 | 1.5975 | 4.710 | 1.5905 | 4.750 | 1.3854 | 3.262 | 1.5878 |
| 7.909 | 1.5991 | 4.760 | 1.5941 | 5.000 | 1.4252 | 3.312 | 1.5922 |
| 7.959 | 1.5996 | 4.810 | 1.5965 | 5.250 | 1.4602 | 3.362 | 1.5961 |
| 8.459 | 1.6000 | 4.860 | 1.5982 | 5.500 | 1.4900 | 3.412 | 1.5987 |
| 8.959 | 1.6000 | 4.910 | 1.5991 | 5.750 | 1.5150 | 3.462 | 1.6000 |
| ... | ... | 4.960 | 1.5998 | 6.000 | 1.5365 | 8.962 | 1.6000 |
| ... | ... | 5.460 | 1.6000 | 6.500 | 1.5718 | ... | ... |
| ... | ... | 8.930 | 1.6000 | 7.000 | 1.5889 | ... | ... |
| ... | ... | ... | ... | 7.700 | 1.5986 | ... | ... |
| ... | ... | ... | ... | 8.960 | 1.6000 | ... | ... |

† Station numbers in this report are given in inches aft from the theoretical tip before the tip radius was applied.

are shown in Fig. 2. The tips were slightly blunted, with tip radii ranging from 0.0025 to 0.0067 body diameters. It is believed that this degree of bluntness did not have a measurable effect on transition.

The base of the models was reamed out for a depth of 0.5 in. so as to leave a 0.031-in. wall thickness. The windshield was provided with a collar of such diameter as to leave a 0.031-in. annular opening between windshield and model base. The reasons for this design and details of the base-pressure instrumentation are discussed in Section 5.

### (4) Wind Tunnel and Instrumentation

Design features of the 20-in. wind tunnel permit its continuous operation in either a variable-density closed circuit or an open circuit. For the present tests it was operated as a closed-circuit tunnel. Any value of test-section Mach Number between 1.33 and 5.04 may be set by remote control from the control-room console. Normal operation is restricted to fourteen Mach Numbers, between 1.33 and 4.54, for which flow surveys have been made; however, three runs were made during the earlier tests at Mach Number 5.04. It is expected that additional runs will be made at 5.04 when planned tunnel modification and calibration make operation at this Mach Number more convenient and reliable. The turbulence level is approximately 0.005, defined as the ratio of the disturbance velocity in the streamwise direction to the stream velocity, and measured in the supply section. Data from flow surveys for the Mach Numbers used are presented in Table 3, together with other test-section flow parameters; at all Mach Numbers the test section is 20 in. high by 18 in. wide. During a given run the air supply is maintained at a constant temperature and within a dew-point range of $-50$ to $-10$°F. Test-section flow parameters were determined by using the Mach Number, the measured supply-section stagnation pressure and temperature, and the assumption of isentropic flow in the nozzle.

Of the various methods which have been used to determine the location of transition, those which were best adapted to the present test were (1) the measurement of drag, and (2) schlieren photography.

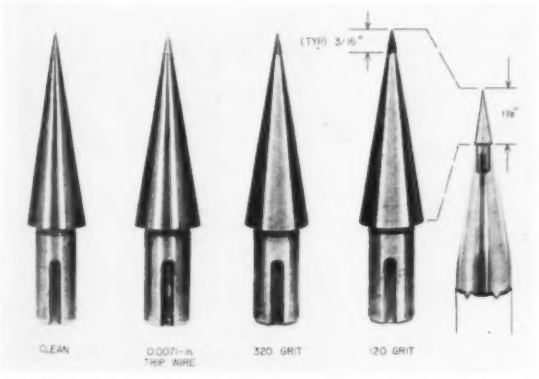


Fig. 2. Model tips with typical roughness elements.

Table 3
Test-Section Flow Conditions

| | Mach Number | | | |
|---|---|---|---|---|
| | 1.63 | 3.07 | 4.09 | 5.04 |
| Total pressure (psia) | | | | |
| Maximum | 24.1 | 29.9 | 52.0 | 65.5 |
| Minimum | 1.9 | 15.4 | 17.0 | 17.0 |
| Dynamic pressure (psia) | | | | |
| Maximum | 10.1 | 4.8 | 3.6 | 2.1 |
| Minimum | 0.8 | 2.5 | 1.2 | 0.9 |
| Static pressure (psia) | | | | |
| Maximum | 5.4 | 0.7 | 0.3 | 0.1 |
| Minimum | 0.4 | 0.4 | 0.1 | 0.05 |
| Reynolds No./in. $\times 10^6$ | | | | |
| Maximum | 0.56 | 0.36 | 0.38 | 0.31 |
| Minimum | 0.05 | 0.18 | 0.13 | 0.13 |
| Mach Number variation | +0.006 | +0.010 | +0.010 | † |
| | −0.004 | −0.030 | −0.003 | † |
| Flow-angle variation | +0.20 | +0.10 | +0.15 | † |
| | +0.00 | −0.03 | −0.00 | † |
| Static-pressure variation ($\Delta p_0/p_0$) | 0.013 | 0.062 | 0.020 | † |

† Flow calibration has not been made at this Mach Number.

The models were sting-supported from a crescent-shaped strut carrier, which may be rotated 30° in pitch. The sting and strut carrier are protected from aerodynamic loads by a windshield which is open to the tank surrounding the external balance. Flow between the test section and the balance tank is prevented by evacuating the tank to the model base pressure. The base pressure used for this purpose was that measured at an orifice located at the periphery of the collar on the windshield, since this pressure should be very nearly equal to that at the annular orifice between the windshield collar and the model base. A second pressure, that in the chamber at the model base, was measured on a mercury micromanometer which could be read to 0.001 cm. of mercury. This pressure, which might differ from the base pressure in the advent of a small flow through the model base, was used in the data reduction.

The balance system mechanically separates the model lift, drag, and side forces and the pitching, rolling, and yawing moments. These forces and moments are sensed by hydraulic load cells and are measured by self-balancing beams. The moments as measured are referred to a set of orthogonal axes which intersect in a point that is coincident with the center of rotation of the support system and the center line of the test-section windows.

Flow in the test section may be observed optically by either the shadowgraph or the schlieren technique. For the first four tests the schlieren system was used with a spark source of approximately 3-microsec. duration. For the fifth test a 1-microsec. source was used and was found to be less satisfactory than the source used for the earlier tests.

### (5) Test Procedure

During each run, data were obtained at four to six stagnation pressures, including the maximum and minimum available, in order to provide variation of Reynolds Number. At each pressure level the drag force and the base pressure were recorded and reduced to coefficient form at 1-min. intervals until the drag co-

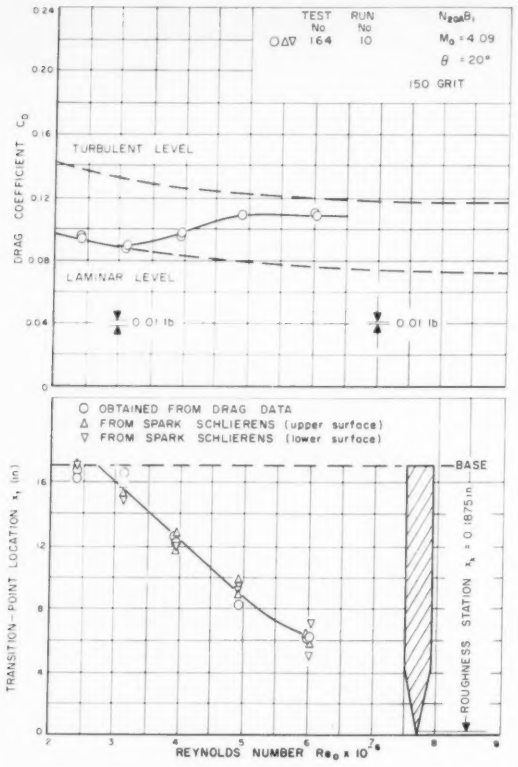


FIG. 3. Typical plot of drag coefficient vs. Reynolds Number.

efficient repeated within the estimated accuracy of the system. Assuming, then, that equilibrium conditions had been reached, the pressure was changed to the next level. A spark-schlieren photograph was taken at each point—i.e., each time the drag data were recorded. A period of 2 to 6 min. was required for the complete procedure at each pressure. Plots of drag coefficient vs. Reynolds Number were made as the run progressed, and any data which did not appear reasonable were checked before the conclusion of the run.

It was noted that the data were very sensitive to the accuracy with which the base pressure and balance-tank pressure were balanced. Accordingly, the pressures were balanced within 1 mm. of mercury when possible. At high Mach Number and low supply pressure (or Reynolds Number) the base pressure was lower than the lowest balance-tank pressure because of limitations of the pumping system; when this condition obtained, the measured drag data were questionable. The data were also affected by the condition of the model surface; as a result, the surface had to be carefully cleaned after each model change.

During several runs the model was pitched, and schlieren photographs were made at several angles of attack; however, drag data were obtained only at zero angle of attack.

### (6) Data Reduction

The drag data were reduced to coefficent form using the relation

$$C_D = [D - (p_0 - p_b)A]/q_0A \quad (1)$$

where $D$ is the drag force recorded by the hydraulic balance, $p_b$ is the base pressure (within the base chamber), $A$ is the base area (equal for these models to the reference area $A$), and $p_0$ and $q_0$ are free-stream static and dynamic pressure, respectively.

The drag coefficients were plotted vs. Reynolds number $Re_0$ and then crossplotted vs. roughness height $k$ at constant Reynolds Numbers. The critical roughness height was inferred from these plots; Figs. 3 and 4 are typical. To aid the fairing and intepretation of the drag-coefficient plots, the transition-point location $x_t$ was measured from the schlieren photographs and plotted vs. Reynolds Number. The same quantity was also computed from the drag data using the relations

$$x_t = f(A_t) \quad (2)$$

$$A_t = A_t[(C_D - C_{DL})/(C_{DT} - C_{LL})] \quad (3)$$

where $A_t$ is the area of the surface forward from station $x_t$, and $C_{DL}$ and $C_{DT}$ are the drag coefficients for the model with a laminar and a turbulent boundary layer, respectively. The values of $C_{DL}$ and $C_{DT}$ were obtained by calculating approximate values, plotting these values vs. Reynolds Number, and shifting these curves to make them conform to the values measured for models which, from the schlieren evidence, had completely laminar or completely turbulent boundary layers.

To attempt correlation with Dryden's roughness parameter[2] ($k\ \delta_k^*$), it was necessary to compute the boundary-layer displacement thickness $\delta_k^*$ at the stations where roughness was applied to the conical tips. For this purpose, the defining equation

$$\delta^* = \int_0^\infty [1 - (\rho\ u/\rho_0 u_0)]dy \quad (4)$$

was used, as was also the solution to the flat-plate boundary-layer problem given by Chapman and Rubesin[5] which reduces Eq. (4) to the form

$$\delta^* = (\nu_{0w}xC/u_0)^{1/2}\{1.7208 + 1.1094(\gamma - 1)M_0^2 + 1.9384[(t_w/t_0) - (t_{aw}/t_0)]\} \quad (5)$$

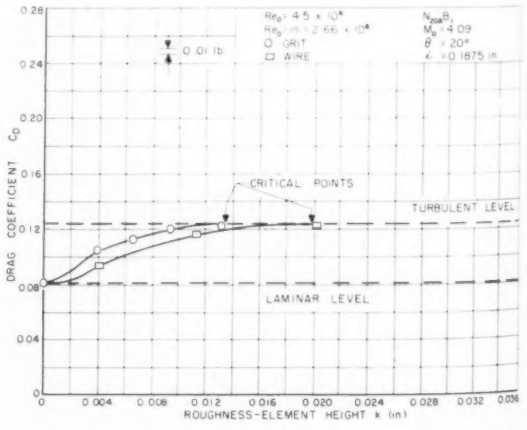


FIG. 4. Typical plot of drag coefficient vs. roughness height.

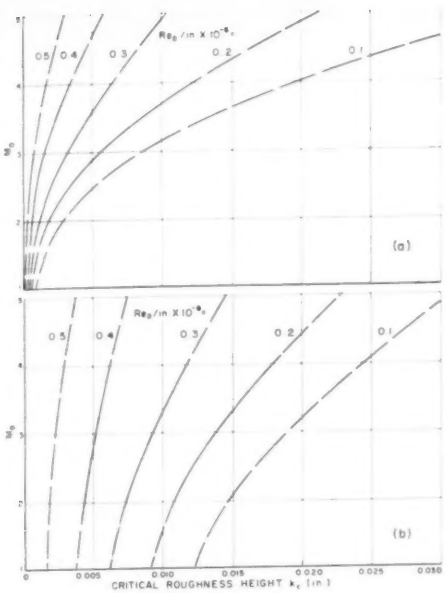


FIG. 5. Effect of Mach Number on critical roughness height for model $N_{12}B_1$ with $x_k = 0.1875$ in. (a) Distributed roughness, (b) Single-element roughness.

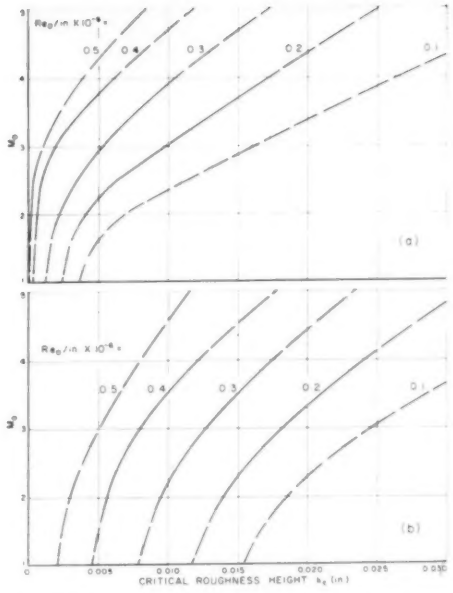


FIG. 7. Effect of Mach Number on critical roughness height for model $N_{20}B_1$ with $x_k = 0.1875$ in. (a) Distributed roughness; (b) Single-element roughness.

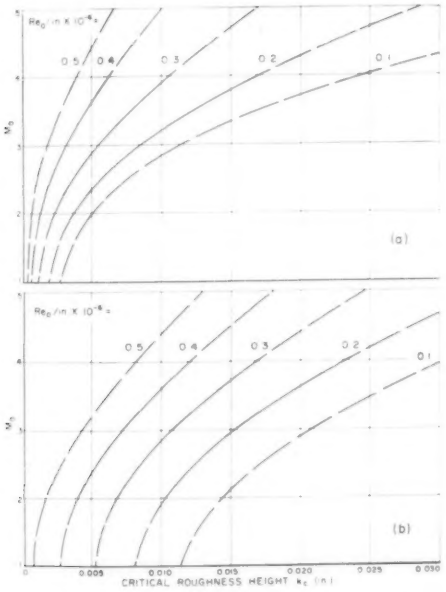


FIG. 6. Effect of Mach Number on critical roughness height for model $N_{20A}B_1$ with $x_k = 0.1875$ in. (a) Distributed roughness, (b) Single-element roughness.

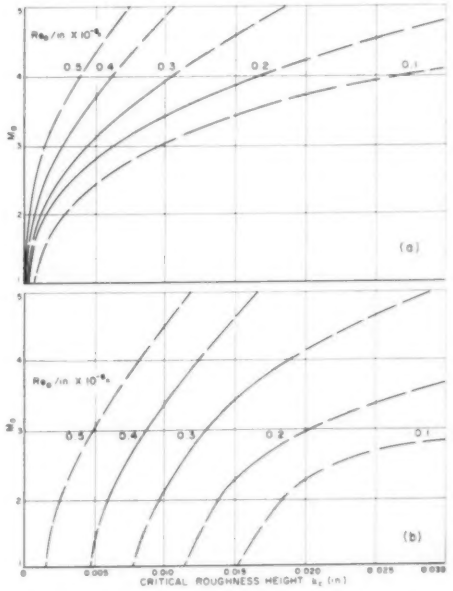


FIG. 8. Effect of Mach Number on critical roughness height for model $N_{20}B_1$ with $x_k = 0.1875$ in. (a) Distributed roughness, (b) Single-element roughness.

where $t_w$ is the wall temperature, $t_{aw}$ is the adiabatic wall temperature, and $\nu_0$, $u_0$, $M_0$, and $t_0$ are free-stream kinematic viscosity, velocity, Mach Number, and static temperature, respectively. The quantity $C$ is a constant defined by the assumed relation

$$\mu / \mu_0 = C(t / t_0) \tag{6}$$

where $\mu$ and $\mu_0$ are the local and the free-stream viscosity. This relation provides reasonable accuracy at moderate Mach Numbers when the constant $C$ is determined by substitution in Sutherland's formula,

$$C = (t_w / t_0)[(t_0 + S) / (t_w + S)] \tag{7}$$

where $S$ is Sutherland's constant (216°R. for air).

The cone solution was obtained using the transformation law which states that the laminar cone solution is the flat-plate solution computed for one third of the Reynolds Number on the cone.[6,7] The "free-stream" quantities in Eqs. (5) and (6) are computed on the cone surface, behind the conical shock.

For an insulated model the last member of the right-hand term of Eq. (5) becomes zero. This approximation was made for the models used in the present tests. Comparison of the computed displacement thickness with the apparent boundary-layer thickness measured on the schlieren negatives showed agreement within the limit of resolution of the film (approx. 0.002 in.).

## (7) Results

### (A) *Critical Roughness Height*

The principal purpose of the tests described herein was to obtain the critical roughness-element height $k_c$ (defined as the minimum height sufficient to produce transition at or very near the roughness element) as a function of model and flow parameters. Figs. 5 to 8 present plots of $k_c$ vs. Mach Number and Reynolds Number per inch for distributed and single-element roughnesses. In these Figures the dashed portions of curves indicate either extrapolations from the measured data or curves based on too few or uncertain points; they should be used with this fact in mind.

A comparison of these figures shows a rapid increase of $k_c$ with increase of Mach Number, particularly at low Reynolds Numbers, as would be expected because of the increase of boundary-layer thickness. It is also seen that, for the same roughness height at the same station $x_k$, the distributed roughness is more effective than the single-element roughness, and that the margin of effectiveness decreases with increase of Mach Number. The difference in effectiveness is not surprising since the distributed roughness extends forward from station $x_k$ to the tip of the cone.

The effect of model geometry can also be seen. At Mach Number 4.09, both the data for distributed roughness and for single-element roughness indicate that $k_c$ tends to increase with increase of cone angle, especially at the lower Reynolds Numbers, and that the effect of ogival radius on $k_c$ is negligible. At Mach Number 1.63 neither of these trends is consistently observed; however, the spread of the curves is relatively small.

To check the effect of the amount of distributed roughness used, data were obtained for model $N_{20}B_1$ at Mach Number 4.09 using grit number 320 with $x_k$ = 0.1875 and 0.500 in. Within the accuracy of the measurements, it was found that covering the additional surface area with roughness did not further affect the character of the boundary layer.

### (B) *Transition Point*

The transition point was obtained from spark-schlieren photographs and from the drag data [cf. Section (6)]. On the average, the drag data indicated a slightly earlier transition than did the optical data, suggesting that the point observed on the schlieren photographs was aft from the transition region (in which the shear stress at the model surface is higher than in the laminar region).

Typical spark-schlieren photographs showing the transition point are presented in Figs. 9 to 12. The effect of Reynolds Number on transition is illustrated Fig. 9, and the effect of grit height is shown in Fig. 10. As the grit height is increased, the transition point moves forward to a point near the ogive and remains fairly constant as the grit height is increased further until a near-critical value is reached, at which time the transition point moves onto the nose. It is believed that, in the absence of the negative pressure gradient over the ogive, the transition point for the models with 120 and 80 grit would be farther forward; it is further believed that the influence of the pressure gradient increases as the transition point approaches the ogive.

The effect of angle of attack on models with and without grit is shown in Figs. 11 and 12. As would be expected, the transition point on the lower surface moves aft and that on the upper surface moves forward with angle of attack, these movements being much less pronounced on the model with roughness added.

To correlate the data on fixing transition by the addition of roughness elements, Dryden[2] suggested the use of the parameter $k / \delta_k^*$, where $k$ is the roughness height and $\delta_k^*$ is the boundary-layer displacement thickness at the location of the roughness element; this parameter provided excellent correlation of data for low-speed flow ($M \simeq 0$) with zero pressure gradient. It was found by Goddard† and by Brinich[8] that data for supersonic Mach Numbers did not correlate well with the roughness parameter, yielding curves that were of similar shape but with values of $k / \delta_k^*$ several times larger. Goddard's data indicate that to obtain a single-curve correlation would require modification of the roughness parameter by additional functions of Mach Number, Reynolds Number, and roughness size.

Plots of $k / \delta_k^*$ vs. the ratio of the transition Reynolds Numbers with and without roughness were prepared using data from the present tests; they are not pre-

† Unpublished data obtained by Frank E. Goddard, Jr., at the Jet Propulsion Laboratory, C.I.T., on cones with single-element roughnesses.

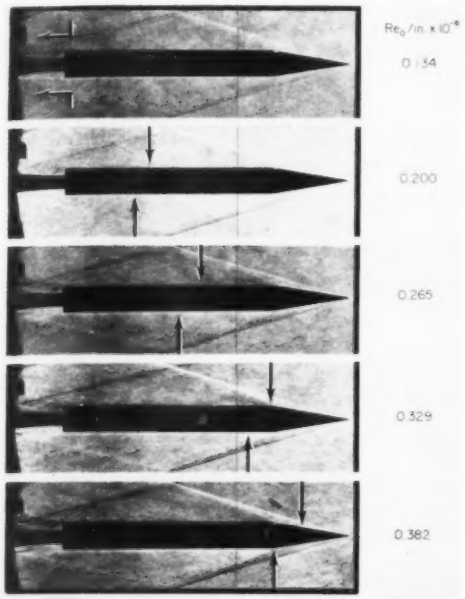


FIG. 9. Effect of Reynolds Number on boundary-layer transition: model $N_{20}B_1$, $M_0 = 4.09$, $\alpha = 0$, $\theta = 20°$, 220 grit.

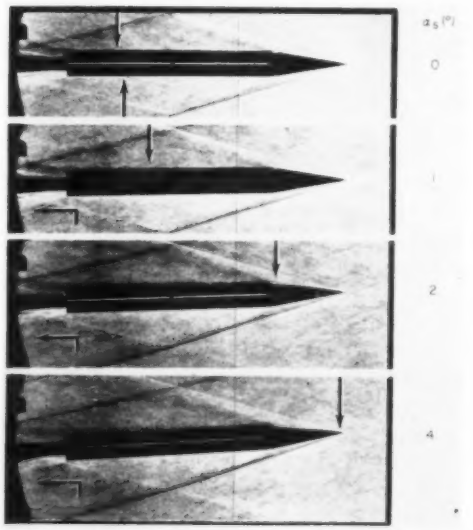


FIG. 11. Effect of angle of attack on boundary-layer transition on model $N_{20}B_1$ without roughness: $M_0 = 4.09$, $Re_0 = 0.38 \times 10^6$/in., $\theta = 20°$.

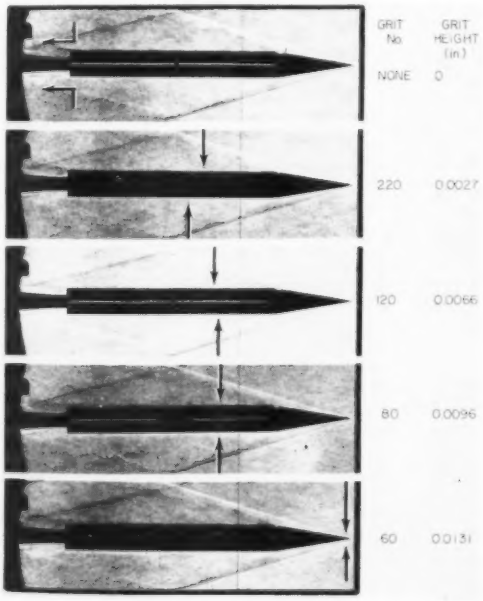


FIG. 10. Effect of distributed-roughness height on boundary-layer transition: Model $N_{20}B_1$, $M_0 = 4.09$, $Re_0 = 0.27 \times 10^6$/in., $\alpha = 0$, $\theta = 20°$.

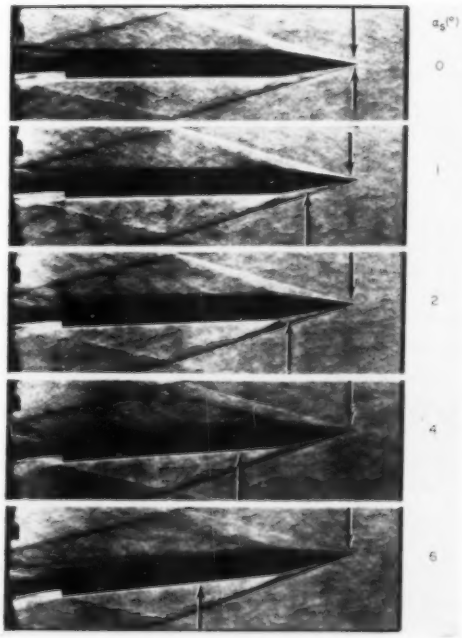


FIG. 12. Effect of angle of attack on boundary-layer transition on model $N_{20}B_1$ with 150 grit: $M_0 = 4.09$, $Re_0 = 0.38 \times 10^6$ in., $\theta = 20°$.

sented in this report, however, since the roughness parameter failed to correlate the data. The curves had the same character as those obtained by Goddard, with the pressure gradient over the ogive as an additional variable.

## (8) Conclusion

Data have been presented showing the effect on boundary-layer transition of adding single-element or distributed roughnesses near the tips of cone-ogive-cylinder models, using roughness height, cone angle, ogival radius, Mach Number, and Reynolds Number as variables. Each model had a fineness ratio of 10.6. Curves are included which show the effect of Mach and Reynolds Numbers on the critical roughness height, defined as the minimum height sufficient to fix transition at the element.

It is concluded that, for the ranges of variables tested, both the single-element and the distributed roughnesses can be used satisfactorily to fix transition, with negligible effect due to the roughness itself on drag (apart from that attributed to movement of the transition point). It is believed that further increase in roughness size may have such an effect on the wave drag, especially at lower Mach Numbers.

## References


[1] Luther, Marvin, *Fixing Boundary-Layer Transition on Supersonic Wind Tunnel Models (II)*, California Institute of Technology, Jet Propulsion Laboratory Progress Report No. 20-287, February 15, 1956.

[2] Dryden, Hugh L., *Review of Published Data on the Effect of Roughness on Transition from Laminar to Turbulent Flow*, Journal of the Aeronautical Sciences, Vol. 20, No. 7, pp. 477–482, July, 1953.

[3] Haines, A. B., Holder, D. W., and Parcy, H. H., *Scale Effects at High Subsonic and Transonic Speeds and Methods for Fixing Boundary-Layer Transition in Model Experiments*, RAE TN Aero. 2338, September, 1954.

[4] Winter, K. G., Scott-Wilson, J. B., and Davies, F. V., *Methods of Determination and of Fixing Boundary Layer Transition on Wind Tunnel Models at Supersonic Speeds*, RAE TN Aero. 2341, September, 1954.

[5] Chapman, Dean R., and Rubesin, Morris W., *Temperature and Velocity Profiles in the Compressible Laminar Boundary Layer with Arbitrary Distribution of Surface*, Journal of the Aeronautical Sciences, Vol. 16, No. 9, pp. 547–565, September, 1949.

[6] Hantsche, W., and Wendt, H., *The Laminar Boundary Layer on a Cone in a Supersonic Air Stream at Zero Angle of Attack*, Jahrbuch 1941 der Deutschen Luftfahrtforschung, Munich, Germany.

[7] Lewis, J. A., *Boundary Layer in a Compressible Fluid*, Air Materiel Command Technical Report No. F-TR-1179-ND, Wright Field, Ohio, 1948.

[8] Brinich, Paul F., *Boundary-Layer Transition at Mach 3.12 With and Without Single Roughness Elements*, NACA TN 3267, December, 1954.


## Flutter of Rectangular Simply Supported Panels . . .

(*Continued from page 573*)


[21] Luke, Y. L., and St. John, A. D., *Panel Flutter at Supersonic Speeds*, Midwest Research Institute, Fifth Quarterly Progress Report to WADC, Contract No. AF 33(616)-2897, October 31, 1956.

[22] Miles, J. W., *A First-Order Formulation of the Unsteady Supersonic Flow Problem for Finite Wings*, Journal of the Aeronautical Sciences, Vol. 23, No. 6, pp. 578–582, June, 1956.

[23] Ashley, H., and Zartarian, G., *Piston Theory—A New Tool for the Aeroelastician*, Journal of The Aeronautical Sciences, Vol. 23, No. 12, pp. 1109–1118, December, 1956.

[24] Evvard, J. C., *Use of Source Distributions for Evaluating Theoretical Aerodynamics of Thin Finite Wings at Supersonic Speeds*, NACA Report 951, 1950.

[25] Sylvester, M. A., and Baker, J. E., *Some Experimental Studies of Panel Flutter at Mach Number 1.3*, NACA RM L52I16, December, 1952.

[26] Bisplinghoff, R. L., and Pian, T. H. H., *On the Vibrations of Thermally Buckled Bars and Plates*, Massachusetts Institute of Technology, Contract No. N5ori-07833, Office of Naval Research (Project NR-064-259), September, 1956.

# The Stability of Thin-Walled Unstiffened Circular Cylinders Under Axial Compression Including the Effects of Internal Pressure†

LEONARD A. HARRIS,* HERBERT S. SUER,* WILLIAM T. SKENE,** AND ROLAND J. BENJAMIN***

*North American Aviation, Inc.*

SUMMARY

In the design of high-speed aircraft the importance of unpressurized and pressurized monocoque cylinders necessitates a reliable analysis procedure for the compressive buckling of cylindrical shells. Analysis by the classical small-deflection theory has proved inadequate. Recent large-deflection theoretical treatments of the problem have shown reasonable correlation with experiments but require a prior knowledge of the initial imperfections of the cylinder. Developed in this paper is a semiempirical procedure which permits a compressive buckling analysis of cylindrical shells with a knowledge of the cylinder geometry only. This analysis is achieved by correlating experimental data statistically with theoretical parameters.

In order to provide data not previously available, an extensive series of axial compression tests of pressurized cylinders has been performed. These data, together with all other known test data, are analyzed semiempirically. In the analysis best-fit curves are presented using theoretical parameters and shapes of curves where applicable. Unpressurized and pressurized cylinder compressive buckling curves are then developed as 90 per cent probability curves from the test data. In general, these statistically defined design curves are significantly lower than previously available design curves.

SYMBOLS

$C$ = buckling stress coefficient in the equation $\sigma_{cr} = CE(t/r)$
$E$ = modulus of elasticity
$K_c$ = buckling stress coefficient in the equation $\sigma_{cr}/\eta = K_c[\pi^2 E/12(1-\mu^2)](t^2/L^2)$
$K_{pl}$ = wide plate column buckling coefficient
$L$ = length of cylinder
$p$ = internal pressure
$r$ = radius of cylinder
$t$ = wall thickness of cylinder
$Z$ = curvature parameter = $(L^2/rt)\sqrt{1-\mu^2}$
$\eta$ = plasticity correction factor
$\mu$ = Poisson's ratio (assumed equal to 0.3)
$\sigma_{cr}$ = unpressurized critical buckling stress
$\sigma_{crp}$ = pressurized critical buckling stress
$\Delta\sigma_{cr}$ = increase in the critical buckling stress due to pressure $= \sigma_{crp} - \sigma_{cr}$

Presented at the Structures Session, Twenty-Fifth Annual Meeting, IAS, New York, January 28–31, 1957.

† The authors gratefully acknowledge the assistance of their colleagues of the Structures Data and Methods Group and of the personnel of the Missile Development Division Structural Test Laboratory who assisted in the development of the test equipment and who conducted the experimental investigation. Valuable assistance in the test program was given by personnel of the Materials Research Plastics Group who assisted in the development of a successful adhesive bonding technique.

* Senior Structures Engineer, Missile Development Division.

** Group Leader, Structures Data and Methods, Missile Development Division.

*** Formerly, Senior Structures Engineer, Missile Development. Now, Senior Aeronautical Engineer, Cook Research Laboratories, Cook Electric Company.

## INTRODUCTION

### *Statement of Problem*

THE BODY STRUCTURE of many current missiles and high-speed aircraft approximate circular cylindrical shells. In the past, such shell structures have usually been stiffened longitudinally by longerons and circumferentially by rings or frames which subdivided the shell into a number of curved panels.

During the past few years, increased emphasis has been placed upon the completely unstiffened (monocoque) circular shell, especially for internally pressurized structures. In addition to obvious manufacturing advantages, the monocoque type of construction reduces thermal gradients and is very well suited for integral fuel tanks. Ring-stiffened shells are a type of construction intermediate between fully stiffened and fully monocoque. If the rings are sufficiently rigid to prevent general instability, the portions of the shell between rings may be considered as monocoque with appropriate end conditions. The present investigation was initiated to develop reliable design information on the critical axial compressive buckling stress for thin-walled circular cylindrical shells with and without internal pressure. This paper, which considers axial loading only, is the first part of a general study covering the buckling of circular cylinders and curved panels under compression, bending, torsion, and combined loads.

The buckling of many structural elements occurs in a smooth wave form which often corresponds closely to the sinusoidal shapes assumed in classical theory. Cylinders, on the other hand, often snap-buckle into a sharply crested large-deflection pattern similar to a series of diamonds. In some instances this large diamond pattern can be seen to grow out of some initial irregularity of the curved surface.

It is well known that for unpressurized cylinders large discrepancies exist between values of the critical buckling stress determined by test and those predicted by the classical, small-deflection theory. Experimental values of the critical stress for unpressurized cylinders are always lower than those calculated theoretically

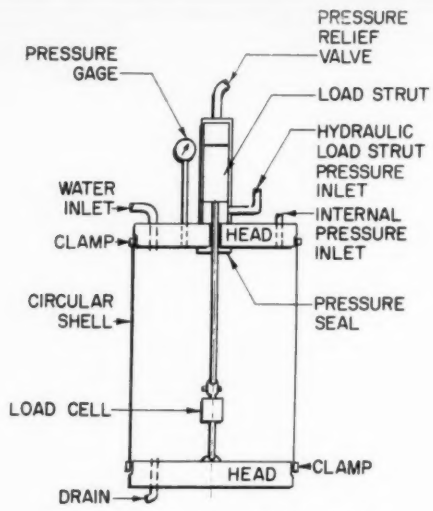


FIG. 1. Schematic drawing of test jig.

and are in some instances only about 10 per cent of the predicted values. Large-deflection theories have been developed by von Kármán and Tsien[1] and others[2, 3] in an attempt to account for this discrepancy. These large-deflection theories explain the so-called snap-buckling phenomena by showing the existence of a large-deflection equilibrium configuration at a lower stress than that computed by the small-deflection theory. Nevertheless, the critical stresses computed by these theories are greater than those found experimentally.

Another explanation of the behavior of unpressurized cylinders in compression has been the derivation by Donnell and Wan[4] of a large-deflection theory which includes the effects of initial irregularities and accounts for the plastic behavior of the shell. This latter approach appears to offer the best correlation with experimental results where the initial eccentricities were known. There results also suggest the dependence of the critical stress coefficient on the $r/t$ ratio because the initial imperfections of an unstiffened cylinder are likely to be greater as the $r/t$ ratio increases. In spite of the theoretical soundness of a large-deflection theory which includes the effects of initial imperfections, the procedure has the disadvantage that it requires a prior knowledge of the initial imperfection.

A discrepancy also exists between theory and test for pressurized cylinders. The compressive buckling of pressurized cylinders was investigated by Flügge[5] who used small-deflection theory. His conclusion that the buckling stress was not affected by internal pressure is in contradiction to experimental results. Based on von Kármán and Tsien's theory, Lo, Crate, and Schwartz[6] have derived a large-deflection analysis for pressurized cylinders. This large-deflection theory indicates an increase in the buckling stress with pressure until a maximum value is reached, but the experimental values are lower than those predicted by theory. This discrepancy, although not as large as for unpressurized cylinders, is likewise thought to be a result of the initial imperfections of the test specimens.

### *Scope of Investigation*

As pointed out above, theory does not adequately describe the compressive buckling behavior of circular shells without a prior knowledge of an initial imperfection parameter. In the authors' opinion, it would be difficult, if possible, for designers or analysts to determine an initial imperfection factor for aircraft structures. Therefore, it has been necessary to resort to a semiempirical development of design curves. This semiempirical method has the disadvantage that there is considerable scatter in the experimental data. However, this approach is thought to offer the most practical solution to the problem at the present time. The basic assumption in this semiempirical method is that the initial imperfections of the test cylinders were representative of those likely to be encountered in actual aircraft structures.

The theoretical parameters derived from Donnell's linear small-deflection theory[7] have been used in the analysis of the unpressurized cylinders. In addition to avoiding a direct prediction of the initial imperfections, the use of the parameters from Donnell's equation has the advantage of allowing an analysis over the wide range of geometry from the flat plate to the long cylinder. Once the theoretical parameters had been chosen, the test data were analyzed using the shape of the theoretical curve as a guide. A best-fit curve is fitted to the test data and statistical design curves are derived on the basis of probability theory.

For pressurized cylinders, parameters from the theory of Lo, Crate, and Schwartz[6] have been used in the determination of an empirical design curve. This procedure avoids the necessity of predicting the effect of initial imperfections. A design curve based on probability theory has been drawn indicating the increase in the critical stress as a function of a pressure parameter to facilitate design interpretation.

In reviewing the prior experimental investigations, it became apparent that a considerable gap existed in the available test data, especially in the tests of pressurized cylinders. In order to overcome this lack of data, an extensive series of tests was performed over a range of parameters likely to be encountered in aircraft structures.

## EXPERIMENTAL INVESTIGATIONS

### *North American Aviation Investigation*

An extensive series of compression tests of unpressurized and pressurized model circular cylinders was performed at the Missile Development Division Structural Test Laboratory. At the initiation of the test program in 1951 only a small amount of data over limited ranges of the parameters was available on the compressive buckling of pressurized cylinders. Because of the scatter in compression tests of unstiffened cylin-

ders, it was deemed necessary to perform an experimental investigation which would extend the test data within the range likely to be encountered in missile or aircraft structures.

A total of 83 tests was performed, 14 of unpressurized cylinders and 69 of pressurized cylinders. The test cylinders were fabricated from 0.005-in.-thick 2S H-18 aluminum foil and 0.0032-, 0.004-, and 0.0087-in.-thick half-hard 18-8 stainless-steel foil. The above sheet thicknesses were the averages of a number of micrometer measurements. The cylinders were prepared with lengths of 10.5 or 21.5 in. and a radius of 8.75 in. and had $r/t$ ratios of approximately 1,000, 1,750, 2,190, and 2,730. The internal pressure was varied from 0 to about 24 psi. Most of the cylinders were fabricated by wrapping the sheet around a form and adhesive bonding a single 3/8-in.-wide longitudinal seam with Epon VI adhesive. Some of the later cylinders were fabricated by seam welding, which proved to be a faster and simpler technique.

A schematic drawing of the test jig with a cylinder in position for testing is shown in Fig. 1. The test cylinders snugly fitted the lower and upper heads of the test jig and were clamped to the heads by metal straps. The straps prevented slippage and leakage between the heads and the cylinder. Internal pressure was pneumatically supplied, but for reasons of safety the cylinders were partially filled with water for all tests in which the internal pressure exceeded 2 psi. A mercury manometer was used to measure the internal pressure. An internal pressure equivalent to a head of water of half the specimen length was added to the applied pneumatic pressure for the analysis of those specimens which were filled with water. The axial compression loading was applied by a hydraulic strut and was measured by an SR-4 load cell.

The geometrical parameters and the buckling stresses of the test cylinders are recorded in Table 1. The buckling loads of the test specimens were determined visually. Buckling occurred at or just prior to the ultimate load the specimen would resist. For most specimens, a visual determination of the buckling load was relatively simple because the buckles often snapped into position. Occasionally, buckles appeared to grow out of relatively large initial irregularities.

Photographs of typical buckle patterns in unpressurized and pressurized cylinders are shown in Figs. 2 and 3. These diamond-shaped buckle patterns are typical for compressive buckling in unstiffened cylinders. Internal pressure changed the buckle pattern by decreasing the axial and circumferential wavelengths, although not in the same proportion. The buckle patterns frequently ran through the vertical seam, but in no case did buckling begin at the seam.

Incipient buckling of a cylinder was often indicated by the formation of small circumferential ripples. Although very shallow, these ripples (similar to the shape of an axisymmetrical compression buckle) could easily be seen in the reflecting surface of the cylinder as shown in Fig. 4. Once the specimen was close to the buckling load, a buckle could be easily induced by jarring or by a small lateral finger pressure. A few test specimens were discarded because buckling was precipitated by finger pressure which caused the buckle pattern to snap suddenly into the cylinder.

TABLE 1

Results of North American Aviation Tests

| Spec. No. | L in. | r/t | p psi | $\sigma_{cr}$ psi | Spec. No. | L in. | r/t | p psi | $\sigma_{cr}$ psi |
|---|---|---|---|---|---|---|---|---|---|
| 2S-H18 aluminum cylinders ($E = 10.5 \times 10^6$, $r = 8.75$") | | | | | | | | | |
| 35(1) | 21.5 | 1750 | 0 | 855 | 33(1) | 21.5 | 1750 | 1.9 | 2,128 |
| 36(1) | ↓ | ↓ | 0 | 818 | 38(1) | ↓ | ↓ | 2.6 | 2,145 |
| 40(1) | | | 1.1 | 1,510 | 39(1) | | | 2.6 | 2,182 |
| 41(1) | | | 1.1 | 1,782 | 34(1) | | | 3.4 | 1,818 |
| 42(1) | | | 1.1 | 1,818 | 37(1) | | | 3.4 | 1,836 |
| 32(1) | 21.5 | 1750 | 1.9 | 2,073 | | | | | |
| 18-8 1/2 hard stainless steel cylinders ($E = 27 \times 10^6$, $r = 8.75$") | | | | | | | | | |
| 43(1) | 21.5 | 1006 | 0 | 5,810 | 23(1) | 9.5 | 2734 | 8.2 | 4,375 |
| 44(1) | ↓ | ↓ | ↓ | 6,570 | 31(1) | ↓ | ↓ | 8.2 | 4,006 |
| 45(1) | | | | 5,800 | 28(1) | | | 24.2 | 3,523 |
| 56(1) | | | 0 | 6,780 | 30(1) | | | 24.2 | 3,295 |
| 303 | | | 1.0 | 8,946 | 10(1) | | | 24.6 | 4,205 |
| 304 | | | 1.0 | 8,654 | 11(1) | 9.5 | | 25.1 | 4,375 |
| 46(1) | | | 4.4 | 9,470 | 69(1) | 21.5 | | 2.0 | 4,063 |
| 47(1) | | | ↓ | 10,930 | 2(1) | ↓ | | 4.4 | 4,347 |
| 55(1) | | | | 8,150 | 2(2) | | | ↓ | 4,119 |
| 57(1) | | | 4.4 | 8,550 | 2(3) | | | | 3,324 |
| 48(1) | | | 8.4 | 10,390 | 3(5) | | | | 4,233 |
| 49(1) | | | 8.4 | 9,050 | 9(1) | | | | 4,460 |
| 50(1) | | | 8.4 | 10,330 | 66(1) | | | | 4,290 |
| 305 | | | 10.4 | 11,787 | 68(1) | | | ↓ | 4,460 |
| 51(1) | | | 16.4 | 11,480 | 2(4) | | | 8.4 | 3,352 |
| 52(2) | | | 16.4 | 11,580 | 2(5) | | | ↓ | 3,864 |
| 53(1) | | | 20.4 | 11,770 | 3(6) | | | | 5,114 |
| 54(1) | | | 20.4 | 11,770 | 3(8) | | | | 4,205 |
| 214(1) | | ↓ | 24.4 | 15,560 | 6(1) | | | | 4,205 |
| 215(1) | | 1006 | ↓ | 13,710 | 8(1) | | | ↓ | 4,290 |
| 231(1) | ↓ | 2188 | ↓ | 7,231 | 9(2) | | | 8.4 | 4,716 |
| 232(1) | 21.5 | 2188 | 24.4 | 6,776 | 70(1) | | | 10.4 | 4,631 |
| 25(1) | 9.5 | 2734 | 0 | 1,739 | 71(1) | | | 10.4 | 4,744 |
| 29(1) | 9.5 | ↓ | ↓ | 1,648 | 2(6) | | | 16.4 | 3,920 |
| 4(1) | 21.5 | | | 1,176 | 3(9) | | | ↓ | 3,920 |
| 4(2) | ↓ | | | 1,148 | 60(1) | | | ↓ | 4,318 |
| 7(1) | | | | 1,097 | 62(1) | | | 16.4 | 4,205 |
| 7(2) | | | | 1,119 | 65(1) | | | 20.4 | 4,205 |
| 58(1) | ↓ | | ↓ | 1,250 | 3(10) | | | 24.4 | 3,580 |
| 67(1) | 21.5 | | 0 | 1,222 | 4(3) | | | ↓ | 4,034 |
| 19(1) | 9.5 | | 4.2 | 4,773 | 13(1) | | | | 3,977 |
| 20(1) | ↓ | | 4.2 | 4,375 | 14(1) | | | | 3,807 |
| 22(1) | | | 4.2 | 4,210 | 15(1) | | | | 4,090 |
| 16(1) | | | 8.2 | 4,489 | 64(1) | | | ↓ | 4,091 |
| 17(1) | ↓ | ↓ | 8.2 | 4,375 | 2(7) | ↓ | ↓ | 24.4 | 3,637 |
| 21(1) | 9.5 | 2734 | 8.2 | 4,205 | 63(1) | 21.5 | 2734 | 24.6 | 3,920 |

### *Summary of Other Investigations*

An important aspect of the semiempirical analysis has been the proper accumulation and utilization of test data. A large number of investigations were carefully reviewed to obtain test data, but only the experimental results from the eleven investigations[6, 8–17] summarized in Table 2 have been used in developing the analysis. The results of other investigations were not included in the study for one or more of the following reasons: Insufficient data were given; test specimens were fabricated from nonmetallic materials such as paper, celluloid, or rubber which frequently exhibit variations in properties and thickness; critical stresses were above the yield point; critical stresses were above the proportional limit and insufficient data were given to make a plasticity correction; the fabrication procedure was not typical of aircraft construction; and the $r/t$ ratio was less than 100.

## Analysis of Unpressurized Cylinder Data

### *Theoretical Considerations*

The compressive buckling behavior of unpressurized cylinders may be considered in four classifications:

FIG. 2 (*top*). Typical buckle patterns for unpressurized cylinders.

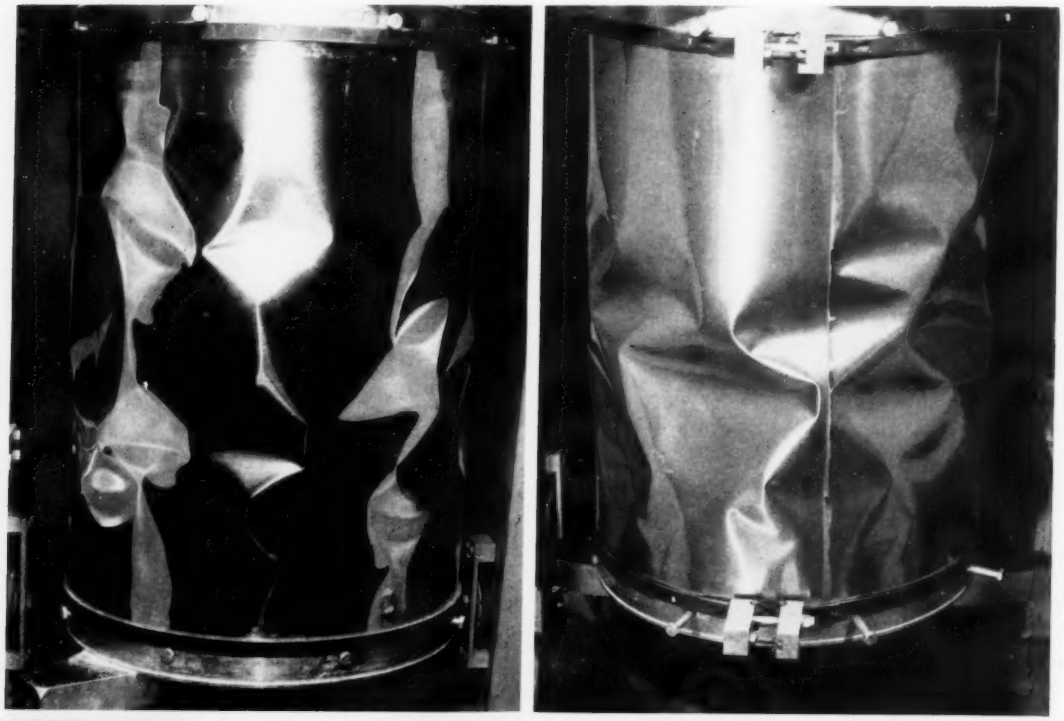

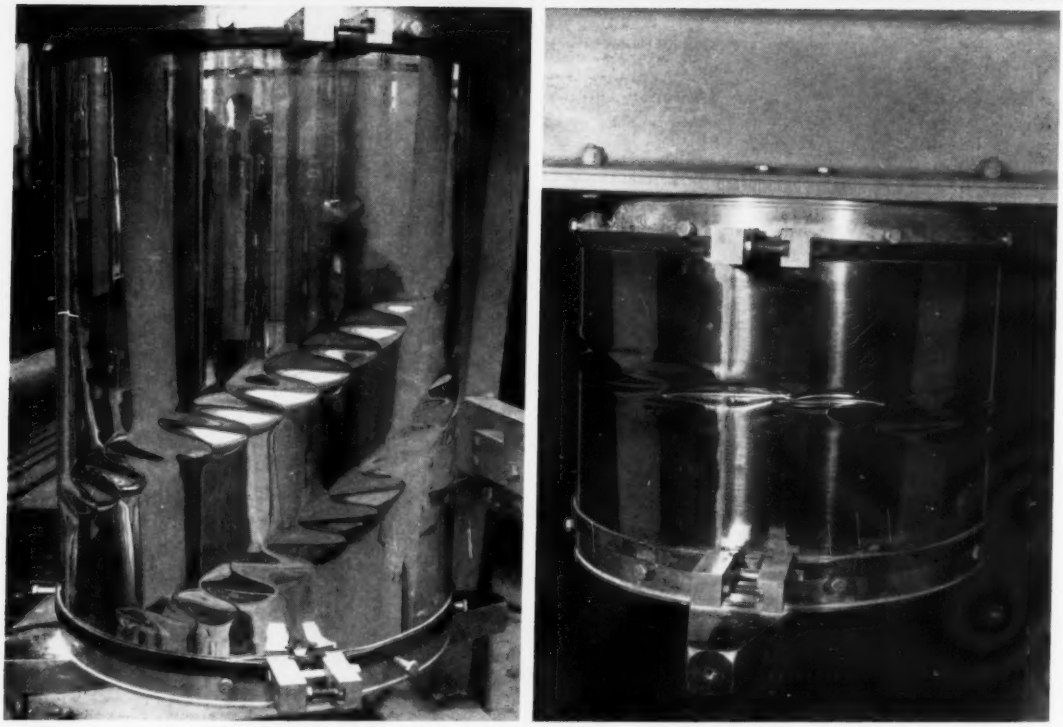

FIG. 3 (*bottom*). Typical buckle patterns for pressurized cylinders.

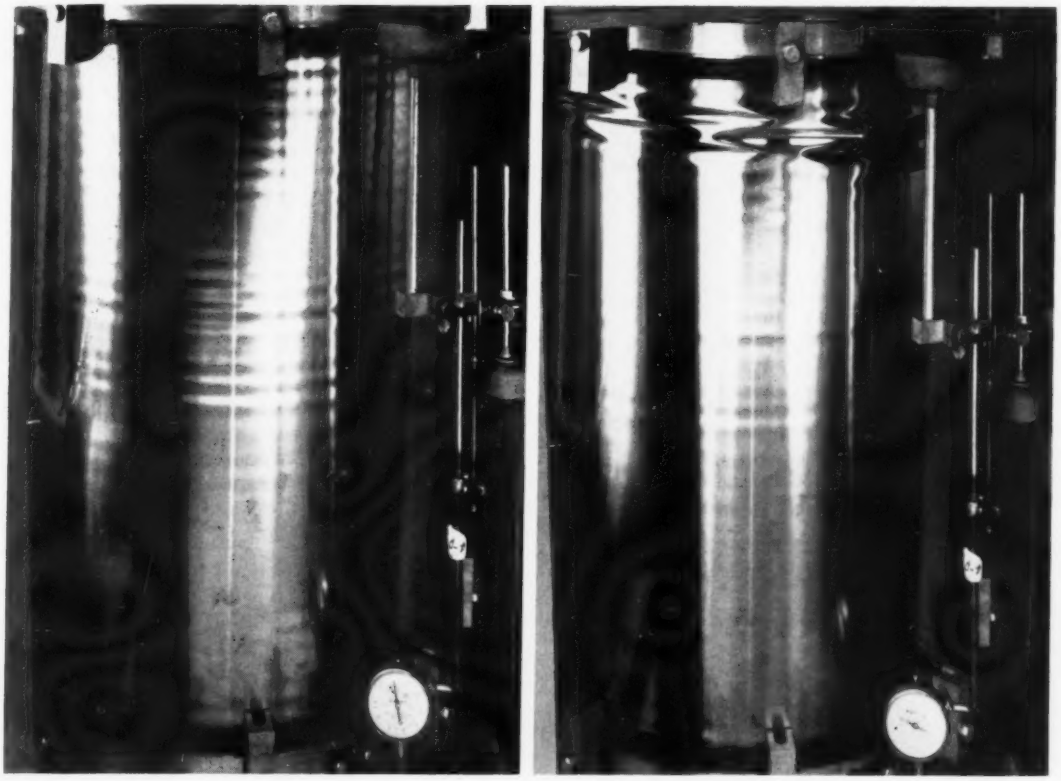

FIG. 4. Ripples and subsequent buckle pattern for a pressurized cylinder. (*Left*) Ripples at 1,500-lb. load. (*Right*) Buckle pattern (maximum load = 1,590 lbs.).

short cylinders, transition cylinders, long cylinders, and very long cylinders. Short cylinders tend to behave as flat plate columns (cylinders with an infinite radius), and buckling occurs in a sinusoidal wave characteristic of flat plate behavior. In contrast, the surface of a long cylinder buckles into a characteristic diamond pattern. In the long cylinder range, the critical buckling stress does not depend on the length of the cylinder or on the end conditions. The transition cylinder behavior occurs between the short and long cylinder ranges. In this intermediate range, the effects of length and of end conditions become important, and buckling probably occurs in some mixed displacement pattern. The very long cylinder buckles by overall column instability without local buckling of the cylinder wall. The behavior of very long cylinders is adequately described elsewhere and will not be considered further here.

Donnell's eighth-order differential equation[7] can be used to provide a small-deflection theoretical solution to the behavior of unpressurized cylinders from the short cylinder to the long cylinder range. A solution of Donnell's equation by Batdorf[18] gives the critical stress in terms of the buckling coefficient $K_c$, which for simply supported edges is defined by the equation

$$K_c = [(m^2 + \beta^2)^2 / m^2] + [12Z^2 m^2 / \pi^4 (m^2 + \beta^2)] \qquad (1)$$

where

$m$ = number of half waves in the longitudinal direction

$\beta = L\lambda$

$\lambda$ = half wavelength of buckles in circumferential direction

The compressive buckling stress is computed from

$$\sigma_{cr} / \eta = K_c [\pi^2 E / 12(1 - \mu^2)](t^2 / L^2) \qquad (2)$$

where $\eta$ is equal to 1 for elastic buckling. Minimization of Eq. (1) with respect to the parameter

$$(m^2 + \beta^2)^2 / m^2$$

TABLE 2
Summary of Other Experimental Investigations

| Reference | Material | No. of Specimens | Geometrical Parameters | | | |
|---|---|---|---|---|---|---|
| | | | $r$ | $\frac{r}{t}$ | $\frac{L}{r}$ | $p$ |
| Ballerstedt and Wagner | Brass | 18 | 3.96, 7.87 | 455 - 4166 | 0.26 - 2.00 | 0 |
| Bridget | Brass and Steel | 16 | 0.94, 1.88 | 238 - 919 | 0.70 - 12.04 | 0 |
| Clark and Holt | 178-T4 Aluminum | 11 | 1.95 | 101 - 629 | 1.01 - 3.06 | 0 |
| Donnell | Brass and Steel | 40 | 0.94 - 2.94 | 158 - 1469 | 2.12 - 31.83 | 0 |
| Fung and Sechler | 248-H Aluminum | 80 | 1.75 | 583 - 1750 | 6.29 | 0 - 7.1 |
| Kanemitsu and Nojima | Steel | 86 | 6.30 | 700 - 3040 | 0.04 - 1.42 | 0 |
| Lo, Crate, Schwartz | 248-T Aluminum | 7 | 15.00 | 602 | 1.87 | 0 - 3.0 |
| Lundquist | Duralumin | 45 | 7.50, 15.00 | 340 - 1420 | 0.25 - 3.00 | 0 |
| Robertson | Steel | 6 | 2.50 - 7.52 | 161 - 510 | 0.39 - 1.15 | 0 |
| Wilson and Newmark | Steel | 11 | 1.94 - 6.04 | 101 - 767 | 1.35 - 10.31 | 0 |

gives the critical buckling coefficient for long cylinders in the following form:

$$K_c = (4\sqrt{3}/\pi^2)Z = 0.702Z \tag{3}$$

where $$Z = (L^2/rt)\sqrt{1 - \mu^2}$$

Substitution of Eq. (3) for the buckling coefficient into Eq. (2) reduces to the classical equation

$$\sigma_{cr} = CE(t/r) \tag{4}$$

where

$$C = 1/\sqrt{3(1 - \mu^2)} = 0.605 \quad \text{for} \quad \mu = 0.3$$

The buckling coefficient for simply supported end conditions in the transition cylinder range can be determined by substituting the limiting values of $\beta = 0$ and $m = 1$ in Eq. (1). A similar solution for cylinders with fixed edges deviates from the solution for simply supported cylinders only in the flat plate and transition ranges.

The theoretical value of the buckling coefficient $K_c$ is given as a function of the geometrical parameter $Z$ in Figs. 5–8. Theoretically, the short cylinder range would occur at $Z = 0$. The values of $K_c$, 1.12 and 4.12, at $Z = 1$ correspond very closely to the buckling coefficients of simply supported and fixed-ended plate columns. The long cylinder behavior is represented by the 45° sloping straight-line portion of the curve. The curve connecting the short and the long cylinder ranges is the transition cylinder range.

### *General Analysis Procedure*

The analysis of unpressurized cylinders has consisted of the following steps: (1) establishment of the pertinent parameters, (2) plotting of test data in terms of

FIG. 5. $r/t$ = 100 to 500.

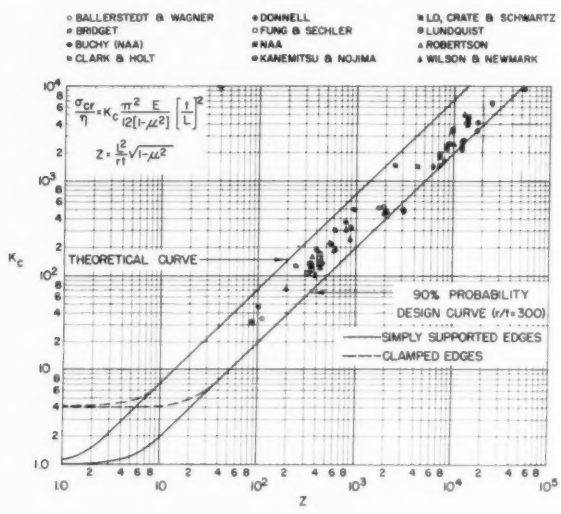


FIG. 6. $r/t$ = 500 to 1,000.

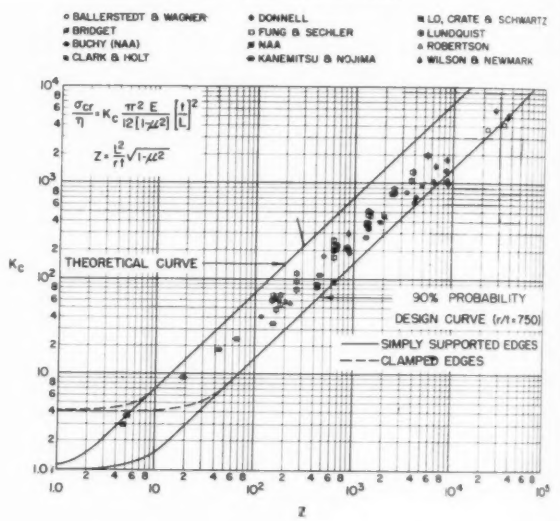


FIG. 7. $r/t$ = 1,000 to 2,000

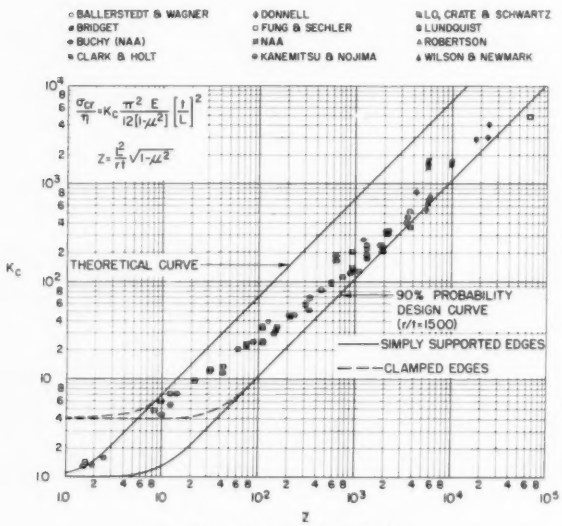


FIG. 8. $r/t$ over 2,000.

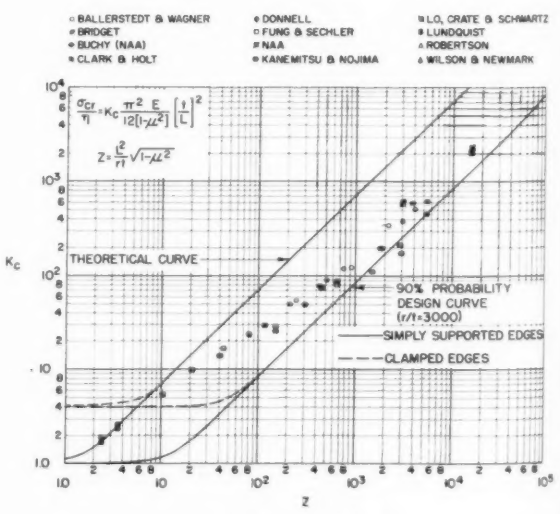


FIGS. 5–8. Compressive buckling stress coefficients for unpressurized circular cylinders

these parameters, (3) establishment of the relationship between the critical buckling coefficient and the $r/t$ ratio, and (4) performance of a statistical analysis on the test data to determine design curves. The reasoning behind the choice of parameters has already been given.

Shown in Figs. 5–8 are 252 experimental values of the critical buckling coefficient from the tests of twelve investigations. The discrepancy between theory and test is clearly shown in these Figures. However, the general trend of the test points follows the theoretical shape of the curve quite well. Batdorf, Schildcrout, and Stein[19] have proposed semiempirical curves to account for this discrepancy between test and theory. Curves at the theoretical slope were faired through the test data in the long cylinder range for several values of $r/t$ on the assumption that the $r/t$ ratio is indicative of the initial imperfections. The analysis employed in the present paper is a refinement of this procedure which includes a statistical basis for the correlation between the buckling coefficient and the $r/t$ ratio. This is accomplished by replotting the buckling coefficient as a function of the $r/t$ ratio. Once the relationship between the buckling coefficient and $r/t$ is determined, the statistical analysis of step (4) is performed, and the design curves are drawn in terms of the theoretical parameters, $K_c$ and $Z$.

### *Buckling Coefficient $K_c$ as a Function of Z*

Examination of the experimental data in Figs. 5–8 indicates that the test points from the various investigations generally overlap, although there is considerable scatter. The test data have been plotted in four increasing ranges of the $r/t$ ratio in these Figures. Comparison of the data indicates a general increase in the deviation of the test values from the theoretical curve with an increase in the $r/t$ range. Because of the large scatter and of the variation in the buckling coefficient with $Z$, it is difficult on these plots to establish a relationship between $K_c$ and $r/t$ or to evaluate the significance of the scatter. It has, therefore, been necessary to replot the test data as a function of $r/t$ only. To do this, the long cylinder test data have been cross-plotted at a constant value of the geometrical parameter $Z$.

In the long cylinder range, the theoretical curve is a straight line at a 45° slope on a plot of log $K_c$ as a function of log $Z$. It has been assumed that in the long cylinder range the variation of $K_c$ with $Z$ for each $r/t$ ratio is given by a line parallel to, but displaced from, the theoretical straight line. The amount by which a line of constant $r/t$ is displaced from the theoretical curve reflects the effects of initial imperfections which are assumed to be a function of the $r/t$ ratio. This assumption will be shown to result in a family of parallel lines for increasing $r/t$.

Each test point in Figs. 5–8 can be used to establish a straight line at the theoretical slope, and the test value of $K_c$ can be projected along this line to some

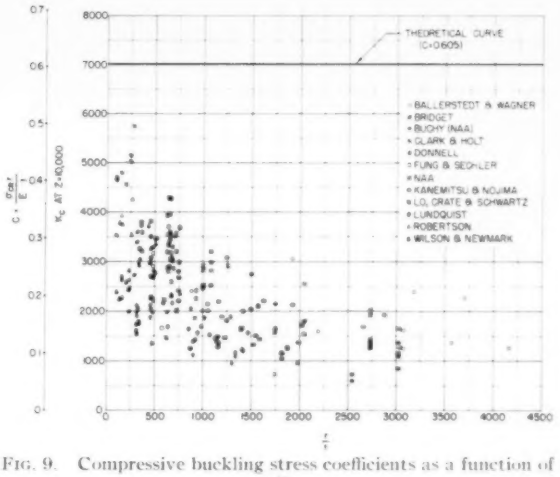


FIG. 9. Compressive buckling stress coefficients as a function of $r/t$.

arbitrarily chosen value of $Z$. A cross plot of the projected values of $K_c$ vs. $r/t$ can then be made at this arbitrary value of $Z$. In reality, each line through a test point at a slope of 45° represents a value of the coefficient $C$ in Eq. (4) different from the theoretical value of 0.605. Therefore, the cross plot could also be used to evaluate the variation of the coefficient $C$ with the $r/t$ ratio.

### *Relationship Between the Buckling Coefficient and r/t*

In Fig. 9, the projections of the experimental buckling coefficients are plotted as a function of the $r/t$ ratio for the arbitrary value of $Z = 10{,}000$. The test points have been projected to a value of $Z = 10{,}000$ along lines parallel to the theoretical curve in the long cylinder range. Two ordinate scales are shown on the graph. The $K_c$ scale is the projected value of the buckling coefficient from Donnell's equation. The second scale gives the equivalent values of the buckling coefficient $C$ in the classical equation.

Also shown in Fig. 9 is a curve representing the classic value of 0.605 for the buckling coefficient $C$. The large discrepancy between small-deflection theory and test is again clearly apparent. Comparison of the test results indicates that the maximum scatter is about 350 per cent.

In order to establish the variation of the buckling coefficient with the $r/t$ ratio, the test results have been replotted in Fig. 10. In this Figure, the log of the projected buckling coefficient $K_c$ has been plotted as a function of the $r/t$ ratio. In addition to more clearly defining the relationship between $K_c$ and $r/t$, the semilog plot has the advantage of producing a more uniform scatter band for the range of $r/t$ considered. The statistical analysis is more readily performed if the distribution of test points is uniform.

A best-fit curve is shown on the log $K_c$ vs. $r/t$ graph. The shape of this curve was selected by the investigators as being representative of the trend of the experimental data. The vertical location of the curve with

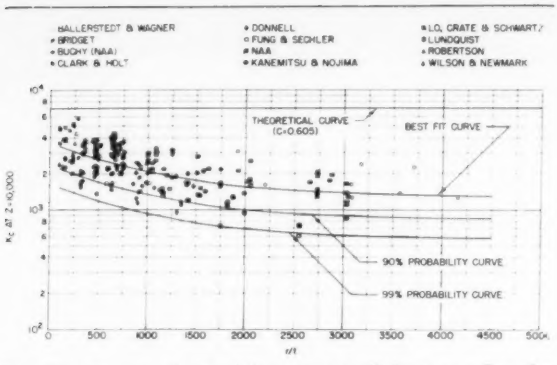


FIG. 10. Compressive buckling stress coefficients as a function of $r/t$ (semilogarithmic grid).

respect to the test data was achieved by satisfying the equation

$$\sum_{i=1}^{N}(y_i - y_a) = 0 \tag{5}$$

where

$y_i$ = log $K_c$ at $Z$ = 10,000 for test points
$y_a$ = log $K_c$ at $Z$ = 10,000 for points from the best-fit curve at $r/t$ of test point $i$

If Eq. (5) is satisfied, it can be shown that the following relationship is also satisfied:

$$\sum_{i=1}^{N}(y_i - y_a)^2 = \text{a minimum} \tag{6}$$

Thus, by satisfying Eq. (5), the assumed curve was in the least square position.

### *Statistical Analysis and Development of Design Curves*

After a best-fit curve had been established with the sum of the squares of the deviations a minimum, a statistical analysis was performed. An IBM 701 digital computer was used to solve the equations of the statistical analysis in the following form:

$$y_p = y_a - C_p S \tag{7}$$

where

$y_p$ = log $K_c$ at $Z$ = 10,000 for a specified probability
$S$ = $\sqrt{(y_i - y_a)^2/(N-1)}$ = the standard deviation
$N$ = number of test points
$C_p$ = probability coefficient

The solution of Eq. (7) for the 222 test points gave a value of 0.138 for the standard deviation of the log of $K_c$. The value of $C_p$ = 1.396 was selected from a small sample statistical table[20] for a 90 per cent probability design curve. The 90 per cent probability design curve is drawn in Fig. 8. This curve agrees well with, and generally parallels, the lower bound of the test data. The 99 per cent probability curve is also shown on this graph. The relatively large difference between the 90 per cent and the 99 per cent probability curves is typical of a statistical analysis of test data with a large scatter.

Final 90 per cent probability design curves were obtained in the following manner: For a particular value of $r/t$, the design value of $K_c$ at $Z$ = 10,000 was read from the 90 per cent probability curve in Fig. 10. This value was plotted on a graph of $K_c$ vs. $Z$, and a straight line at the theoretical slope of 45° was drawn through the point. At low values of the $Z$ parameter, the buckling coefficient approaches the wide plate column value which depends on the end conditions. For design purposes, values of 1 and 4 have been assumed for simply supported and fixed ends, respectively, at a value of $Z$ = 1. A transition curve has been fitted between the long cylinder range defined by the straight line and the flat plate value at $Z$ = 1.

The procedure suggested in reference 21 has been used to construct the design curve in the transition range. In the authors' investigation of the compressive buckling of curved panels, sufficient data were available in the transition region to indicate that the method would give a reasonable design curve. Although there were not enough data to check the transition curve for cylinders, the procedure was adopted on the basis of its success in the case of curved panels. Basically, this transition curve is defined by

$$K_c = K_{pl} + (12Z^2/\pi^4 K_{pl}) \tag{8}$$

where $K_{pl}$ = the simply supported or fixed-end wide plate column buckling coefficient. This equation can be made to coincide with the flat plate values at $Z$ = 1 and is tangent to the design curve in the long cylinder range. The complete design curves for the range of $r/t$ likely to be encountered in aircraft structures are shown in Fig. 11. A comparison with the theoretical curve indicates the large difference between theory and the 90 per cent probability design curves. For instance, the design curve for an $r/t$ of 3,000 is only about 12½ per cent of the classical theoretical values in the long column range. The 90 per cent probability curves can be compared with the experimental data in Figs. 5–8. In general, these statistically defined design

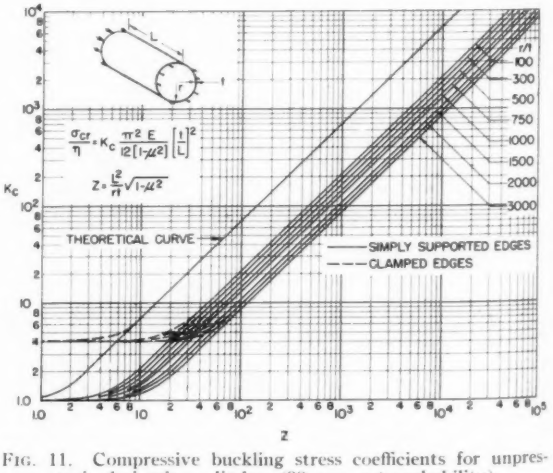


FIG. 11. Compressive buckling stress coefficients for unpressurized circular cylinders (90 per cent probability).

curves are significantly lower than previously available design curves.

### *Statistical Design Criteria*

The load at which buckling of a thin monocoque shell occurs can be considered as ultimate since no further load-carrying capacity remains. Because the final design curve of this study is defined in terms of a statistical probability of failure, it is incumbent on the user of these data to decide what probability is required by the design criteria demands of his particular structure. In some ways, this is a new concept for the analyst, since in the past many accepted analytical procedures could not be conveniently related to failure probability.

The structures engineer usually has two design loads to consider—limit load and ultimate load. In general, limit load is defined as the maximum expected operating load. Ultimate load is usually defined as the limit load times a factor of safety which accounts for uncertainties of load, analysis, material, etc. Ultimate load may normally be experienced by an aircraft only in a static test. Traditionally, piloted aircraft have required larger factors of safety than unpiloted missiles.

To illustrate the placement of design curves and to discuss the weight-saving possibilities of a failure philosophy, 90 and 99 per cent probability curves have been plotted in Fig. 10. These probabilities are identical to those used for determining the A and B material properties in ANC-5.

As shown in Fig. 10, the 99 per cent probability curve is about 30 per cent lower than the 90 per cent probability curve. With reference to Eq. (7) it can be seen that this would be characteristic of data with considerable scatter which causes a large standard deviation.

If the 99 per cent probability curve is used for ultimate load, there is a slim 1 per cent probability of failure at ultimate and practically no possibility of failure at limit load. If the 90 per cent probability curve is selected, there is a 10 per cent probability of failure at ultimate load and a probability of failure at limit load

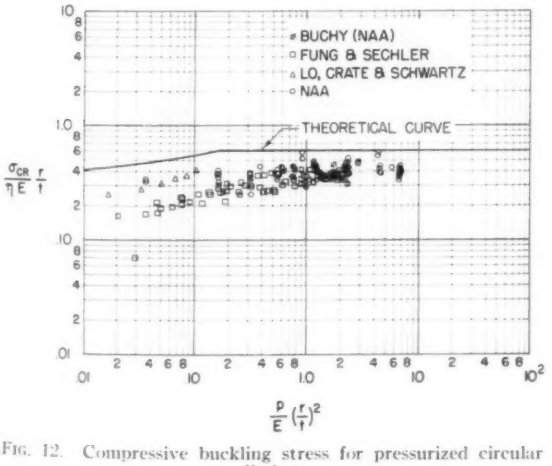


FIG. 12. Compressive buckling stress for pressurized circular cylinders.

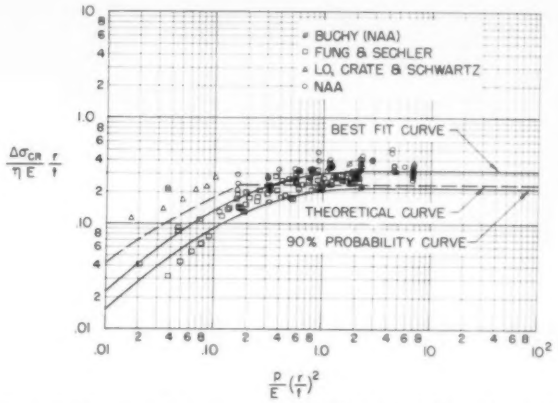


FIG. 13. Increase in compressive buckling stress due to internal pressure.

which would probably be less than 2 per cent depending on the ultimate to limit ratio. Accompanying the 10 per cent risk, a significant weight saving in the shell is achieved. Since present missile reliability philosophies are being established on a statistical basis, this type of analysis offers attractive weight-saving possibilities.

## Analysis of Pressurized Cylinder Test Data

### *Theoretical Considerations*

Experimental investigations have shown that the critical buckling stress is significantly increased by internal pressure. Application of the small-deflection theory to the compressive stability of cylinders with internal pressure has been unsuccessful. However, Lo, Crate, and Schwartz[6] have analyzed the problem of long pressurized cylinders using an extension of the large-deflection theory of von Kármán and Tsien.[1] Plotting their results in terms of the nondimensional parameters $(P/E)(r/t)^2$ and $(\sigma_{cr}/E)(r/t)$, they found that the buckling coefficient $C$ increased from the Tsien[3] value of 0.375 at zero pressure to the maximum classical value of 0.605 at $(p/E)(r/t)^2 = 0.169$. The large-deflection theoretical curve is shown in Fig. 12. Also shown are the experimental values of Lo, Crate, and Schwartz with the experimental data obtained in the present investigation and that of reference 13. It is apparent that, as for unpressurized cylinders, large discrepancies exist between the theoretically predicted and the experimentally determined buckling stresses. For example, in the region of maximum critical stress, the experimental values of $C$ vary from about 0.3 to 0.585, whereas theory predicts 0.605. Lo, Crate, and Schwartz suggested that better correlation with experimental results could be obtained if the increment in the buckling stress parameter, $(\Delta\sigma_{cr}/E)(r/t)$, were plotted as a function of the pressure parameter as shown in Fig. 13. The increase in the critical stress $\Delta\sigma_{cr}$ due to internal pressure directly represents the beneficial effect of internal pressure. The total critical stress is obtained by adding the critical stress for the

unpressurized cylinder to the increase in the critical stress due to pressure.

The theoretical curve and the test results are shown in Fig. 13 in terms of the incremental stress parameter. In order to plot these data it was first necessary to determine the unpressurized critical buckling stress for each specimen. The 90 per cent probability design curves of Fig. 11 were used for this purpose. As can be observed in Fig. 13, the general trend of the experimental data agrees quite well with the theoretical curve. It was this agreement between test and theory which suggested the feasibility of a semiempirical analysis of the data using these parameters.

### *Development of Design Curve*

The analysis of the pressurized cylinder data was achieved by first selecting a best-fit curve which is shown in Fig. 13 together with the experimental data. This curve has been drawn to approach an asymptote at large values of the pressure parameter and to decrease at low values with essentially the same slope as the theoretical curve. The agreement between the best-fit curve and the experimental data is apparent from Fig. 13. The best-fit curve has been drawn so that the sum of the squares of the deviations of the experimental data from the curve is a minimum.

A statistical analysis of the test data was performed to establish the 90 per cent probability design curve of Fig. 13. This design curve is to be used in conjunction with the unpressurized design curves of Fig. 11. The curve approximates a lower bound to the test data. The standard deviation of the log of the stress parameter = 0.116. The theoretical curve nearly coincides with the proposed design curve at large values of the pressure parameter. For small values of the pressure parameter, the design curve is appreciably lower than the theoretical curve.

## Conclusions

The axial compressive buckling of thin-walled circular cylinders has been analyzed semiempirically. Theoretical parameters and shapes of curves were used and the test data were fitted statistically. The basic approach to this method is that the initial imperfections of the test cylinders were equivalent to those which would be encountered in aircraft structures. Design curves based on a 90 per cent probability criterion have been presented. For unpressurized cylinders, the critical buckling stress coefficient for short and long cylinders is given as a function of the geometrical parameters $Z$ and $r/t$. For long, pressurized cylinders, the increase in the critical stress due to pressure is given as a function of pressure and geometry. In general, these statistically defined curves are significantly lower than previously available design curves. It is proposed that the use of statistically defined buckling curves can be correlated with missile reliability philosophies.

## References


[1] von Kármán, T., and Tsien, H. S., *The Buckling of Thin Cylindrical Shells Under Axial Compression*, Journal of the Aeronautical Sciences, Vol. 8, No. 8, pp. 302–312, June, 1941.

[2] Leggett, D. M. A., and Jones, R. P. N., *The Behavior of a Cylindrical Shell Under Axial Compression When the Buckling Load has been Exceeded*, British ARC R&M No. 2190, August, 1942.

[3] Tsien, H. S., *A Theory for the Buckling of Thin Shells*, Journal of the Aeronautical Sciences, Vol. 9, No. 10, pp. 373–384, August, 1942.

[4] Donnell, L. H., and Wan, C. C., *Effect of Imperfections on Buckling of Thin Cylinders and Columns Under Axial Compression*, J. Appl. Mech., Vol. 17, No. 1, pp. 73–88, 1950.

[5] Flügge, W., *Die Stabilitat Der Kreiszylinderschale*, Ing-Archiv, Bd. III, Heft 5, pp. 463–506, December, 1932.

[6] Lo, H., Crate, H., and Schwartz, E. B., *Buckling of Thin-Walled Cylinder Under Axial Compression and Internal Pressure*, NACA TN 2021, January, 1950.

[7] Donnell, L. H., *Stability of Thin-Walled Tubes Under Torsion*, NACA Rept. 479, 1933.

[8] Ballerstedt, W., and Wagner, H., *Versuche über die Festigkeit dünner unversteifter Zylinder unter Schub-und Längskräften*, Luftfahrtforschung, Vol. 13, pp. 309–312, 1936.

[9] Bridget, F. J., Jerome, C. C., and Vosseller, A. B., *Some New Experiments on Buckling of Thin-Wall Construction*, Trans. ASME, Vol. 56, pp. 569–578, 1934.

[10] Classified.

[11] Clark, J. W., and Holt, M., Discussion of the Paper *Effect of Imperfections on Buckling of Thin Cylinders and Columns Under Axial Compression* by L. H. Donnell and C. S. Wan. J. Appl. Mech., Trans. ASME, Vol. 72, pp. 340–342, 1950.

[12] Donnell, L. H., *A New Theory for the Buckling of Thin Cylinders Under Axial Compression and Bending*, Trans. ASME, Vol. 56, pp. 795–806, 1934.

[13] Fung, Y. C., and Sechler, E. E., *Buckling of Thin-Walled Circular Cylinders Under Axial Compression and Internal Pressure*, Journal of the Aeronautical Sciences, Vol. 24, No. 5, pp. 351–356, May, 1957. (Also, Report No. AM 5-1, Guided Missile Research Division, The Ramo-Wooldridge Corp., August 1, 1955.)

[14] Kanemitsu, S., and Nojima, N. M., *Axial Compression Tests of Thin Circular Cylinders*, M.S. Thesis, Dept. of Aeronautical Engineering, California Institute of Technology, 1939.

[15] Lundquist, E., *Strength Tests of Thin-Walled Duralumin Cylinders in Compression*, NACA Rept. 473, 1933.

[16] Robertson, A., *The Strength of Tubular Struts*, Proc. Royal Society London, Series A., Vol. 121, 1928.

[17] Wilson, W. M., and Newmark, N. M., *The Strength of Thin Cylindrical Shells as Columns*, University of Illinois, Engineering Experiment Station Bulletin No. 255, February, 1933.

[18] Batdorf, S. B., *A Simplified Method of Elastic-Stability Analysis for Thin Cylindrical Shells*, NACA Rept. 874, 1947.

[19] Batdorf, S. B., Schilderout, M., and Stein, M., *Critical Stress of Thin-Walled Cylinders in Axial Compression*, NACA TN 1343, June, 1947.

[20] Dixon, W. J., and Massey, Frank J., Jr., *Introduction to Statistical Analysis*, 1st Ed., pp. 334–339; McGraw Hill Book Company, Inc., New York, 1951.

[21] Gerard, G., and Becker, H., *Handbook of Structural Stability, Part III, Buckling of Curved Plates and Shells*, Research Division, College of Engineering, New York University, April, 1955.

# Effects of Leading-Edge Separation on Thin Wings in Two-Dimensional Incompressible Flow†

L. F. CRABTREE*

*Royal Aircraft Establishment, Farnborough, England*

SUMMARY

The flow over an airfoil with a laminar separation bubble near the leading edge is treated. There are thus two attachment lines and two separation lines, in contrast with the viscous flow over an airfoil with separation only near the trailing edge and with one attachment line near the leading edge.

A physical picture of such bubble flows is constructed, and a solution is sought by splitting up the problem into three parts. These concern the viscous flow inside the bubble, the turbulent mixing region of reattachment, and the inviscid external flow. Little is as yet known about the internal flow of a bubble, but the other two problems are treated in some detail.

Attention is also paid to the problem of transition in the separated shear layer. Schubauer and Klebanoff's condition for the growth of turbulent spots in a boundary layer is employed to explain the success achieved by Owen's criterion. This was suggested as a means of distinguishing between the two types of bubbles ("long" and "short") commonly observed on thin airfoils at incidence.

The picture of laminar separation bubbles thus obtained offers an explanation of the differences in behavior of long and short bubbles, and a hypothesis concerning the leading-edge stall or abrupt change from a short to a long bubble is put forward.

Finally the problem of predicting maximum lift is discussed; while this is still not possible in any specific case, the scale effect on the stalling characteristics of thin and moderately thin airfoils is explained in some detail.

The whole paper is in the nature of a summary report, however incomplete, of recent work done mainly at the Royal Aircraft Establishment on the problem of regions of separated flow on two-dimensional airfoils at low speed.

## INTRODUCTION—VISCOUS FLOW WITH SEPARATION ONLY AT THE TRAILING EDGE

THE THEORY of viscous flow over an airfoil with separation only at the trailing edge is now fairly well established. It will be recapitulated here in order to emphasize the comparison with the flow over an airfoil including regions of separated flow on the surface. In the former flow there is one attachment line near the leading edge and one separation line near the trailing edge, as sketched in Fig. 1(a). The presence of a viscous region around the airfoil in the form of a boundary layer and wake does not change this type of flow but affects primarily the shape of the displacement surface and the value of the circulation.

The circulation about an airfoil may be predicted from detailed calculations of the boundary layer and wake; this was first done successfully by Preston.[1] Some improvements of this method have been effected recently by Spence.[2] The theory rests largely on G. I. Taylor's theorem regarding the overall circulation, and the lift force on the airfoil may be calculated once the overall circulation has been predicted and the circulation in the wake subtracted. Maskell[3] has shown that the wake circulation is usually a small term; it is given by $-(V_\infty c \cdot C_D \cdot \alpha)$ for a symmetrical airfoil.

The pressure distribution over the surface of the airfoil can be found, and from it the pitching moment and the position of the aerodynamic center, by allowing for the displacement effect of the boundary layer. This may be done by simply adding the displacement thickness of the boundary layer to the actual profile shape—i.e., the shape of the boundary of the external inviscid stream is taken from the solution of the viscous flow but the boundary condition is still the same, namely, that there is no normal velocity. An example where all the various steps have been performed in detail from experimental data has been given by Brebner and Bagley.[4]

In principle the drag force due to viscosity can also be determined. A convenient practical method is due to Squire and Young,[5] and simpler developments of this theory have been proposed by Holt[6] and Tetervin.[7]

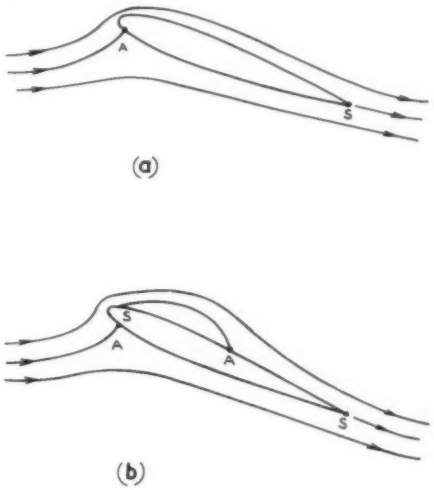


FIG. 1. Two types of viscous flow over an airfoil.

Presented at the Aerodynamics—I Session, Twenty-Fifth Annual Meeting, IAS, New York, January 28–31, 1957.

† The author is deeply grateful to his colleagues at the Royal Aircraft Establishment, and in particular Dr. D. Küchemann, for their advice and encouragement in the preparation of this paper.

* Senior Scientific Officer, Ministry of Supply.

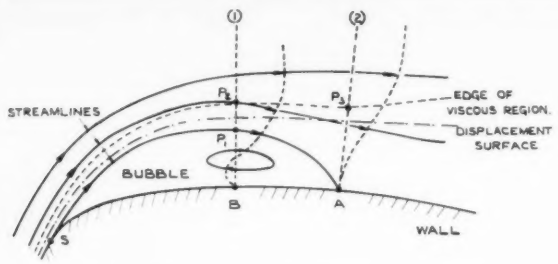


FIG. 2. Laminar separation bubble on an airfoil.

## FLOW WITH A BUBBLE DUE TO LEADING-EDGE SEPARATION

The type of flow considered so far is no longer adequate when separation occurs elsewhere than only near the trailing edge—as, for instance, near the leading edge on some airfoils near maximum lift or on thin airfoils even at moderate or low values of lift. This is the case we wish to consider here. The flow with only trailing-edge separation is then no longer possible; it would imply a high suction peak near the leading edge followed by a severe adverse pressure gradient which would lead to a separation of the laminar boundary layer there. The viscous region now loses the character of a boundary layer since, as Maskell points out,[8] the so-called singular separation along a line normal to the stream must lead to the formation of a bubble in this case. The bubble includes air which is separated from the mainstream and is carried along with the body. We shall consider the case where the bubble length is smaller than the wing chord—i.e., the flow reattaches to the surface. Thus, as sketched in Fig. 1(b), there are two attachment lines, A, and two separation lines, S, in direct contrast to Fig. 1(a).

We now consider how the flow in and around such a bubble is likely to look, and Fig. 2 has been constructed as follows. We assume a closed bubble so that a "zero" streamline leaves the surface at S and joins it again at A. Further streamlines from infinity upstream stay outside this boundary. The boundary layer is of finite thickness at S, and since there is no longer a boundary condition requiring zero tangential velocity along the zero streamline (as there is on the solid surface) the "shear layer" must diffuse and extend inside the zero streamline. The air is thus set into motion inside the bubble and for a closed bubble continuity demands a circulatory flow inside the bubble.

The flow over the front part of the bubble is entirely consistent with laminar flow in the viscous region. If the bubble reattaches, however, there must be a considerable widening of the streamlines over the rear end. This cannot be imagined as a laminar process at the Reynolds Numbers we are concerned with, but is more akin to turbulent mixing as it occurs in, say, a pipe with a sudden enlargement of cross section. We are, therefore, led to assume that there is transition to a turbulent state and that this is likely to occur near station (1) or slightly further upstream. We also arrive at velocity profiles as shown in Fig. 2; since there is zero skin friction at station (2) the profile there will show the vertical tangent characteristic of a separation profile. The velocity profile at station (2), however, is not necessarily identical with the usual separation profile of a fully developed turbulent boundary layer.

With this picture of the flow we note that there are likely to be large pressure changes (in fact, a pressure recovery) between $P_1$ and A, but a nearly constant pressure between S and $P_1$.

We note also, in searching for a solution, that this is not like an ordinary boundary-layer problem. It may be possible, however, to retain some of the assumptions of boundary-layer theory; for example, that inside the viscous region there is no variation of static pressure with distance normal to the surface. It may also be possible to proceed on the assumption that the problem can be subdivided into three partial problems—namely, solutions for the three main regions: (1) inside the bubble, within the zero streamline; (2) the turbulent mixing region, the major part of which may possibly be limited to $P_1P_2P_3$ A; and (3) the external inviscid stream along the displacement surface, the pressure distribution along which may be taken as approximately that along the wall.

Little work has been done as yet on the internal flow of the bubble. However, the work of Squire[9] and Batchelor[10] on similar problems assuming a "core" of constant vorticity surrounded by a layer in which boundary-layer assumptions can be made may be applicable and fruitful. This work should be extended to include a consideration of the (assumed) laminar surrounding layer so as to investigate its stability and determine the transition point.

The mixing region will be considered later; this may be used to estimate the order of the pressure recovery and hence the level of suction in the bubble, and also the energy transport across the zero streamline $P_1$ A needed to maintain the flow in the bubble. Strictly speaking, of course, such quantities can only be found from a complete solution of the entire flow field. The separate solutions for the three regions cannot be unique in themselves, and it is only by matching all three that a unique solution can be found. A rough answer can be obtained from any one region though, provided its interaction with the other two is adequately represented.

The problem of the external stream will also be considered more fully later. This again differs from the earlier problem of airfoils with ordinary boundary layers because the shape of the displacement surface is not known to begin with. Following Maskell,[11] we propose a different course: use is made of two experimental observations (a) that the pressure is constant over the forward part of the bubble, and (b) that the displacement thickness of the viscous region is of the order of the bubble thickness downstream of the bubble. These lead to the assumptions that the region (a) extends back to the maximum height of the bubble,

and that the variation of the displacement thickness aft of this point is negligible.

Finally, as emphasized above, the three solutions must be joined together and matched. For instance the basic solution for the external stream is not unique in that the level of suction in the bubble is undetermined. This will be obtained by matching the pressure recovery with that in the turbulent mixing region.

### The Effect of Transition in the Shear Layer

So far no characteristic dimension of the flow has been fixed. The size of the bubble—i.e., its length in relation to the airfoil chord—must depend very much on whether transition occurs a long way downstream of separation, S, or almost instantaneously. In tests of a flat plate held normal to the stream Flachsbart[12] found that transition in the free shear layers behind the plate jumped forward suddenly at some critical Reynolds Number. This is also related to the critical Reynolds Number for transition in the wake behind a cylinder observed by Linke.[13] We may, therefore, expect a discontinuous change in the length of path from S to $P_1$ (say) needed to produce transition to a turbulent state, and, therefore, either a very short bubble or a fairly long one. It may also be expected that the sudden switch-over depends on a Reynolds Number related to conditions at separation, for example that based on boundary-layer displacement thickness at S, $(V\delta_1/\nu)_S = (R_{\delta 1})_S$.

This is confirmed by experiment. Owen and Klanfer[14] have analyzed tests in which bubbles were observed with this in mind, and found a relation between bubble length and $(R_{\delta 1})_S$. It appears that there are two distinct types of bubble.

(1) A short bubble for which $(R_{\delta 1})_S$ is always greater than about 500. Its length is of the order of 1 per cent of the chord or less [say 100 times the boundary-layer displacement thickness at separation $(\delta_1)_S$] and the bubble contracts as the angle of incidence is increased.

(2) A long bubble for which $(R_{\delta 1})_S$ is always less than about 500, and whose length is of the order of 2 or 3 per cent of the chord on formation at low incidences [the ratio of bubble length to $(\delta_1)_S$ being of the order of $10^4$ or more]. The long bubble grows rapidly with increasing angle of incidence until the separated layer fails to reattach to the airfoil surface and the bubble extends out into the wake.

Owen's criterion has been confirmed by the analysis[15,16] of more recent tests, but it appears that a short bubble does not always break down into a long bubble at the *same* value of $(R_{\delta 1})_S$. Since the breakdown also gives rise to a marked change in the external flow field this is not altogether surprising. In a sense the Owen criterion—by distinguishing between the two types of bubble—does tell one that the breakdown will be abrupt. We must have one kind or the other, with no intermediate state. The success achieved in distinguishing between the two types of bubble can be more completely explained, however, on the basis of Schubauer and Klebanoff's condition[17] for the growth of turbulent spots. In their experiments on the boundary layer on a flat plate as part of an investigation into the mechanism of transition they found that turbulent spots grew only very slowly if $R_{\delta 1}$ was less than about 450, and a much faster rate of growth was obtained when $R_{\delta 1}$ exceeded this value. Now McGregor[18] has found that the displacement thickness of the laminar shear layer of a bubble grows only very slowly from separation up to the onset of transition. It is clear, therefore, that, if $(R_{\delta 1})_S$ is less than about 450–500, a long path from S to $P_1$ (say) is required for transition, whereas if $(R_{\delta 1})_S > 450$–500 transition may occur quite rapidly. In the first case a long bubble would be formed, and in the second a short bubble.

The actual mechanism of the abrupt change from a short to a long bubble (of which the leading-edge stall is a particular example) will be discussed later.

### The Turbulent Mixing Region

A simplified model of a type of flow with a bubble on a two-dimensional airfoil has been considered by Norbury and Crabtree,[19] and particular attention was given to the reattachment process. They assumed that the principal mixing process and the corresponding pressure recovery occur in the region $P_1P_2P_3A$ of Fig. 2. The velocity profile across $P_1P_2$ was assumed to be linear, while that at A was assumed to be of the characteristic separation type with a vertical tangent at the wall, the profile being represented by a simple power law. It was also assumed that fluid passing through $P_1P_2$ at station (1) is diffused to form a boundary layer of depth $AP_3$ at station (2) while the velocity of the flow at the upper boundary of the mixing region falls from $V_1$ to $V_2$ without loss of energy. To simplify the analysis the following further assumptions were made.

(1) $P_2P_3$ is a streamline. Further, no fluid enters or leaves the region across $BP_1$ on the average, from the definition of the bubble boundary.

(2) The curvature of the airfoil surface SBA may be neglected.

(3) $P_2P_3$ is parallel to BA.

Applying the momentum theorem and the equation of continuity, an expression was obtained for the coefficient of pressure rise, $\sigma$, over the rear part of the bubble, where

$$\sigma = (P_2 - P_1)/(1/2)\rho\, V_1^2 = (C_{P_2} - C_{P_1})/(1 - C_{P_1})$$

It was found that the value of $\sigma$ varied only slightly with the ratio of thicknesses $\delta_B/\delta_A$ (where $\delta_B = \overline{P_1P_2}$ and $\delta_A = \overline{AP_3}$) and with the velocity profile across $P_1P_2$. For instance, if the latter is given by

$$v_1/V_1 = a + (1 - a)\cdot(y/\delta_B)$$

and the profile at A is given by

$$v_2/V_2 = (y/\delta_A)^n$$

in the limiting case $n = 1$, $\sigma$ varies from 0.37 to 0.45 as the constant $a$ varies from 1.0 (a uniform profile) to 0.5.

A further way of predicting a reasonable value of $\sigma$ is suggested by a consideration of the rate of spreading of the turbulent mixing region between two parallel streams of different velocities. This problem has been analyzed by Kuethe,[20] and from his results it may be surmised that when the pressure rise through turbulent mixing ceases (roughly with the return of the zero streamline to the wall) the depth of the mixing region, $AP_3$ in Fig. 2, will be about three times as great as the original depth of flow involved in the mixing ($P_1P_2$ in Fig. 2). This yields a value of $\sigma$ of 0.32, which is of the same order as before. Also the fact that the turbulence spreads at a much greater angle into the more slowly moving stream supports the assumption that $P_2P_3$ is parallel to BA.

The analysis of pressure distributions obtained by Dimmock[21] in tests of a jet-flapped airfoil where the long bubble is fairly well defined shows that the value of $\sigma$ is in fact roughly constant at 0.35.

In view of the assumptions made in the analysis this value of $\sigma$ may be considered to be an upper limit. The pressure recovery may be less than this in some cases, but it cannot be much greater. It may be recalled that the pressure recovery due to complete mixing after a sudden enlargement in a pipe yields a maximum possible value for $\sigma$ of 0.5 (for an area ratio of 0.5).

In the particular case of a short bubble, Crabtree[16] has shown by analysis of the experimental results in references 18 and 22 that the value of $\sigma$ gradually rises with increase of incidence (or decrease in Reynolds Number at constant incidence). When a limiting value of about 0.35 is reached the short bubble suddenly "bursts" and the flow pattern breaks down into that associated with a long bubble. This has been proposed as part of the mechanism of the leading-edge stall, and will be more fully discussed later.

## The External Inviscid Flow

The problem of the external flow has been treated successfully by Maskell[11] for the simple case of a two-dimensional flat plate. The presence of a long bubble necessarily implies a thick boundary layer behind the bubble and a thick wake, neither of which can be neglected in a treatment of the external flow problem. Maskell's displacement boundary, therefore, consists of a constant pressure region—assumed to extend up to the maximum thickness of the bubble—followed by a constant displacement thickness up to the trailing edge, and a wake of nearly constant thickness which leaves the trailing edge smoothly and curves back to the mainstream direction at infinity downstream.

The model gives rise to a rapid pressure rise just downstream of the constant pressure region, after which the pressure distribution steadily approaches that in the absence of a bubble—i.e., for the flow with one separation line and one attachment line sketched in Fig. 1(a).

Clearly a long bubble could not exist with the same value of peak suction ($C_{p_{min}}$) as in the flow of Fig. 1(a) at the same incidence: the required pressure rise could not be supplied by turbulent mixing. The peak suction, therefore, collapses. Now let us consider the effect of an increase in incidence for this type of flow. If the level of suction in the bubble remains unchanged, then in the above model the bubble length increases, as sketched in Fig. 3. This also fits with the hypothesis of a constant pressure recovery $\sigma$ in a long bubble. In fact, the level of suction usually falls with increasing incidence, which means that the bubble expands even more rapidly.

The effect of incidence on a short bubble is represented schematically in Fig. 4. In this case boundary-layer calculations indicate that separation moves forward toward the leading edge. This can be seen, for instance, by application of the simple criterion that the ratio of velocity at separation to the maximum velocity, $V_s/V_m$, is about 0.94 in a typical case of this sort. The level of suction in the bubble is, therefore, higher at a higher incidence. This implies a more highly curved flow to maintain the increased suction, and, therefore, the bubble is shorter. Here, turbulent mixing can supply enough pressure recovery to bring the pressure back to that which would exist in the absence of the bubble. Therefore, while the bubble shortens as incidence increases the pressure distribution is much the same as in attached flow, except for a very small region. The bubble is only a means of producing a turbulent boundary layer and making possible a flow which is, practically, "attached" near the leading edge.

These arguments are largely confirmed by experiment. That the short bubble has only a very small effect on the pressure distribution is shown by the comparison in Fig. 5 where the experimental pressure distribution is taken from tests on a NACA 63-009 section by McCullough and Gault.[23] Consequently the values of lift, drag, and pitching moment are likewise little affected by the presence of a short bubble.

A preliminary comparison between Maskell's theory of a long-bubble flow and experimental results for a NACA 64A-006 section in Fig. 6 shows that the pressure distribution is well represented provided the thickness of the airfoil is taken into account. This was done by the simple expedient of subtracting the measured pressure distribution at zero lift. As stated above the value of the suction in the bubble, on which the shape depends, is left open in the theory. A unique solution can be obtained by applying the condition obtained from an analysis of the turbulent mixing region, that the pressure recovery coefficient $\sigma$ is equal to 0.35. This value of $\sigma$ may be used to choose the physically possible solution from Maskell's infinite number of mathematical solutions such that the pressure distribution downstream of the bubble approaches that calculated for attached flow at the same lift coeffi-

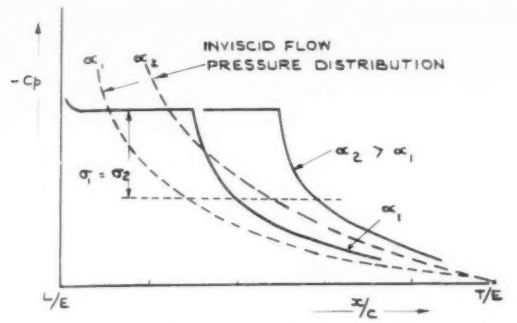


FIG. 3. Effect of incidence on long bubbles (schematic).

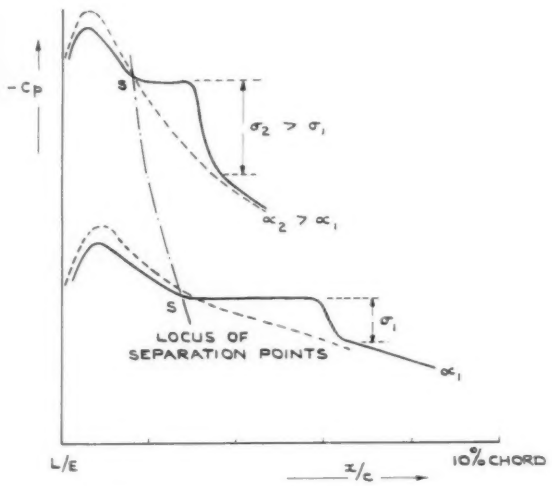


FIG. 4. Effect of incidence on short bubbles (schematic).

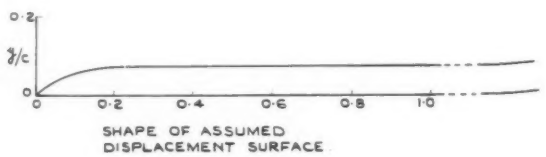


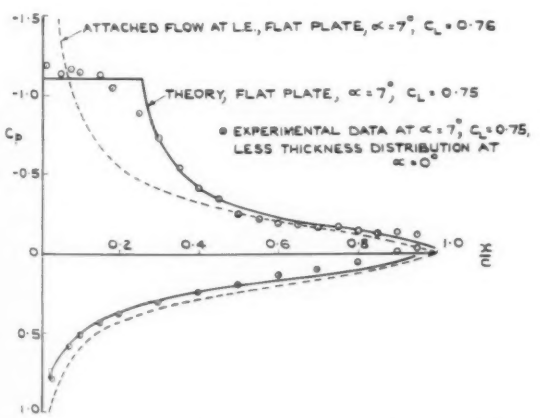
ATTACHED FLOW AT L.E., FLAT PLATE, $\alpha = 7°$, $C_L = 0·76$
THEORY, FLAT PLATE, $\alpha = 7°$, $C_L = 0·75$
● EXPERIMENTAL DATA AT $\alpha = 7°$, $C_L = 0·75$,
LESS THICKNESS DISTRIBUTION AT
$\alpha = 0°$
$C_p$
x/c

FIG. 6. Pressure distribution over NACA 64A-006 airfoil with long bubble. Comparison of theory and experiment.

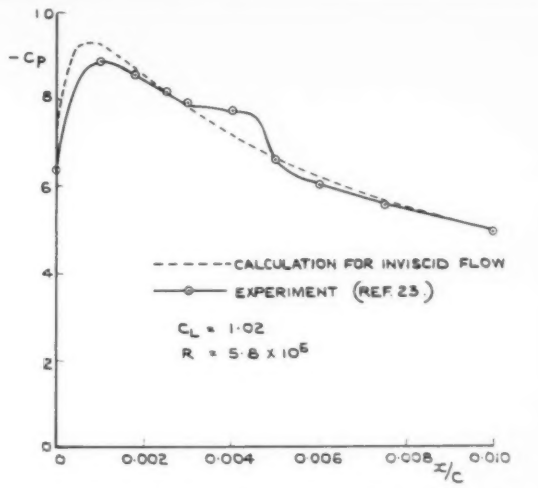


FIG. 5. Pressure distribution near the leading edge of NACA 63-009 section showing effect of short bubble.

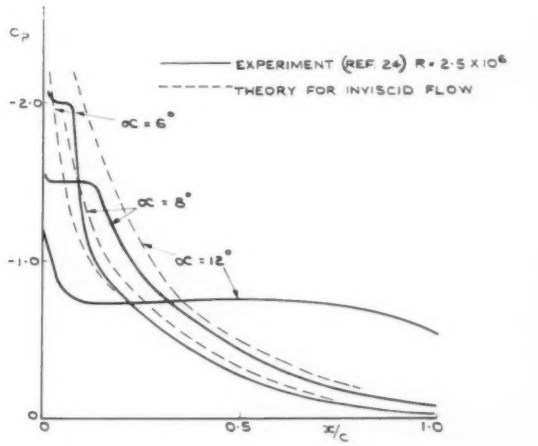


FIG. 7. Effect of incidence on pressure distribution on upper surface of 6 per cent thick RAE 101 section with long bubble.

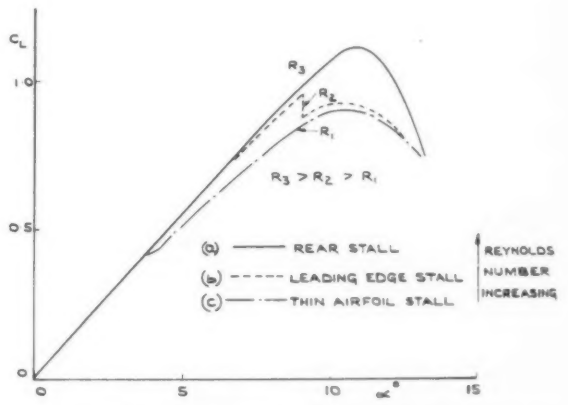


FIG. 8. Possible scale effect on maximum lift of a moderately thin airfoil section.

cient. We have assumed that in the case of Fig. 6 the turbulent mixing is practically over by about 45 per cent chord where the pressure and loading distributions with bubble approach those for attached flow. Thus $C_{p_2} = -0.35$ and $C_{p_1} = (C_{p_2} - \sigma)/(1 - \sigma) = -1.1$ (for $\sigma = 0.35$) which leads to the solution drawn. The difficulty always lies in defining $C_{p_2}$—i.e., the location of reattachment. The example does show, however, that there is some prospect of developing and combining these methods into one of practical utility.

The long bubble, of course, has a great effect on the pressure distribution, and some further examples are given in Fig. 7, from tests by Butler.[24] The large drag increase associated with a long bubble obviously stems from the breakdown of the high suction peak near the leading edge, and the shift of the center of pressure is linked with the gradual lengthening of the bubble as the incidence is increased. Note that the trailing-edge pressure is appreciably reduced when the length of the constant pressure part of the bubble exceeds about half the chord.

This brings us to one of the limitations of our picture of bubble flows: if reattachment (A in Fig. 2) approaches the trailing edge, then the static pressure there falls since not *all* of the mixing occurs upstream of the trailing edge. Consequently, (1) there is more circulation in the wake, and, therefore, less lift, and (2) the circulation is not "fixed" so that fluctuations are much more likely to occur. This leads to buffeting—a problem of great current interest, but which is unfortunately outside the scope of this paper.

## Maximum Lift and Stalling Characteristics

The influence of the type of bubble formation on the aerodynamic characteristics of an airfoil section is now fairly clear. In particular, the effect on stalling characteristics (defined here as the behavior at maximum lift) has been described in a classic report by McCullough and Gault.[23]

Altogether there are three main types of stall: (a) trailing-edge stall, with the separation point of the turbulent boundary layer moving forward from the trailing-edge as the incidence increases; (b) leading-edge stall, caused by an abrupt separation of the flow near the nose without subsequent reattachment—i.e., short bubble "bursting"; and (c) thin-airfoil stall with laminar separation near the leading-edge and turbulent reattachment at a point which moves progressively rearward with increasing incidence—i.e., a long bubble.

On the basis of previous discussions a hypothesis concerning the leading-edge stall has been proposed.[16] Thus the sequence of events in the breakdown of a short bubble could be as follows.

(1) A short bubble is no longer possible, because the maximum possible value of $\sigma$ has been reached so that the flow cannot reattach immediately.

(2) The peak suction collapses, and, as a result of the redistribution of pressures around the nose and the consequent effect upon the development of the laminar boundary layer, the value of $(R_{\delta 1})_S$ falls to below, say, 500.

(3) Thus turbulent spots are unable to grow and the separated shear layer remains laminar for a much greater distance.

(4) Eventually, however, the value of $R_{\delta 1}$ of the separated layer exceeds 500 so that transition ensues and finally turbulent mixing occurs.

(5) Now the suction in the bubble is low enough and the pressure distribution is such that the bubble can close with a small enough value of the pressure recovery factor $\sigma$. The closure of the bubble, however, may occur behind the trailing edge.

Thus all three regions of the bubble flow as outlined above have accommodated themselves again so that a possible flow results. The loss of lift is abrupt on the breakdown of a short bubble if the closure of the subsequent long bubble is near or aft of the trailing edge.

We must bear in mind, however, that the condition for the growth of turbulent spots was formulated for an attached flow; the situation may be different for a shear layer away from the solid surface. The problem of the stability of laminar wakes is being studied by McKoen[25] and Curle,[26] and their results should later be applied to our particular problem.

Long bubbles, on the other hand, must lead to an abrupt change in the lift force on formation. As they lengthen with incidence, the rate of increase of the overall circulation is gradually slowed down and the circulation in the wake increases, so that the lift curve departs from the straight line and bends over. Long bubbles can have significant effects on the drag and pitching moment characteristics of an airfoil as well as on the lift, as has already been pointed out. These have been discussed by Küchemann[27] and Crabtree.[16] There must also be differences in the actual values of maximum lift coefficient $C_{L_{max}}$ achieved in the different types of stall. Clearly, the lift force on an airfoil section with long bubble will always be below that on an airfoil with short bubble and so will their respective maximum lift values, as is indeed observed in experiments. The prediction of the actual value of $C_{L_{max}}$ is very difficult, and, as yet, only general trends can be noted. For example Multhopp[28] has constructed curves of $C_{L_{max}}$ against $t_{0.05}$, the ratio of thickness at 0.05 chord to the chord length, for a number of airfoil sections, while others have used the nose radius as an empirical parameter.

We are now also in a position to discuss the possible scale effect on the maximum lift of airfoils experiencing bubble separations. Possible lift curves for a thin airfoil at three different Reynolds Numbers are sketched in Fig. 8. For the lowest value of $R$ the curve (c) shows a kink at a certain (fairly low) incidence, representing the formation of a long bubble which still reattaches upstream of the trailing edge. An increase in $R$ shortens the length of laminar separated layer over the front part of the bubble so that the pressure-recovery coefficient $\sigma$ is reduced. Thus a

higher incidence may be attained before the maximum possible value of $\sigma$ is reached and the bubble bursts into the long type, which is then accompanied by a loss of lift. If the Reynolds Number is sufficiently high the change in the type of bubble formation may be postponed to such a high incidence that the resulting long bubble covers most of the chord (or even extends out into the wake) so that maximum lift had been attained. Curve (b), therefore, illustrates a typical leading-edge stall.

On the other hand, the thinner boundary layer obtained at a higher Reynolds Number means that there is less loss of lift due to viscous effects. Therefore, at a given incidence the suction peak is higher and the following adverse pressure gradient is steeper. The pressure recovery $\sigma$ is higher on this score so that in some cases an increase in $R$ may mean that the short bubble breaks down at a lower incidence. Although this may be expected to be usually a secondary effect, cases where it is predominant have been observed—e.g., in McCullough's tests[29] of a NACA 0006 section.

The curve (a) representing the highest free-stream Reynolds Number shows a typical rear-stalling behavior. For such a case, it may be that $R$ is so high that transition to turbulence in the boundary layer occurs ahead of laminar separation. Crabtree[28] has given as an empirical condition for this to be so that $(R_{\delta_1})_S$ must be greater than about 2,700. The first separation other than at the trailing edge is then one of the turbulent layer somewhere at the rear of the section. This leads again to a bubble extending into the wake, and its gradual growth with angle of incidence causes the lift to reach a maximum value. Also some thick and some cambered airfoils stall in this manner while still exhibiting a short bubble near the leading edge. The rear stall is then accelerated by the thicker boundary layer which results from the short leading-edge bubble. Similar ideas have been put forward independently by McGregor.[18]

It must be remembered that the curves of Fig. 8 represent the *same* airfoil at different Reynolds Numbers. It is still possible for a thin airfoil with leading-edge stalling behavior to attain a higher $C_{L_{max}}$ than does a *thicker* airfoil with a rear-stalling behavior. In Fig. 8, however, the rear-stall pattern produces the highest $C_{L_{max}}$.

At a given incidence below the stall the difference in lift coefficient $C_L$ between the long bubble flow of curve (c) and those at higher Reynolds Numbers may be explained, according to Maskell,[2] almost entirely by a consideration of the wake circulation. He does in fact find that all the main characteristics of the lift-curve in the case of a thin-airfoil stall can be explained in terms of wake circulation—i.e., the break in the lift-curve and the subsequent loss of slope. Whatever the type of stall though, the flow patterns should eventually be very similar for the same airfoil and so we expect all three lift curves of Fig. 8 to run together beyond their respective incidences for maximum lift.

However, although it is impossible to calculate the complete lift curve in any specific case (including the prediction of $C_{L_{max}}$) we can design a section on which laminar separation with a long bubble is avoided, up to a point. This can be done by specifying the basic pressure distribution, and camber is a suitable means of fulfilling such requirements. Boundary-layer control can also be effective, and either suction or blowing out of small holes has been suggested (see reference 16).

## Concluding Remarks

A fairly complete picture of the phenomenon of laminar separation bubbles on thin airfoils at incidence is now available, but a number of points, such as the viscous flow inside the bubble, require further investigation. The complications of the whole problem have been emphasized by comparison with the well-established theory of viscous flow over an airfoil with separation only near the trailing edge.

Only the case of two-dimensional airfoils has been considered, so that a major problem which remains is the study of three-dimensional separations.

Of the two types of laminar separation bubble commonly observed, long and short, the former is perhaps the more significant due to its large effect on the aerodynamic characteristics of an airfoil. Short bubbles must also be considered further in their capacity as an agent for initiating a turbulent boundary layer. There is further the important problem of buffeting caused by the long bubble type of separation; although this has only just begun to be studied the results are already finding practical application.

The effect of compressibility on long bubbles and the question of transonic reattachment are also important, and have been touched on in reference 31. Also Chapman *et al.*[32] have made a preliminary general study of separated flows in supersonic (and subsonic) streams. The work of Holder and Gadd[33] and of Pearcey[34] are significant contributions to these problems, in which it may be expected that the general approach of the present paper will be helpful.

Finally, a hypothesis concerning the mechanism of the leading-edge stall has emerged from the physical picture of laminar separation bubbles given here. This helps to explain the scale effect on the stalling characteristics of airfoils experiencing bubble separations, but it is still not possible to calculate the maximum lift achieved in a particular case.

## References

[1] Preston, J. H., *The Approximate Calculation of the Lift of Symmetrical Aerofoils Taking Account of the Boundary Layer*, ARC R&M 1996, 1943.

[2] Spence, D. A., *Prediction of the Characteristics of Two-Dimensional Airfoils*, Journal of the Aeronautical Sciences, Vol. 21, No. 9, pp. 577–587, 618, September, 1954.

[3] Maskell, E. C., *Wake Circulation and its Influence on Lift in Two-Dimensional Compressible Flow*, To be published as a Ministry of Supply Report.

[4] Brebner, G. G., and Bagley, J. A., *Pressure and Boundary Layer Measurements on a Two-Dimensional Wing at Low Speed*, ARC R&M 2886, 1955.

[5] Squire, H. B., and Young, A. D., *The Calculation of the Profile Drag of Aerofoils*, ARC R&M 1838, 1937.

[6] Holt, M., *Calculation of Wing Profile Drag*, Aircraft Engineering, Vol. XV, No. 176, pp. 278–280, 1943.

[7] Tetervin, N., *A Method for the Rapid Estimation of Turbulent Boundary Layer Thicknesses for Calculating Profile Drag*, NACA Advance Confidential Report No. L4G14 (Issued as NACA Wartime Report L.16), 1944.

[8] Maskell, E. C., *Flow Separation in Three-Dimensions*, RAE Report No. Aero. 2565, Nov., 1955. [Any request for this report must be made to NACA.]

[9] Squire, H. B., *Note on the Motion Inside a Region of Recirculation (Cavity Flow)*, Journal of the Royal Aeronautical Society, vol. 60, no. 543, pp. 203–205, March, 1956.

[10] Batchelor, G. K., *On Steady Laminar Flow with Closed Streamlines at Large Reynolds Number*, Journal of Fluid Mechanics, Vol. 1, Part 4, October, 1956. See also Vol. 1, Part 2, July, 1956.

[11] Maskell, E. C., *A Theoretical Treatment of the Thin-Aerofoil Stall*. To be published as a Ministry of Supply Report.

[12] Goldstein, S., (Ed.), *Modern Developments in Fluid Dynamics*, Vol. II, Chap. XIII, p. 553, Oxford, 1938.

[13] Goldstein, S. (Ed.), *Modern Developments in Fluid Dynamics*, Vol. II, Chap. XIII, pp. 555–556, Oxford, 1938.

[14] Owen, P. R., and Klanfer, L., *On the Laminar Boundary Layer Separation From the Leading Edge of a Thin Aerofoil*, ARC Current Paper No. 220.

[15] Crabtree, L. F., *The Formation of Regions of Separated Flow on Wing Surfaces. Part I: Low Speed Tests on a Two-Dimensional Unswept Wing With a 10% Thick R.A.E. 101 Section*, RAE Report No. Aero. 2528, Nov., 1954. [Any request for this report must be made to NACA.]

[16] Crabtree, L. F., *The Formation of Regions of Separated Flow on Wing Surfaces. Part II: Laminar Separation Bubbles and the Mechanism of the Leading-Edge Stall*. Unpublished Ministry of Supply Report.

[17] Schubauer, G. B., and Klebanoff, P. S., *Contributions to the Mechanics of Boundary Layer Transition*, NACA TN 3489, 1955.

[18] McGregor, I., *Regions of Localised Boundary Layer Separation and Their Role in the Nose-Stalling of Aerofoils*, Ph.D. Thesis, Queen Mary College, London, June, 1954.

[19] Norbury, J. F., and Crabtree, L. F., *A Simplified Model of the Incompressible Flow Past Two-Dimensional Aerofoils with a Long Bubble Type of Flow Separation*, RAE Technical Note No. Aero. 2352, June, 1955. [Any request for this report must be made to NACA.]

[20] Kuethe, A. M., *Investigations of the Turbulent Mixing Regions Formed by Jets*, Journal of Applied Mechanics, Vol. 2, pp. 87–95, 1935.

[21] Dimmock, N. A., *Some Further Jet-Flap Experiments*, NGTE Memo. No. M.255, May, 1956. [Any request for this report must be made to NACA.]

[22] Gault, D. E., *An Experimental Investigation of Regions of Separated Laminar Flow*, NACA TN 3505, September, 1955.

[23] McCullough, G. B., and Gault, D. E., *Examples of Three Representative Types of Airfoil-Section Stall at Low Speed*, NACA TN 2502, September, 1951.

[24] Butler, S. F. J., *Low Speed Tests of a 6% Thick R.A.E.101 Aerofoil Section*, unpublished Ministry of Supply Report.

[25] McKoen, C. H., *On the Stability of a Laminar Wake*, ARC Current Paper 303, October, 1955.

[26] Curle, N., *Hydrodynamic Stability of Laminar Wakes*, unpublished National Physical Laboratory Report.

[27] Küchemann, D., *Types of Flow on Swept Wings With Special Reference to Free Boundaries and vortex sheets*, Journal of the Royal Aeronautical Society, Vol. 57, pp. 683–699, November, 1953.

[28] Multhopp, H., *On the Maximum Lift Coefficient of Aerofoil Sections*, RAE Technical Note No. Aero. 1980, Dec., 1948. [Any request for this report must be made to NACA.]

[29] McCullough, G. B., *The Effect of Reynolds Number on the Stalling Characteristics and Pressure Distributions of Four Moderately Thin Airfoil Sections*, NACA TN 3524, November, 1955.

[30] Crabtree, L. F., *Prediction of Transition in the Boundary Layer on an Aerofoil*, to be published as a Ministry of Supply Report.

[31] Crabtree, L. F., and Weber, J., *Some Effects of Flow Separations on Thin Wings With Unswept Leading Edges*, unpublished Ministry of Supply Report.

[32] Chapman, D. R., Kuhn, D. M., and Larson, H. K., *Preliminary Report on a Study of Separated Flows in Supersonic and Subsonic Streams*, NACA RM A55L14, June, 1956.

[33] Holder, D. W., and Gadd, G. E., *The Interaction Between Shock Waves and Boundary Layers and its Relation to Base Pressure in Supersonic Flow*, Proc. of the Symposium on Boundary Layer Effects in Aerodynamics, N.P.L. Paper No. 8, March–April, 1955.

[34] Pearcey, H. H., *Some Effects of Shock-Induced Separation of Turbulent Boundary Layers in Transonic Flow Past Aerofoils*, Proc. of the Symposium on Boundary Layer Effects in Aerodynamics, N.P.L. Paper No. 9, March–April, 1955.

## Notice to Contributors

Manuscripts submitted for publication *must* be double- or triple-spaced originals. There should be wide margins on all sides of the sheets and triple spacing around formulas to allow for the marking of directions for the printer.

Original drawings (jet black India ink on white paper or tracing cloth) should accompany the manuscript. *(Blueprints are not acceptable.)* Photographs *must* be on glossy white paper. The smallest lettering on 8- by 10-in. figures should be no less than 1/4 in. high.

Only the simplest formulas should be typewritten; all others should be carefully written in pen and ink. The difference between capital and lower-case letters and Greek symbols should be clearly distinguished.

***See Inside Back Cover of this issue for further details***

# Bending Strength of Tubing in the Plastic Range†

CLIFFORD S. ADES*

*Bendix Products Division, Bendix Aviation Corporation*

## Summary

A method is presented for determining the total work of a bent and deformed tube subjected to stresses in the plastic range. By using the principle of least work, it is shown that it is possible to determine the shape of the cross section of the tube as a function of its longitudinal curvature and also, after the shape is found, to determine the bending moment carried by the tube. With this latter available, bending modulus of rupture charts for round tubing are constructed which appear to agree well with experimental results.

## Symbols

$A$ = area
$a$ = semimajor axis of ellipse
$b$ = semiminor axis of ellipse
$D$ = outside diameter of round tube
$E$ = modulus of elasticity
$E_s$ = secant modulus
$e_i$ = strain intensity
$F_b$ = bending modulus of rupture
$F_{tu}$ = ultimate tensile strength
$M$ = bending moment
$n$ = shape parameter in equation for stress-strain curve
$r$ = mean radius of circular cylinder
$s$ = length measured along middle surface
$t$ = tubing wall thickness
$W$ = work
$W_0$ = work per unit volume
$V$ = volume
$\alpha$ = slope angle of middle surface of deformed cross section
$\delta$ = elastic dilatation
$\epsilon_L$ = longitudinal strain
$\epsilon_{LM}$ = mean longitudinal strain
$\epsilon_{PL}$ = proportional limit strain
$\epsilon_T$ = transverse strain
$\zeta$ = coordinate normal to middle surface
$\mu$ = Poisson's ratio
$\mu_{PL}$ = Poisson's ratio in elastic range
$\rho$ = longitudinal radius of curvature
$\rho_T$ = radius of curvature of middle surface of deformed cross section
$\rho_T'$ = initial transverse radius of curvature of middle surface
$\sigma_i$ = intensity of stress
$\sigma_L$ = longitudinal stress
$\sigma_T$ = transverse stress
$\sigma_{0.7}$ = secant yield stress corresponding to secant line of slope $0.7E$

Received February 21, 1957

† This work was sponsored by the Bendix Products Division at the request of the ANC-5 Panel. The purpose was to investigate the need for a revision of certain allowables appearing in Government Document ANC-5, *Strength of Metal Aircraft Elements*.

* Head of Structures Development, Airframe Equipment Section.

The author thanks Dr. L. H. N. Lee of the University of Notre Dame and J. N. Herrmann of the Bendix Products Division for their valuable suggestions used in the preparation of this paper. He is also indebted to R. C. Lowery of the Bendix Products Division for the extensive programing and computer work required in its preparation and to H. Doyle and the Bendix Computer Division for their help with the use of the Bendix G-15 Digital Computer.

## Introduction

It is known that the cross sections of some beams deform during bending and that this deformation is sufficient to affect the bending strength.[1-3] Two papers on this general subject, those by Brazier and Chwalla, were concerned with the same subject—the bending strength of round tubing. All were concerned with stresses in the elastic range. There is much need, however, in the aircraft industry for information on the bending strength of tubing, particularly initially round tubing, which fail with some of the bending stresses in the plastic range. Design curves have been developed using available test data; but the proper shape for these curves was always in doubt, due to the fact that, in general, only a relatively small percentage of the total test data required was available. The writer sought to correct this by the derivation of a theoretical approach, which is presented in what follows.

## Basic Concepts and Assumptions

During the bending of hollow round tubes, either initially curved or straight, it is known[4] that an ovalization of the cross section takes place. As the bending continues this ovalization increases. At first the resisting moment also increases, but eventually it reaches a maximum and then starts to decrease because of the increased ovalization. This phenomenon can occur in thin metal tubes stressed below the elastic limit but can also occur in relatively thick metal tubes

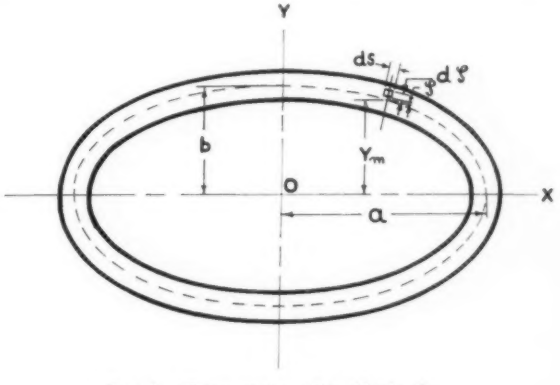


Fig. 1. Cross section of ovalized tube

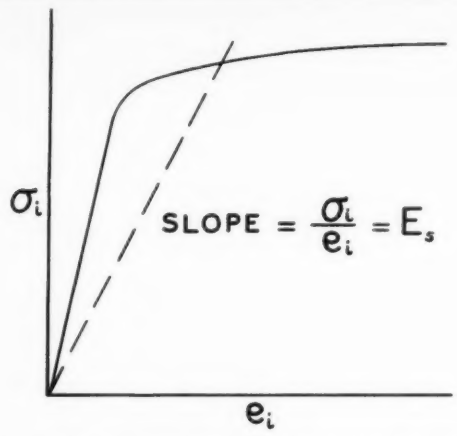


FIG. 2. Typical stress-strain curve used in this investigation.

stressed above the elastic limit or in the plastic range for the material.

During ovalization, it is assumed here that tubes which are initially round become elliptical in shape, that this circumferential deformation is inextensional, and that lines originally normal to the middle surface remain so after loading; these are the same assumptions used by Chwalla. Other assumptions are (1) that the tube is subjected to pure bending and is of sufficient length so that the end conditions have a negligible effect on the strength at its center and (2) that the material is isotropic and has the same stress-strain curve in tension and compression.

## ANALYSIS

### *Work of Deformation*

In order to establish a theory, a way must be evolved to determine the amount of ovalization of the cross section of the tube for a given longitudinal radius of curvature. It will be shown that this can be done by using the principle of least work or, in other words, by minimizing the total internal work of the bent tube. In order to show that the method used to determine the internal work applies in both the elastic and plastic ranges, an expression for the former will be derived first. Referring to Fig. 1, we see that in the elastic range the work per unit length is

$$dW = [(1/2)\sigma_L\epsilon_L + (1/2)\sigma_T\epsilon_T]\, d\zeta\, ds$$

where $\sigma_L$, $\epsilon_L$, $\sigma_T$, and $\epsilon_T$ are, respectively, the longitudinal and transverse stress and strain.

Substituting for $\sigma_L$ and $\sigma_T$ their values as functions of $E$, $\mu$, and $\epsilon$

$$\left.\begin{aligned} dW &= [E/2(1-\mu^2)][(\epsilon_L + \mu\epsilon_T)\epsilon_L + (\epsilon_T + \mu\epsilon_L)\epsilon_T]d\zeta ds \\ &= [E/2(1-\mu^2)][\epsilon_L^2 + \epsilon_T^2 + 2\mu\epsilon_L\epsilon_T]d\zeta ds \end{aligned}\right\} \quad (1)$$

This may be written

$$dW = (E/2)(e_i^2)d\zeta ds \quad (2)$$

If

$$e_i = \sqrt{[1/(1-\mu^2)](\epsilon_L^2 + \epsilon_T^2 + 2\mu\epsilon_L\epsilon_T)} \quad (3)$$

Eq. (2) may also be written

$$dW = (1/2)(Ee_i)e_i d\zeta ds = (1/2)\sigma_i e_i d\zeta ds$$

where $\sigma_i$ and $e_i$ are coordinates of the stress-strain curve for the material. Since $(1/2)\sigma_i e_i$ equals the area under the stress-strain curve, it is readily seen that the work per unit volume at any point in a two-dimensional stress system can be determined by first computing $e_i$ using Eq. (3) and then determining the corresponding area under the stress-strain curve for the material. So far this has only been proved to hold for stresses still within the elastic range for the material.

In the plastic range let us begin in the usual manner by assuming $\mu = 1/2$. Eq. (3) then reduces to the following:

$$e_i = (2/\sqrt{3})\sqrt{\epsilon_L^2 + \epsilon_T^2 + \epsilon_L\epsilon_T} \quad (4)$$

which is the equation for the strain intensity in the plastic range in accordance with the deformation theory.[5] If it can be shown that the corresponding area under the stress-strain curve also gives the work per unit volume, then the theory will be continuous in the elastic and plastic ranges. This is important here since a section can at the same time have stresses in both ranges. Let us begin by assuming that this is so, or that (see Fig. 2)

$$\left.\begin{aligned} W_0 &= \int \sigma_i de_i = \int E_s e_i de_i \\ &= \int E_s(2/\sqrt{3})(\epsilon_L^2 + \epsilon_T^2 + \epsilon_L\epsilon_T)^{1/2} \times [(1/\sqrt{3})(\epsilon_L^2 + \epsilon_T^2 + \epsilon_L\epsilon_T)^{-1/2} \times (2\epsilon_L d\epsilon_L + 2\epsilon_T d\epsilon_T + \epsilon_L d\epsilon_T + \epsilon_T d\epsilon_L)] \\ &= (4/3)\int E_s\{[\epsilon_L + (1/2)\epsilon_T]d\epsilon_L + [\epsilon_T + (1/2)\epsilon_L]d\epsilon_T\} \\ &= \int (\sigma_L d\epsilon_L + \sigma_T d\epsilon_T) \end{aligned}\right\} \quad (5)$$

since[5] $\sigma_L = (4/3)E_s[\epsilon_L + (1/2)\epsilon_T]$

and $\sigma_T = (4/3)E_s[\epsilon_T + (1/2)\epsilon_L]$

Eq. (5) represents the total work per unit volume. This means that the work per unit volume can be determined in both the elastic and plastic ranges by taking it equal to the area under the stress-strain curve corresponding to the value of $e_i$ given by Eq. (3). This has another advantage in that a varying value of $\mu$ can be used which can be important in elastic-plastic cases since $\mu$ for some materials might vary by as much as 100 per cent (0.25 to 0.50 as stress increases from elastic to plastic range). The total work may then be determined by computing the work per unit volume at various points using the above process and integrating over the total volume of the material.

### *Application of Principle of Least Work*

In what follows it will be shown that this principle applies in both the elastic and plastic ranges for the problem being considered. Let us take a round tube

and bend it into a fixed circular arc of radius $\rho$. The tube will ovalize and assume a position of stable equilibrium. Since the assumed cross section is elliptical (see above), let us further assume that the semimajor axis varies by a small amount. With the ends fixed against rotation no change in the external work occurs. The internal work therefore remains the same, and we can write the following equations:

$$\int \Delta W_0 dV = \Delta \int W_0 dV = 0$$

where $W_0$ is the work per unit volume and $V$ is the volume of the tube. If the shape of the ellipse is defined by the quantity $a/r$, the ratio of its semimajor axis and the radius of the original round, the above equations signify that at this point of stable equilibrium the change in internal work due to a small change in $a/r$ is equal to zero, or that

$$\partial W/\partial(a/r) = 0$$

This means then that at the stationary point the total internal work with $\rho$ held constant and $a/r$ varied must be either a maximum or minimum. Reference to $W$ vs. $a/r$ curves which were obtained by a process of numerical integration (see Fig. 4) indicates that this point is always a minimum. More extensive plots of $W$ vs. $a/r$ also show that no other maximum or minimum points for which the slope is zero occur, at least within the physical limitations of the problem.

Hill[12] also discusses extremum and variational principles for the plastic-elastic range which could be applied to a certain extent here. These would indicate of course that the absolute minimum of total internal work would be realized by use of the proper cross-sectional shape. The assumption of an ellipse is, however, a convenient one and apparently sufficiently accurate for the purposes here.

### *Application to Round Tubing*

This general theory will be applied to determine the bending strength of round tubing. Since the stresses in all transverse sections are identical, we only need to consider a tube of unit length; and also, because of the symmetrical condition of a transverse section, the integration need be performed only over one half of it

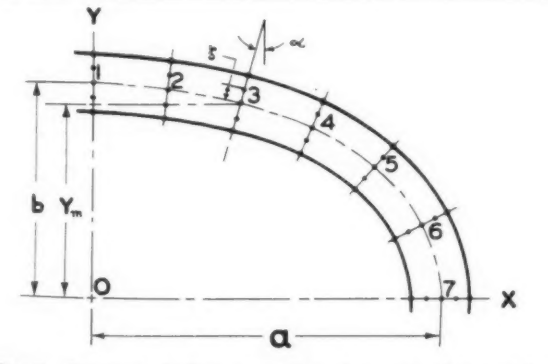


FIG. 3. Quadrant of ellipse showing sections and points used in numerical integration.

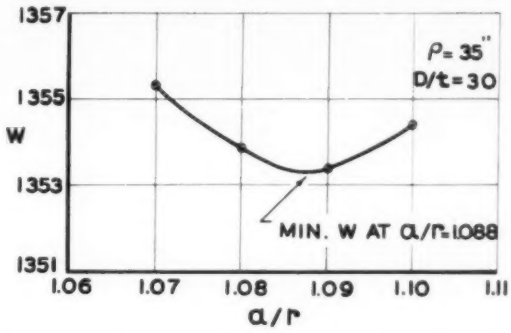


FIG. 4. Curve illustrating method for obtaining $a/r$ corresponding to given value of $\rho$ using principle of least work.

(one quarter above and below the neutral axis). The section is not quite symmetrical about the neutral axis owing to small differences in the states of stress and strain, although the resultant forces above and below the neutral axis are practically identical for the case examined. Even with these simplifications, however, no closed solution for the required integration was found, and therefore a numerical integration process was resorted to. In this, the one-quarter circumference of the ellipse was divided into six equal parts (1–7, Fig. 3). Elliptic integrals were used in order to secure sufficient accuracy. At each of these division points the wall was divided into four equal parts. Taking section 1 for example, the work per unit volume was computed at each of the five division points, and the integration across the wall was performed by use of Simpson's rule. After this process was completed at each of the remaining sections 2–7, the circumferential integration was carried out, again by use of Simpson's rule. This process of course was repeated for a quadrant below the neutral axis and the total work found by adding the results and multiplying by two.

### *Deformation Relationships*

The data to be substituted in Eq. (3) are as follows:

$$\epsilon_L = y/\rho = (1/\rho)(y_m + \zeta \cos \alpha) \tag{6}$$

where $\rho$ is the longitudinal radius of curvature of the bent beam, and $\alpha$ is the slope angle of the middle surface.

$$\cos \alpha = \pm \frac{1}{[1 + (dy/dx)^2]^{1/2}} = \pm \frac{1}{\{1 + (b^2/a^2)[(1 - y_m^2/b^2)/(y_m^2/b^2)]\}^{1/2}} \tag{7}$$

$$\epsilon_T = \zeta[(1/\rho_T) - (1/r)] - \mu\epsilon_{LM} = \zeta[(1/\rho_T) - (1/r)] - \mu(y_m/\rho) \tag{8}$$

Here $\rho_T$ and $r$ are the mean radii of curvature of the ellipse and circle, respectively, and $\epsilon_{LM} = y_m/\rho$ is the mean or middle surface strain for the ellipse.

$$1/\rho_T = (d^2y/dx^2)/[1 + (dy/dx)^2]^{3/2} = ab/[b^2 - y_m^2 + (a^2/b^2)y_m^2]^{3/2} \tag{9}$$

$$\mu = \{1 - [(1 + \delta)/(1 + e_t)]^{1/2}\}/e_t \tag{10}$$

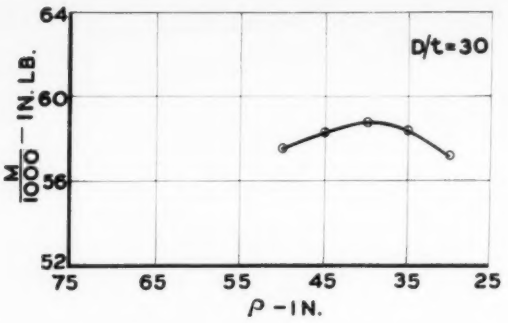


FIG. 5. Curve illustrating method of obtaining maximum moment.

where $\delta = (1 + \epsilon_{PL})(1 - \mu_{PL}\epsilon_{PL})^2 - 1$

For $e_i \leqslant \epsilon_{PL}, \quad \mu = \mu_{PL}$

This value of Poisson's ratio $\mu$ appears to check well with experimental results.[6] Since the values of $\mu$ and $e_i$ are interdependent, the latter have to be determined by trial.

### *Determination of Ovalization*

The amount of tube ovalization corresponding to a given value of longitudinal curvature $\rho$ also has to be determined by trial and is accomplished as follows:

(1) Assume a value for $\rho$.

(2) Assume a certain amount of ovalization or, in other words, a value for $a/r$.

(3) With this and other information given above, the value of $e_i$ at any point may then be determined; and the corresponding work per unit volume may be determined by use of the following equations for the stress-strain curve:[11]

$$e_i = (\sigma_i/E)[1 + (3/7)(\sigma_i/\sigma_{0.7})^{n-1}] \qquad (11)$$

$$A = (\sigma_i^2/E)[(1/2) + [3n/7(n+1)](\sigma_i/\sigma_{0.7})^{n-1}] \qquad (12)$$

Eq. (12) is the area under the stress-strain curve and is obtained from Eq. (11) by integration.

(4) The total work for the deformed section is obtained by the numerical integration process as previously explained.

(5) Since the correct value of ovalization for a given $\rho$ is obtained when the work is minimum, this process is repeated until the minimum is obtained. In doing this $\rho$ is held constant and $a/r$ varied, and the results are plotted as a curve of $W$ vs. $a/r$ as shown in Fig. 4.

Obviously the above process is too laborious for hand calculation, but it was found that it could be programed and accomplished using a fairly high-speed, high-capacity digital computer. The data shown plotted in Fig. 4, for example, was computed using a Bendix G-15 in a matter of approximately 1 hour.

### *Transverse Deformation Relationship—Tubes Other Than Round*

This method can also be used for cylindrical sections which are not initially round by substitution of the following equation for $\epsilon_T$:

$$\epsilon_T = \zeta[(1/\rho_T) - (1/\rho_T')] - \mu(y_m/\rho)$$

Here $(1/\rho_T) - (1/\rho_T')$ represents the change in transverse curvature. This equation can also be used for tubes which are supposed to be initially round but which have some ovality. For convenience, the initial cross-sectional shape would again be assumed elliptical.

### *Determination of Bending Moment*

Once the ovalization corresponding to a given radius of curvature is determined, the next step is to determine the moment carried by the ovalized tube. This is done by summing up the moments of the longitudinal stresses about the neutral axis. The equation for the longitudinal stress is as follows:

$$\sigma_L = [E_s/(1 - \mu^2)](\epsilon_L + \mu\epsilon_T) \qquad (13)$$

where $\mu$, $\epsilon_L$, and $\epsilon_T$ are as given by Eqs. (6)–(10). $E_s = \sigma_i/e_i$ and can be determined from the stress-strain curve for the material. $e_i$ is determined by Eq. (3) as previously explained. After the $dM = \sigma_L y d\zeta ds$ is obtained at each point (see Fig. 3), the total moment for the section is obtained by the same numerical integration process used for the determination of the total work.

In order to determine the maximum moment that a given section can carry, several values of moment must be determined for varying values of $\rho$. As the tube bends and $\rho$ decreases, at some point the moment carrying capacity of the tube reaches a maximum and then starts to decrease due to the excessive ovalization. A curve illustrating this is shown in Fig. 5.

## DISCUSSION OF RESULTS

### *Ultimate Bending Strength of Round Tubing*

A study of this subject indicates that the mode of failure varies and that it can be divided into ranges in accordance with the diameter to thickness or $D/t$ ratio somewhat as follows:

(1) At a $D/t = 2$ (solid round) the failure is a material failure with some, but not appreciable, ovalization or other distortion of the cross section. The strength can be computed conservatively by the method of reference 7.

(2) In the range of $D/t$'s from 3–10, the failure is still a material failure but takes place with some ovalization of the cross section. The amount of ovalization increases as the $D/t$ increases.

(3) In the range from 10–50, failure is by excessive ovalization in the manner already explained. It should be noted that in a test the apparent mode of failure in this range would be either material failure or failure by buckling, since one or the other of these would certainly occur after the maximum moment had been reached. Some carefully run tests are needed in order to determine this point accurately.

(4) In the range of $D/t$'s $> 50$, failure may be by buckling which takes place after some ovalization of the cross section. In order to indicate the buckling type of failure, however, rather large imperfection factors[8, 9] have to be used, and this indicates that the initial imperfections have quite an effect on the failure mode and strength of the tube. A more accurate theory for the elastic and plastic buckling of bent and ovalized tubes is needed in order to secure a better check on this point. A method of computing the buckling curve will not be given here since it is quite an extensive problem in itself and one which needs considerably more investigation and refinement.

Fig. 6 shows curves for 260,000 ultimate tensile strength steel which were plotted in accordance with items (1)–(3) given just above. In accordance with item (3) then, for those sections which do not fail by material failure, excessive ovalization rather than buckling is considered to be the cause of failure. The constants used in Eq. (11), the stress-strain curve for the material, were as follows: $E = 29{,}000{,}000$, $n = 16.0$, and $\sigma_{0.7} = 214{,}000$. The $F_b$ plotted is the computed ultimate moment divided by the section modulus of the original round cross section. The failure with no ovalization curve was computed by the method of reference 7. The failure with ovalization curve was determined by computing data for tubes with $D/t$ values of 10, 30, and 50.

### *Bending Modulus of Rupture Curves for Round Tubing*

The two curves shown in Fig. 6 will form a smooth curve since the ovalization is gradually and continuously increasing and the longitudinal stresses, in general, gradually decreasing as the $D/t$ increases. By taking the curves shown in Fig. 6 and plotting them as a continuous curve (see Fig. 7), there is obtained a curve which can be used to obtain the bending modulus of rupture for the material in question. Similar curves for a number of different steels have been plotted, and the agreement with available test data has in all cases been about the same.

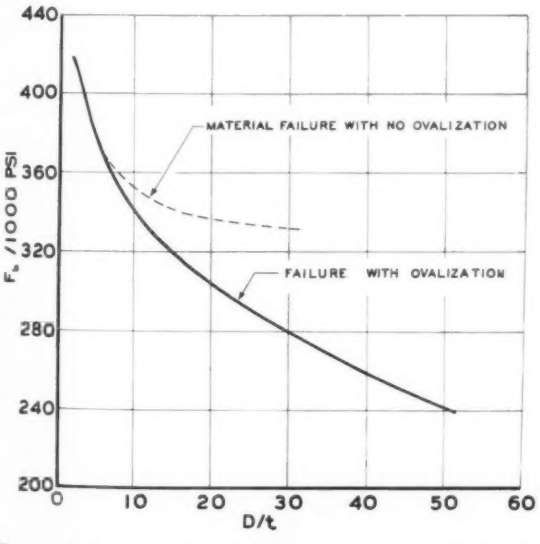


Fig. 6. Computed ultimate moment curves—260,000 U.T.S. round tubing.

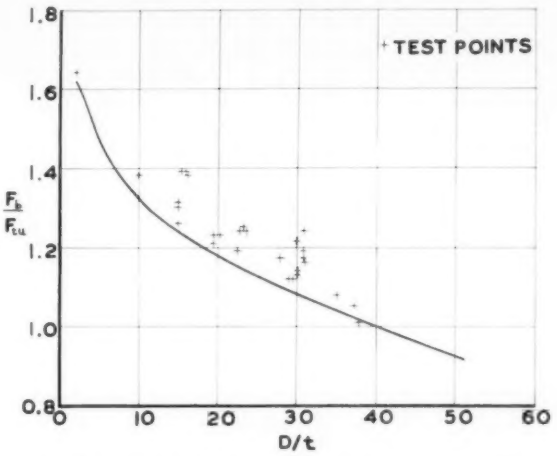


Fig. 7. Computed and experimental bending modulus of rupture data—260,000 U.T.S. round tubing.

### *Stress-Strain Curves*

In plotting these curves, the conventional rather than the so-called true[10] stress-strain curve was used. Since the latter is higher, particularly at the ultimate strength end, the corresponding bending modulus curve would be higher at the left end but about the same at the right end. This would tend then to rotate the curve so that it would appear to lie closer to a mean curve for all the test data. This was not investigated, however, for the following reason: the curves were being constructed to be used as design curves, and many designers or stress analysts would probably not use them if they found that some of the available test data plotted below the curves.

## Conclusions

(1) The assumptions and method of numerical integration employed apparently give sufficiently accurate results for practical purposes.

(2) Use of the deformation theory again appears to lead to sufficiently accurate results.[5, 13]

(3) In some test data, a failure moment smaller than the maximum moment taken during the test might readily be reported. This is due to the fact that, because of the ovalization, the moment can reach a maximum and then start to decrease before the more apparent type of failure, by fracture or buckling, occurs. Also, some test data will indicate higher moments than those obtained by the theory due to the effect of some local restraint.

(4) The use of the true stress-strain curve would probably give a bending modulus curve more in line with the mean test curve, but it would not be generally acceptable for design use because some of the test points would fall below the curve.

(5) The methods used to construct the bending modulus curves appear to give results in line with the available test data even for some of the materials which are known to be somewhat anisotropic—e.g., 260,000 U.T.S. steel.

In order to check more completely the methods employed and conclusions reached, there is need for a more accurate theory for the elastic and plastic buckling of bent and ovalized tubes and also for several carefully conducted tests run with some of the above-mentioned points in mind.

### References


[1] Timoshenko, S., *Bending Stresses in Curved Tubes of Rectangular Cross Section*, Trans. ASME, Vol. 45, pp. 135–140, 1923.

[2] Brazier, L. G., *On the Flexure of Thin Cylindrical Shells and Other Thin Sections*, Proc. Royal Soc., London, Ser. A, Vol. 116, pp. 104–111, 1927.

[3] Chwalla, E., *Reine Biegung schlanker, dünnwandiger Rohre mit gerader Achse*, ZAMM, Vol. 13, pp. 48–53, 1933.

[4] Timoshenko, S., *Theory of Elastic Stability*, pp. 465, 466; McGraw-Hill Book Company, Inc., New York, 1936.

[5] Stowell, E. Z., *A Unified Theory of Plastic Buckling of Columns and Plates*, NACA Rep. 898, 1948.

[6] Stang, A. H., Greenspan, M., and Newman, S. B., *Poisson's Ratio of Some Structural Alloys for Large Strains*, J. Res., National Bureau of Standards, Vol. 37, pp. 211–221, October, 1946.

[7] Cozzone, F. P., *Bending Strength in the Plastic Range*, Journal of the Aeronautical Sciences, Vol. 10, No. 5, pp. 137–151, May, 1943.

[8] Donnell, L. H., and Wan, C. C., *Effects of Imperfections on Buckling of Thin Cylinders and Columns Under Axial Compression*, Trans. ASME, Vol. 72, pp. 73–83, 341–343, 1950.

[9] Loo, T. T., *Effects of Large Deflections and Imperfections on the Elastic Buckling of Cylinders Under Torsion and Axial Compression*, Proc., Second U.S. National Congress of Applied Mechanics, pp. 345–357, 1954.

[10] Nadai, A., *Theory of Flow and Fracture of Solids*, 2nd Ed., Vol. 1, pp. 70–79; McGraw-Hill Book Company, Inc., New York, 1950.

[11] Ramberg, W., and Osgood, W. R., *Description of Stress-Strain Curves by Three Parameters*, NACA TN 902, July, 1943.

[12] Hill, R., *The Mathematical Theory of Plasticity*, pp. 60–66; Oxford University Press, London, 1950.

[13] Lee, L. H. N., and Ades, C. S., *Plastic Torsional Buckling of Cylinders Including the Effects of Imperfections*, Journal of the Aeronautical Sciences, Vol. 24, No. 4, pp. 241–248, April, 1957


## Aerodynamic Action of Triangular Horn-Balanced Control Surfaces . . .

(*Continued from page 578*)

considered by Coale enables the final formulas to be reduced to functions of just one parameter, the reduced aspect ratio of the balance. This simplification could not be achieved in the case of a triangular balance.

### References


[1] Puckett, A. E., *Supersonic Wave Drag of Thin Airfoils*, Journal of the Aeronautical Sciences, Vol. 13, No. 9, pp. 475–484, September, 1946.

[2] Evvard, J. C., *Distribution of Wave Drag and Lift in the Vicinity of Wing Tips at Supersonic Speeds*, NACA TN 1382, 1947.

[3] Evvard, J. C., *Use of Source Distributions for Evaluating Theoretical Aerodynamics of Thin Finite Wings at Supersonic Speeds*, NACA Report 951, 1950.

[4] Robinson, A., *Aerofoil Theory of Flat Delta Wing at Supersonic Speeds*, ARC RM 2548, 1946.

[5] Tucker, W. A., and Nelson, R. L., *Theoretical Characteristics in Supersonic Flow of Two Types of Control Surfaces on Triangular Wings*, NACA Report 939, 1949.

[6] Tucker, W. A., *Characteristics of Thin Triangular Wings With Constant Chord Full Span Control Surfaces at Supersonic Speeds*, NACA TN 1601, 1948.

[7] Coale, C. W., *Supersonic Characteristics of Rectangular Horn Balanced Ailerons*, Douglas Report SM-13718.



An Authorized Binding for
Journal of the Aeronautical Sciences

Arrangements have been made by the Institute of the Aeronautical Sciences for members and subscribers to have their Journals bound carefully and economically. Simply write for details to:

Publishers' Authorized Bindery Service

5809 West Division St. Chicago 51, Ill.

# A Simple Model Study of Transient Temperature and Thermal Stress Distribution Due to Aerodynamic Heating†

GABRIEL ISAKSON*
*University of Michigan*

SUMMARY

The present work is concerned with the determination of transient temperatures and thermal stresses in simple models intended to simulate parts or the whole of an aircraft structure of the built-up variety subjected to aerodynamic heating.

The first case considered is that of convective heat transfer into one side of a flat plate, representing a thick skin, and the effect of the resulting temperature distribution in inducing thermal stresses associated with bending restraint at the plate edges. Numerical results are presented for the transient temperature differentials in the plate when the environment temperature first increases linearly with time and then remains constant, the period of linear increase representing the time of acceleration of the aircraft. Corresponding thermal stress information is presented.

The second case is that of the wide-flanged I-beam with convective heat transfer into the outer faces of the flanges. Numerical results are presented for transient temperature differentials for a wide range of values of the applicable parameters and for an environment temperature variation as described above. Corresponding thermal stresses in a beam of infinite length are determined. A theoretical analysis of the stress distribution in a beam of finite length is carried out and numerical results obtained for one case. An experimental investigation of temperatures and stresses in such a beam is described, and results are presented which indicate good agreement with corresponding theoretical results.

SYMBOLS

| | |
|---|---|
| $b$ | = semiwidth of I-beam |
| $C_p$ | = specific heat of plate or beam material |
| $f(\xi)$ | = nondimensional temperature distribution in plate, $(T - T_{x=0})/\Delta T$ |
| $h$ | = heat-transfer coefficient at heated surface |
| $h_j$ | = heat-transfer coefficient at joint between beam flange and web |
| $k$ | = thermal conductivity of plate or beam material |
| $l$ | = semilength of I-beam |
| $s$ | = semidepth of I-beam |
| $t$ | = time |
| $t_a$ | = time of linear increase of environment temperature |
| $u$ | = displacement in $x$-direction |
| $x$ | = coordinate in plate representing distance from insulated surface, positive toward heated surface |
| $x, y, z$ | = coordinates of I-beam (Fig. 8) |
| $A_f, A_w$ | = cross-sectional area of flanges and web, respectively, of I-beam |
| $A_{mn}$ | = coefficients in series for Airy stress function for flange |
| $B_{mn}$ | = coefficients in series for Airy stress function for web |
| $E$ | = Young's modulus of elasticity |
| $K_c$ | = stress correction factor for compression (Eq. 5) |
| $K_t$ | = stress correction factor for tension (Eq. 6) |
| $K_c'$ | = modified stress correction factor for compression (Eq. 7) |
| $K_t'$ | = modified stress correction factor for tension (Eq. 8) |
| $T$ | = temperature in plate or beam |
| $T_0$ | = temperature at middle of beam web |
| $\Delta T$ | = temperature differential between surfaces of plate, temperature differential between middle of web and edge of flange |
| $T_i$ | = initial temperature in plate or beam |
| $T_e$ | = environment temperature |
| $T_{er}$ | = reference environment temperature |
| $V$ | = strain energy |
| $\alpha$ | = coefficient of thermal expansion |
| $\gamma$ | = ratio of flange thickness to web thickness, $\delta_f/\delta_w$ |
| $\delta$ | = plate thickness |
| $\zeta$ | = nondimensional beam coordinate, $z/l$ |
| $\eta$ | = nondimensional beam coordinate, $y/s$ |
| $\kappa$ | = thermal diffusivity of plate or beam material, $k/\rho C_p$ |
| $\lambda$ | = nondimensional heating parameter; $h\delta/k$ in plate, $hs^2/k\delta_f$ in I-beam |
| $\lambda_j$ | = nondimensional heat-transfer coefficient at web-flange joint, $h_j s/k$ |
| $\mu$ | = $2 + \nu$ |
| $\nu$ | = Poisson's ratio |
| $\xi$ | = nondimensional beam coordinate, $x/\delta$ in plate, $x/s$ in I-beam in Section (4), $x/b$ in I-beam in Sections (5) and (6) |
| $\rho$ | = density of plate or beam material |
| $\sigma_x, \sigma_y, \sigma_z$ | = normal stress components |
| $\sigma_0$ | = intensity of normal force applied on end of beam |
| $\tau$ | = nondimensional time variable, $\kappa t/\delta^2$ in plate, $\kappa t/s^2$ in beam |
| $\tau_a$ | = nondimensional time of linear increase of environment temperature |

Received August 3, 1956. Revised and received March 7, 1957.

† This paper represents a condensation of portions of a thesis[13] submitted by the author to the Massachusetts Institute of Technology in March, 1953, in partial fulfillment of the requirements for the degree of Doctor of Science. The work was carried out in connection with U.S. Air Force Contract AF33(616)-3259 in the Aero-elastic and Structures Research Laboratory at the Massachusetts Institute of Technology under the direction of Prof. R. L. Bisplinghoff. The author is especially indebted to C. W. Brenner for assistance with the Whirlwind I digital computations and W. Campbell for assistance in the experimental phases of the work. Availability of time on the Whirlwind I digital computer was made possible by the Office of Naval Research. The preparation of this paper was aided materially by the Industry Program of the College of Engineering of the University of Michigan, which made possible also the publication of a less severely condensed version of the original thesis.

* Associate Professor of Aeronautical Engineering.

$(\tau_\varrho)_\tau$ = $\dfrac{\tau_\varrho}{\tau \text{ at } (\Delta\phi)_{max_{\tau_\varrho=0}}}$

$\tau_{xy}$, $\tau_{yz}$, $\tau_{zx}$ = shear stress components

$\phi$ = nondimensional temperature $(T_{e_r} - T) \div (T_{e_r} - T_i)$, Airy stress function

$\phi_e$ = nondimensional environment temperature, $(T_{e_r} - T_e)/(T_{e_r} - T_i)$

$\Delta\phi$ = $\Delta T/(T_{e_r} - T_i)$

$\psi$ = ratio of I-beam length to width, $l/b$

$\omega$ = ratio of I-beam width to depth, $b/s$

*Subscripts*

$f$ = flange

$w$ = web

## (1) Introduction

In the rapid acceleration of an aircraft to very high speed, friction in the boundary layer may raise the temperature of the surface of the aircraft with sufficient rapidity that large temperature differentials may occur in the structure before interior portions heat up. This may result in thermal stresses of considerable magnitude.

The heat transfer into the surface of the aircraft may be treated in a manner similar to convective heat transfer in low speed flow. An appropriate heat-transfer coefficient is used in conjunction with the difference between the temperature at the solid surface and the so-called "adiabatic wall temperature," or temperature which would be attained in the air at the solid surface if that surface were insulated.[1] The heat-transfer coefficient and adiabatic wall temperature depend upon the properties of the ambient air, the velocity of flow outside the boundary layer, and the thickness and type of boundary layer (laminar or turbulent).

Determination of the transient temperature and thermal stress distribution in the case of a typical built-up aircraft structure is exceedingly difficult and cumbersome. Much of a general nature can be learned, however, from the analysis of simple structures representing parts of the built-up structure or constituting simple models intended to represent the whole structure.

Thus, in the present work, attention is concentrated on the flat plate with convective heat transfer into one face and the wide-flanged I-beam with convective heat transfer into the outer faces of the flanges. The former is intended to represent the thick skin of a high-speed aircraft, while the latter is intended to represent a simple type of built-up wing structure. The interior surfaces of the structure are assumed to be insulated. Heat transfer by radiation or convection between parts of the structure is neglected.

Studies of this type have been reported in a number of publications in recent years,[5–11] particularly on the wide-flanged I-beam of infinite length, and results have been presented for selected values of the significant parameters. In the present work, these results are extended to cover large ranges of values of the parameters reduced to nondimensional form, and the problem of thermal stresses in a wide-flanged I-beam of finite length is considered in some detail.

## (2) Transient Temperature Distribution in a Flat Plate

The case of a flat plate insulated on one side with convective heat transfer on the other side is first considered. The following assumptions are made.

(1) The environment temperature and heat-transfer coefficient are uniform over the heated surface, the latter being constant with time.

(2) The temperature in the plate is initially uniform.

(3) There is no heat transfer through the edges of the plate, so that the flow of heat takes place only in a direction normal to the surface of the plate.

(4) Variation of the thermal properties of the material of the plate with temperature may be neglected.

An equivalent problem for the special case of constant $T_e$ is a familiar one in the field of heat transfer, and its solution is well known. It is the problem of an infinite plate at initial uniform temperature $T_i$, subjected suddenly to an environment at constant temperature $T_e$ on both sides. Heat flows into the surfaces of the plate by convective heat transfer.

This problem is seen to be identical with the present problem if, in the former, only half the thickness of the plate is considered, since, because of symmetry, there is no heat flow across the middle surface, which may thus be considered as an insulated surface.

The classical solution to this problem is given as an infinite transcendential series.[2] Numerous charts and tables presenting results for various values of the parameter $\lambda$ are available in the literature (see reference 2, pp. 274, 285, 415, and 416, and reference 3, p. 122). These results are used here to plot a curve of $(\Delta\phi)_{max}$—that is, the nondimensionalized maximum temperature differential across the two faces of the plate during the heating period—versus the parameter $\lambda$. The nondimensional time $\tau$ at which this maximum occurs has also been plotted. These plots are shown in Fig. 1. It will be shown in the next section that this maximum temperature differential provides a measure of the maximum thermal stress in the plate.

The assumption of constant $T_e$ and $h$ is not realistic for the case of aerodynamic heating, since it implies an infinite acceleration, that is, an instantaneous achievement of high-speed flight. In reality, the period of acceleration may be of the order of several minutes, during which time the adiabatic wall temperature, represented here by the environment temperature, and the heat-transfer coefficient are increasing. The introduction of a variable heat-transfer coefficient would complicate the problem very greatly, however. On the other hand, the introduction of a variable environment temperature does not complicate the problem unduly if its variation is assumed to be of a simple form. Because of the linearity of the governing differential equation, such a variation of $T_e$ may be taken into account by the application of Duhamel's integral in conjunction with the time history of temperature in the plate following a sudden change in environment tempera-

ture.[4] While the problem may be handled analytically in this manner, it was decided, after considerable investigation, that the use of a finite difference numerical method in conjunction with an automatic digital computing machine would be more expeditious in the generation of a large volume of data. Consequently, a finite difference procedure was set up.

The time history of $T_e$ was assumed to have the form shown in Fig. 2 and is represented mathematically as follows:

$$\left.\begin{aligned} T_e &= T_i + (T_{e_f} - T_i)(t/t_\theta) && \text{for } 0 \le t \le t_\theta \\ &= T_{e_f} && \text{for } t > t_\theta \end{aligned}\right\} \quad (1)$$

A program of computations was carried out on the Whirlwind I automatic digital computer at the Massachusetts Institute of Technology for a variety of values of the parameters $\lambda$ and $\tau_\theta$. The effect of these parameters on the maximum temperature differential attained in the plate is shown in Fig. 3.

In addition to the maximum temperature differential, it is also important, for the purpose of thermal stress determination, to know the distribution of temperature through the thickness of the plate. This distribution may be expressed conveniently in terms of the nondimensional function,

$$f(\xi) = (T - T_{x=0})/\Delta T \quad (2)$$

The computed results indicate that, at the time of maximum temperature differential, the function $f(\xi)$ approaches the parabolic form, $f(\xi) = \xi^2$, for low values of $\lambda$ when $T_e$ varies as a step-function, and for all values of $\lambda$ when $T_e$ has an initial linear gradient and the nondimensional gradient time $\tau_\theta$ is sufficiently large. It is thus convenient to adopt this parabolic distribution as a reference distribution. At large values of $\lambda$ and zero or small values of $\tau_\theta$, the temperature gradient at the heated surface is more pronounced than that given by the parabolic distribution.

### (3) Thermal Stresses in a Flat Plate

The thermal stresses resulting from transient temperature distributions in a flat plate, as discussed in the preceding section, are now considered.

The usual assumption in plate theory—namely, that stresses in planes normal to the plate may be neglected—is made here. Furthermore, it is assumed that the plate is free to stretch or contract in its middle surface, but is restrained against rotation at its edges, and that $\alpha$ and $E$ do not vary with temperature. Under these circumstances it is easily shown that the thermal stresses in the plate are given by

$$\sigma_y = \sigma_z = -[\alpha E \Delta T/(1-\nu)] \times \left\{ f(\xi) - \int_0^1 f(\xi)\,d\xi \right\} \quad (3)$$

For a linear temperature distribution, Eq. (3) becomes

$$\sigma_y = \sigma_z = -[\alpha E \Delta T/(1-\nu)][\xi - (1/2)] \quad (4)$$

giving a compressive stress $\alpha E \Delta T/2(1-\nu)$ at the heated surface and an equal tensile stress at the insulated surface.

Such a temperature distribution is not consistent with the boundary condition for heat flow at the insulated surface, and, as seen in the preceding section, the actual temperature distribution for the type of heating considered will be approximately parabolic in most cases, and the stress will be as shown in Fig. 4. It is, however, convenient to use the linear distribution for the purpose of computing a reference thermal stress to which a correction factor may then be applied for other temperature distributions. Thus, stress correction factors for compression and tension, respectively, are defined as follows:

$$K_c = 2\left\{1 - \int_0^1 f(\xi)\,d\xi\right\} \quad (5)$$

$$K_t = 2\int_0^1 f(\xi)\,d\xi = 2 - K_c \quad (6)$$

For a parabolic distribution of temperature [$f(\xi) = \xi^2$],

$$K_c = 4/3, \quad K_t = 2/3$$

When the temperature gradient at the heated surface is still more pronounced, $K_c$ will be larger, with 2 as its limiting value, while $K_t$ will reduce toward zero.

The transient temperature data obtained from the digital computation program have been used to obtain transient stress data. Fig. 5 shows the variation of $K_c$ and $K_t$ with time for a typical case. Because of this variation, the maximum stresses in the plate are not reached simultaneously with the maximum temperature differential.

In order to express the maximum stresses in terms of the maximum temperature differential, it is desirable to define modified stress correction factors as follows:

$$K_c' = [\Delta\phi/(\Delta\phi)_{max}]\,K_c \quad (7)$$

$$K_t' = [\Delta\phi/(\Delta\phi)_{max}]\,K_t \quad (8)$$

The maximum values of these modified factors, when multiplied by the maximum temperature differentials, will give the maximum stresses. Their variation with time is shown in Fig. 5. It is seen that the maximum compressive stress is reached somewhat earlier and the maximum tensile stress somewhat later than the maximum temperature differential. The maximum value of $K_c'$ is 1.55, and consequently considerably greater than the value (1.333) of $K_c$ for a parabolic temperature distribution. On the other hand, the maximum value of $K_t'$ is 0.64 and, consequently, only slightly less than the value (0.667) of $K_t$ for a parabolic distribution.

In general, for large values of the parameter $\lambda$ and $\tau_\theta = 0$, the maximum value of $K_c'$ tends to be substantially larger than the value of $K_c$ for a parabolic temperature distribution, while the maximum value of $K_t'$ tends to be slightly less than the value of $K_t$ for a parabolic temperature distribution. As $\lambda$ decreases,

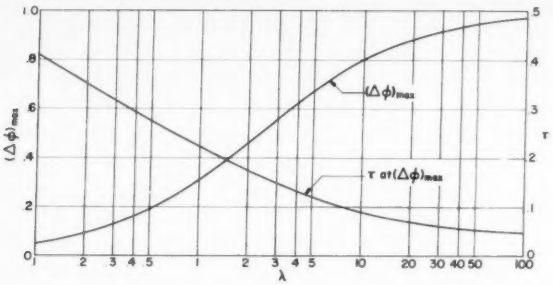


FIG. 1. Maximum temperature differential across the surfaces of a flat plate subjected to a sudden change in environment temperature.

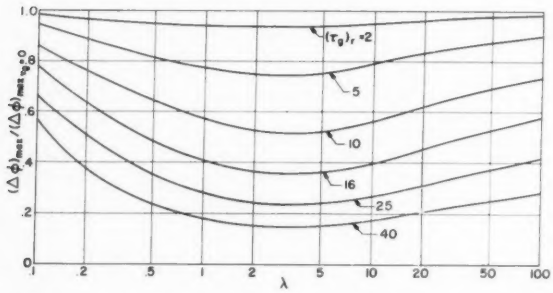


FIG. 3. Effect of gradient time on the maximum temperature differential across the surfaces of a flat plate.

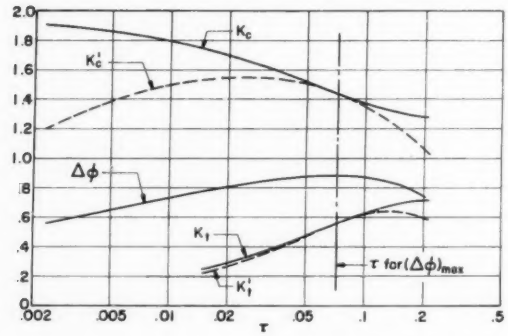


FIG. 5. Variation of stress correction factors with time during heating of a flat plate; $\lambda = 20$, $\tau_g = 0$.

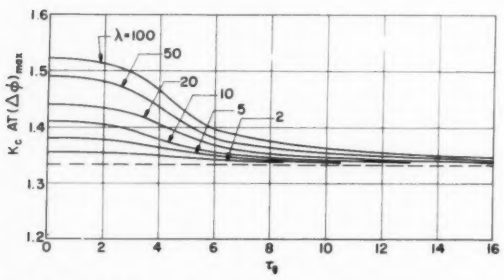


FIG. 7. Effect of gradient time on the stress correction factor at maximum temperature differential in a flat plate.

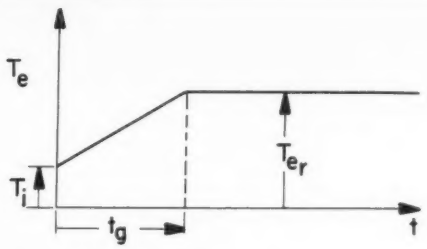


FIG. 2. Assumed variation of environment temperature with time.

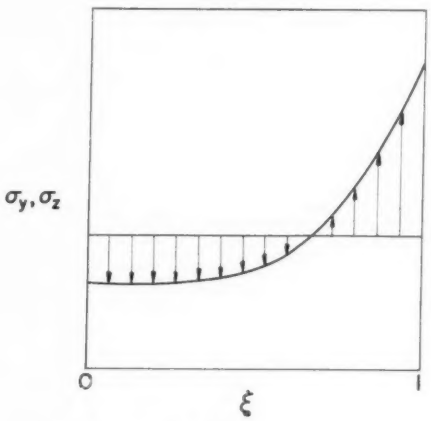


FIG. 4. Thermal stress distribution in a flat plate with edges restrained against bending.

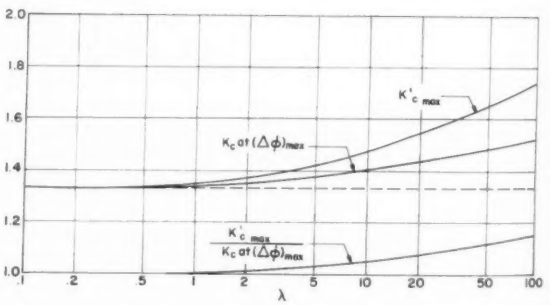


FIG. 6. Variation of stress correction factors with $\lambda$. Flat plate. $\tau_g = 0$.

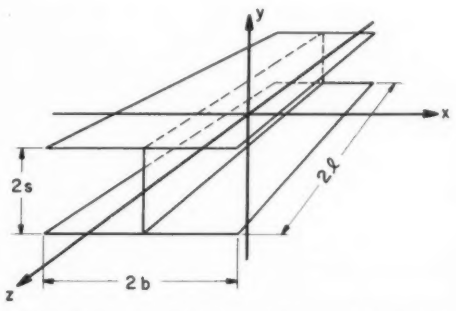


FIG. 8. Coordinate axes and dimensions of a wide-flanged I-beam.

the times at which $K_c'$ and $K_t'$ reach their peak values approach the time for $(\Delta\phi)_{max}$, and the peak values of these correction factors approach the corresponding values for a parabolic temperature distribution—namely, 1.333 and 0.667, respectively. These results are shown for compressive stress in Fig. 6, along with the variation of $K_c$ at $(\Delta\phi)_{max}$ with $\lambda$. In the case of tensile stress, the maximum value of $K_t$ is either equal to or slightly less than 0.667 throughout the range considered, and may thus be taken as 0.667 in any practical computation.

The effect of $\tau_g$ on the value of $K_c$ at $(\Delta\phi)_{max}$ is shown in Fig. 7. It is seen that $K_c$ at $(\Delta\phi)_{max}$ approaches the value 1.333 as $\tau_g$ increases. The effect of $\tau_g$ on the maximum value of $K_c'$ was not obtained. It is reasonable to expect, however, that this quantity will approach the value 1.333 as $\tau_g$ increases. The maximum value of $K_t'$ can be expected, in all cases, to remain close to the value 0.667.

## (4) Transient Temperature Distribution in a Wide-Flanged I-Beam

A simple model of a built-up type of wing structure is the I-beam with wide flanges. The present section is concerned with the transient temperature distribution associated with the heating of such a beam by convective heat transfer into the outer surfaces of the flanges.

The following assumptions are made.

(1) The environment temperature and convective heat transfer coefficient are uniform over the outer surfaces of the flanges, the latter being constant with time as well.

(2) The temperature in the beam is initially uniform.

(3) The flow of heat takes place entirely in directions parallel to planes representing cross sections of the beam. That is, the heat loss out of the ends of the beam may be neglected, so that the temperature distribution at any instant is the same in all cross sections of the beam.

(4) The flanges and web are sufficiently thin that temperature variation through their thickness may be neglected.

(5) The inner surfaces of the flanges and both surfaces of the web are insulated, so that heat transfer between parts of the beam takes place by conduction only.

(6) There is no heat transferred through the edges of the flanges.

(7) Variation of the thermal properties of the material with temperature may be neglected.

The problem thus reduces to one of one-dimensional heat flow in the flange and in the web.

A simplified treatment of this problem has been given by Hoff and Torda,[5] in which the heat loss from the flanges into the web is neglected in the determination of the transient temperature variation in the flanges, and this temperature variation is then applied as a boundary condition on the web. More refined analyses, based on assumptions which are the same as those made here, have been given by Pohle and Oliver,[6] Schuh,[8] and Parkes.[9] In the present work, the results of this previous work are extended considerably and information is provided on the effect of a finite period of build-up of the environment temperature.

The present analysis satisfies the transition conditions at the joints between the flanges and web exactly. The beam is assumed initially to be built-up, in the sense that the flanges and web are not integral but are connected by screws or pins or some similar arrangement, leaving a surface between the flange and web across which there may be effectively a temperature discontinuity. The solution for a beam with integral flange and web is then obtained as a special case.

The coordinates and dimensions of the beam cross section are shown in Fig. 8. The depth of the beam is measured between the middle surfaces of the flanges.

The partial differential equations in nondimensional form for the temperature in the flanges and web are, respectively,

$$\partial\phi_f/\partial\tau = (\partial^2\phi_f/\partial\xi^2) - \lambda(\phi_f - \phi_e) \tag{9}$$

$$\partial\phi_w/\partial\tau = \partial^2\phi_w/\partial\eta^2 \tag{10}$$

Taking symmetry into account, it is necessary to consider the flange only in the range $0 \leq \xi \leq b/s$, and the web only in the range $0 \leq \eta \leq 1$. The boundary and initial conditions may now be written

(1) at $\xi = b/s$, $\partial\phi_f/\partial\xi = 0$

(2) at $\eta = 0$, $\partial\phi_w/\partial\eta = 0$

(3) at $\xi = 0, \eta = 1$,
$$2\gamma(\partial\phi_f/\partial\xi) = \lambda_j(\phi_f - \phi_w) = \partial\phi_w/\partial\eta$$

(4) at $\tau = 0$, $\phi_f = \phi_w = 1$

As in the case of the plate, a finite difference numerical method was used in the solution of Eqs. (9) and (10).

A program of computations was carried out on the Whirlwind I computer for a variety of values of the parameters $\lambda$, $\gamma$, and $\tau_g$, the time history of the environment temperature being assumed to have the form shown in Fig. 2. The influence of the parameters $\lambda$ and $\gamma$ on the maximum temperature differential in the beam is shown in Fig. 9 for the case of $\tau_g = 0$. The width of the flange was taken to be twice the depth of the web in all cases. The web and flange were assumed to be integral.

The influence of the gradient time, $\tau_g$, is shown in Fig. 10 for the case of $\gamma = 1$. The results are expressed as a factor modifying the results obtained for the case of $\tau_g = 0$. The effect of $\tau_g$ is seen to be greatest at intermediate values of $\lambda$.

## (5) Thermal Stresses in a Wide-Flanged I-Beam of Infinite Length

The thermal stresses due to the transient temperature distribution in the I-beam described in the preceding section are now considered.

The beam is first assumed to be infinitely long. Since the temperature distribution is the same in all cross sections of the beam and is symmetrical about the $x$ and $y$ axes (see Fig. 8), it follows that cross sections must remain plane and parallel during heating of the beam.

The assumption of thinness of the flange and web and the fact that the temperature is uniform through their thickness results in a condition of plane stress in each.

As the beam is free to deform within any cross section, the only stresses present will be in the longitudinal direction, that is, $\sigma_x = \sigma_y = 0$. It is easily shown[6] that under these circumstances the longitudinal stress is given by

$$\sigma_{z_f}/\alpha E(\Delta T)_{max} = [1/(\Delta\phi)_{max}]\{\phi_f(\xi) - A\} \quad (11)$$

$$\sigma_{z_w}/\alpha E(\Delta T)_{max} = [1/(\Delta\phi)_{max}]\{\phi_w(\eta) - A\} \quad (12)$$

where

$$A = \frac{2\gamma\omega}{2\gamma\omega + 1}\int_0^1 \phi_f(\xi)d\xi + \frac{1}{2\gamma\omega + 1}\int_0^1 \phi_w(\eta)d\eta \quad (13)$$

It should be noted that $\xi$ is defined differently here than in the preceding section.

It is seen that

$$(\sigma_{z_w})_{\eta=0} - (\sigma_{z_f})_{\xi=0} = \alpha E(\Delta T)_{max} \quad (14)$$

The temperature data of the preceding section have been used to compute stress data for the wide-flanged I-beam. In addition to the parameters $\lambda$, $\gamma$, and $\tau_\theta$, the parameter $\omega$ is now significant. While the temperature distributions were computed for $\omega = 2$, it is in most cases sufficiently accurate to use these distributions for other flange widths, cutting the distribution curve off at the appropriate point for a narrower flange and extending it horizontally for a wider flange. This procedure introduces the greatest error at low values of $\lambda$, where the effect of heat loss to the web is felt far out on the flange.

Fig. 11 shows, for $\tau_\theta = 0$, how the stress range in the beam at the time of maximum temperature differential divides between maximum tensile stress and maximum compressive stress. The maximum tensile stress occurs at the middle of the web, while the maximum compressive stress occurs at the edge of the flange. The curves are identified in groups of constant ratio of flange to web cross-sectional areas, $A_f/A_w = 2\gamma\omega$.

The effect of gradient time on the maximum values of $\sigma_z/\alpha E(\Delta T)_{max}$ was found to be slight in all cases. In the extreme case of $\lambda = 100$, the maximum tensile stress is increased about 1.5 per cent and the maximum compressive stress is decreased about 8 per cent when the relative gradient time $(\tau_\theta)_r$ is increased from 0 to 8. In any practical application the stress may be determined by the use of Fig. 11 in conjunction with the temperature data of the preceding section.

### (6) Thermal Stresses in a Wide-Flanged I-Beam of Finite Length

The effect of free ends on the thermal stress distribution in the wide-flanged I-beam is now considered. The assumptions regarding temperature distribution remain unchanged. The coordinate axes of the beam are shown in Fig. 8. The origin is at the center of the beam.

The flanges and web are again assumed to be sufficiently thin that stresses normal to their surface may be neglected. Stresses in the plane of the flange and web are considered to be uniform through their thicknesses. Deflections of the flange and web normal to their respective planes are assumed not to occur. This precludes buckling of the flanges under compressive stress.

On the basis of these assumptions, the problem reduces to one of plane stress in the flange and web, with the satisfaction of boundary conditions at the joints connecting them and at their free edges.

The stress distribution may be found conveniently as the superposition of two component stress distributions. The first component stress distribution is that corresponding to the beam of infinite length. The second component stress distribution is that necessary to result in satisfaction of the boundary conditions on the ends of the beam, and is obtained by applying to the ends of the beam a longitudinal load distribution equal and opposite in sign to the stress distribution in a cross section of the infinite beam. Since this load distribution is self-equilibrating, its effect will, according to Saint-Venant's principle, be large only near the ends of the beam, and will diminish rapidly with increasing distance from the ends of the beam.

The second component stress distribution is now analyzed by the methods of the mathematical theory of elasticity for plane stress.

The boundary conditions are as follows:

(1) at $\xi = \pm 1$, $\sigma_{x_f} = \tau_{xz_f} = 0$

(2) at $\zeta = \pm 1$,
$\sigma_{z_f} = \sigma_{0_f}$, $\sigma_{z_w} = \sigma_{0_w}$, $\tau_{xz_f} = \tau_{yz_w} = 0$

(3) at $\xi = 0$, $\eta = \pm 1$, $\tau_{yz_w} = 2\gamma\tau_{xz_f}$

where $\sigma_{0_f}$ and $\sigma_{0_w}$ are the negative of the longitudinal stresses in the flange and web, respectively, of the beam of infinite length.

In an exact treatment of the problem, two additional conditions would have to be satisfied at the joint between flange and web. The first of these is the continuity condition that longitudinal strain in the flange and web should be equal at this joint. In terms of stress this condition may be written as follows:

(4) at $\xi = 0$, $\eta = \pm 1$, $\sigma_{z_w} = \sigma_{z_f} - \nu\sigma_{x_f}$

The second additional condition arises from the fact that the curve of displacement of an orginally straight line in the $x$-direction in the flange is discontinuous in slope at $x = 0$, due to the shear flow into the flange from

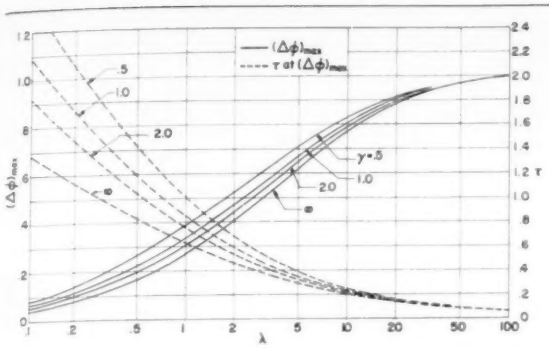


FIG. 9. Maximum temperature differential in a wide-flanged I-beam subjected to a sudden change in environment temperature.

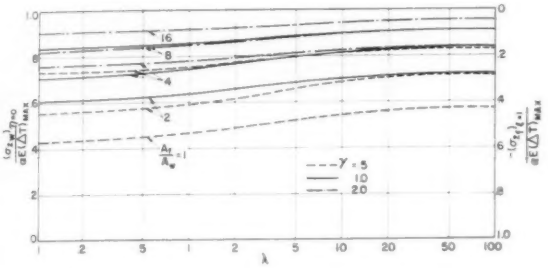


FIG. 11. Effect of λ on relative proportions of maximum tensile and compressive stresses in stress range of wide-flanged I-beam.

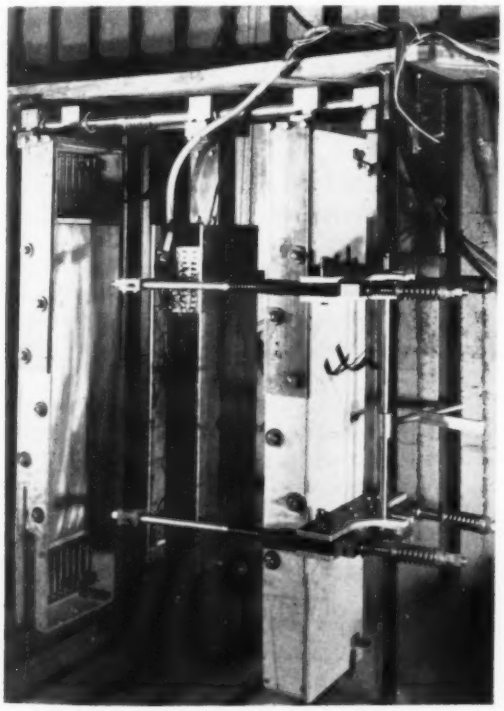

FIG. 12. Experimental setup for I-beam heating and therma stress measurements.

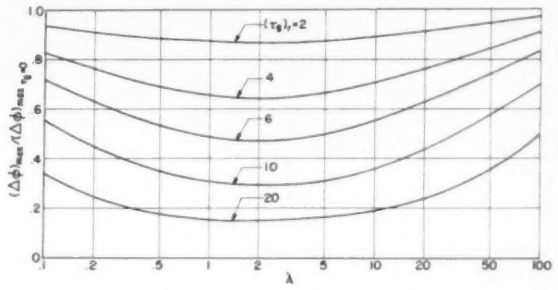


FIG. 10. Effect of gradient time on the maximum temperature differential in a wide-flanged I-beam.

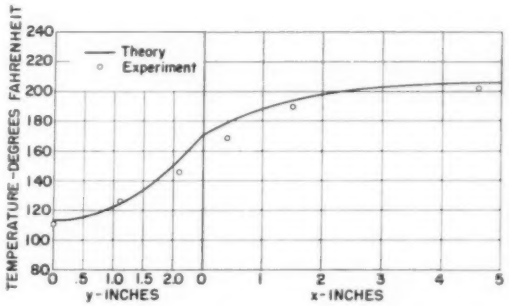


FIG. 13. Distribution of temperature in middle section of I-beam at time of maximum temperature differential; comparison between theory and experiment.

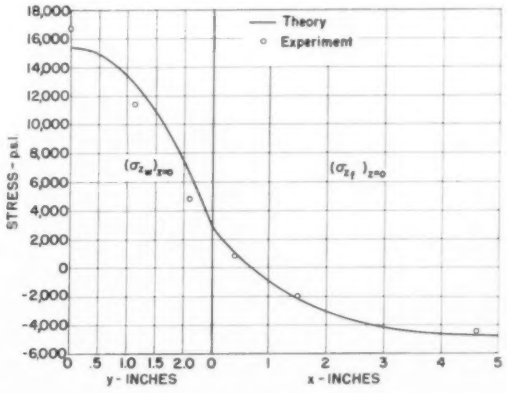


FIG. 14. Distribution of longitudinal stress in middle section of I-beam at time of maximum temperature differential; comparison between theory and experiment.

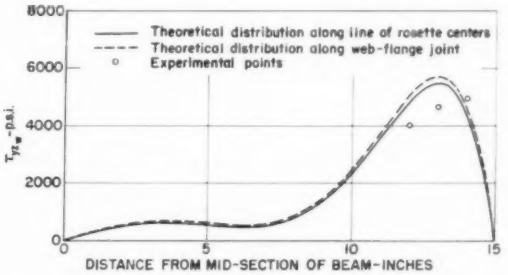
Theoretical distribution along line of rosette centers
Theoretical distribution along web-flange joint
Experimental points
$\tau_{yz_w}$ - p.s.i.
DISTANCE FROM MID-SECTION OF BEAM - INCHES

FIG. 15. Distribution of shear stress in web of I-beam at time of maximum temperature differential; comparison between theory and experiment.

the web. Because of this discontinuity, it is convenient to treat the two halves of the flange lying in the positive and negative directions of $x$ separately, and to define a condition establishing continuity between them. Such a condition is one requiring that, along a line in the flange coincident with the joint,

$$\partial^2 u_f/\partial z^2 = 0$$

where $u_f$ represents displacement in the $x$-direction. This condition may be expressed in terms of stresses as follows:

(5) At $\xi = 0$, $(\mu/\psi)(\partial \tau_{xz_f}/\partial \zeta) = \partial \sigma_{z_f}/\partial \xi$

An exact determination of the stress distribution is not feasible in the present case. This distribution may, however, be determined approximately by application of the principle of least work in conjunction with the Ritz procedure of representing the stress function for web and flange regions as a superposition of a finite number of assumed functions in initially unknown proportions.[12]

It was found, after considerable investigation, that assumed functions in the form of polynomial expressions would be most suitable for the satisfaction of boundary conditions and convenient in subsequent mathematical manipulations. In consequence, the following series expressions for the stress functions in the flange and web regions were chosen:

$$\phi_f = \phi_{0_f} + \sum_{m=0}^{p} \sum_{n=0}^{p} A_{mn}(\xi - 1)^2(\zeta^2 - 1)^2 \xi^m \zeta^{2n} \qquad (15)$$

where $$\phi_{0_f} = b^2 \int\int \sigma_{0_f} d\xi \, d\xi$$

$$\phi_w = \phi_{0_w} + \sum_{m=0}^{p} \sum_{n=0}^{p} B_{mn}(\eta^2 - 1)(\zeta^2 - 1)^2 \eta^{2m} \zeta^{2n} \qquad (16)$$

where $$\phi_{0_w} = s^2 \int\int \sigma_{0_w} d\eta \, d\eta$$

It should be noted that the expression for $\phi_f$, as written, applies only in the range of positive $\xi$. This is unavoidable for reasons discussed previously in connection with the development of boundary condition (5). Because of symmetry, the strain energy in the two halves of the flange will be equal, so that only one side need be considered in the energy minimization process.

Continuity between the two halves could be established on an exact basis by the application of boundary condition (5). It was found, however, that an exact satisfaction of boundary conditions (4) and (5) greatly increases the difficulty of obtaining a satisfactory solution with a reasonable number of assumed functions.

Even if boundary conditions (4) and (5) are not applied explicitly in the analysis, the energy minimization process will tend toward their satisfaction. This follows from the fact that minimization of the strain energy on an exact basis leads to the true stress distribution only if the forces applied at the boundaries of the various regions do not change during the variation process or if no net work is done by changes in these forces (see reference 12, p. 166). The first of these conditions is seen to be automatically satisfied at the free edges of the beam by each of the assumed stress functions individually. At the joint between flange and web the shear forces will be equal in magnitude and opposite in direction in each because of boundary condition (3). If changes in these shear forces are to do no net work, the displacements through which they act must be equal. Consequently, this provides for the satisfaction of boundary condition (4). The assumed functions provide for stresses $\sigma_z$ in the flange at its centerline ($\xi = 0$), and, consequently, changes in these stresses will do no work only if the displacement through which they act is zero. This, in turn, provides for the satisfaction of boundary condition (5).

On the basis of these considerations, the analysis was carried out with boundary conditions (4) and (5) eliminated from explicit consideration. Boundary conditions (1) and (2) are seen to be satisfied by the assumed stress functions. Satisfaction of boundary condition (3) leads to the following relations between the unknown coefficients $A_{mn}$ and $B_{mn}$:

$$(\gamma/\omega)(2A_{0n} - A_{1n}) = -\sum_{m=0}^{p} B_{mn} \quad (n = 0, 1, 2, \ldots p) \qquad (17)$$

Eq. (17) provides $p + 1$ relations which permit the expression of $p + 1$ of the unknowns as linear functions of the remaining unknowns in the total set of $2(p + 1)^2$ unknowns.

The strain energy in the beam may be expressed as follows (see reference 12, p. 167):

$$V = (4bl\,\delta_f/E) \int_0^1 \int_0^1 \{\sigma_{x_f}^2 + \sigma_{z_f}^2 - 2\nu\sigma_{x_f}\sigma_{z_f} + 2(1 + \nu)\tau_{xz_f}^2\} d\xi \, d\zeta + (2sl\delta_w/E) \int_0^1 \int_0^1 \{\sigma_{y_w}^2 + \sigma_{z_w}^2 - 2\nu\sigma_{y_w}\sigma_{z_w} + 2(1 + \nu)\tau_{yz_w}^2\} d\eta \, d\zeta \qquad (18)$$

With

$$\sigma_{x_f} = \partial^2\phi_f/\partial z^2, \quad \sigma_{z_f} = \partial^2\phi_f/\partial x^2, \quad \tau_{xz_f} = -(\partial^2\phi_f/\partial x \partial z)$$

and corresponding relations for the web region, Eqs. (15) and (16) may be introduced into Eq. (18) along with Eq. (17) to yield a quadratic form in the independent unknown coefficients plus a sum of linear terms in these unknowns.

The strain energy is then minimized by equating the partial derivative of the resulting expression with respect to each of the independent unknowns in turn to zero. This yields a set of $(p + 1)(2p + 1)$ simultaneous linear algebraic equations in these unknowns, which may be solved to yield the information needed in the determination of the stress distribution in the beam.

The preceding analysis was applied to the case, $\psi = 3$, $\omega = 2$, $\gamma = 1$. The loading corresponded to a condition of thermal stress resulting from transient heating as described in Section (4), with $\lambda = 2.42$, $\tau_g = 0$. These parametric values were chosen to correspond with those appropriate to the experiment described in

the following section. The temperature distribution was that corresponding to the maximum temperature differential between the edges of the flange and the middle of the web. The stress distribution for the case of an infinitely long beam was first determined by the method of Section (5). This stress distribution was then reversed in sign and applied as an external loading on the ends of the finite beam to determine the end effect. A total of eighteen terms in the two stress function expressions were employed; that is, $m = 0, 1, 2$, $n = 0, 1, 2$.

The distribution of normal stress in the middle cross section of the beam and the distribution of shear stress in the web-flange joint are shown in Figs. 14 and 15, respectively. The former distribution was found to be only slightly modified by the effect of the free ends. The waviness of the latter distribution in the central portion of the beam is probably not realistic, but is rather a consequence of the limitations of the approximate solution. It is believed, however, as a result of other computations performed, that the analysis provides a good indication of the magnitude of the maximum shear stress.

## (7) Experimental Investigation of the Transient Temperature Distribution and Thermal Stresses in a Wide-Flanged I-Beam

The theory of the preceding sections was checked experimentally by means of the apparatus shown in Fig. 12. The specimen used was built up of $^1/_4$ inch steel plate, with the web-flange joints brazed in order to provide an unimpeded path for heat flow from the flanges into the web. The remaining dimensions of the beam were $2l = 30$ in., $2b = 10$ in., $2s = 5$ in.

Convective heat transfer into the outer faces of the flanges was simulated by the transfer of heat from large heated aluminum blocks across a small air gap (0.007 in.). The proper gap was maintained by means of suitably located spacers, and the effect of flange warpage was eliminated by providing an initial concave outward curvature and exerting enough pressure across the two heating blocks to bend the flanges back to a flat shape.

The blocks were preheated by means of electric resistance rods, and then brought up to the specimen and clamped tightly. The surface temperature of the blocks was intended to simulate an environment temperature varying as a step function, and the thermal conductance of the air gap was intended to simulate the convective heat transfer coefficient. As heat flowed across the gap, there was found to be a drop in the surface temperature of the block, thus violating the assumption of a step function variation of environment temperature. However, there was simultaneously an increase in the conductivity of the air in the gap due to a rise in its temperature, and the two effects were found to be largely compensating. The value of the parameter $\lambda$ was estimated to be 2.42.

Temperature was measured at selected stations on the inner faces of the flanges and on the web surfaces by means of electric resistance gages and stress was measured at similar locations by temperature-compensating wire resistance strain gages. Both temperature and stress were recorded continuously by means of oscillograph equipment.

The temperature and longitudinal stress distributions in the middle cross section at the time of maximum temperature differential are shown in Figs. 13 and 14, respectively.

Shear stress was measured by means of strain rosettes at locations on the surface of the web near one end of the beam and close to the web-flange joint. The experimental values obtained at the time of maximum temperature differential are shown in Fig. 15 along with the corresponding theoretical distribution as obtained from the analysis of Section (6). The experimental results indicate that the peak value of shear stress occurs closer to the end of the beam than is indicated by the approximate theoretical result, and is slightly lower in value.

The results in general indicate good agreement between theory and experiment, and encourage confidence in the theoretical method.

### References


[1] Johnson, H. A., and Rubesin, M. W., *Aerodynamic Heating and Convective Heat Transfer—Summary of Literature Survey*, Trans. ASME, Vol. 71, No. 5, pp. 447–456, July, 1949.

[2] Jakob, M., *Heat Transfer*, Vol. I; John Wiley & Sons, Inc., New York, 1949.

[3] Austin, J. B., *The Flow of Heat in Metals*, U.S. Steel Corporation, Research Labs. (Kearney, N.J.), Series of Lectures Presented to ASM 23rd National Metal Congress and Exposition, Philadelphia, October 20–25, 1941.

[4] Carslaw, H. S., and Jaeger, J. C., *Conduction of Heat in Solids;* Oxford, 1947.

[5] Hoff, N. J., *Structural Problems of Future Aircraft*, Proceedings of the Third Anglo-American Aeronautical Conference, Brighton, England, September, 1951.

[6] Pohle, F. V., and Oliver, H., *Temperature Distribution and Thermal Stresses in a Model of a Supersonic Wing*, Journal of the Aeronautical Sciences, Vol. 21, No. 1, pp. 8–16, January, 1954.

[7] Schuh, H., *On the Calculation of Temperature Distribution and Thermal Stresses in Parts of Aircraft Structures at Supersonic Speeds*, Readers' Forum, Journal of the Aeronautical Sciences, Vol. 21, No. 8, pp. 575, 576, August, 1954.

[8] Schuh, H., *Transient Temperature Distributions and Thermal Stresses in a Skin-Shear Web Configuration at High-Speed Flight for a Wide Range of Parameters*, Journal of the Aeronautical Sciences, Vol. 22, No. 12, pp. 829–836, 866, December, 1955.

[9] Parkes, E. W., *Transient Thermal Stresses in Wings*, Aircraft Engineering, Vol. XXV, No. 298, p. 373, December, 1953.

[10] Kaye, J., and Yeh, V. C. M., *Design Charts for Transient Temperature Distribution Resulting from Aerodynamic Heating at Supersonic Speeds*, Journal of the Aeronautical Sciences, Vol. 22, No. 11, pp. 755–762, 786, November, 1955.

[11] Heldenfels, R. R., and Roberts, W. M., *Experimental and Theoretical Determination of Thermal Stresses in a Flat Plate*, NACA TN 2769, 1952.

[12] Timoshenko, S., and Goodier, J. N., *Theory of Elasticity*, Second Edition; McGraw-Hill Book Co., Inc., New York, 1951.

[13] Isakson, G., *A Study of Thermal Stresses in Aircraft Structures Due to Aerodynamic Heating*, Doctoral Thesis, Massachusetts Institute of Technology, June, 1953.

# The Effect of Amplitude on the Torsional Vibrations of Solid Wings Subjected to Aerodynamic Heating†

JOSEF SINGER*

*Polytechnic Institute of Brooklyn*

SUMMARY

The torsional vibrations of a long thin solid wing subjected to aerodynamic heating are analyzed by the Rayleigh-Ritz method. The effect of the change in thermal stresses due to finite amplitudes is included. To simplify the solution of the resulting nonlinear equations, a single-term deflection function is assumed, and the assumption is justified. An explicit expression is obtained for the relative frequency for any given temperature distribution and initial amplitude of vibration. A typical example is worked out to indicate the significance of the alleviating effect of the initial amplitude.

The assumption of harmonic vibrations used in the Rayleigh-Ritz approach is examined by a more accurate analysis yielding elliptic time functions and is shown to be satisfactory for practical purposes.

## SYMBOLS

$A_{pq}$ = coefficient of amplitude function
$A_{mn}$ = coefficient of main term
$a$ = semispan of wing, in.
$b$ = semichord of wing, in.
$C$ = effective polar moment of the cross section, in.$^4$
$D$ = bending stiffness = $Eh^3/12(1-\nu^2)$, lb. in.
$E$ = Young's modulus, psi
$F$ = time function
$G$ = shear modulus, psi
$g$ = gravitational constant, in. per sec.$^2$
$h$ = thickness of wing, in.
$H$ = second moment of area about vertical axis of symmetry, in.$^4$
$I$ = second moment of the fictitious edge force $h\sigma_x/R$, in.$^4$
$K$ = constant defined by Eq. (9), in.$^6$
$k$ = twist per unit length, rad. per in.
$m$ = number of nodal lines parallel to $x$ axis
$n$ = number of nodal lines parallel to $y$ axis
$R$ = coefficient of thermal stress = $\alpha E T_1$, psi
$T$ = temperature, °F.
$T_1$ = temperature parameter
$V$ = potential energy, lb. in.
$w$ = deflection, in.
$\alpha$ = coefficient of thermal expansion, in. per in. − °F.
$\gamma$ = specific weight, lbs. per in.$^3$
$\lambda$ = parameter defined by Eq. (17)
$\mu$ = parameter defined by Eq. (18)
$\nu$ = Poisson's ratio
$\omega$ = circular frequency of vibration, rad. per sec.
$\omega_0$ = circular frequency of vibration when $T_1 = 0$, rad. per sec.

Received January 18, 1957. Revised and received April 2, 1957.

† Excerpt from a thesis submitted to the Polytechnic Institute of Brooklyn in partial fulfillment of the requirements for the degree of Doctor of Aeronautical Engineering. The work was carried out under Contract AF 33(616)-3214 sponsored by the Aeronautical Research Laboratory of the Wright Air Development Center of the U.S. Air Force.

*Research Fellow.

The author would like to express his gratitude to his thesis adviser Dr. N. J. Hoff for his helpful advice and criticism.

## DISCUSSION

THE RAYLEIGH-RITZ METHOD is often used to obtain an approximate solution to the problem of the vibration of a rectangular plate, all edges of which are free. In this method, the maximum potential energy is equated to the maximum kinetic energy for harmonic vibrations, yielding an expression for the angular frequency in terms of the amplitude $w(x, y)$. The amplitude function $w$ is taken as a series

$$\sum_{p=0}^{\infty} \sum_{q=0}^{\infty} A_{pq} \vartheta_p(x) \varphi_q(y)$$

and the coefficients $A_{pq}$ are adjusted to minimize the expression for the angular frequency.

The method can also be used for torsional vibrations of a thin solid wing subjected to aerodynamic heating. The resulting thermal stresses reduce the torsional rigidity and, hence, the frequency of vibration.[1–4] However, since the thermal stresses change with amplitude,[5] the amplitude of vibration affects the frequency—i.e., the larger the amplitude the less the reduction in frequency due to the thermal stresses. This alleviating effect is noticeable even for small vibrations.

For simplicity, a long wing is considered for which the local stress effects at the tips can be disregarded and the thermal stresses can be approximated by those of a wing of infinite aspect ratio. Hence, as in reference 1, the thermal stresses are $\sigma_x = R\,f\,(y)$ and $\sigma_y = \tau_{xy} = 0$ when the wing is in the neutral position (see Fig. 1).

As the wing twists, displacements $w$ perpendicular to the plane of the wing give rise to a strain

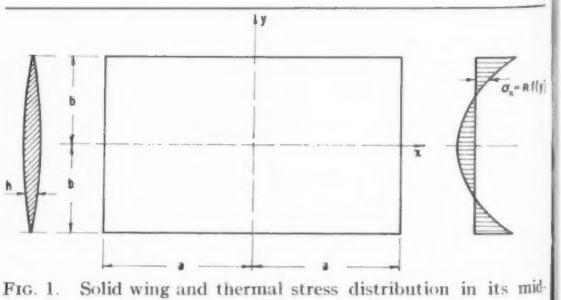


FIG. 1. Solid wing and thermal stress distribution in its midsection.

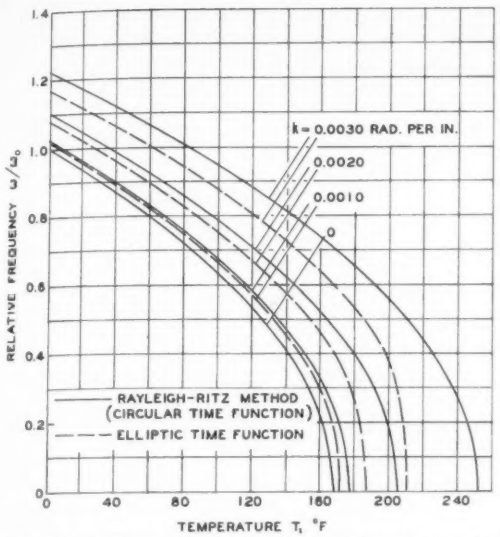


FIG. 2. Relative frequencies for circular time function (Rayleigh-Ritz method) and elliptic time function.

$$(1/2)(\partial w/\partial x)^2 - \left(1\Big/\int_{-b}^{b} h\,dy\right)\int_{-b}^{b}(h/2)(\partial w/\partial x)^2 dy \quad (1)$$

for a long wing with no force or moment resultants applied to its ends. The effective thermal stress is, therefore,

$$\sigma_x = R f(y) - (E/2) \times \left[(\partial w/\partial x)^2 - \left(1\Big/\int_{-b}^{b} h\,dy\right)\int_{-b}^{b} h(\partial w/\partial x)^2 dy\right] \quad (2)$$

compressive stress being considered positive.[5]

The maximum potential energy becomes

$$V = (1/2)\int_{-b}^{b}\int_{-a}^{a}\{D(\nabla^2 w)^2 - 2(1-\nu)[(\partial^2 w/\partial x^2)\times(\partial^2 w/\partial y^2) - (\partial^2 w/\partial x\partial y)^2]\}dxdy - (1/2)\int_{-b}^{b}\int_{-a}^{a} h \times \left\{R f(y)(\partial w/\partial x)^2 - (1/2)(E/2)\left[(\partial w/\partial x)^2 - \left(1\Big/\int_{-b}^{b} h\,dy\right)\int_{-b}^{b} h(\partial w/\partial x)^2 dy\right](\partial w/\partial x)^2\right\}dxdy \quad (3)$$

Note that the potential energy of the change in thermal stress, the second term in the second integral of Eq. (3), is multiplied by an additional factor (1/2). This factor appears since the change in thermal stress varies from zero to its value at the amplitude $w$ while $R f(y)$ remains constant.

The circular frequency is then

$$\omega^2 = 2V\Big/\left[(\gamma/g)\int_{-b}^{b}\int_{-a}^{a} h\,w^2 dxdy\right] \quad (4)$$

If the assumed amplitude function has more than one term, a set of nonlinear simultaneous equations are obtained after minimization. The solution of these equations may present considerable difficulties.

However, Pavlik[6] found, while investigating the vibrations of rectangular plates of constant thickness with all edges free by the Rayleigh-Ritz method, that the coefficients of all terms of the amplitude function other than the main term are small and can be neglected for approximate frequency calculations. The main term is $A_{mn}\vartheta_m(x)\varphi_n(y)$, where $m$ and $n$ are the number of nodal lines parallel to the $x$ and $y$ axes for the mode of vibration considered.

This, and other similar results (some also verified experimentally—e.g., reference 7) led to Warburton's approximate frequency formula for rectangular plates of constant thickness with various types of boundary conditions,[8] which is based on a single-term amplitude function and has been shown to be in good agreement with more exact calculations.

For the first torsional mode, $m = 1$ and $n = 1$, the single-term deflection function (or main term of the series) is

$$w = kxy \quad (5)$$

where $k$ is the angle of twist per unit length.

Pavlik and Warburton have justified this form of deflection function only for rectangular plates of constant thickness without any axial loads. For the case of self-equilibrating axial stresses of the type resulting from aerodynamic heating the author has compared the frequencies calculated for the single-term deflection function of Eq. (5) with those calculated for a three-term deflection function

$$w = A_{11}xy + A_{31}x^3y + A_{13}xy^3 \quad (6)$$

He found errors of the order of 5 per cent near the critical temperatures where the axial stresses are largest. Errors of the same magnitude are found for plates of parabolic chordwise thickness variation.

These results of small deflection analysis justify the assumption that, for the purpose of investigating the effect of amplitude on the vibrations, Eq. (5) represents a first approximation also for a thin wing of chordwise varying thickness subjected to thermal stresses given by Eq. (2).

With this assumption, Eq. (4) becomes

$$\omega^2 = [GC - RI + (E/2)K k^2]/[\gamma a^2 H/3g] \quad (7)$$

where $GC$ is the torsional rigidity and

$$I = \int_{-b}^{b} h\,y^2 f(y)dy \quad (8)$$

$$K = \int_{-b}^{b} h\left[y^4 - y^2\left(1\Big/\int_{-b}^{b} h\,dy\right)\int_{-b}^{b} h\,y^2\,dy\right]dy \quad (9)$$

$$H = \int_{-b}^{b} hy^2 dy \quad (10)$$

Hence, the frequency depends on $k$, the twist per unit length. Since the amplitude of vibration depends on the initial amplitude, the frequency can be estimated for any initial $k$ from Eq. (7) if damping is neglected. The relative frequency, the ratio of the frequency to that for no temperature variation, is given by

$$(\omega/\omega_0)^2 = 1 - [RI - (E/2)K k^2]/GC \qquad (11)$$

Fig. 2 presents numerical values of this ratio computed for a wing of constant thickness $h = 1/4$ in. (flat plate) when the chord $2b$ is 20 in. The temperature distribution is given by $T = T_0 + T_1(y/b)^6$; the material constants are $E = 29 \times 10^6$ psi, $\alpha = 7.5 \times 10^{-6}$°F.$^{-1}$, and Poisson's ratio $\nu = 0.3$. The effect of the initial amplitude on the relative frequency is significant even for small amplitudes—e.g., for $k = 0.0020$ (corresponding to a maximum tip rotation of 4.1° for a wing of span 80 in.), the relative frequency is 0.471 at the critical temperature instead of zero as given by the small deflection analysis.

In the Rayleigh-Ritz approach used above the vibrations were assumed to be harmonic. Actually, the time functions become elliptic functions when the changes in thermal stresses are taken into account. This can be shown by assuming, as before, that Eq. (5) represents the deflection for the first torsional mode of vibration. Hence, for a wing constrained by the above assumption to vibrate in this mode, the displacement at any time is

$$w = k\,x\,y\,F(t) \qquad (12)$$

where $F$ is the time function associated with the mode $kxy$. Substitution of Eq. (12) into Eq. (3) gives the potential energy*

$$V = GC\,ak^2F^2 - RI\,ak^2F^2 + (E/4)ak^4KF^4 \qquad (13)$$

and the kinetic energy

$$T = (\gamma/2g)\int_{-b}^{b}\int_{-a}^{a} h\,w^2 dx dy = \gamma a^3 k^2 H \dot{F}^2/3g \qquad (14)$$

where $I$, $K$, and $H$ are given by Eqs. (8)–(10).

Lagrange's equation becomes

$$(d/dt)(\partial T/\partial \dot{F}) + \partial V/\partial F = 0 \qquad (15)$$

since $F$ can be considered the generalized coordinate. If the operations indicated are carried out, one obtains

$$\ddot{F} + \lambda F + \mu F^3 = 0 \qquad (16)$$

where

$$\lambda = (GC - RI)/(\gamma a^2 H/3g) \qquad (17)$$

$$\mu = [(E/2)K k^2]/(\gamma a^2 H/3g) \qquad (18)$$

* $V$ in Eq. (3) is the maximum potential energy only when $w$ is the maximum displacement—i.e., the amplitude—as in the Rayleigh method.

Eq. (16) is the same nonlinear ordinary differential equation as the one obtained by Burgreen[9] for the free vibrations of a pin-ended column with constant distance between pin ends. The initial conditions

$$w(x, y, 0) = kxy \quad \text{and} \quad \dot{w}(x,y,0) = 0 \qquad (19)$$

and the boundary conditions

$$F(0) = 1 \quad \text{and} \quad \dot{F}(0) = 0 \qquad (20)$$

are also the same. Burgreen's solutions for $F$ in terms of Jacobi cosine and delta cosine elliptic functions hold therefore for the present problems also, the form of the solution depending on the value of $\lambda/\mu$.

However, it can be shown that, except for nearly vanishing frequencies, the shape of the time function is fairly close to that of the circular cosine function and that the relative frequencies obtained by the Rayleigh-Ritz method differ only slightly from those obtained by the more accurate analysis unless $k$ becomes large.

For the example considered, this can be seen from Fig. 2 where the more accurate relative frequencies are also plotted for comparison. In view of the approximate nature of the physical assumptions, the Rayleigh-Ritz method appears to be sufficiently accurate for the present purpose.

## References


[1] Hoff, N. J., *Approximate Analysis of the Reduction in Torsional Rigidity and of the Torsional Buckling of Solid Wings Under Thermal Stresses*, Readers' Forum, Journal of the Aeronautical Sciences, Vol. 23, No. 6, pp. 603, 604, June, 1956.

[2] Budiansky, Bernard, and Mayers, J., *Influence of Aerodynamic Heating on the Effective Torsional Stiffness of Thin Wings*, Journal of the Aeronautical Sciences, Vol. 23, No. 12, pp. 1,081–1,093, 1,108, December, 1956.

[3] Duberg, John E., *Aircraft Structures Research At Elevated Temperatures*, AGARD Report 3, September, 1955.

[4] Vosteen, Louis F., and Fuller, Kenneth E., *Behavior of a Cantilever Plate Under Rapid-Heating Conditions*, NACA RM L55E20c, July, 1955.

[5] Singer, Josef, and Hoff, N. J., *Effect of the Change in Thermal Stresses Due to Large Deflections on the Torsional Rigidity of Wings*, Readers' Forum, Journal of the Aeronautical Sciences, Vol. 24, No. 4, pp. 310, 311, April, 1957.

[6] Pavlik, B., *Biegungsschwingungen rechteckiger Platten*, Annalen der Physik, Vol. 27, p. 532, Leibzig, 1936.

[7] Waller, Mary D., *Vibrations of Free Rectangular Plates*, Proc. Phys. Society, Vol. 62B, p. 277, 1949.

[8] Warburton, G. B., *The Vibration of Rectangular Plates*, Proc. Institution of Mechanical Engineers, Vol. 168, p. 371, 1954.

[9] Burgreen, David, *Free Vibrations of a Pin-Ended Column With Constant Distance Between Pin Ends*, J. Appl. Mech., Vol. 18, No. 2, p. 135, June, 1951.

# Readers' Forum

*BRIEF REPORTS of investigations in the aeronautical sciences and discussions of papers published in the JOURNAL are presented in this special department. Entries must be restricted to a maximum of 1,300 words or the equivalent of one JOURNAL page including formulas and illustrations. Publication is completed as soon as possible after receipt of the material. The Editorial Committee does not hold itself responsible for the opinions expressed by the correspondents.*

## Contents


Laminar Boundary Layer With Nonadiabatic Rotational Free Stream ..... FRANKLIN D. HAINS 623

Extension of "An Aeroelastic Parameter for Estimation of the Effects of Flexibility on the Lateral Stability and Control of Aircraft" ..... WILLIAM P. RODDEN 624

A Short Static-Pressure Probe Independent of Mach Number ..... ERIK L. MOLLO-CHRISTENSEN, MARTEN T. LANDAHL, AND JOHN R. MARTUCCELLI 625

On the Exact Solution of Compressible Couette Flow With Mass Addition and Binary Diffusion ..... NATHAN NESS 626

A Note on the Sonic-Wedge Leading-Edge Approximation in Hypersonic Flow ..... M. H. BERTRAM AND D. L. BARADELL 627

Rule of Thumb Equation for Predicting Lifting-Surface-Theory Values of Lift ..... JOHN DEYOUNG 629

Vortex-Ring Cascade and Turbulence Transition ..... VIVIAN O'BRIEN 629

Shock-Wave Curvature for Hypersonic Axisymmetric Flow ..... R. SEDNEY 630

Prediction of Turbulent Boundary-Layer Separation ..... JAMES M. ROBERTSON 631

Erratum—"Inversion of the Prandtl-Meyer Relation for Specific Heat Ratios of 5/3 and 5/4" ..... RONALD F. PROBSTEIN 632


## Laminar Boundary Layer With Nonadiabatic Rotational Free Stream


Franklin D. Hains

*Aerodynamicist, Research Division, Bell Aircraft Corporation, Buffalo*



April 5, 1957


THE POSSIBLE IMPORTANCE of vorticity behind curved shocks in high-speed flow was discussed by Ferri.[1] Recently, shear flow over a flat plate was considered by several authors.[2–5]

This note describes a method of solving the flow over a flat plate with heat conduction and transfer of momentum into the boundary layer from the external flow. It is assumed that the normal gradients of temperature and velocity in the free stream are small so that a boundary layer exists adjacent to the plate where these gradients are large.

The boundary-layer equations in the Crocco form are

$$\tau^2\tau_{uu} - \rho\mu u\tau_x = 0 \tag{1}$$

$$(1 - P)\tau\tau_u h_u + (h_{uu} + P)\tau^2 - \rho\mu u P h_x = 0 \tag{2}$$

A constant Prandtl Number and linear viscosity-temperature relation are assumed.

The boundary conditions are

$$\left.\begin{aligned} u = 0: &\quad \tau_u = 0, \quad h = h_w \\ u = u_\infty: &\quad h = h_\infty, \quad \tau = \mu_\infty\alpha, \quad h_u = \beta/\alpha \end{aligned}\right\} \tag{3}$$

where $\alpha$ and $\beta$ are the slopes of the velocity and enthalpy profiles at the outer edge of the boundary layer.

A solution to Eqs. (1) and (2) is assumed of the form

$$\tau = \sum_{i=1}^{\infty} f_i(u)\Phi^{i-1}/\sqrt{2x} \tag{4}$$

$$h = \sum_{i=1}^{\infty} l_i(u)\Psi^{i-1} + \sum_{n=0}^{k}\sum_{i=1}^{\infty} a_n x^n g_{in}(u)\Psi^{i-1} \tag{5}$$

### Contributors Please Note

Readers' Forum items must be confined to the equivalent of one page in the *Journal*. Contributions that exceed this limit will be returned to the authors for condensation and rewrite. To avoid inconvenience and delay, please adhere to the following specifications:

(1) Five, double-spaced, typewritten, manuscript pages ($8\frac{1}{2}$ by 11 in.), including wide margins, formulas, and headings equal one printed page.

(2) For every illustration, deduct at least one-half or as much as one manuscript page, depending on the size of the illustration.

where

$$\left.\begin{aligned}\Phi &= (\alpha^2\nu_\infty x/u_\infty{}^3)^{1/2}\\ \Psi &= \beta u_\infty \Phi/\alpha h_\infty\end{aligned}\right\} \tag{6}$$

It is assumed that $\Phi$ and $\Psi$ are small so that higher order terms in $\Phi$ can be neglected. The constants $a_n$ in Eq. (5) are determined by the wall-temperature distribution which is represented by a polynomial in $\sqrt{x}$.

Substitution of Eqs. (4) and (5) into Eqs. (1) and (2) and equating to zero coefficients of like powers of $\Phi$ yields

$$f_1 f_1'' + \rho\mu u = 0 \tag{7}$$

$$f_1 f_2'' + 2f_1'' f_2 = 0 \tag{8}$$

$$(1 - P)f_1' t_1' + f_1(t_1'' + P) = 0 \tag{9}$$

$$(1 - P)[f_1 f_1' t_2'\theta + (f_1 f_2)' t_1'] + 2f_1 f_2 t_1'' + f_1^2 t_2''\theta + 2f_1 f_2 P - \rho\mu u P\theta t_2 = 0 \tag{10}$$

$$(1 - P)f_1 f_1' g_{1n}' + f_1^2 g_{1n}'' - 2\rho\mu u P n g_{1n} = 0 \tag{11}$$

$$(1 - P)[(f_1 f_2)' f_{1n}' + f_1 f_1' g_{2n}'\theta] + f_1^2 g_{2n}''\theta + 2f_1 f_2 g_{1n}'' - (2n + 1)\rho\mu u\theta P g_{2n} = 0 \tag{12}$$

where

$$\theta = \beta u_\infty/\alpha h_\infty \tag{13}$$

The boundary conditions are:

$$\left.\begin{aligned}u = 0: \quad & f_1' = f_2' = 0\\ u = u_\infty: \quad & f_1 = t_2 = t_2' = g_{1n} = g_{2n} = g_{1n}' = g_{2n}' = 0\\ & t_1 = h_\infty, \quad t_1' = \beta/\alpha, \quad f_2 = \sqrt{2\mu_\infty \rho_\infty u_\infty{}^3}\end{aligned}\right\} \tag{14}$$

The unknown quantities in Eqs. (4) and (5) are obtained from the solutions of Eqs. (7) through (12). Eq. (7) can be transformed into the Blasius equation, while the remaining equations are linear. Irregular singular points occur in the remaining equations at $u = u_\infty$ so that asymptotic solutions are assumed near the outer edge of the boundary layer.

At the present time, numerical solutions are being obtained for problems of aerodynamic interest.

### References


[1] Ferri, A., and Libby, P. A., *Note on an Interaction between the Boundary Layer and the Inviscid Flow*, Readers' Forum, Journal of the Aeronautical Sciences, Vol. 21, No. 2, p. 130, February, 1954.

[2] Li, T. Y., *Simple Shear Flow Past a Flat Plate in an Incompressible Fluid of Small Viscosity*, Readers' Forum, Journal of the Aeronautical Sciences, Vol. 22, No. 9, pp. 651, 652, September, 1955.

[3] Li, T. Y., *Simple Shear Flow Past a Flat Plate in a Compressible Viscous Fluid*, Readers' Forum, Journal of the Aeronautical Sciences, Vol. 22, No. 10, pp. 724, 725, October, 1955.

[4] Yen, K. T., *Approximate Solutions of the Incompressible Laminar Boundary-Layer Equations for a Flat Plate in a Shear Flow*, Readers' Forum, Journal of the Aeronautical Sciences, Vol. 22, No. 10, pp. 728–730, October, 1955.

[5] Sakurai, Takeo, *The Shear Flow Along a Flat Plate With Uniform Suction*, Readers' Forum, Journal of the Aeronautical Sciences, Vol. 24, No. 1, p. 79, January, 1957.


## Extension of "An Aeroelastic Parameter for Estimation of the Effects of Flexibility on the Lateral Stability and Control of Aircraft"[1]


William P. Rodden*
*Senior Flutter Engineer, North American Aviation, Inc., Los Angeles*

April 1, 1957

A SIMILARITY PARAMETER is suggested in reference 1 to simplify the modification of rigid stability derivatives in a flexible stability and control analysis. It is the purpose of this note to make a refinement of one of the approximations and to present some experimental correlation of the method.


* The author wishes to thank the Douglas Aircraft Company, Inc., in particular Kermit E. Van Every and Ervin R. Heald of the El Segundo Division, for permission to use the data of Fig. 1.


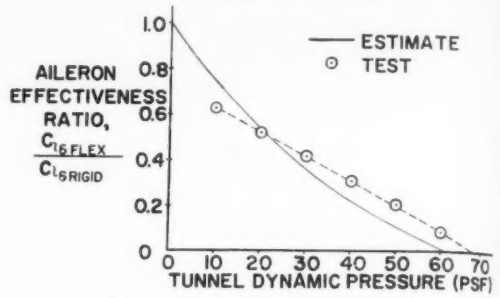


FIG. 1. Experimental correlation.

We write, as before, the twist at the wing tip, $\epsilon$, as an infinite series of twists:

$$\epsilon = \epsilon_1 + \epsilon_2 + \epsilon_3 + \ldots \tag{1}$$

where $\epsilon_1$ is the twist resulting from the initially applied loads

$$\epsilon_1 = \epsilon_\delta \delta_a + \epsilon_p(pb/2V) + \epsilon_{\dot{p}}\dot{p} \tag{2}$$

and each successive $\epsilon_{i+1}$ is caused by the loads resulting from $\epsilon_i$. Now we expand each $\epsilon_i$ in terms of its components from the initial value

$$\epsilon_i = \epsilon_{i\delta} + \epsilon_{ip} + \epsilon_{i\dot{p}} \tag{3}$$

so that the series (1) becomes

$$\epsilon = (\epsilon_1 + \epsilon_2 + \epsilon_3 + \ldots)_\delta + (\epsilon_1 + \epsilon_2 + \epsilon_3 + \ldots)_p + (\epsilon_1 + \epsilon_2 + \epsilon_3 + \ldots)_{\dot{p}} \tag{4}$$

Then, assuming a constant ratio of successive twists,

$$\left.\begin{aligned}\epsilon_{(i+1)_\delta}/\epsilon_{i_\delta} &= -k_\delta\\ \epsilon_{(i+1)_p}/\epsilon_{i_p} &= -k_p\\ \epsilon_{(i+1)_{\dot{p}}}/\epsilon_{i_{\dot{p}}} &= -k_p\end{aligned}\right\} \tag{5}$$

The series for $\epsilon$ becomes a geometric series whose sum is

$$\epsilon = [(\epsilon_\delta \delta_a)/(1 + k_\delta)] + [\epsilon_p(pb/2V)/(1 + k_p)] + [\epsilon_{\dot{p}}\dot{p}/(1 + k_{\dot{p}})] \tag{6}$$

provided that $k > -1$. As pointed out recently by Gaugh and Slap,[2] the condition $k \leq -1$ corresponds to antisymmetrical wing divergence. They also have shown in their earlier work[3] that Eq. (6) is still valid for $k \geq 1$ by extending the radius of convergence of the geometric series. The modified rolling-moment equation now becomes

$$C'_{l_{\dot{p}}}\dot{p} = C'_{l_\delta}\delta_a + C'_{l_p}(pb/2V) \tag{7}$$

where

$$C'_{l_{\dot{p}}} = C_{l_{\dot{p}}} - [1/(1 + k_{\dot{p}})](C_{l_\epsilon})_{\dot{p}}\epsilon_n \tag{8}$$

$$C'_{l_\delta} = C_{l_\delta} + [1/(1 + k_\delta)](C_{l_\epsilon})_\delta \epsilon_\delta \tag{9}$$

$$C'_{l_p} = C_{l_p} + [1/(1 + k_p)](C_{l_\epsilon})_p \epsilon_p \tag{10}$$

in the notation of reference 1, and the various $k$ become

$$k_{\dot{p}} = -(\partial\epsilon/\partial L_\epsilon)_{\dot{p}}(C_{l_\epsilon})_{\dot{p}} qSb \tag{11}$$

$$k_\delta = -(\partial\epsilon/\partial L_\epsilon)_\delta (C_{l_\epsilon})_\delta qSb \tag{12}$$

$$k_p = -(\partial\epsilon/\partial L_\epsilon)_p (C_{l_\epsilon})_p qSb \tag{13}$$

where the twist aeroelastic parameters, $\partial\epsilon/\partial L_\epsilon$, now are found from each twisting mode. This extension from the development given previously eliminates the restriction of computing $k$ from a mean twisting mode and increases the generality of the method.

It has been suggested[2] that a better example for correlation would be one with a lower stiffness level than that previously presented. In Fig. 1 an experimental correlation of aileron effectiveness is shown based on some low-speed wind-tunnel tests of a flexible swept-wing model by the El Segundo Division of Douglas Aircraft Company, Inc. The estimate was based on the aileron effectiveness obtained from rigid models and the structural

characteristics of the full-scale airplane. The agreement in aileron reversal speed is again seen to be satisfactory.

### References


[1] Rodden, William P., *An Aeroelastic Parameter for Estimation of the Effects of Flexibility on the Lateral Stability and Control of Aircraft*, Journal of the Aeronautical Sciences, Vol. 23, No. 7, pp. 660–662, July, 1956.

[2] Gaugh, William J., and Slap, Joseph K., *On Aeroelastic Solutions*, Readers' Forum, Vol. 24, No. 1, pp. 76, 77, January, 1957.

[3] Gaugh, William J., and Slap, Joseph K., *Determination of Elastic Wing Aerodynamic Characteristics*, Journal of the Aeronautical Sciences, Vol. 19, No. 3, pp. 173–182, March, 1952.


## A Short Static-Pressure Probe Independent of Mach Number†


Erik L. Mollo-Christensen,* Marten T. Landahl,** and John R. Martuccelli***

*Massachusetts Institute of Technology, Cambridge, Mass.*


April 8, 1957


### Summary

Using slender-body theory it is possible to shape the nose of a pressure probe such that it measures stream static pressure independent of Mach Number. The pressure holes can be placed so far forward that the effects of the boundary layer are insignificant. Such a probe has been built and tested, and the probe performs as predicted by theory.


### Introduction

In reference 2, Korkegi presents means of static-pressure error compensation by suitably shaping the boundary in the vicinity of the pressure orifice.

This note provides some additional experimental results which are thought to be of general interest. The results given are in terms of per cent static-pressure error rather than in terms of pressure error in per cent of impact pressure as in reference 2.

### Discussion

Consider the problem of shaping the nose of a body of revolution such that, at a distance $x$ from the nose, the pressure equals static pressure in the stream far ahead of the body for any free-stream Mach Number.

Slender-body theory gives the following formula for the pressure coefficient:[1]

$$C_p(x) = [p(x) - p_\infty]/(1/2)\rho U^2 = (1/\pi)\left\{S''(0)\ln x + S''(x)\ln\left[2/R(x)\sqrt{M^2-1}\right] + \int_0^x \ln(x-t)\,dS''(t)\right\} - [R'(x)]^2 \quad (1)$$

where

| | | |
|---|---|---|
| $p$ | = | local pressure |
| $p_\infty$ | = | pressure in the undisturbed stream |
| $(1/2)\rho U^2$ | = | dynamic pressure |
| $x$ | = | distance from the nose of the body |
| $R(x)$ | = | body radius at $x$ |
| $S(x)$ | = | $\pi[R(x)]^2$, body cross-sectional area |
| $M$ | = | Mach Number of the undisturbed stream |

Inspecting Eq. (1), it can be seen that if, at $x_1$, where the pressure holes will be drilled in the probe, $S''(x_1) = 0$, $C_p(x_1)$ becomes independent of $M$. Therefore, impose the condition

$$S''(x_1) = 0 \quad (2)$$

† This work was in part supported by the U.S. Navy, Bureau of Aeronautics, under Contract No. NOas 56-556-d.


* Assistant Professor.

** Research Engineer, Flygtekniska Forsoksanstalten, Ulvsunda, Sweden.

*** Research Engineer, Aeroelastic and Structures Research Laboratory.


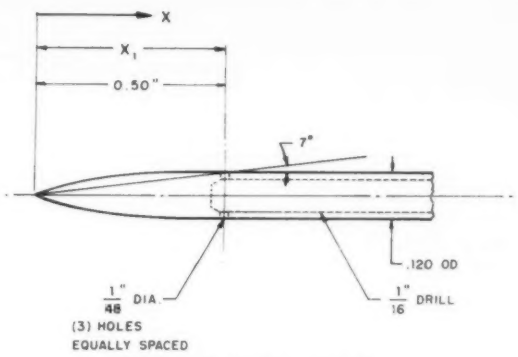


FIG. 1. Static-pressure probe.

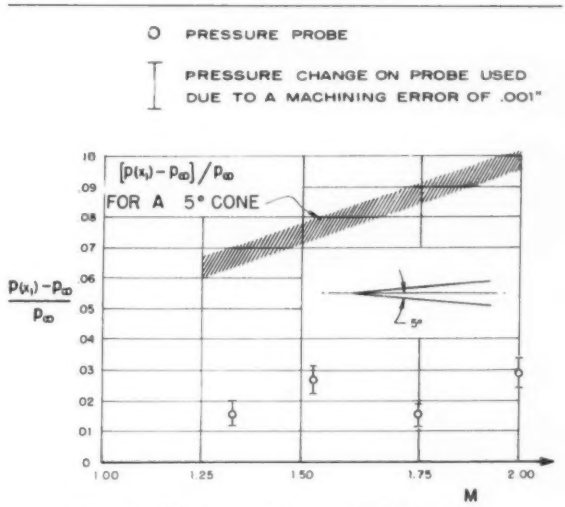


FIG. 2. $[p(x_1) - p_\infty]/p_\infty$ vs. Mach Number.

The other terms in $C_p(x_1)$ can be made to vanish by a suitable choice of $S(x)$ over the interval $0 < x < x_1$.

For example, $S(x)$ can be expressed as a fourth-degree polynomial in $x$ and the coefficients chosen so as to make $C_p(x_1) = 0$. The result is

$$R(x) = (\delta/\sqrt{\pi})\sqrt{x^2 - 0.968x^3 + 0.317x^4} \quad (3)$$

where $\delta$ is a thickness parameter which can be chosen freely.

The resulting probe contour is shown in Fig. 1.

If now three holes are drilled at $x_1$, 120° apart around the circumference of the probe, slender-body theory shows that the mean pressure in the three holes when the probe is at an angle of yaw is the same as when the probe is aligned with the stream.

A probe of the dimensions shown in Fig. 1 was built and tested in the M.I.T. 2 × 2½-in. supersonic tunnel. The probe pressure was compared with the pressures measured in static orifices in a flat plate in the wind-tunnel wall. The wall boundary layer was removed at the leading edge of the plate. Visual inspection of the flow using schlieren apparatus provided information of probe-wall interference, and such interference does not occur in the results shown in Fig. 2, where $[p(x_1) - p_\infty]/p_\infty$ is plotted versus Mach Number.

The results show an almost constant error over the Mach Number range. This error is probably due to imperfections in the probe contour which is difficult to machine accurately for the size used. With some further refinement, such a probe may prove a useful tool in wind-tunnel work and in flight testing

### References

[1] Liepmann, H. W., and Roshko, A., *Elements of Gasdynamics;* New York, 1956.

[2] Korkegi, R. H., *An Aerodynamic Means of Static Pressure Compensation for Transonic and Supersonic Aircraft,* Aeronautical Engineering Review, Vol. 16, No. 4, pp. 64–68, April, 1957.


# On the Exact Solution of Compressible Couette Flow With Mass Addition and Binary Diffusion


Nathan Ness*

*Research Scientist, Missile and Ordnance Systems Department, General Electric Company, Philadelphia, Pa.*


April 8, 1957


### Summary

An exact, closed-form solution of the system of equations describing compressible Couette flow with mass injection and binary diffusion is obtained. Velocity, enthalpy, and diffusion profiles are expressed in terms of simple integrals for the completely general variation of all fluid properties.


### Symbols

$a$ = $u_e^2/(e^{\eta\Delta_v} - 1)^2$
$C_i$ = mass fraction of species $i$; $C_i = \rho_i/\rho$, $i = 1, 2$
$c_p$ = specific heat at constant pressure of mixture
$c_{p_i}$ = specific heat at constant pressure of species $i$; $i = 1, 2$
$\mathfrak{D}_{12}$ = binary mixture diffusion coefficient
$F$ = definite integral defined by Eq. (23)
$h_1$ = static enthalpy, $h_1 = \int_0^T c_{p_1}\,dT$
$K_1$ = constant of integration, defined by Eq. (21)
$k$ = coefficient of thermal conductivity of mixture
$Pr_1$ = Prandtl Number, $Pr_1 = \mu c_{p_1}/k$
$Sc$ = Schmidt Number, $Sc = \mu/\rho\mathfrak{D}_{12}$
$T$ = absolute temperature of mixture
$u$ = velocity of mixture parallel to wall
$v$ = velocity of mixture normal to wall
$v_2$ = absolute velocity of species 2 normal to wall
$y$ = coordinate normal to wall
$\beta$ = $\int_0^\eta Pr_1 d\eta = \rho v \int_0^y Pr_1(dy/\mu)$
$\Delta$ = film thickness
$\eta$ = $\rho v \int_0^y (dy/\mu)$
$\mu$ = coefficient of viscosity of mixture
$\rho$ = density of mixture
$\varphi$ = $\rho v \int_0^y Sc(dy/\mu)$

*Subscripts*

1 = injected fluid
2 = mainstream fluid
$D$ = diffusion film layer
$e$ = outer edge of film layer
$T$ = temperature film layer
$v$ = velocity film layer
$w$ = at the stationary wall

### Discussion

Illingworth[1] obtained an exact solution for the system of equations describing compressible Couette flow; Liepmann and Bleviss[2] extended the analysis to include the effects of dissociation and ionization. The present analysis considers compressible Couette flow with mass addition and diffusion. An exact solution results with completely general variation of all fluid properties.

The system of equations describing a binary mixture, compressible Couette flow is[3]

Continuity: $$(d/dy)(\rho v) = 0 \tag{1}$$

Momentum: $$\rho v(du/dy) = (d/dy)[\mu(du/dy)] \tag{2}$$

Diffusion: $$\rho v(dC_1/dy) = (d/dy)[\rho\mathfrak{D}_{12}(dC_1/dy)] \tag{3}$$

Energy: $$\rho v c_p(dT/dy) = (d/dy)[k(dT/dy)] + \mu(du/dy)^2 + \rho\mathfrak{D}_{12}(c_{p_1} - c_{p_2})(dT/dy)\cdot(dC_1/dy) \tag{4}$$

The boundary conditions are:

$$y = 0: \quad u = 0, \quad \rho v = (\rho v)_w, \quad T = T_w, \quad C_1 = C_{1_w} \tag{5}$$

$$y = \Delta: \quad u = u_e, \quad T = T_e, \quad C_1 = C_{1_e} \tag{6}$$

The solution of Eq. (1) is $\rho v$ = constant. The boundary condition $y = 0$, $\rho v = (\rho v)_w$ indicates that the flux of the mixture normal to the main flow is constant throughout the film layer. Consequently, to satisfy continuity across the flow, it is necessary that the moving wall be considered porous with a suction flux equal to $(\rho v)_w$.

Defining a new variable $\eta$ by

$$\eta = \rho v \int_0^y (dy/\mu) \tag{7}$$

enables the momentum equation to be written in the form

$$du/d\eta = (d/d\eta)(du/d\eta) \tag{8}$$

whose solution, satisfying the boundary conditions $y = 0$: $u = 0$, $y = \Delta_v$, $u = u_e$ is

$$u/u_e = (e^\eta - 1)/(e^{\eta\Delta_v} - 1) \tag{9}$$

In a similar manner, the introduction of a new variable $\varphi$ defined by

$$\varphi = \rho v \int_0^y Sc(dy/\mu) \tag{10}$$

enables the diffusion equation to be expressed as

$$dC_1/d\varphi = (d/d\varphi)(dC_1/d\varphi)$$

whose solution, satisfying the boundary conditions $y = 0$, $C_1 = C_{1_w}$, $y = \Delta_D$, $C_1 = C_{1_e}$ is

$$(C_{1_w} - C_1)/(C_{1_w} - C_{1_e}) = (e^\varphi - 1)/(e^{\varphi\Delta_D} - 1) \tag{11}$$

The absolute velocity of the air is equal to its diffusion velocity plus the observed macroscopic velocity of the mixture. The diffusion velocity is given by Fick's law; hence, for the $y$-direction, the above statement gives[4]

$$v_2 = -(\mathfrak{D}_{12}/C_2)\cdot(dC_2/dy) + v \tag{12}$$

or, since $C_2 = \rho_2/\rho$, the resultant flux of the air normal to the walls is

$$\rho_2 v_2 = -\rho\mathfrak{D}_{12}(dC_2/dy) + \rho_2 v \tag{13}$$

The term $\rho\mathfrak{D}_{12}(dC_2/dy)$ represents the mass flow of air by diffusion across any control surface parallel to the walls; the term $\rho_2 v$ represents the convective mass flow of air across the same control surface. To ensure continuity it is necessary at any point in the flow that

$$\rho_2 v = \rho\mathfrak{D}_{12}(dC_2/dy) \tag{14}$$

Therefore, from a comparison of Eqs. (13) and (14), it follows that $\rho_2 v_2 = 0$ everywhere in the flow. The implication of this result may be more readily seen by considering the relationship that exists between the flux of the mixture and the flux of the respective components:

$$\rho v = \rho_1 v_1 + \rho_2 v_2$$

As $\rho_2 v_2 = 0$, it follows that the flux of the mixture across the flow is equal to the flux of the coolant in the same direction. Using the condition that the sum of the mass fractions of the coolant and the air is unity—i.e., $C_1 + C_2 = 1$—enables Eq. (14) to be written

$$\rho v = -[\rho\mathfrak{D}_{12}/(1 - C_1)]\cdot(dC_1/dy) \tag{15}$$

Eq. (15) is substituted into Eq. (4) to give

$$\rho v c_p(dT/dy) = (d/dy)[k(dT/dy)] + \mu(du/dy)^2 - \rho v(1 - C_1)(c_{p_1} - c_{p_2})(dT/dy)$$

* The author would like to express his gratitude to Drs. Eckert, Hartnett, and coworkers at the University of Minnesota for helpful discussions during the preparation of this note.

Since $c_p = C_1 c_{p_1} + C_2 c_{p_2}$, the energy equation simplifies to

$$\rho v c_{p_1}(dT/dy) = (d/dy)\,[k(dT/dy)] + \mu(du/dy)^2 \qquad (16)$$

Defining the Prandtl Number by $Pr_1 = \mu c_{p_1}/k$ and the enthalpy by

$$h_1 = \int_0^T c_{p_1}\,dT, \quad dh_1 = c_{p_1}\,dT \qquad (17)$$

enables the last equation to be written in the form

$$dh_1/d\eta = (d/d\eta)\,(dh_1/Pr_1 d\eta) + (du/d\eta)^2 \qquad (18)$$

Using Eq. (9), Eq. (18) becomes

$$dh_1/d\eta = (d/d\eta)\,(dh_1/Pr_1 d\eta) + a\,e^{2\eta} \qquad (19)$$

where

$$a = u_e^2/(e^{\eta\Delta\tau} - 1)^2 \qquad (20)$$

Introducing a new variable $\beta$ defined by

$$\beta = \rho v \int_0^y Pr_1(dy/\mu) \qquad (21)$$

gives Eq. (19) in the form

$$dh_1/d\beta = (d/d\beta)\,(dh_1/d\beta) + (a/Pr_1)\cdot e^{2\int_0^\beta (d\beta/Pr_1)}$$

Integrating once results in

$$(dh_1/d\beta) - h_1 = -(a/2)e^{2\int_0^\beta (d\beta/Pr_1)} - K_1$$

where $K_1$ is the constant of integration. This is a first-order, linear differential equation whose solution satisfying the boundary condition

$$y = 0, \quad T = T_w \qquad \therefore\ h_1 = h_{1_w} = \int_0^{T_w} c_{p_1} dT$$

is

$$h_1 - h_{1_w} = e^{\beta} \times \left[ -(a/2) \int_0^\beta e^{\int_0^\beta [(2/Pr_1) - 1]\,d\beta}\, d\beta + K_1(e^{-\beta} - 1) \right] \qquad (22)$$

The constant $K_1$ is evaluated from the boundary condition

$$y = \Delta_T, \quad T = T_e \qquad \therefore\ h_1 = h_{1_e} = \int_0^{T_e} c_{p_1} dT$$

and is

$$K_1 = \frac{(h_{1_e} - h_{1_w})e^{-\beta\Delta\tau} + (a/2)\int_0^{\beta\Delta\tau} e^{\int_0^\beta [(2/Pr_1) - 1]\,d\beta}\, d\beta}{e^{-\beta\Delta\tau} - 1} \qquad (23)$$

The enthalpy distribution through the film layer becomes

$$(h_1 - h_{1_w})/(h_{1_e} - h_{1_w}) = [(e^\beta - 1)/(e^{\beta\Delta\tau} - 1)] + [a/2(h_{1_e} - h_{1_w})]\,\{[(e^\beta - 1)/(e^{\beta\Delta\tau} - 1)]e^{\beta\Delta\tau}\cdot F_{\Delta\tau} - e^\beta \cdot F\} \qquad (24)$$

where

$$F = \int_0^\beta e^{\int_0^\beta [(2/Pr_1) - 1]\,d\beta}\, d\beta \qquad (25)$$

## References


[1] Illingworth, C. R., *Some Solutions of the Equations of Flow of a Viscous Compressible Fluid*, Proc. Cambridge Philos. Society, Vol. 46, p. 469, 1950.

[2] Liepmann, H. W., and Bleviss, Z. O., *The Effects of Dissociation and Ionization on Compressible Couette Flow*, Douglas Aircraft Report No. SM-19831, May, 1956.

[3] Hall, N. A., *Flow Equations for Multicomponent Fluid Systems, Part I, General Equations, Part II, Binary Boundary Layer Equations*, Univ. of Minn., Mech. Engrg. Dept., Tech. Report No. 2, August, 1955.

[4] Eckert, E. R. G., *Introduction to the Transfer of Heat and Mass*, 1st Ed., p. 236; McGraw-Hill Book Company, Inc., New York, 1950.


# A Note on the Sonic-Wedge Leading-Edge Approximation in Hypersonic Flow


M. H. Bertram and D. L. Baradell

*Langley Aeronautical Laboratory, NACA, Langley Field, Va.*


April 18, 1957

Investigations in the Princeton helium tunnel[1] have cast doubt on the validity of approximatiag the blunt leading edge on a flat plate by a sonic wedge as proposed by the senior author.[2] Recent theoretical papers[3, 4] using a blast-wave analogy have indicated the parameters governing the effect of a blunt leading edge on the pressures and shock shape over a flat plate, at least in the vicinity of the leading edge. The parameter governing the bluntness effect on surface pressure is $K \equiv M_\infty{}^3 kt/x$, where $k$ is the nose-drag coefficient and $t$ is the nose thickness. The corresponding shock shape is a function only of $\sqrt{k(x/t)}$. The present authors have re-examined the sonic-wedge leading-edge concept in the light of these parameters.

Shown in Fig. 1a are the surface pressures given by rotational characteristics theory,[5] $\gamma = 7/5$. Also in this Figure is the characteristics solution for a cylindrical leading-edge flat plate.[1] By Newtonian theory for a cylinder, $k = (2/3)C_{P\,max}$. To hypersonic approximation, the equation given by Lees[6] may be

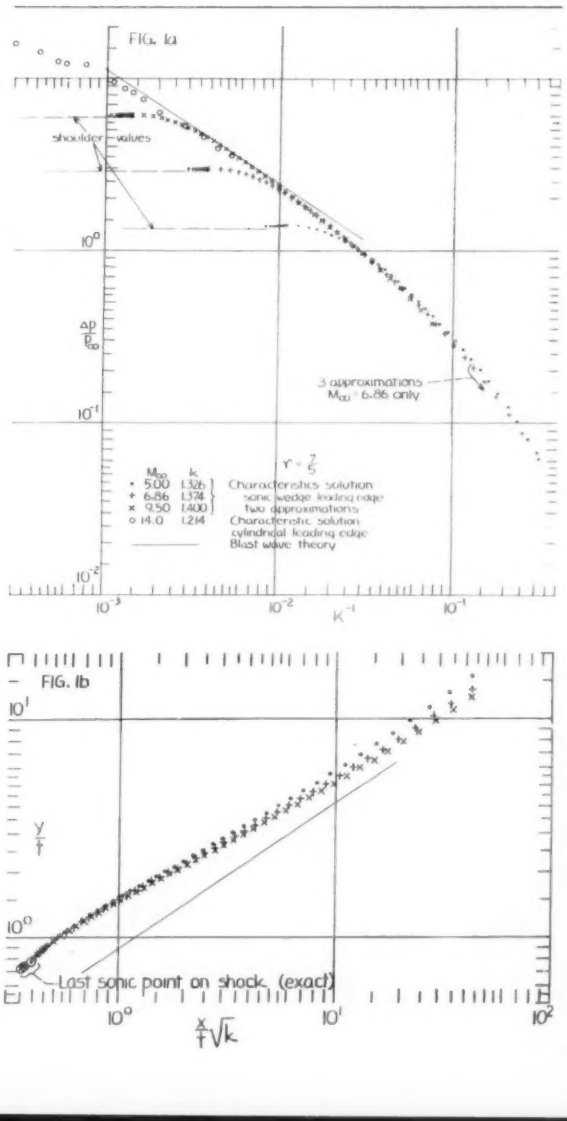

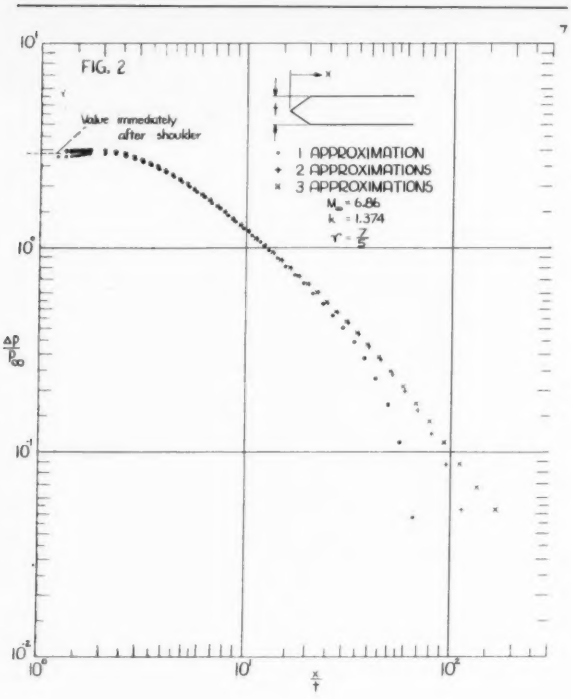


used:

$$C_{P\,max} = [(\gamma + 3)/(\gamma + 1)]\,\{1 - 2/[(\gamma + 3)M_\infty{}^2]\} \quad (1)$$

The sonic-wedge drag coefficient is, by hypersonic approximation,

$$k = (2/\gamma)\,\{1 - (\gamma + 3)/[(\gamma + 1)M_\infty{}^2]\} \quad (2)$$

The correlation of the various characteristics solutions in Fig. 1a is good except very near the shoulder, and there is reasonable agreement of the correlated portions of the characteristic solutions with the blast-wave analogy to a value of $K$ of about 100. There is a compression above the pressure obtained immediately after the expansion around the shoulder at each Mach Number shown. A quick first approximation to the pressure distribution for the sonic-wedge leading-edge flat plate (and probably the cylindrical leading-edge plate as well) is obtained by taking the pressure as constant at the shoulder value to the intersection with the correlation curve or the line for the blast-wave analogy, which is used thereafter in its range of validity. A good fit to the correlation curve is obtained by adding an empirical constant to the first-order blast-wave theory result, thus obtaining an equation analogous in form to Sakurai's second-order three-dimensional result.[5] In this case using the Cheng-Pallone equation,[4] $\gamma = 7/5$, $\Delta p/p_\infty = 0.112\ K^{2/3} - 0.2$, where 0.20 may also be used for $\gamma = 5/3$.

For the sonic-wedge leading-edge flat plate the shoulder pressure is, to hypersonic approximation,

$$\Delta p/p_\infty = (\gamma M_\infty{}^2/2)a[1 - (b/M_\infty{}^2)]$$

where, for $\gamma = 7/5$, $a = 0.10082$ and $b = 6.5$, while, for $\gamma = 5/3$, $a = 0.092819$ and $b = 5.85$.

Shock shapes corresponding to these pressure distributions are shown in Fig. 1b. Characteristics theory indicates the shock shape to be independent of $M_\infty$ only in the immediate vicinity of the leading edge to $M_\infty$ as low as 5 but with an increasing extent of correlation as $M_\infty$ increases.

The question arises as to how many approximations to each characteristic point are required for an arbitrary accuracy. For $M_\infty = 6.86$, the characteristics solution was carried out to one, two, and three approximations for $\gamma = 7/5$. As for all these solutions, the expansion at the shoulder was carried out in 1/10° steps for the first degree and 1° steps thereafter. The extent of $x/t$ over which the solution is valid is clearly shown in Fig. 2. In this case to get good accuracy for the pressure distribution for $x/t > 100$, at least a three-approximation solution is required. There is little difference between the one-, two-, and three-approximation solutions for the corresponding shock shapes. In Fig. 1a the solutions were all cut off at what was considered their limit of good accuracy, and the solution for $M_\infty = 6.86$ was extended by the three-approximation result.

Given in Fig. 3 is a comparison with the Princeton helium tunnel data.[1] Only data considered to have a small to negligible viscous effect are included, and $k = C_{P\,max}$ [Eq. (2)] is assumed. Considering the Mach Number gradient in the Princeton helium nozzle, the agreement between characteristic theory (two approximations) and experiment in Fig. 3a is considered good. This characteristic solution does not agree with the one presented in Fig. 7 of reference 1. The differences between these two solutions are large and are apparently attributable to an oversimplification of the flow model in reference 1. Of interest is the fact that the characteristic solution presented in Fig. 3a correlates (excepting the region near the shoulder) with the air results in Fig. 1a if corrected to $\gamma = 7/5$ according to the constants given in reference 4.

The experimental points for shock shape, shown in Fig. 3b, lie between blast-wave and characteristic theory. However, the effect of the nozzle pressure gradient is unknown, and in the region very near the nose the differing nose shapes and shock origins must be important as regards shock shape.

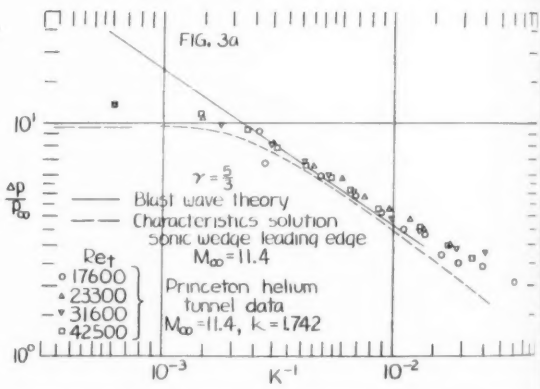


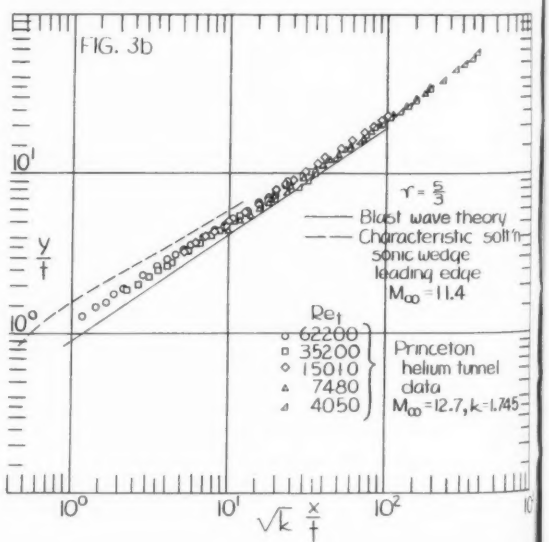

### References

[1] Hammitt, A. G., and Bogdonoff, S. M., *Hypersonic Studies of the Leading Edge Effect on the Flow over a Flat Plate*, Jet Propulsion, Vol. 26, No. 4, pp. 241–246, April, 1956.

[2] Bertram, Mitchel H., *Viscous and Leading-Edge Thickness Effects on the Pressures on the Surface of a Flat Plate in Hypersonic Flow*, Readers' Forum, Journal of the Aeronautical Sciences, Vol. 21, No. 6, pp. 430, 431, June, 1954.

[3] Lees, Lester, and Kubota, Toshi, *Inviscid Hypersonic Flow Over Blunt-Nosed Slender Bodies*, Journal of the Aeronautical Sciences, Vol. 24, No. 3, pp. 195–202, March, 1957.

[4] Cheng, H. K., and Pallone, A. J., *Inviscid Leading-Edge Effect in Hypersonic Flow*, Readers' Forum, Journal of the Aeronautical Sciences, Vol. 23, No. 7, pp. 700–702, July, 1956.

[5] Ferri, Antonio, *Application of the Method of Characteristics to Supersonic Rotational Flow*, NACA Rep. 841, 1956.

[6] Lees, Lester, "Hypersonic Flow," *Fifth International Aeronautical Conference*, (Proceedings), IAS-RAeS, Los Angeles, June 20–23, 1955; Institute of the Aeronautical Sciences, New York, 1956.


## Rule of Thumb Equation for Predicting Lifting-Surface-Theory Values of Lift


John DeYoung

*ITA, Centro Técnico de Aeronáutica, São José dos Campos, Estado Sao Paulo, Brazil*


April 18, 1957

FOR WINGS a function is derived that is almost as easy to remember as the familiar equation of lifting-line theory. Compare (elliptic loading; $C_{L\alpha}$, lift-curve slope; $A$, aspect ratio)

$$C_{L\alpha_{\text{line}}} = 2\pi A/(A + 2)$$

$$C_{L\alpha_{\text{surface}}} = 2\pi A/\{A + 2[(A + 4)/(A + 2)]\}$$

The line exceeds the surface values by 44.4, 25.0, 8.4, and 2.9 per cent for $A = 1$, 2, 5, and 10, respectively. The section lift-curve slope, $a_0$, and the compressibility, $\beta = \sqrt{1 - M^2}$, are taken into account by substituting $(\beta C_{L\alpha}/\kappa)$ for $C_{L\alpha}$ and $(\beta A/\kappa)$ for $A$, where $\kappa = \beta a_0(\beta)/2\pi$.

A lifting-surface method is derived which is used to set the limits as $A \to 0$ and $A \to \infty$ for a simple but well-fitted function. Assume an elliptic load distribution on a straight-load line and an elliptic chord distribution; and, at the three-quarter chord line, assume that the induced angle of attack is constant spanwise and equal to the wing angle of attack. With these conditions, a solution of the integral equation of loading is simply a single solution at the wing plane of symmetry. The results are

$$C_{L\alpha} = 2\pi A/[(A/k)E + 2] \qquad (1)$$

where $E$ is the complete elliptic integral of the second kind with modulus $k$, and

$$k = (\pi A/4)/\sqrt{1 + (\pi A/4)^2}$$

In the limit conditions as $A \to \infty$, $E/k \to 1$; and, as $A \to 0$, $E/k \to 2/A$; thus this $C_{L\alpha}$ approaches the line-theory value for large $A$ and slender-wing theory for small $A$.

For determining a fitted function, assume

$$C_{L\alpha} = 2\pi A/[A + 2f(A)]$$

Taking the first and second derivatives of $C_{L\alpha}$ with respect to $A$ and likewise of Eq. (1), then, letting $A \to 0$, the derivatives of Eq. (1) require that (a) $f(0) = 2$, and (b) $f'(0) = -(1/2)$. Also, similarly, for $A \to \infty$, then (c) $f(\infty) = 1$, and (d) $f'(\infty) = 0$. Assume $f(A) = (a_1 + A)/(a_2 + A)$. Then condition (a) requires that $a_1 = 2a_2$, and (c) is satisfied by the form of the chosen function. Condition (b) requires that $a_2 = 2$, and condition (d) is also satisfied by the form of the function. Then $f(A) = (4 + A) \div (2 + A)$.

The lift-curve slope given by

$$C_{L\alpha} = 2\pi A/\{A + 2[(A + 4)/(A + 2)]\}$$

compares very accurately with that predicted by other surface theories—e.g., Krienes' solution; electromagnetic-analogy methods; three-quarter chord line solutions; formulas used in the past such as the R. T. Jones edge-velocity method for elliptic loading, which for $A \simeq 6$, leads to $C_{L\alpha} = 2\pi A/(A + 2.5)$; and an experimental formula for rectangular wings, which for $A \simeq 6$, leads to $C_{L\alpha} = 2\pi A/(A + 3)$. For other than elliptic loading

$$C_{L\alpha} = 2\pi A/\{A + 2[(A + 4)/(A + 2)]\ (1 + \tau)\}$$

where $\tau$ is given by line theory, gives acceptable engineering accuracy. For the $A \cong 6$ rectangular wing, $\tau \cong 0.2$. Putting $A = 6$ inside the brackets gives directly the previous two formulas.

Applying simple-sweep theory to the section coefficient leads to acceptable values of $C_{L\alpha}$ for swept wings having approximately elliptic loading. Then substitute $(\beta C_{L\alpha}/\kappa \cos \Lambda_\beta)$ for $C_L$ and $(\beta A/\kappa \cos \Lambda_\beta)$ for $A$, where $\tan \Lambda_\beta = \tan \Lambda_{1/2}/\beta$ and where $\Lambda_{1/2}$ is the sweep angle of the mid-chord line of the wing.

## Vortex-Ring Cascade and Turbulence Transition


Vivian O'Brien

*Applied Physics Laboratory, The Johns Hopkins University, Silver Spring, Md.*


April 29, 1957

THE FACT that vortex rings tend to decay by a cascade process has been known for some time (see, for example, Sadron[1]), and interest in the process has recently been revived by Hsu[2] who describes the ring behavior under density variations. The following brief comments are prompted by personal observations over a period of time.

The direction of growth of the subvortices is found to depend on the relative densities of the ring fluid and the still medium and the ring orientation with respect to gravity force—i.e., up for dye rings less dense than surrounding water, down for more dense, and no growth for no density difference. However, the number of such subrings and the speed with which they form is a function of other properties of the ring. Most important is the viscosity of the fluid. Dyes and inks are suspensions with non-Newtonian viscosity. If rings are formed by drops of the same volume but different concentrations of ink, the initial number of subrings and the number of steps in the cascade process increase with concentration. (The density can be adjusted by adding a little alcohol.) Also, using dissolved salts as, or with, the marking fluid makes the ring quite active. Since the instability of the ring seems closely connected to the nonhomogeneous, non-Newtonian fluid, this chain reaction may very well be peculiar to this case and not descriptive of the usual transition from laminar to turbulent flow. As this instability is only manifest when the ring is moving with small translational velocity relative to the receiving fluid (not specifically mentioned in reference 2), the shearing force should be considerably smaller than that occurring in a boundary layer.

The vorticity of the ring fluid probably plays an important part in the instability mechanism if the redistribution of vorticity shown by the subvortices is taken as significant. If the mathematical formulation of such an instability could be made, it would no doubt add to the knowledge of viscous vortices. The similarity of this phenomenon to others such as the swellings on the rim of a distended water drop falling in air,[3,4] the beading of liquid at the edge of a spinning disk sprayer,[4] and the breakup of liquid jets indicate that such vorticity instability effects may share the responsibility with surface tension effects. Recall Reiner[5] credited vorticity with the "teapot effect" so long ascribed to surface tension.

The significance of the cascade process to turbulence transition is felt to be due to the interaction of the vortex rings. The vorticity induced by a tripping device projected into the boundary layer takes time to grow into turbulence, but the details of the growth period are hazy. Since organized vorticity is known to be present at the beginning of the period and the random distribution of vorticity characteristic of turbulence is the end result, the possibility of studying viscous vorticity modification and interaction to arrive at a mechanism for transition seems to hold promise.

### References


[1] Sadron, C., *Contribution à l'étude experimentale des phenomenes aerodynamiques aux faibles vitesses*, Publ. Sci. et Tech. du Min. de l'Air, No. 22, 1933.

[2] Hsu, C. S., *Vortex-Ring Cascade and a Conjectured Model of Transition to Turbulence*, Readers' Forum, Journal of the Aeronautical Sciences, Vol. 24, No. 4, pp. 313, 314, April, 1957.

[3] Magarvey, R. H., and Taylor, B. W., *Free Fall Breakup of Large Drops*, J. Appl. Phys., Vol. 27, No. 10, October, 1956.

[4] Lane, W. R., and Green, H. L., "The Mechanics of Drops and Bubbles," *Surveys in Mechanics*, p. 187, Plates 2 and 3; also p. 172; Cambridge University Press, 1956.

[5] Reiner, M., *The Teapot Effect, a Problem*, Physics Today, Vol. 9, No. 9, September, 1956.


## Shock-Wave Curvature for Hypersonic Axisymmetric Flow


R. Sedney

*Ballistic Research Laboratories, Aberdeen Proving Ground, Md.*


April 22, 1957

### Introduction

THERE IS GREAT current interest in the hypersonic flow problem involving blunt bodies. The flow near the stagnation point is of particular interest since, for certain kinds of body shapes, the aerodynamic heating is most severe in this region. A number of attempts have been made to represent analytically the axisymmetric flow in this region. Only two of these will be mentioned here. Li and Geiger[1] have given an approximate solution and find that a number of their computed results agree with experimental measurements. In particular, the stagnation-point velocity gradient—made suitably nondimensional—is found to agree fairly well with experimental results even for Mach Numbers as low as 2. However, in arriving at their final results Li and Geiger assume that the radii of curvature of the shock wave and body are equal. The purpose of this note is to report some measurements which were made of the ratio of these radii. It is found that if $2.5 < M < 9$, where $M$ is the free-stream Mach Number, this ratio decreases from 1.7 to 1.2.

If the measured ratio is used instead of the assumed value of unity, the results of reference 1, say for the stagnation-point velocity gradient, will disagree considerably with experimental results for the lower Mach Numbers. Of course the analysis of reference 1 was specifically for hypersonic flows where the ratio of radii is quite close to unity. It would appear that, in some manner, compensating errors were made in the analysis of reference 1 so that agreement at lower Mach Numbers was obtained. Thus it is misleading to take this agreement to be verification of the analytical solution.

It is interesting to notice that if one takes the modified Newtonian approximation—i.e., $C_P = C_{P\,max} \cos^2 \beta$, where $\beta$ is the angle between the normal to the body and the free-stream direction together with $\gamma = 1.4$—then the Bernoulli equation gives a value of the stagnation-point velocity gradient which differs insignificantly from that of reference 1 and thus agrees with experimental data even at the lower Mach Numbers.

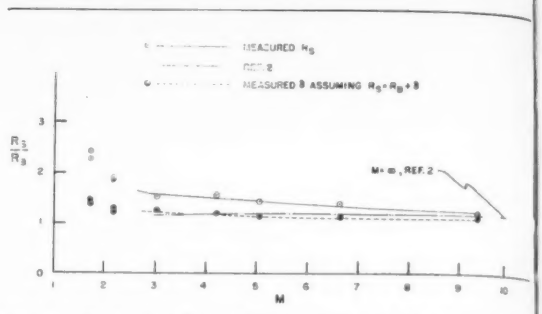


FIG. 1. Ratio of radii of shock wave and body vs. free-stream Mach Number.

### Measurements

To measure the radius of curvature of the shock wave $R_S$, the position of the shock wave in the vicinity of the axis of symmetry was measured on a modified Universal Telereader. The measured points were fitted by both a sphere and parabola. In all cases the two average values of $R_S$ differed by no more than 2 per cent. It is important to take only points "sufficiently close" to the vertex of the shock. The criterion for being sufficiently close was that succeeding points should not give consistently increasing values of $R_S$. The results are presented in Fig. 1 where $R_B$ is the body radius of curvature.

The measurements were made on shadowgraphs and interferograms from three sources: (1) for $M = 1.73$ and 2.17 shadowgraphs of spherically blunted cones, $R_B = 0.385$ in. and 0.770 in., from the Ballistic Research Laboratory supersonic wind tunnel; (2) for $M = 3.05$, 4.22, and 5.08 shadowgraphs of spheres, $R_B = 0.25$ in., from the BRL transonic range; (3) for $M = 6.66$ and 9.4 interferograms of spheres, $R_B = 0.25$ in., from the BRL controlled temperature-pressure range. For the latter the working medium was $N_2$ at 90°K. For the higher Mach Numbers interferograms are convenient because the optical distortion is negligible while the shock wave is still easy to locate.

The shock detachment distance $\delta$ was also measured. Corrections for optical distortion were made when necessary.

### Discussion

In Fig. 1 the measured values of $R_S/R_B$ are given as a function of $M$. The four points for the two lowest Mach Numbers are not joined to the curve because the dissimilarity of the spherically blunted cones is noticed at these low Mach Numbers. This is evidenced by the fact that the higher points correspond to the larger value of $R_B$. The curve, properly extended, should fall below the points for $M = 1.73$ and 2.17.

Using measured values of $\delta$, the curve obtained by assuming $R_S = R_B + \delta$ is shown also. It is seen that this approximation underestimates $R_S$, and this is noticeable even for the highest Mach Numbers.

Finally, the result from reference 2 is given. This analysis[2] uses a perturbation method starting from the basic Newtonian flow results. The perturbation parameters are $M^{-2}$ and $(\gamma-1)\div(\gamma+1)$. For the case shown $\gamma = 1.4$ was used. The agreement is fairly good for the higher Mach Numbers. It is interesting to note that agreement over a larger range of $M$ would be obtained if $R_S/R_B$ was assumed to be independent of $M$, taking it equal to the value for $M = \infty$.

### References


[1] Li, T. Y., and Geiger, R. E., *Stagnation Point of a Blunt Body in Hypersonic Flow*, Journal of the Aeronautical Sciences, Vol. 24, No. 1, pp. 25-32, January, 1957.

[2] Chester, W., *Supersonic Flow Past a Bluff Body with a Detached Shock Part II, Axisymmetrical Body*, Journal of Fluid Mechanics, Vol. 1, Part 5, p. 490, November, 1956.

# Prediction of Turbulent Boundary-Layer Separation

James M. Robertson
Professor, Department of Theoretical and Applied Mechanics, University of Illinois, Urbana, Ill.
May 6, 1957

## Introduction

One of the major problems of turbulent boundary-layer flow in adverse pressure gradients is the prediction of separation. Several papers have recently discussed this question. D. A. Spence[1] notes that the velocity outside the boundary layer may only decrease in a ratio of seven tenths to a half without separation and that an increase in overall Reynolds Number should delay separation. H. Schuh[2, 3] relates the separation conditions to the initial value of the shape parameter $H$.

The present communication indicates another method of turbulent boundary-layer analysis which leads to qualitative indications regarding the occurrence of separation in two-dimensional boundary layers subjected to adverse pressure gradients.

## Method of Boundary-Layer Analysis

The prediction of separation is based on an analysis method developed by D. Ross.[4, 5] Following the observation of the existence of an inner, or wall, and an outer velocity distribution region, Ross employed a separate form parameter $D$ to characterize the outer flow. Since the flow in the outer region is not intimately related to that at the wall, the advantages of this approach are considerable. For the inner region, Ross uses the logarithmic wall-type law which is commonly accepted as suitably depicting the velocity distribution, even when the flow is acted on by strong pressure gradients.

For the outer flow region, the three-halves power-deficiency law of Darcy (1858) and Prandtl (1925) is found to be most appropriate.

$$1 - (u/U) = D(1 - y/\delta)^{3/2} \tag{1}$$

where $u$ is the velocity at wall distance $y$, $U$ is the velocity just outside the boundary layer, $\delta$ is a boundary-layer disturbance thickness, and $D$ is a parameter descriptive of outer region alone. Ross[4, 5] has found good agreement between this law and measured velocity profiles under a wide variety of conditions. For flat plates he finds $D = 8.4\sqrt{c_f/2}$ and for smooth (and rough[6]) pipes $D = 5.1\sqrt{c_f/2}$. The differences in $D$ for these two cases is thought to be due to intermittancy at the outer edge of the boundary layer.

For predicting the behavior of turbulent boundary layers under various external conditions, Ross[4, 5] develops an outer flow parameter which is a function of distance but not local conditions, thus,

$$\delta U_\theta/DU = \text{function}\,(X) = A(X - X_0) + (\delta/D)_0 \tag{2}$$

where the subscript 0 refers to the initial conditions. Eq. (2) is found to apply to plane two-dimensional flows of all kinds with the factor $A = 0.025\,(1 + 12\sqrt{c_f})$ computed for the initial constant-pressure boundary layer. One might expect that axisymmetrical flows would also follow Eq. (2), but studies at The Pennsylvania State University[7, 8] and recently at the University of Illinois have indicated otherwise.

The wall shear stress coefficient is given by Ross' approach as

$$c_f = 2\gamma^2/[0.7 + 5\log(\gamma R_\theta)]^2 \tag{3}$$

where $R_\theta$ is the momentum thickness Reynolds Number and the parameter $\gamma$ is given by the empirical relation $\gamma = 0.90\,(1 - 0.68D)$. The conventional shape parameter is given by the approximate relation illustrated in Fig. 1,

$$H = 0.82 + D + 0.3D^4 + 4\sqrt{c_f/2} \tag{4}$$

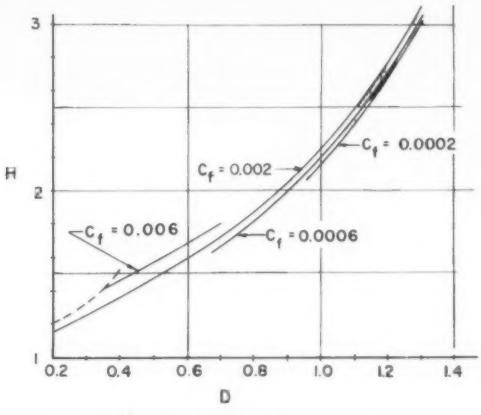


Fig. 1. Relation between shape parameters $H$ and $D$ for various local skin-friction coefficients.

## Separation in Plane Two-Dimensional Flow Past Smooth Plates

With the aid of a simple empirical expression for the rate of boundary-layer growth, developed by Ross and Robertson,[9] Eq. (2) permits one to make quantitative predictions for the occurrence separation in two-dimensional flows along smooth plates. Ross finds that the outer shape parameter $D$ must have a value of about 1.3 for separation. Eq. (2) is rewritten as

$$(\delta/\theta)/D = \{A[(X - X_0)/\theta_0] + [(\delta/\theta)/D]_0\}\,(U\theta_0/U_0\theta) \tag{5}$$

where $\theta$ is the boundary-layer momentum thickness. Within certain limitations,[9]

$$\theta/\theta_0 = (U_0/U)^{2+G} \tag{6}$$

where $G$ is a unique function of the initial value of $R_\theta$. One thus obtains the relation

$$f = (\delta/\theta)/D = [A(\Delta X/\theta_0) + f_0]\,(U/U_0)^{2+G} \tag{7}$$

where $f = (\delta/\theta)/D = \text{function}\,(D)$.

Ross finds the linear relation of Eq. (2) to hold for $\Delta X/\delta_0 \leq 50$. At the initial station the conversion from $\Delta X/\theta_0$ to $\Delta X/\delta_0$ is a unique function of Reynolds Number, and we get the following relation for the allowable velocity reduction without separation:

$$U_s/U_0 = \{f_s/[A'(\Delta X/\delta_0) + f_0]\}^{1/(G+3)} = \{5/[A'(\Delta X/\delta_0) + f_0]\}^{1/(G+3)} \tag{8}$$

where the subscript $s$ is used to denote conditions at separation. The value of $f_s = 5$ corresponds to the separation condition $D = 1.3$. The other parameters $G$, $A'$, and $f_0$ are functions of the initial conditions as represented by the Reynolds Number $R_\theta$. The solution does depend upon how fast separation is approached—i.e., on $\Delta X/\delta_0$—but apparently not on the details of the adverse pressure gradient. The solution of Eq. (8) for the range of Reynolds Number of interest is shown in Fig. 2. The effect of high initial Reynolds Numbers and slower rates of velocity deceleration in delaying separation are clearly evident.

Comparison of the terminal conditions with those found experimentally is also shown in Fig. 2. Excellent agreement is apparent with the experiments by B. G. Newman[10] while only fair agreement appears with that of G. B. Schubauer and P. S. Klebanoff.[11]

## Effect of Surface Roughness on Separation

The analysis just presented has been for plane two-dimensional turbulent boundary-layer flow past a smooth surface. Actual surfaces are sometimes rough, and one is therefore led to the question of whether this helps or inhibits separation. A review of our knowledge of the effect of roughness on turbulent boundary

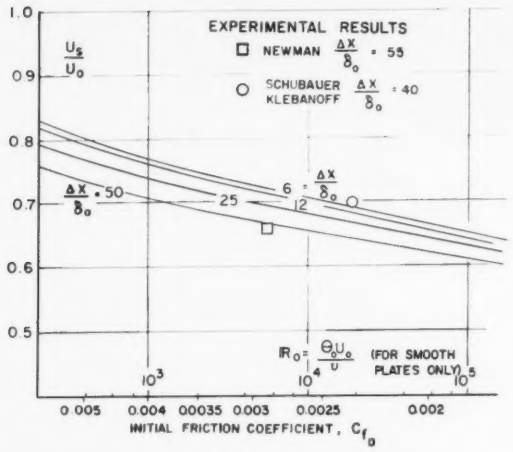


FIG. 2. Free-stream velocity reduction ratio for separation.

layers[6, 12] indicates that the effect of roughness is limited to the inner, or wall, region. Except as the skin friction enters into $D$, the outer flow is independent of surface roughness in the zero pressure gradient case. The outer shape parameter $D$ is found to be given by the same relation in terms of $c_f$ as for smooth surfaces.

Considering $c_f$, rather than $R_\theta$, as the basic parameter defining the flow, it appears that we can simply transfer our analysis to rough surfaces with no further ado. The scale for $c_f$ is thus added to the $R_\theta$ abscissa in Fig. 2 to include rough surfaces in the prediction.

The resultant prediction appears reasonable although it seems a bit surprising that roughness effects enter in only through the initial conditions.

## REFERENCES

[1] Spence, D. A., *The Development of Turbulent Boundary Layers*, Journal of the Aeronautical Sciences, Vol. 23, No. 1, pp. 3–15, January, 1956.

[2] Schuh, H., *On Calculating Incompressible Turbulent Boundary Layers with Arbitrary Pressure Distribution*, Royal Institute of Technology, Division of Aeronautics, Stockholm, Sweden, Tech. Note 41, 1954.

[3] Schuh, H., *On Determining Turbulent Boundary Layer Separation in Incompressible and Compressible Flow*, Journal of the Aeronautical Sciences, Vol. 22, No. 5, pp. 333, 334, May, 1955.

[4] Ross, Donald, *A Study of Incompressible Turbulent Boundary Layers*, Ph.D. Thesis, Harvard University, April, 1953. (Limited distribution as Ordnance Research Laboratory Tech. Memo: ONR Project NR 062-139-1, Penn. State University, June, 1953.

[5] Ross, Donald, *A Physical Approach to Turbulent Boundary Layer Problems*, Trans. American Society of Civil Engineers, Vol. 121, pp. 1219–1254, 1956.

[6] Robertson, J. M., *The Turbulent Velocity Distribution in Rough Pipe*, Paper presented at the Midwest Conference on Fluid Mechanics, Ann Arbor, Michigan, April, 1957.

[7] Uram, E. M., *The Growth of an Axisymmetric Turbulent Boundary Layer in an Adverse Pressure Gradient*, Proc. Second U.S. National Congress of Applied Mechanics, pp. 687–696, ASME, 1955.

[8] Robertson, J. M., and Holl, J. W., *Effect of Adverse Pressure Gradients on Turbulent Boundary Layers in Axisymmetric Conduits*, ASME Paper 56-A-25; Journal of Applied Mechanics, Vol. 24, No. 2, pp. 191–196, June, 1957.

[9] Ross, Donald, and Robertson, J. M., *An Empirical Method for Calculation of the Turbulent Boundary Layer*, Journal of the Aeronautical Sciences, Vol. 21, No. 5, pp. 355–358, May, 1954.

[10] Newman, B. G., *Some Contributions to the Study of the Turbulent Boundary-Layer Near Separation*, Report ACA-53, Aeronautical Research Consultative Committee, Australia, March, 1951.

[11] Schubauer, G. B., and Klebanoff, P. S., *Investigation of Separation of the Turbulent Boundary Layer*, NACA Rep. 1030, 1951.

[12] Hama, F. R., *Boundary-Layer Characteristics for Smooth and Rough Surfaces*, Trans. American Society of Naval Architects and Marine Engineers, Vol. 62, pp. 353–358, 1954.

## Erratum—"Inversion of the Prandtl-Meyer Relation for Specific Heat Ratios of 5/3 and 5/4"*

Ronald F. Probstein
Associate Professor, Division of Engineering, Brown University, Providence, R.I.

May 24, 1957

IN EQ. (4) $\psi$ should read

$$\psi = \left[\frac{\eta^3 + 1}{\eta + 1}\right]^{1/2} + \left\{(\eta + 1)\left[(2 - \eta) + 2\left(\frac{\eta^3 + 1}{\eta + 1}\right)^{1/2}\right]\right\}^{1/2}$$

* Readers' Forum, Journal of the Aeronautical Sciences, Vol. 24, No. 4, pp. 316, 317, April, 1957.

## Change of Address

Since the Post Office Department does not as a rule forward magazines to forwarding addresses, it is important that the Institute be notified of changes in address 30 days in advance of publishing date to ensure receipt of every issue of the JOURNAL and REVIEW.

Notices should be printed legibly and sent directly to:

Institute of the Aeronautical Sciences, Inc.
2 East 64th Street, New York 21, N.Y.